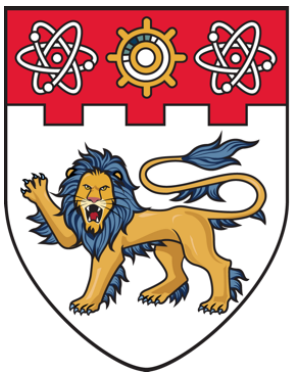

NANYANG TECHNOLOGICAL UNIVERSITY
SINGAPORE

UNDERSTANDING THE IMPACT OF MOLECULAR DESIGN ON SINGLET FISSION FOR POTENTIAL PHOTOVOLTAIC APPLICATIONS

XIAO XINGCHI

SCHOOL OF MATERIALS SCIENCE AND ENGINEERING

2023

UNDERSTANDING THE IMPACT OF MOLECULAR DESIGN ON SINGLET FISSION FOR POTENTIAL PHOTOVOLTAIC APPLICATIONS

XIAO XINGCHI

SCHOOL OF MATERIALS SCIENCE AND ENGINEERING

A thesis submitted to the Nanyang Technological University in partial fulfilment of the requirement for the degree of Doctor of Philosophy

2023

Statement of Originality

I hereby certify that the work embodied in this thesis is the result of original research, is free of plagiarised materials, and has not been submitted for a higher degree to any other University or Institution.

12/09/2023

. . . . . .

Date

. . . . . .

Xiao Xingchi

Supervisor Declaration Statement

I have reviewed the content and presentation style of this thesis and declare it is free of plagiarism and of sufficient grammatical clarity to be examined. To the best of my knowledge, the research and writing are those of the candidate except as acknowledged in the Author Attribution Statement. I confirm that the investigations were conducted in accord with the ethics policies and integrity standards of Nanyang Technological University and that the research data are presented honestly and without prejudice.

12/09/2023

. . . . . .

Date

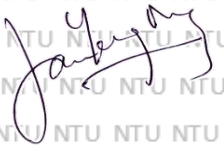

. . . . . .

Prof. Lam Yeng Ming

Authorship Attribution Statement

This thesis contains material from paper published in the following peer-reviewed journal in which I am listed as an author.

Chapter 4 is published as X. Xiao, L. Cheng, D. Bao, Q. Y. Tan, T. Salim, C. Soci, E. E. M. Chia and Y. M. Lam, Unveiling Charge-Transfer Dynamics at Singlet Fission Layer/Hybrid Perovskite Interface. *ACS Appl. Mater. Interfaces* 2023, **15**, 31, 38049-38055. DOI: 10.1021/acsami.3c06933.

The contributions of the co-authors are as follows:

- Prof Lam Yeng Ming provided the initial project direction and edited the manuscript drafts.
- I prepared the manuscript drafts. The manuscript was revised by Dr Teddy Salim, Dr. Bao Di and Prof. Elbert E. M. Chia.
- I co-designed the study with Prof Lam Yeng Ming and performed all the laboratory work at the School of Materials Science and Engineering and the School of Physical and Mathematical Sciences. I also analyzed the data.
- All microscopy, including sample preparation, was conducted by me in the Facility for Analysis, Characterization, Testing and Simulation.
- Dr Cheng Liang assisted in the collection of the transient absorption data.
- Dr Bao Di assisted in the collection of the optical-pump terahertz-probe data.
- Dr Tan Qi Ying assisted in the collection and provided guidance in the interpretation of the time-resolved photoluminescence data.

12/09/2023 Xiao Xingchi

. . . . . .

Date

. . . . . .

Xiao Xingchi

Abstract

Singlet fission (SF) is a multiple exciton generation process, where two or more exciton pairs can be generated with one absorbed photon. By involving the SF process into photovoltaic (PV) devices, the power conversion efficiency (PCE) of the single-junction solar cell is believed to be able to circumvent the theoretical Shockley-Queisser limit. As one of the most promising PV devices, perovskite solar cell (PSC) has achieved a remarkable progress in terms of the PCE during the last decade. However, due to the insufficient understanding of the electronic dynamics at the SF/perovskite interface, the SF-enhanced PSC has never been truly realized. In this thesis, the charge transfer dynamics of SF/perovskite heterojunctions has been comprehensively studied by combining the commercial SF material and perovskite with well-matched energy structures, and the impact of molecular geometries on SF process has been systematically investigated by synthesizing a series of new nitrogen and sulfur-substituted polyacenes. All these findings will contribute to the development of future SF-enhanced PV devices.

First, the charge transfer dynamics of TIPS-pentacene/$Cs_{0.05}(FA_{0.85}MA_{0.15})_{0.95}PbI_{2.55}Br_{0.45}$ heterojunction was investigated. The well-matched energy structures of two layers fulfilled the energy requirements of charge transfer process from the triplet state of TIPS-pentacene to the conduction band of perovskite in 1.2 ps, along with an effective hole transfer process from the valence band of perovskite to the ground state of TIPS-pentacene in nanoseconds. The efficient charge transfer process at the interface resulted in an increase by 20% in the free carrier density of perovskite. These results validate the possibility of augmentation in the carrier density of perovskite by the sensitization of SF process, thus shedding a light on the improvement in the PCE of SF-enhanced solar cells.

Next, a series of novel SF materials consisting of nitrogen and sulfur incorporated polyacenes has been successfully synthesized to investigate the impact of molecular structures on their electronic properties. The energy structure results demonstrated the stabilization effect of substituted nitrogen atoms on the frontier molecular orbitals, which thus would improve the chemical stability. More importantly, the SF process that

was only observed in the dimers, presented a significant structure-function relationship. For the anthrathiadiazole (ATDA) dimers, the directly-linked geometry delivered the fastest triplet generation rate of 1.09 ps, while the phenylene-linked meta geometry showed the lowest triplet generation rate of 270.2 ps. This work reveals the relationship between the SF property and the molecular structures and thus provides a design guide for the novel SF materials applied in the PV devices.

Last, the ATDA-based thin films were fabricated by spin-coating method to investigate their SF properties in solid states. All SF films showed ultrafast SF process occurred in picoseconds with high triplet yield over 100%. The huge improvement of SF dynamics for ATDA monomer and meta-ATDA-dimer from solution to thin film demonstrates the crucial role of intermolecular SF process. While the resemblance of SF dynamics for ortho-ATDA-dimer in both solution and thin film indicates the insignificant impact of intermolecular interaction on the SF process, highlighting the dominance of intramolecular SF pathway in the ortho dimer. Thes results support the hypothesis that SF dimers are more suitable to be applied to the SF-enhanced PV devices.

Lay Summary

The concerns regarding the scarcity and pollution associated with the current market-dominate fossil fuel have led to a growing societal demand of the environmental-friendly and sustainable energy sources. Although photovoltaic cells, which convert the solar energy to electricity, have found extensive applications in both daily life and industrial production, numerous research groups persistently strive for higher power conversion efficiency. Unlike the traditional photovoltaic materials, which generate only one electron-hole pair per absorbed photon, singlet fission (SF) materials are believed to possess the theoretical potential to double the efficiency, given their ability to produce two electron-hole pairs per absorbed photon. However, the study of SF-enhanced solar cells is still far from sufficient. In the first part of this work, the capability of SF materials to increase the charge density of photovoltaic layer has been demonstrated by constructing a well-aligned SF/perovskite heterojunction. In the second part of this work, a series of novel SF materials has been synthesized and systematically examined, which demonstrated that the SF rate and triplet generation yield were remarkably influenced by molecular structures. The last part of this work focused on the SF process in thin-film state, which suggests that the molecular packing patterns have a marginal effect on the molecules with efficient intramolecular SF process. Additionally, an effective hole transfer process at the SF/perovskite interface has been observed. These collective findings proved that SF process can be finely modulated by molecular engineering, thus enabling its application in photovoltaic devices to enhance the charge density.

Acknowledgements

This dissertation would not have been possible without the scholarship and AcRF Tier 1 Grant funded by the Ministry of Education, Singapore.

I would like to express special thanks to my research project supervisor Professor Lam Yeng Ming for her continual guidance and support on both my academic and daily life. She was willing to accept my various ideas and trials, and always able to provide appropriate comments and suggestions. Every time I encountered difficulties, she would never spare her encouragement and patience, and finally put forward feasible solutions.

I want to thank the valuable contributions of Dr. Teddy Salim, as he patiently reviewed numerous drafts of the thesis and improved the quality of the English expression.

I am also grateful to Prof. Elbert E. M. Chia and Prof. Sum Tze Chien for the significant transient absorption measurements conducted by their labs.

Thanks all my group members to provide me with a supportive and heartwarming environment for my PhD life. Specifically, I want to thank Dr. Cho Sung Ju for his guidance on the organic synthesis, Dr. Rao Haixia and Dr. Chen Bingbing for their knowledge on the perovskite solar cells, and Miss Liang Caihong for her calculation work.

Many thanks are conveyed to the support from the Organic Service Laboratory and the Faculty for Analysis, Characterization, Testing and Simulation.

Finally, I really appreciate my family for supporting me to continue my study abroad.

Table of Contents

Table Captions

Figure Captions

dash). Reprint with permission from Ref. 74. Copyright © 2013 American Association for the Advancement of Science.

Figure 2.9 (a) Device schematic and energy diagram with proposed working mechanism of pentacene-PbS QD solar cells. (b) EQE spectrum of the device (blue), along with the absorption spectra of pure pentacene (green) and PbS nanocrystal film (black), the inset shows the absorption onset of PbS nanocrystals in the infrared region. Reprinted with permission from Ref. 78. Copyright©2012 American Chemical Society.

Figure 2.10 (a) Current density plot with a function of ZrO_2 deposition cycle number. The inset is the plot a higher ZrO_2 concentration. (b) Injection yield predicted from kinetic simulation: S_1 injection (blue), T_1 injection (red), and total injection (gray). The dash line is based on the assuming of 50% T_1 injection efficiency. Reprint with permission from Ref. 82. Copyright©2015 American Chemical Society.

Figure 2.11 (a) Device schematic structure and proposed working mechanism of pentacene/PbSe/a-Si solar cell. (b) EQE spectra of device with (green) and without (orange) pentacene layer, the red solid line is the difference in EQE with a scaling factor of three, and the dash line is the pentacene absorption spectra. Reprinted from Ref. 85, with the permission of AIP Publishing.

Figure 2.12 (a) Device architecture of the parallel tandem solar cell. The thickness of each layer in pentacene-C_{60} OPV cell is labeled. (b) EQE spectra measured in tandem solar cell with a reflective silver contact on the pentacene-C_{60} OPV cell. Red line shows the EQE of the whole device, and green line shows the EQE contributed from pentacene-C_{60} cell. Reprint with permission from Ref. 86. Copyright © 2022 American Chemical Society, Open Access.

Figure 2.13 (a) Schematic diagram of the electron transfer dynamics from triplet states of TIPS-pentacene to conduction band of $MAPbI_3$ perovskite. Reprint with permission from Ref. 93. Copyright © 2017 American Chemical Society. (b) Schematic diagram of the two-electron transfer dynamics from correlated triplet states of TIPS-pentacene to conduction band of $MAPbI_3$ perovskite, along with a hole transfer process from

valence band of $MAPbI_3$ perovskite to the highest occupied molecular orbital of TIPS-pentacene. Reprint with permission from Ref. 94. Copyright © 2020 Royal Society of Chemistry.

Figure 3.1 Four steps of spin-coating process.

Figure 3.2 Schematic illustration of thermal evaporation system. Reprinted from *Materials Science in Photocatalysis*, E. I. García-López, G. Marcì, Chpater3 – Preparation of photocatalysts by physical methodologies, Page 37-62, Copyright © 2021, with permission from Elsevier.

Figure 3.3 Magnetic moment rotation in a uniform constant field $\mathbf{B_0}$ with an applied radiofrequency pulse. Reprint with permission from Ref. 8. Copyright © 1973 Springer Nature.

Figure 3.4 Schematic illustration of Bragg's Law.

Figure 3.5 Schematic diagram of AFM. Reprint with permission from Ref. 7. Copyright © 2012 INTECH.

Figure 3.6 Specimen interaction volume.

Figure 3.7 Schematic illustration of a three-electrode system for CV measurements. Reprint with permission from Ref. 17. Copyright © 2018 American Chemical Society, Open Access.

Figure 3.8 (a-g) Concentration profiles of Fc (green) and Fc^+ (blue) vs the distance from the working electrode at different points shown in h. (h) Cyclic voltammogram of Fc^+ and Fc. (i) Potential profile of a whole cycle. Reprint with permission from Ref. 17. Copyright © 2018 American Chemical Society, Open Access.

Figure 3.9 Schematic presentation of electronic transitions.

Figure 3.10 Photophysical process in a molecule after absorbing photon. S_0 = ground state, S_1 = first excited singlet state, T_1 = first excited triplet state, A = absorption, F = fluorescence, P = phosphorescence, ISC = inter system crossing.

Figure 3.11 UPS spectrum of bulk MoS_2 with energy level diagram (inset).

Figure 3.12 Scheme of TA spectroscopy. Reprint with permission from Ref. 24. Copyright © 2009, Springer Nature, Open Access.

Figure 3.13 Illustration of different contributions to TA spectrum. [25]

Figure 3.14 Scheme of an OPTP experimental setup. Reprint with permission from Ref. 27. Copyright © 2011 American Physical Society.

Figure 3.15 (a) Schematic illustration of OPTP measurement on single-walled carbon nanotube (SWCNT) dispersion. (b) Photoconductivity dynamics of functionalized SWCNT with different defect densities. Reprint with permission from Ref. 28. Copyright © 2022 The Authors. Published by American Chemical Society, Open Access.

Figure 4.1 FESEM images of as-fabricated films: (**a, d**) perovskite, (**b, e**) TIPS-pentacene and (**c, f**) bilayer films in low (up) and high (down) magnification, respectively.

Figure 4.2 (**a**) Cross-sectional FESEM image of bilayer film. Vertical distance profiles and AFM images of (**b**) perovskite and (**c**) TIPS-pentacene films.

Figure 4.3 Thin film XRD patterns of as-fabricated films: perovskite (red), TIPS-pentacene (blue) and bilayer (black). The green circles denote the XRD peaks of ITO substrate.

Figure 4.4 (**a**) UV−vis absorption spectra of perovskite (red), TIPS-pentacene (blue) and bilayer (black) films. (**b**) Zoomed-in UV−Vis absorption spectrum of TIPS-

dash-dot lines are ascribed to the ITO substrate.

Figure 6.3 (**a**) UV-Vis absorption spectra of ATDA-based SF films. Tauc plots of (**b)** ATDA, (**c**) ortho-ATDA-dimer, (**d**) meta-ATDA-dimer and (**e**) para-ATDA-dimer. (Replotted from the corresponding UV-Vis absorption spectra).

Figure 6.4 UPS spectra of (**a**) ATDA, (**b**) ortho-ATDA-dimer, (**c**) meta-ATDA-dimer and (**d**) para-ATDA-dimer films at cut-off (up) and edge (down) region.

Figure 6.5 Transient absorption spectra under pump pulse at 610 nm of (**a**) ATDA, (**b**) ortho-ATDA-dimer, (**c**) meta-ATDA-dimer and (**d**) para-ATDA-dimer films.

Figure 6.6 Normalized transient absorption kinetic profiles (scattering dots) and fitting plots (solid lines) under excitation wavelength of 610 nm of (**a**) ATDA, (**b**) ortho-ATDA-dimer, (**c**) meta-ATDA-dimer and (**d**) para-ATDA-dimer films at probe wavelength of singlet and triplet signals.

Figure 6.7 Energy structure diagram of ATDA-based films and perovskite film.

Figure 6.8 FESEM images of (**a**) perovskite, (**b**) ATDA/PVK, (**c**) ortho-ATDA-dimer/PVK and (**d**) meta-ATDA-dimer/PVK films in (up) low and (down) high magnification.

Figure 6.9 Cross-sectional FESEM images of (**a**) ATDA/PVK, (**b**) ortho-ATDA-dimer/PVK and (**c**) meta-ATDA-dimer/PVK films on the ITO glass substrate.

Figure 6.10 AFM images of (**a**) perovskite, (**b**) ATDA/PVK, (**c**) ortho-ATDA-dimer/PVK and (**d**) meta-ATDA-dimer/PVK films.

Figure 6.11 Effects of SF films on crystallinity and photophysical properties of in SF/PVK bilayer films. (**a**) Thin film XRD patterns (the green stars denote the diffraction peaks of ITO substrate), (**b**) UV-vis spectra, (**c**) Steady-state photoluminescence (PL) spectra and (**d**) time-resolved PL spectra of perovskite and SF/PVK bilayer films.

Abbreviations

AFM	Atomic Force Microscopy
ATDA	Anthrathiadiazole
BFN	9,9'-Bisfluorenylidene
BPA	Bisphenol
BTA	Benzothiadiazole
CB(M)	Conduction Band (Minimum)
CR	Charge Resonance
CV	Cyclic Voltammetry
DAP	Diazapentacene
DCM	Dichloromethane
DFT	Density Functional Theory
DI	Deionized
DMAP	N,N-dimethyl-4-aminopyridine
DMF	Dimethylformamide
DMSO	Dimethyl Sulfoxide
DPIBF	1,3-Diphenylisobenzofuran
DSSC	Dye Sensitized Solar Cell
EDX	Energy-Disperse X-ray
EQE	External Quantum Efficiency
ESA	Excited State Absorption
ETL	Electron Transport Layer
FA	Formamidinium
FID	Free-Induced Decay
(FT)IR	(Fourier Transform) Infrared
GSB	Ground State Bleaching
HOMO	Highest Occupied Molecular Orbit
HTL	Hole Transport Layer
IBX	2-Iodoxybenzoic Acid
IPA	Isopropanol
IQE	Internal Quantum Efficiency
IRF	Instrument Response Function

ISC	Intersystem Crossing
ITO	Indium Tin Oxide
LUMO	Lowest Unoccupied Molecular Orbit
MA	Methylammonium
MEG	Multiple Exciton Generation
NIR	Near Infrared
NMR	Nuclear Magnetic Resonance
OPTP	Optical-Pump Terahertz-Probe
OPV	Organic Photovoltaic
PCE	Power Conversion Efficiency
PDI	Perylenediimide
PhTDA	Phenazinothiadiazole
PSC	Perovskite Solar Cell
QA	Quinacridone
QD	Quantum Dot
RF	Radio Frequency
SE	Stimulated Emission
SEM	Scanning Electron Microscopy
SF	Singlet Fission
SPM	Scanning Probe Microscopy
SQ	Shockley-Queisser
TA	Transient Absorption
TGA	Thermogravimetric Analysis
THF	Tetrahydrofuran
TIPS	triisopropylsilylethynyl
TLC	Thin Layer Chromatography
TRPL	Time-Resolved Photoluminescence
UPS	Ultraviolet Photoelectron Spectroscopy
UV-vis	Ultraviolet-Visible
VB	Valence Band
XRD	X-Ray Diffraction
XPS	X-ray Photoelectron Spectroscopy

Chapter 1

Introduction

In this chapter, the significance of constructing the singlet fission-perovskite heterojunction is discussed followed by the research gap in the realization of practical singlet fission-enhanced solar cells. The hypothesis and objectives of this project are described, and a brief overview of each chapter is presented. Finally, the major results obtained in this thesis are briefly summarized.

1.1 Hypothesis

Perovskite solar cells (PSCs) have attracted much attention of the scientists and engineers worldwide among the emerging photovoltaic (PV) technologies due to the superior advantages of halide perovskite as light absorber, such as extremely high light extinction coefficient up to 10^5 cm^{-1}, tunable energy bandgap ranging from 1.2 to 2.3 eV, and long excitons diffusion length over micrometers. [1-5] In terms of the power conversion efficiency (PCE), which is considered as the most significant criterion for PV devices, PSCs have made a great progress since 2009 from 3.8% [6] to a remarkable value of 25.7% [7] with outstanding stability satisfying the industrial standards. [8] However, the PCE of single-junction solar cell is still restricted by the theoretical Shockley-Queisser (SQ) efficiency limit of 34% as the excess energy of absorbed photons with energy above the bandgap cannot be utilized. [9,10]

A process to avoid the loss of absorbed energy and boost the PCE of solar cells beyond the SQ limit to 45% is splitting the high energy of absorbed photons into two parts and hence producing more than one exciton, which is called multiple exciton generation (MEG) known in inorganic semiconductors. Like MEG process, in organic molecular chromophores, an analogous pathway is also available, namely the singlet fission (SF) process, where one photoexcited organic chromophore in singlet state (S_1) shares its energy with the neighbouring chromophore in ground-state (S_0) to form a correlated triple pair state (T_1T_1) and finally two separate triplet excitons (T_1). [11-15] The implementation of SF materials in solar cells has been investigated and realized in different architectures, such as organic photovoltaic devices (OPV), [16] quantum dot (QD) solar cells, [17] dye-sensitized solar cells (DSSCs) [18] and silicon solar cells [19]. Pentacene, one of the most known SF molecules, has been applied in PSCs as the hole transport layer (HTL) in literature to enhance the short circuit current and PCE due to the high charge extraction efficiency and favourable energy-level alignment at the pentacene/perovskite heterojunction. [20,21] However, the study on taking the advantages of SF process to boost the PCE of PSCs by designing an efficient SF-perovskite donor-acceptor (D-A) heterojunction has remained without any significant breakthrough to date. [22,23]

Understanding how SF/perovskite heterojunction works is essential to guide the design

of PSCs that can efficiently utilize the triplet excitons generated from the SF process and realize both high power conversion efficiency and external quantum efficiency. As the SF-enhanced PSC has never been demonstrated so far, herein, the hypothesis of this thesis is as follows:

> *This thesis tests the hypothesis that when singlet fission materials with correct molecular design and optimum film morphology are combined with the right photovoltaic absorber, the potential for increase in the charge generation efficiency and higher power conversion efficiency beyond the Shockley-Queisser limit can be realized.*

1.2 Objectives and Scope

The main objectives of this project are to reveal the charge transfer dynamics at the SF/perovskite heterojunctions, and to elucidate the influence of the molecular structures on the electronic dynamics.

First, a standard SF/perovskite heterojunction was prepared by thermally evaporating well-studied SF molecule (6,13-Bis(triisopropylsilylethynyl)pentacene, TIPS-pentacene) film onto a triple-cation perovskite $Cs_{0.05}(FA_{0.85}MA_{0.15})_{0.95}PbI_{2.55}Br_{0.45}$ film. The thickness of each layer was adjusted based on the photochemical and electrochemical measurements. Their morphologies and crystal structures were characterized by X-ray diffraction (XRD) spectroscopy and scanning electron microscopy (SEM). The charge transfer process from TIPS-pentacene to perovskite was proved by transient absorption (TA) and time-resolved photoluminescence (TRPL) measurements, and the enhancement in carrier density brought by charge transfer process was determined by optical-pump-terahertz-probe (OPTP) technique.

Next, several novel SF materials based on polyacene derivatives were synthesized. Incorporation of heteroatoms, such as nitrogen (N) and sulfur (S), is an effective way to tune the electronic properties of polyacenes. The nitrogen substitution will lower the energy levels of the highest occupied molecular orbital (HOMO) and the lowest unoccupied molecular orbital (LUMO), which will lead to a closer π-π stacking and higher energetically stability. [24,25] In addition, the diradical character and frontier

orbital energies of pentacene molecules can be tuned by the introduction of a thiophene ring, resulting in a favourable energy alignment condition for SF. [26] Furthermore, polyacene dimers can undergo intramolecular SF, which is independent to the molecular packing and more suitable for the application in devices. [27] Based on these principles, a series of polyacene derivatives with incorporation of N and S atoms have been successfully synthesized. Their chemical structures were characterized by Fourier transfer infrared (FTIR) spectroscopy and nuclear magnetic resonance (NMR) spectroscopy, and their optical physical properties were measured by ultraviolet-visible (UV-Vis) absorption spectroscopy. The energy structures were determined by cyclovoltammetry (CV) method and ultraviolet photoelectron spectroscopy (UPS).

Finally, the SF dynamics of the as-synthesized materials were measured by TA spectroscopy in both solution and thin film state to study the relationship between intra/intermolecular SF process and molecular geometries. The preliminary study of the charge transfer process in the SF/perovskite heterojunctions was conducted by combining the TA and TRPL measurements.

1.3 Dissertation Overview

The thesis elucidates the charge transfer dynamics at the SF/perovskite heterojunctions and the impact of molecular geometries on the SF electronic dynamics. The findings lead the way to the potential SF-enhanced photovoltaic devices.

Chapter 1 discusses the significance and research gap presented in the thesis on the charge dynamics of SF/perovskite heterojunctions. The objectives and scopes are described followed by a brief summary of main findings and outcomes.

Chapter 2 reviews the development of perovskite and singlet fission materials. The recent studies focusing on SF-enhanced solar cells are summarized. Specifically, the research gap on the SF/perovskite heterojunctions is presented.

Chapter 3 discusses the rational for the selection of materials and characterization techniques used in the thesis. The synthesis routes of novel SF molecules, and fabrication procedures of SF, perovskite and bilayer films are presented followed by the

illustration on the underlying principles and data collection procedures of the characterization methods.

Chapter 4 investigates the charge dynamics in the TIPS-pentacene/perovskite bilayer film. The mechanism of electron transfer process from the triplet states of TIPS-pentacene to perovskite was revealed by the TA, TRPL and terahertz techniques.

Chapter 5 presents the synthesis routes of N and S substituted polyacenes and their dimers. The optical and electronic properties were measured, and the singlet fission dynamics in solution was investigated by TA measurements.

Chapter 6 presents the study of surface morphologies, crystallinity, photophysical properties and singlet fission dynamics in thin film states. The charge transfer dynamics at the SF/perovskite interface was also investigated.

Chapter7 draws together the threads of the thesis and points out the potential future work based on the outcomes obtained from this project. The major results are summarized from the perspective of materials, bilayer heterojunctions towards the implications on the future applications.

1.4 Findings and Outcomes/Originality

This research focuses on the charge transfer dynamics of SF/perovskite heterojunctions and leads to several novel outcomes summarized as follows:

1. The charge dynamics at the interface of TIPS-pentacene and perovskite has been thoroughly elucidated. The electron transfer process from TIPS-pentacene to perovskite has been proved to occur in 1.2 ps after the fast SF process, which increases the charge density by 20% in the perovskite layer.
2. A series of novel SF materials based on N and S substituted polyacenes has been successfully synthesized. The electronic properties and electronic coupling are finely tuned by chemical modification. The variety in SF rate, triplet yield and triplet lifetime demonstrated significant dependence of SF dynamics on the molecular geometries.
3. The analysis on the electronic dynamics of as-synthesized molecules in thin film

states reveals the synergistic effect of intramolecular and intermolecular coupling on SF process. Effective hole charge transfer process at the SF/perovskite interface has been determined, demonstrating the potential for SF-enhanced photovoltaic devices.

References

[1] J. S. Manser, J. A. Christians, and P. V. Kamat, *Chem. Rev.* **2016**, 116, 12956-12008.

[2] J. P. Correa-Baena, A. Abate, M. Saliba, W. Tress, T. J. Jacobsson, M. Grätzel and A. Hagfeldt, *Energy Environ. Sci.*, **2017**, 10, 710-727.

[3] Y. Rong, Y. Hu, A. Mei, H. Tan, M. I. Saidaminov, S. II Seok, M. D. McGehee, E. H. Sargent, and H. Han, *Science*, **2018**, 361, 1214-1221.

[4] A. R. bin M. Yusoff, M. Vasilopoulou, D. G. Georgiadou, L. C. Palilis, A. Abate, and M. K. Nazeeruddin, *Energy Environ. Sci.*, **2021**, 14, 2906-2953.

[5] C. Fu, Z. Gu, Y. Tang, Q. Xiao, S. Zhang, Y. Zhang, and Y. Song, *Angew. Chem. Int. Ed.*, **2022**, 134, e202117067.

[6] A. Kojima, K. Teshima, Y. Shirai, and T. Miyasaka, *J. Am. Chem. Soc.*, **2009**, 131, 6050-6051.

[7] The National Renewable Energy Laboratory (NREL), Best Research-Cell Efficiency Chart, https://www.nrel.gov/pv/assets/pdfs/best-research-cell-efficiencies-rev220630.pdf.

[8] Y. Zhou, L. M. Herz, A. K-Y. Jen, and M. Saliba, *Nature Energy*, **2022**, 7, 794-807.

[9] W. Shockley and H. J. Queisser, *J. App. Phys.*, **1961**, 32, 510-519.

[10] L. C. Hirst and N. J. Ekins-Daukes, *Prog. Photovolt: Res. Appl.*, **2011**, 19, 286-293.

[11] M. B. Smith and J. Michl, *Chem. Rev.* **2010**, 110, 6891-6936.

[12] M. B. Smith and J. Michl, *Annu. Rev. Phys. Chem.* **2013**, 64, 361-386.

[13] N. Monahan and X.-Y. Zhu, *Annu. Rev. Phys. Chem.* **2015**, 66, 601-618.

[14] D. Casanova, *Chem. Rev.* **2018**, 118, 7164-7207.

[15] K. Miyata, F. S. Conrad-Burton, F. L. Geyer, and X.-Y. Zhu, *Chem. Rev.* **2019**, 110, 4261-4292.

[16] J. Lee, P. Jadhav, and M. A. Baldo, *Appl. Phys. Lett*., **2009**, 95, 033301.

[17] B. Ehrler, M. W. B. Wilson, A. Rao, R. H. Friend, and N. C. Greenham, *Nano Lett.*, **2012**, 12, 1053-1057.

[18] J. N. Schrauben, Y. Zhao, C. Mercado, P. I. Dron, J. L. Ryerson, J. Michl, K. Zhu, and J. C. Johnson, *ACS, Appl. Mater. Interfaces*, **2015**, 7, 4, 2286-2293.

[19] M. Einzinger, T. Wu, J. F. Kkmpalla, H. L. Smith, C. F. Perkinson, L. Nienhaus, S. Wieghold, D. N. Congreve, A. Kahn, M. G. Bawendi, and M. A. Baldo, *Nature*, **2019**, 571, 90-94.

[20] G. Ji, B Zhao, F. Song, G. Zheng, X. Zhang, K. Shen, Y. Yang, S. Chen, and X. Gao, *Appl. Surf. Sci.*, **2017**, 393, 417-421.

[21] X. Yang, G. Wang, D. Liu, Y. Yao, G. Zhou, P. Li, B. Wu, X. Rao, and Q. Song, *Current Applied Physics*, **2018**, 18, 1095-1100.

[22] R. Casillas, I. Papadopoulos, T. Ullrich, D. Thiel, A. Kunzmann, and D. M. Guldi, *Energy Environ. Sci.*, **2020**, 13, 2741-2804.

[23] A. J. Baldacchino, M. I. Collins, M. P. Nielsen, T. W. Schmidt, D. R. McCamey, and M. J. Y. Tayebjee, *Chem. Phys. Rev.*, **2022**, 3, 021304.

[24] J. Herz, T. Buckup, F. Paulus, J. Engelhart, U. H. F. Bunz, and M. Motzkus, *J. Phys. Chem. Lett.* **2014**, 5, 2425-2430.

[25] T. Zeng, S. K. Mellerup, D. Yang, X. Wang, S. Wang, and K. Stamplecoskie, *J. Phys. Chem. Lett.* **2018**, 9, 2919-2917.

[26] N. Alagna, J. Han, N. Wollscheid, J. L. P. Lustres, J. Herz, S. Hahn, S. Koser, F. Paulus, W. H. F. Bunz, A, Dreuw, T. Buckup, and M. Motzkus, *J. Am. Chem. Soc.*, **2019**, 141, 8834-8845.

[27] J. Xia, S. N. Sanders, W. Cheng, J. Z. Low, J. Liu, L. M. Campos, and T. Sun, *Adv. Mater.* **2017**, 29, 1601652.

Chapter 2

Literature Review

A review of perovskites, singlet fission and solar cells is provided in this chapter. The crystal structure of perovskites and the development of perovskite solar cells are first briefly reviewed. The fundamental mechanism of the singlet fission process is then illustrated, and the categorization of singlet fission materials is summarized. It is specifically discussed how the incorporation of the heteroatoms (nitrogen and sulfur) affects the optoelectronic properties. In addition, a brief summary of intra- and intermolecular singlet fission is also provided. The recent research advances on implementation of singlet fission materials in different type of solar cells are outlined. At the end, this chapter covers the singlet fission materials-perovskite heterojunctions and presents the remaining outstanding questions.

2.1 Introduction

Renewable energy, especially solar energy, has played an increasingly significant role in the world energy market recently and becomes a choice for solving the global energy crisis and environmental challenges. Solar cells with improved power conversion efficiency (PCE) and lower cost are required to meet the increasing demands of photovoltaic (PV) devices. [1] The perovskite-based solar cell has attracted much attention due to its superiority over other types of solar cells and has made great progress in terms of efficiency since it was first published in 2009. [2] However, the PCE of the single-junction solar cells is limited to the Shockley-Queisser (SQ) value of 34% by its inner depletion. [3] As a result, two major strategies for the photovoltaic devices to improve the PCE have been developed: constructing tandem junction solar cells and implementing multiple-exciton generation (MEG) process.

The tandem junction structure is already quite mature among solar cell technologies, but excessive cost tends to restrict its application. [4] On the other hand, singlet fission (SF), one of the multiple exciton generation processes, can produce two electron-hole pairs with one absorbed photon, which is believed to break the SQ limit when applied in PV devices. [5] The PCE limit of a MEG-based solar cell was theoretically calculated to be 41.9%, which can be even higher (45.9%) than that of a two-junction tandem solar cell (44.6%) if the applied MEG process is an endothermic SF process. In addition, the construct of an SF-based solar cell is much simpler as it can avoid the need for current matching and tunnel junction optimization introduced by tandem junction solar cells. As the thermalization losses are reduced by SF, the lifetime of SF-based solar cells can also be improved due to the reduced working temperature. [6]

In the following sections, a brief review of the molecular structures of perovskite and SF materials is presented. The material selection criteria for SF molecules and acceptors applied in the SF-based solar cells will be outlined. The different types of SF-based solar cells will be highlighted in terms of device structure and efficiency, followed by the prospective realization of SF-perovskite heterojunctions that will deliver enhanced quantum efficiency.

2.2 Overview of Perovskites and Perovskite Solar Cells

2.2.1 Crystal Structures of Perovskites

The perovskites are a class of compounds that share the same crystal structure as calcium titanate ($CaTiO_3$), of which the conventional formula can be described as ABX_3. Specifically, the perovskite used to fabricate solar cells is metal halide perovskite, of which the X site is a halogen anion including fluoride (F^-), chloride (Cl^-), bromide (Br^-) and iodide (I^-) ions. The cations at A site can be either organic, inorganic, or mixture ions, such as potassium (K^+), rubidium (Rb^+), cesium (Cs^+), methylammonium ($CH_3NH_3^+$, MA^+), or formamidinium ($CH(NH_2)_2^+$, FA^+) ions. The most common metal ions at B site are lead (Pb^{2+}) and tin (Sn^{2+}) ions. The variations of each component provide halide perovskites with alternative chemical structures and energy bandgaps, showing excellent adaptability with other materials to achieve high-efficiency solar cells. The ideal perovskite structure applied for PV devices is the α-cubic structure with highest symmetry, as illustrated in Figure 2.1. The BX_6 octahedrals connected by corner sharing to form the backbone strcuture, while the A cations occupy the voids. This hybrid organometal halide perovskite has been known to possess excellent optical and electric properties, including high photon absorption coefficient, long carrier diffusion length, and low exciton binding energy, making it a promising optoelectronic material applied in lasers, photodetectors and solar cells. [7-10]

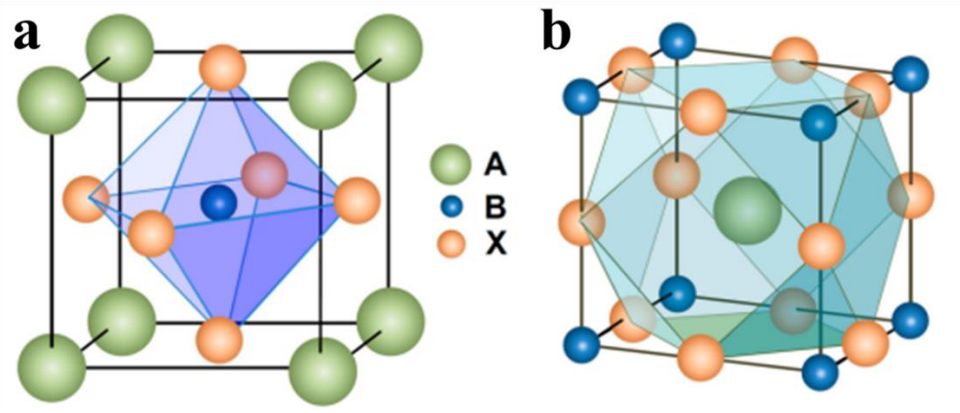

Figure 2.1 ABX_3 perovskite structure showing (a) BX_6 octahedral and (b) AX_{12} cuboctahedra geometry. Reprint with permission from Ref. 7. Copyright © 2014 American Chemical Society

The crystal structure of perovskite can be easily predicted from its chemical formula by using the Goldschmidt tolerance factor t given by [11]

$$t = \frac{1}{\sqrt{2}}\left(\frac{r_A + r_X}{r_B + r_X}\right) \quad \textbf{(Equation 2.1)}$$

where r_A, r_B, and r_X represent the ionic radii of A, B cations and X anions, respectively. In general, the perovskite is believed to have stable photoactive structure when its tolerance factor t lies in the range of 0.75 to 1.00. [12] If the tolerance t decreases below 0.75 with A cations smaller than B cations, the perovskite prefers to form an orthorhombic, rhombohedral, or tetragonal structure rather than a cubic structure. [13] If the tolerance t increases over 1.00 with much larger A cations, two-dimensional (2D) layer or one-dimensional (1D) chain perovskites will be formed. By controlling the composition of A cations with different ionic radii, perovskite with mixed structure of 2D and three-dimensional (3D) can be achieved, which possesses both high moisture resistance and excellent optical properties. [14,15]

Methylammonium lead iodide ($MAPbI_3$) is the first [2] and most extensively investigated perovskite material used for solar cells. The crystal structure of $MAPbI_3$ is normally tetragonal symmetry at room temperature and will undergo phase transitions as the temperature changes. The phase transition to orthorhombic symmetry occurs at −113 ^oC, while the phase transition to ideal cubic symmetry occurs at a higher temperature of over 57^oC. [11,16] The substitution of halide ions by chloride and bromide ions of $MAPbI_3$ can significantly increase the energy bandgap in the corresponding films from 1.55 to 3.1 and 2.4 eV, respectively, as the smaller ionic radius will increase the bandgap, while the substitution of cations by FA^+ only has a slight effect on the bandgap. But the issues associated with $FAPbI_3$ are mainly the higher energy barrier and phase transition from ideal cubic to hexagonal symmetry at room temperature. [17-19]

Perovskites with mixed cations and halides have attracted much more researchers' attention due to the combination of advantages and avoidance of disadvantages brought by each component. Introducing FA^+ can permit higher efficiency, while MA^+ can prevent the perovskite structure from changing from photoactive cubic phase to photoinactive hexagonal phase. [19] Cs^- can also enhance the crystal quality of the perovskite film. [20] Br^- can modify the energy bandgap and give the devices with high performance, while I^- can eliminate the poor stability and phase segregation brought about by Br^-. [19,21] Therefore, mixing cations (Cs^+, FA^+, MA^+, etc.) and halide ions

(Br^- and I^-) has become an important principle for designing new perovskite materials for photovoltaic devices.

2.2.2 Architectures of Perovskite Solar Cells

Miyasaka's group [2] first published a dye-sensitized solar cell in 2009 using perovskite $MAPbI_3$ as a visible-light sensitizer in a liquid electrolyte, achieving an efficiency of 3.8%. Three years later, the first solid-state perovskite solar cell was introduced by Kim and coworkers [22] by applying Spiro-OMeTAD as the solid hole transport layer (HTL). Due to the instability of the liquid electrolyte used in dye-sensitized solar cells, the solid-state configuration has subsequently become the better received architecture by most researchers. From then on, the perovskite solar cells share the similar device architecture, as shown in the Figure 2.2a, consisting of five basic components, including the transparent electrode (indium-doped tin oxide, ITO layer), electron transport layer (ETL), light absorber layer (perovskite), hole transport layer, and metallic electrode (Ag, Au, etc.). Adopted from the configuration of organic solar cells, an inverted structure (Figure 2.2b) has also been established by reversing the sequence of ETL and HTL in regular structures.[23]

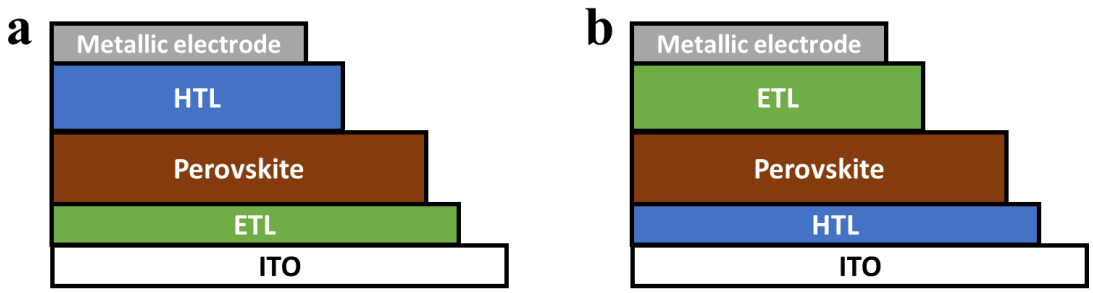

Figure 2.2 Basic structure of perovskite solar cells in (a) regular and (b) inverted configuration.

Favorable energy level alignments of HTL-perovskite and ETL-perovskite junctions are significant for a solar cell to achieve high performance. For HTL material, its highest molecular occupied orbital (HOMO) level and lowest unoccupied molecular orbital (LUMO) level should be higher than the valence band (VB) and conduction band (CB) of perovskite, respectively, to permit the collection of holes and block the electrons from the perovskite layer. For ETL material, its HOMO and LOMO level should be lower than the VB and CB of perovskite, respectively, to permit the collection

of electrons and block the holes from the perovskite layer. In addition, suppression of non-radiative recombination, elimination of hysteretic extension, non-toxicity, and good chemical/thermal stability are also required for charge transport layers. [24]

Open-circuit voltage (V_{oc}), short-circuit current density (J_{sc}), fill factor are the major parameters that determine the power conversion efficiency (PCE) and performance of a perovskite solar cell. The energy bandgap of perovskite is the main factor that decides V_{oc}, of which the thermodynamic limit is relatively lower than the energy bandgap due to the radiative recombination. A sharp absorption onset is also beneficial for reaching a high V_{oc}. Another factor that will reduce the V_{oc} is the non-radiative recombination, which can be diminished by forming compact and pin-hole free perovskite and transport layers. [25-27] Light absorption coefficient and thickness of perovskite layer mainly determine J_{sc}. Reducing the parasitic absorption by other layers and reflection by perovskite layer can increase J_{sc} as well. Morphology of perovskite film can also affect J_{sc}, large perovskite grains with fewer grain boundaries have been reported to enhance the quantum efficiency and J_{sc} of solar cells. [28,29] Fill factor is closely related to V_{oc}, external series resistance and shunt paths. The charge recombination will result in a lower value of the fill factor. [30]

The rate-dependent hysteresis phenomenon, which describes the difference in current-voltage curves of a same perovskite solar cell obtained by scanning in two opposite bias directions, needs consideration as well. Although the hysteretic behavior of PSC depends on the cell measurement parameters, it is inherently dominated by the perovskite layer, including the ferroelectricity, charge trapping at the defects and ionic migration. Consequently, reducing the concentration of defects, restricting the motion of free ions and enhancing the charge transfer process by film processing strategies can effectively reduce the hysteresis. [31,88]

2.3 Overview of Singlet Fission

2.3.1 Fundamental Mechanisms of Singlet Fission

An organic chromophore at ground state S_0 can be excited by external energy (such as heat and light) to a higher energy state, namely singlet state S_1, which can share its energy with adjacent chromophore at S_0. After the energy transfer, both chromophores will reach the same energy state, a triplet excited state T_1. The process that involves the conversion of a singlet exciton into two triplet excitons is called singlet fission (SF), as illustrated in Figure 2.3. The discovery and study of this photophysical phenomenon can be traced back to almost sixty years ago, when Singh and Swenberg found an intermediate excited state formed as two coupled triplet excitons in anthracene and tetracene. [32,33] However, the SF process has not attracted much attention in the photovoltaic field until Hanna and Nozik suggested that a maximum efficiency of over 44.4% for solar cells could be achieved based on SF molecules. [34]

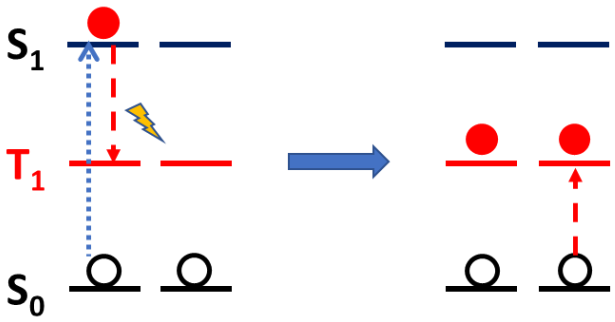

Figure 2.3 Schematic illustration of singlet fission process.

The simplified kinetic scheme of the SF process is generally described as a two-step process,

$$S_0 + S_1 \leftrightarrow {}^1(TT) \leftrightarrow T_1 + T_1 \qquad \textbf{(Equation 2.2)}$$

where ^{1}(TT) is an intermediate correlated triplet pair state, which is the singlet state formed by two coupling triplet states on neighboring identical or different chromophores. [35] The dissociation of ^{1}(TT) into two separate triplet states T_1 occurs through the Dexter mechanism by directly exchanging electrons with the nearest chromophores. The triplet pair then loses its electronic coupling but remains its spin coherence as a singlet, which is sometimes denoted as ${}^1(T \cdots T)$. [36]

It is well-known that an efficient and spontaneous chemical reaction should be exergonic, i.e., the free energy of products is lower than that of reactants. Hence, as

Equation 2.2 indicates, the energy of two triplet excitons T_1 produced should be lower than the energy of a singlet exciton S_1, namely

$$2E(T_1) \leq E(S_1) \pm (0.2\sim0.3)eV \quad \textbf{(Equation 2.3)}$$

However, two issues should be addressed if the materials undergoing exothermic SF are applied in photovoltaic devices, including the low efficiency limited by the low triplet energy and the poor utilization of photon energy due to the energy loss in SF. [37] Consequently, materials undergoing slightly endergonic SF are more suitable for photovoltaic applications. Triplet-triplet annihilation to the next higher triplet state T_2 or quintet excited state Q should be suppressed as well. The energy of Q is normally much higher than twice the energy of T_1, resulting in the formation of Q by triplets' recombination being energetically forbidden. The remaining issue of the formation of T_2 can be avoided if the condition

$$2E(T_1) \leq E(T_2) \quad \textbf{(Equation 2.4)}$$

is satisfied. In addition, the SF process should be more competitive than other decay pathways, such as fluorescence, intersystem crossing, and internal conversion. [38,39]

The intermediate ^{1}(TT) usually proceeds to nine sublevels due to the coupling of two triplet states, which consist of three sublevels each. Since the spin wavefunctions of the nine sublevels are subjected to the external magnetic field, the SF rate and T_1 quantum yield are influenced by the strength and direction of the applied magnetic field. Specifically, increasing the magnetic field leads to a decrease in the population of free triplet excitons. [40,41]

2.3.2 Singlet Fission Materials

Singlet fission materials can be divided into two categories, namely small molecules (monomers, dimers, and oligomers) and large conjugated polymers. Examples of these materials are shown in Figure 2.4.

SF phenomenon was first discovered in anthracene single crystals, and its temperature dependence was then demonstrated in tetracene. [32,33] Pentacene later became the most attractive SF material since its exergonic SF process promises much higher fission rate and efficiency compared with tetracene. [40] However, the poor solubility and high sensitivity to light and oxygen of these acenes restrict their applications in SF-based

devices. The incorporation of side groups, such as 6,13- Bis(triisopropylsilylethynyl) (TIPS), has been demonstrated to improve the solubility and stability by preventing the aggregation. [42,43] Monomers consisting of para-quinone, benzofuran, and perylenediimide (PDI) structures have been studied as SF candidates as well, as shown in Figure 2.4a. Due to the higher stability and larger absorption coefficients compared with acenes and benzofurans, PDI molecules have already been applied as industrial pigments and are considered as the promising candidates for practical SF-based devices because of their more useful range of T_1 energy levels. [44,45] Although these monomers are treated as model chromophores for investigating the SF mechanism in solutions, films and devices, deeper study and further development for real-world applications require the discovery of new alternative SF materials. [6]

Unlike the unexpected influences on SF process brought by complex defect states in molecular crystals or films of monomers, the SF mechanism and dynamics in covalently bonded dimers (Figure 2.4b) of two monomers can be explored in detail by easily controlling the orientation, distance and interaction between monomers. [38] Following the development history of SF monomers, tetracene dimers linked by phenylene and biphenylene were firstly demonstrated to generate triplets via SF process by Bardeen's work in 2006. [46] TIPS-pentacene dimers were then studied theoretically and experimentally by many research groups with different bridge moieties and molecular strategies after the SF phenomenon was first demonstrated by Zirzlmeier's work. [47] By now, the potential of efficient SF has been investigated in many dimers by linking typical monomer chromophores with various bridge moieties, which tend to result in a stronger electronic coupling by directly participating in the interaction between linked chromophores. [38,48] For a SF-utilized device, however, a complete SF process to generate separate triplets is required, which might be an issue in the isolated dimers due to the strong electronic coupling and triplet-triplet annihilation. [49] In this case, either a favorable acceptor or introducing intermolecular coupling is needed to facilitate the separation and diffusion of triplets.

Oligomers (Figure 2.4c) such as *p*-Terphenyl [50] and *p*-sexiphenyl [51] have been studied but were found to deliver poor SF efficiency at low excitation density. Carotenoids was proposed to exhibit SF behavior because of the different fluorescence under magnetic fields. [52] The analysis on the energy of S_1 and T_1 states further

supports that the SF process is favorable in carotenoids. Conjugated polymers (Figure 2.4d) with sufficiently long double bonds can undergo the SF process and exhibit broad light absorption bands due to the π-electron system. The triplet quantum efficiencies of conjugated polymers are typically low; for example, polydiacetylene, the first conjugated polymer that was discovered to show the SF phenomenon by Austin in 1989, [53] only had a yield on the order of 0.1%. Later, many conjugated polymers, such as poly(diethyl dipropargylmalonate), poly (p-phenylene), poly(p-phenylene vinylene) and polythiophene, [5] have been investigated and observed to undergo the SF process. In 2018, Hu and coworkers [54] demonstrated a high triplet yield of over 160% in an isoindigo-based donor-acceptor polymer (IIDDT-Me) and provided a new structural design perspective on the existing D-A polymers to impart SF property.

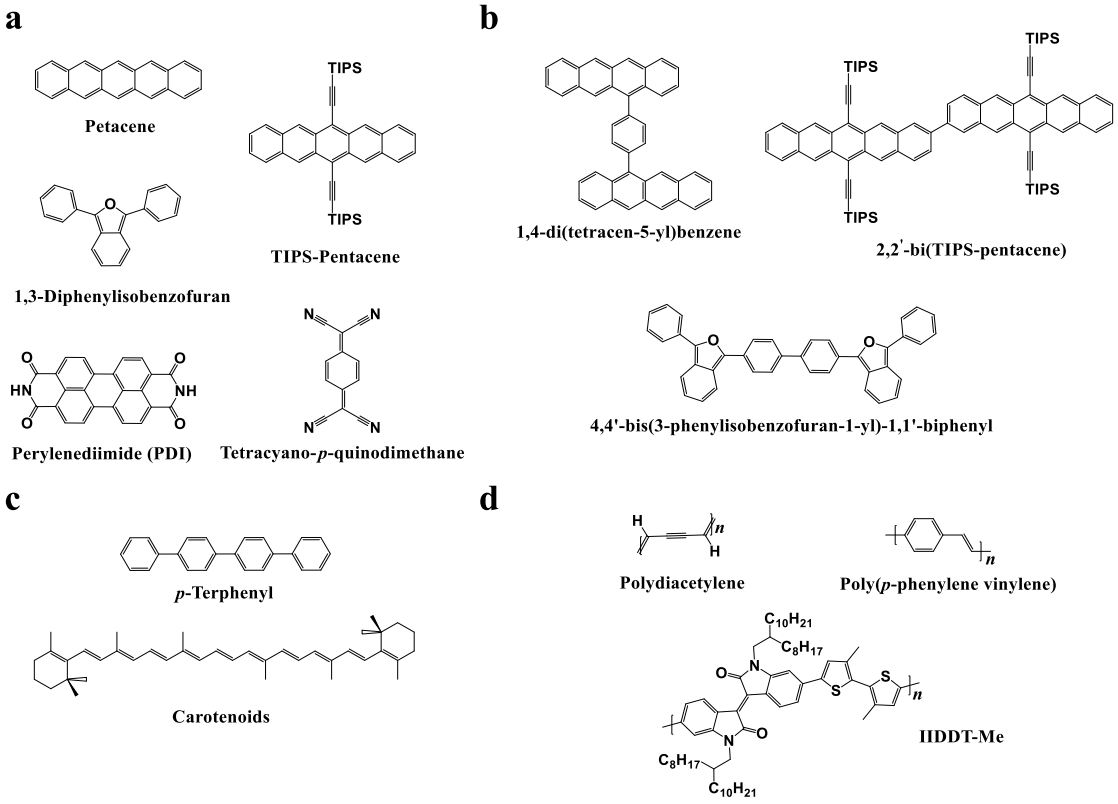

Figure 2.4 Example molecular structures of singlet fission (a) monomers, (b) dimers, (c) oligomers and (d) polymers.

2.3.3 Inter- and Intramolecular Singlet Fission

Depending on the number of molecules involved in the SF process, there are two types of SF: intermolecular SF (involving two or more molecules) and intramolecular SF

(involving only one molecule). [55] Intermolecular SF has been extensively studied in the monomers discussed above. The packing of the monomers and morphology of the deposited films determine both the intrinsic SF rate and the diffusion of triplet excitons. Substitution of side groups will increase the intermolecular distance, resulting in more amorphous films. On the other hand, intramolecular SF has been observed in dimers, oligomers and polymers in which chromophores are covalently linked. The strength of coupling can be modified by the lengths of linking bonds and positions of two chromophores. In addition, intramolecular SF efficiency is independent of the packing of molecules in the film state. However, the strong coupling may also lead to critical triplet-triplet annihilation, restricting the separation and diffusion of triplet excitons. [48] Xia's group has developed a series of terphenyl-bridged TIPS-pentacene tetramers, that took advantages of both inter- and intramolecular SF. By controlling the positions of TIPS-pentacene groups, a rapid triplet pair generation rate can be achieved with weak intermolecular coupling. [56]

2.3.4 Heteroatom Substitutions

Polyacenes, such as tetracene and pentacene, have historically piqued the interest of many research groups as model molecules to systematically investigate SF mechanism and guide the design of new SF compounds through substitution with heteroatoms. [38]

Nitrogen−substituted heteroacenes have been studied for decades as promising n-type organic semiconductors applied in optoelectronic devices because the electron-withdrawing property of N atoms can lower and well delocalize the LUMO energy level. [57] This electron-withdrawing effect can also benefit the SF process when N atoms are introduced in pentacene derivatives by decreasing the S_1-T_1 energy gap and reducing the energy loss during SF. In addition, the solubility and chemical resistance to oxygen and light are improved due to the lower energy levels of frontier molecular orbitals. By changing the position and number of incorporated N atoms, the electronic properties of N-substituted pentacene derivatives can be modified. [58,59] Herz' work [60] proved that diaza-TIPS-pentacene incorporated with two N atoms exhibits an accelerated SF rate compared with pristine TIPS-pentacene, as shown in Figure 2.5. The stabilized frontier molecular orbitals and closer π-π stacking can explain the faster dynamics in diaza-TIPS-pentacene.

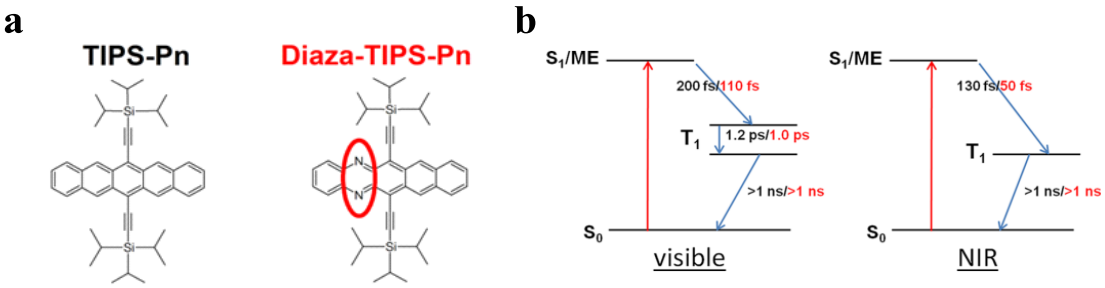

Figure 2.5 (a) Molecular structures of TIPS-pentacene and diaza-TIPS-pentacene; (b) Schematic illustration of singlet fission dynamics in TIPS-pentacene (black numbers) and diaza-TIPS-pentacene (red numbers) for visible and NIR spectral region. Reprint with permission from Ref. 60. Copyright © 2014 American Chemical Society

Due to their excellent electronic and optical properties, thiophene derivatives have been the star molecules applied in high-performance organic optoelectronic fields, which have motivated researchers to investigate the potential SF property of a polyacene in which a benzene ring is replaced by thiophene ring. It has been demonstrated that the substitution of pentacene with thiophene can result in a high absorption coefficient and good charge transport property. Computational calculation results also reveal how the position, number and connection pattern of the thiophene ring will affect the energy levels of frontier molecular orbitals and excited molecular states. [58] Figure 2.6 presents two connection patterns between thiophene and benzene rings, the (α, β) connection pattern can lower the HOMO energy level, while the (β, β) connection pattern can promote an exoergic SF process with fast dynamics.

Figure 2.6 Structure of thiophene-substituted tetracene with (a) (α, β) connection and (b) (β, β) connection.

2.3.5 Optical Cavity-Assisted Singlet Fission

Optical cavity is created by two mirrors to trap the light with correct angle and wavelength, which provides a powerful method to tune the photophysical and

photochemical properties of molecules within confined light fields by formimg hybrid light-matter states (i.e., exciton polaritons). Motivated by the advantages of optical cavity, it is logical to implement SF molecules into such cavity to exploit the possibility of manipulating SF process and thus enhancing SF rate and efficiency. [61-63] S. Takahashi's work [64] has successfully demonstrated that it is possible to modulate the photochemical dynamics of SF process of amorphous rubrene thin films constrained in optical microcavities by changing the cavity photon energy. On the other hand, the triplet-triplet annihilation process, which is the reverse process of SF, can also be controlled in an optical cavity. According to M. Gudem's simulation results [65], the upconversion efficiency of naphthalene was improved by more than 50% in an optical cavity, which rationalized the similar observation in an experimental study.

Recent experimental and theoretical studies have demonstrated the potential of optical cavity-assisted SF to achieve higher efficiency and to tune the properties of the resulting triplet excitons. Despite some remained challenges, including optimizing the cavity designs, improving the material compatibility and understanding the underlying mechanisms, continued research efforts hold the potential to pave the way for next-generation photovoltaic devices with optical cavities. [66,67]

2.4 Singlet Fission Solar Cells

2.4.1 Requirements for Singlet Fission Materials and Acceptors

As discussed in Section 2.3.1, an efficient SF material should satisfy fundamental condition in terms of the energy requirement, as shown in Equation 2.3 and 2.4. The higher energy of T_2 prevents the triplet-triplet annihilation, which prolongs the triplet lifetime and benefits the diffusion and harvest of triplets in devices.

In terms of Equation 2.3, if $E(S_1) > 2E(T_1)$, then SF is exothermic, which permits a fast SF rate and makes the SF process more competitive than other decay pathways since this reaction is both energetically and entropically favorable. However, the exothermic SF process will result in energy loss as waste heat and generate triplets with too low an energy to reach common acceptors. On the other hand, if $E(S_1) < 2E(T_1)$, then SF is endothermic, which is energetically unfavorable but still possible due to the entropy

gain. Because of an extra energy gain, the theoretical efficiency limit of solar cells using endothermic SF is higher than those using exothermic SF. [68] However, the slower SF rate allows other decay pathways to restrict the overall SF yield and efficiency. Both exothermic and endothermic SF can be applied in solar cells, but the merits and drawbacks must be evaluated in each case.

In addition, some other requirements should also be satisfied. First, SF molecules should possess a strong photon absorption with a high coefficient over 10^5 in the visible region, which can significantly reduce the film thickness and increase the number of excitons generated by the SF layer. The high absorption coefficient can be achieved by increasing the conjugated π-electrons in SF molecules. [38] Second, in order for the triplets to be harvested by the absorb layer, the lifetimes and diffusion lengths of triplet excitons should be long enough to allow them to reach the interface. Third, the energy structure of the SF molecule should be aligned with that of the adjacent layer in devices to permit efficient exciton diffusion. The idea energy gap of the acceptor layer is better to be half of the energy gap of SF material, to ensure the photons in different energy regions can be sufficiently absorbed by two layers, respectively. [69] The stability of SF materials is another issue that should be taken into consideration. The acceptable lifetime of a practical SF-based solar cell should be at least five to ten years. Organic molecules including many SF materials, usually have poor stability, which can degrade under light illumination. As discussed in Section 2.3, the addition of side-functional groups and the substitution of heteroatoms can significantly improve the resistance of SF materials to air, light and heat.

Besides the intrinsic properties of SF molecules, the morphology and crystallinity of SF-materials layers can as well strongly influence the performance of SF-based solar cells, especially for the intermolecular SF materials. For example, slip-stacked packing is generally better than edge-on packing for most SF materials. For intramolecular SF, the distance and configuration of two chromophores determine the electronic coupling strength. Since the performance of intramolecular SF is not much related to the packing of molecules, it is much preferable to be applied in solar cells with bulky heterojunction structures. However, the triplet-triplet annihilation caused by strong electronic coupling must be mitigated. [39, 70]

The basic requirement for an ideal acceptor applied in the SF-based device is the energy alignment with SF chromophore. The CB or LUMO energy level of the acceptor should be aligned with the T_1 energy level of the SF molecule. If the CB or LUMO level is higher than the T_1 level, the exciton transfer between the acceptor and SF layer will not occur or will occur at a much slower rate. If the CB or LUMO level is much lower than the T_1 level, a huge amount of energy will be lost as heat waster during the transfer process, which will result in poor efficiency in the end. In addition, the acceptor must perform an efficient charge transfer mechanism to accommodate the electrons/holes and possess an efficient charge extraction property to diffuse the exciton and restrict the annihilation loss.

2.4.2 Singlet Fission-Enhanced Solar Cells

The first demonstrations of the implementation of SF materials, which are mostly organic molecules, for solar cells were in organic photovoltaic (OPV) devices in the early 2000s. In 2004, Yoo and coworkers [71] fabricated an OPV using a pentacene-C_{60} heterojunction (Figure 2.7a) and achieved a peak external quantum efficiency (EQE) of 58% at the wavelength where the pentacene layer absorbs most (λ_{max} = 670 nm). This high EQE was attributed by the authors to the long exciton diffusion length of pentacene. The SF process has not been the primary interest in the OPV community until 2009. The first work demonstrating the huge potential of SF material is based on an organic photodetector consisting of 30 multilayered pentacene-C_{60} heterojunctions (Figure 2.7b) fabricated by Baldo's group. [72] Each pentacene-C_{60} bilayer was made up of a 2 nm pentacene layer and a 1 nm C_{60} layer, aiming to reduce the exciton losses during the diffusion process from the pentacene layer to the interface. The SF contribution to the EQE under a working voltage of -3.5 V as high as 145% was demonstrated by detecting a photocurrent reduction of 2.7% under a magnetic field. This work also indicates the influence of pentacene layer thickness on the triplet diffusion efficiency and SF yield.

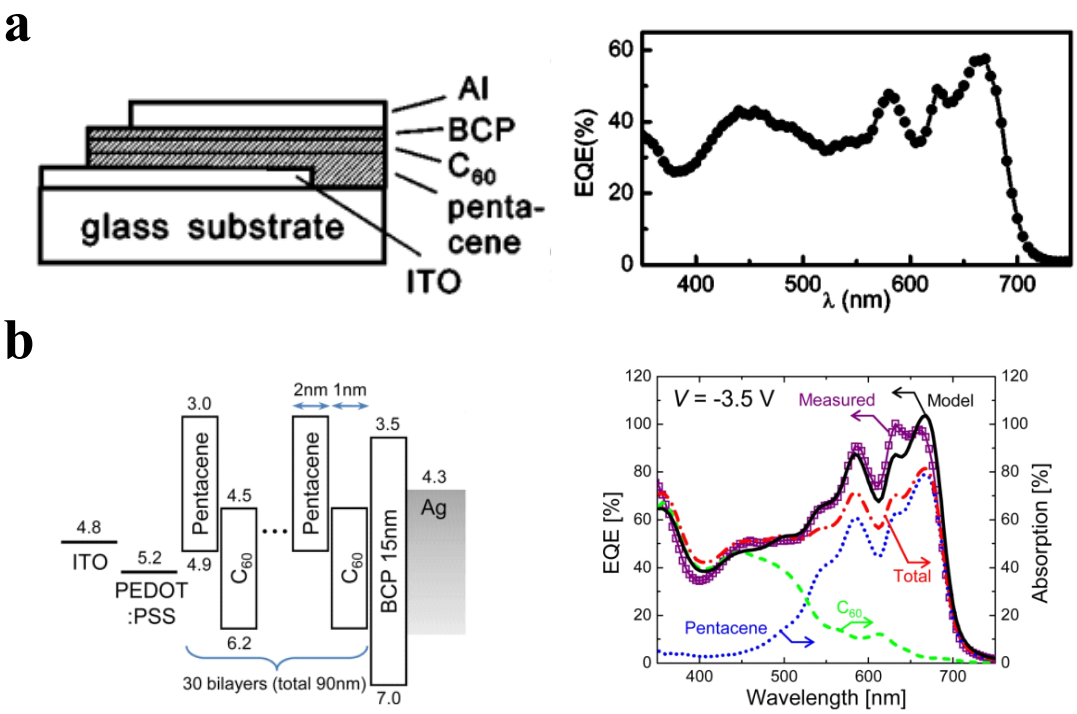

Figure 2.7 (a) Schematic device structure of pentacene/C_{60} heterojunction based OPV (left) and EQE spectrum at different incident light wavelength of the device (right), Reprinted from Ref 71, with the permission of AIP Publishing; (b) Schematic energy diagram of pentacene/C_{60} multilayer OPV (left) and EQE spectrum of the device (right), Reprinted from Ref 72, with the permission of AIP Publishing.

In 2011, Jadhav *et al*. [73] constructed the first SF-involved OPV solar cell by inserting a thin copper phthalocyanine (CuPC) layer between tetracene and C_{60}. The CuPC layer modified the energy level alignment, allowing the corresponding devices to show a superior EQE over the devices without CuPC at wavelengths over 550 nm. In 2013, Congreve and coworkers [74] successfully demonstrated a pentacene-enhanced OPV device with an EQE over 100% at the wavelength of 670 nm (Figure 2.8b) by adding an additional poly(3-hexylthiophene-2,5-diyl) (P3HT) layer as the electron blocking layer. This structure, as illustrated in Figure 2.8a, later became the standard OPV structure consisting of polyacene-C_{60} heterojunction followed by other groups. Some other SF materials have also been applied to OPV devices. Pandey demonstrated that the crystallinity of rubrene film can significantly affect the SF rate and triplet-triplet annihilation in the OPV device with rubrene/C_{60} heterojunction. [75] In 2017, Kawata *et al*. fabricated OPV devices using 9,9'-bifluorenylidene (BFN) and its derivatives as *p*-type materials. The density functional theory (DFT) calculations of the energy

structures indicated the SF character of BFN and its derivatives. By detecting the photocurrent under a changing magnetic field, the contribution of triplet excitons to the photocurrent was demonstrated in alkylbithiophene-substituted BFN devices. [76]

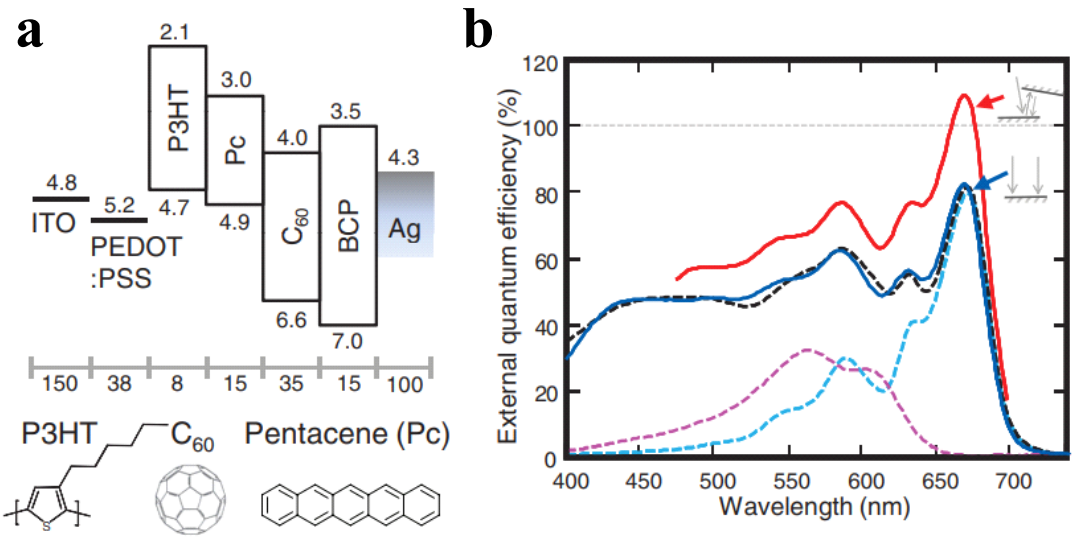

Figure 2.8 (a) Schematic energy diagram of a pentacene/C_{60} OPV with P3HT layer. The thickness of each layer was labeled in nanometers. (b) EQE spectrum of the device without optical trapping (blue line), and device with a mirror reflecting the residual pump light (red line). The dash lines are EQE spectra obtained from modelling: modeled pentacene (blue dash), modeled P3HT (purple dash), modeled device (black dash). Reprint with permission from Ref. 74. Copyright © 2013 American Association for the Advancement of Science.

Since the PCE of OPV devices was generally low (<10%), the chance of SF-based OPV devices to exceed the SQ limit is not high. [41] However, the high EQE over 100% observed in SF-based OPV devices has enticed researchers to implement SF materials in other solar cells. Quantum dot (QD) solar cells share a similar donor-acceptor structure to OPV devices but use the QDs as the electron acceptors. QDs are inorganic nanocrystals with sizes smaller than the exciton Bohr radius (a few nanometers), which endows them the tunable discrete energy levels due to quantum confinement effects. [77] Therefore, the energy levels of QDs can be precisely adjusted to match SF chromophores by controlling the sizes of nanoparticles. QDs are also solution processable, which makes the QD solar cells more promising when produced commercially to reduce the production costs.

In 2012, Greenham's group reported their work on SF-enhanced QD solar cells with the hybrid pentancene-PbS nanocrystal heterojunction (Figure 2.9a). [78] The energy gap of PbS nanocrystals was finely tuned to 0.7 eV to match the energy of T_1 generated from pentacene through the SF process. As shown in the EQE spectrum (Figure 2.9b), a prominent rise at the pentacene absorption maximum (680 nm) was observed, which indicated the contribution of pentacene to the photocurrent. They also investigated the influence of the addition of an extra ETL on the device performance, such as a 100 nm of ZnO nanocrystal film, which successfully improved the PCE from 0.16% to 0.85%. The same group later changed the type of nanocrystals from PbS to PbSe and achieved a high EQE of over 80% and a PCE of 4.7%. [79] The energy bandgap of PbSe nanocrystal films could be controlled in the range of 0.67 − 1.20 eV, and the pentacene contribution on the EQE spectra from corresponding solar cells presented a significant decrease when the PbSe film bandgap was in the range of 1.08 − 1.2 eV. This correlation between EQE results and bandgap of nanocrystals can be used to estimate the T_1 energy of pentacene to be 0.85 − 1.0 eV after the photocurrent correction. TIPS-pentacene, a pentacene derivative with higher stability and solubility, was then applied in the same configuration with a 1.25 eV PbS nanocrystal film as the acceptor, providing the highest PCE of 4.8% and internal quantum efficiency (IQE) of 170% to date in SF-based QD solar cells. [80]

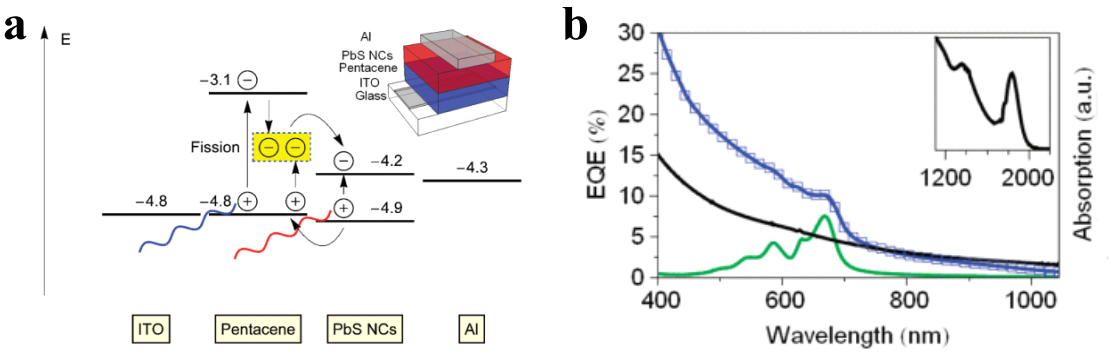

Figure 2.9 (a) Device schematic and energy diagram with proposed working mechanism of pentacene-PbS QD solar cells. (b) EQE spectrum of the device (blue), along with the absorption spectra of pure pentacene (green) and PbS nanocrystal film (black), the inset shows the absorption onset of PbS nanocrystals in the infrared region. Reprinted with permission from Ref. 78. Copyright©2012 American Chemical Society.

One common issue that limits the potential of OPV and QD solar cells is the high triplet diffusion loss caused by the long SF-acceptor distance. Dye-sensitized solar cells (DSSCs), which consist of a bulk dye-semiconductor heterojunction, can significantly decrease the exciton diffusion loss due to the short diffusion distance and large charge collection area as the dye molecules are directly absorbed onto the semiconductor surface. [81] The first SF-enhanced DSSC was fabricated by Schrauben *et al*. in 2015. [82] The 1,3-diphenylisobenzofuran (DPIBF) was coated as the sensitizer on the mesoporous TiO_2 with a varying thickness of ZrO_2 space layer which can reduce the electron injection rate of the S_1 state from DPIBF layer and thus allow the triplet formation via the SF process. As shown in Figure 2.10, the photocurrent density shows a discontinuity in an overall decreasing trend when the modeled injection rate of T_1 surpasses the injection rate of S_1 as a function of ZrO_2 film thickness. Although the DSSCs delivered poor performance (PCE = 1.1%, V_{oc} = 0.51 V, J_{sc} = 3.3 mA/cm^2) and a low IQE of 70%, they still provided a convenient platform to investigate the triplet injection rate after SF incorporation at the interface.

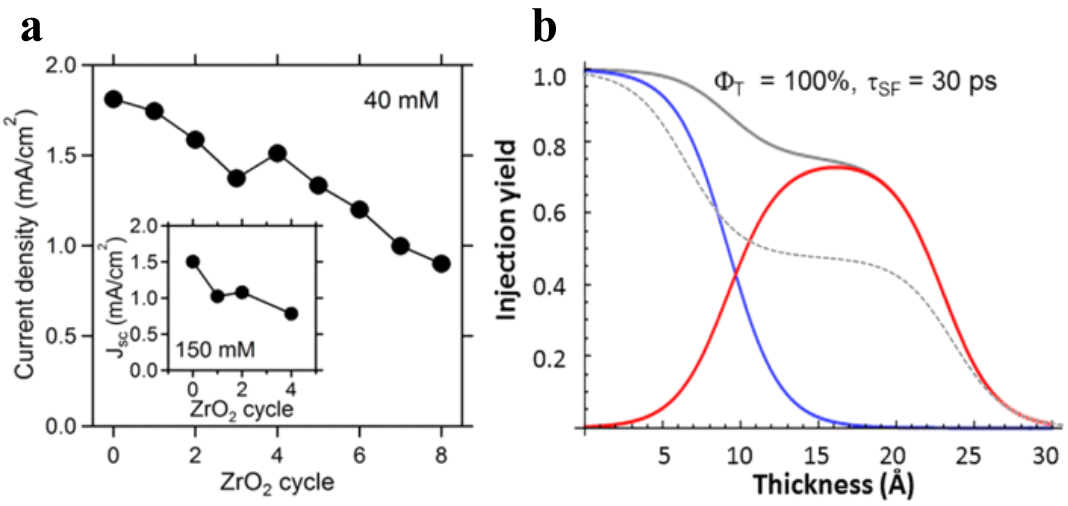

Figure 2.10 (a) Current density plot with a function of ZrO_2 deposition cycle number. The inset is the plot a higher ZrO_2 concentration. (b) Injection yield predicted from kinetic simulation: S_1 injection (blue), T_1 injection (red), and total injection (gray). The dash line is based on the assumption of 50% T_1 injection efficiency. Reprint with permission from Ref. 82. Copyright©2015 American Chemical Society.

The first paper on DSSCs incorporated with pentacene derivatives was published by Kunzmann and coworkers in 2018. [83] Based on the pump-probe femtosecond-

transient absorption (fs-TA) experiments, the interfacial charge injection from low-lying triplet states of pentacene-based monomer to metal oxide substrate occurred through the intercrossing system (ISC) pathway. While for the pentacene-based dimer, the interface charge injection was mainly contributed by the triplets from the efficient intramolecular SF process. A peak IQE of nearly 130% was achieved for pentacene-dimer based DSSCs on the $In_{60}Zn_{40}O$ substrate in the presence of 0.1 M Li^+ electrolyte, which clearly demonstrated the photocurrent contribution from triplet excitons. This work also provides a pathway to efficient SF-based DSSCs through intramolecular SF in dimers, other than intermolecular SF in monomers, of which the efficiency is notably restricted by precise morphological control of the deposited layer on the nanostructured semiconductor surface.

Compared to OPVs, QD solar cells and DSSCs, silicon solar cells are by far the most prevalent commercial photovoltaic devices worldwide. The PCE of a single-junction silicon solar cell has reached 27.6% [84], which approaches the SQ limit. It is no doubt that applying the SF materials to further boost the performance of commercial silicon solar cells presents an exciting prospect.

The investigation on SF-based silicon solar cells began in 2012, when Ehrler *et al*. [85] fabricated a triple-layered device consisting of amorphous silicon, PbSe nanocrystals and pentacene film, as shown in Figure 2.11a. The photons in the visible range are absorbed by the pentacene layer to generate triplet excitons via SF, which then diffuse through the PbSe nanocrystal layer to the amorphous silicon layer. No photocurrent was detected in the device without the protective PbSe layer, which indicates the pentacene film might be damaged during the sputtering process of the amorphous silicon layer. As shown in Figure 2.11b, the difference in the EQE spectra between the device with and without pentacene can be attributed to the absorption of the pentacene layer, which clearly demonstrated the photocurrent contribution from pentacene triplets as pentacene undergoes an ultrafast and highly efficient SF process.

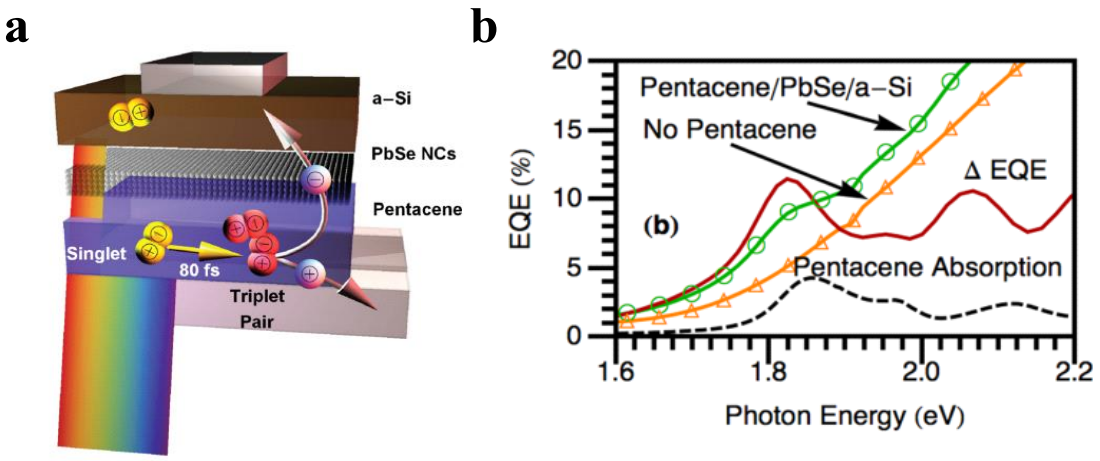

Figure 2.11 (a) Device schematic structure and proposed working mechanism of pentancene/PbSe/a-Si solar cell. (b) EQE spectra of device with (green) and without (orange) pentacene layer, the red solid line is the difference in EQE with a scaling factor of three, and the dash line is the pentacene absorption spectra. Reprinted from Ref. 85, with the permission of AIP Publishing.

The first tandem solar cell utilizing SF by electrically connecting a pentacene-C_{60} OPV cell in parallel with a commercial crystalline silicon cell was also constructed by Ehrler's group in 2017, as illustrated in Figure 2.12a. [86] This parallel tandem cell configuration can avoid the efficiency drop caused by the current mismatch in conventional series tandem cells under diffuse illumination and is thus more cost-effective to gain a larger market share. The decreasing trend of photocurrent under an increasing magnetic field confirmed the photocurrent contribution from triplet excitons generated via SF process that occurred in the top pentacene-C_{60} OPV cell. To avoid the light losses during EQE measurements, the device was measured in a modified configuration, as shown in Figure 2.12b, in which the light can be absorbed twice by the SF OPV layer before reaching the silicon cell. The peak EQE reaches 106% at the photon energy of around 1.85 eV where the pentacene layer absorbs most strongly and contributes 60% of EQE. The EQE exceeding 100% implies that the MEG process is involved in this tandem solar cell.

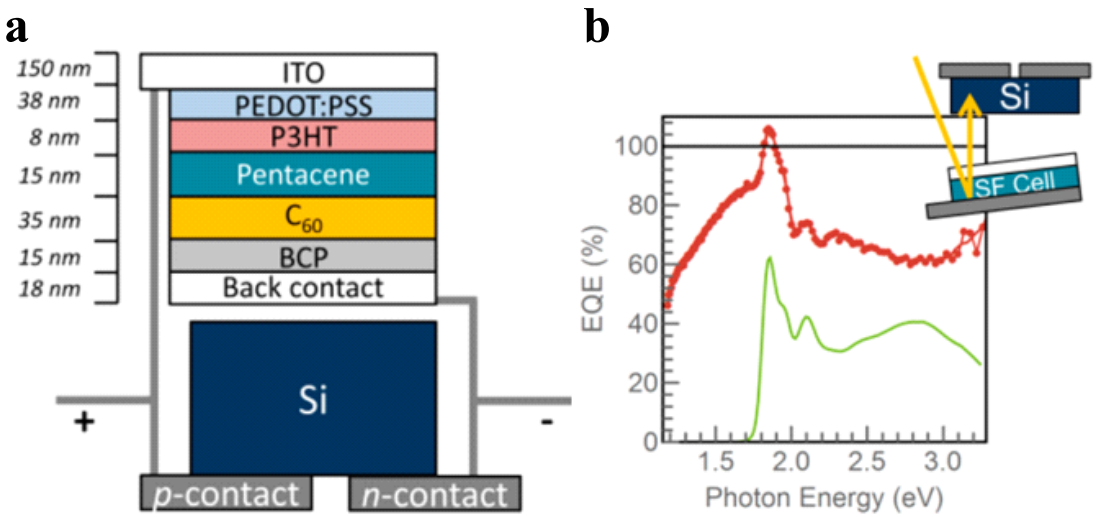

Figure 2.12 (a) Device architecture of the parallel tandem solar cell. The thickness of each layer in pentacene-C_{60} OPV cell is labeled. (b) EQE spectra measured in tandem solar cell with a reflective silver contact on the pentacene-C_{60} OPV cell. Red line shows the EQE of the whole device, and green line shows the EQE contributed from pentacene-C_{60} cell. Reprint with permission from Ref. 86. Copyright © 2022 American Chemical Society, Open Access.

Triplets directly transferred from SF molecules to crystalline silicon can also be used in SF-enhanced silicon solar cells. In this configuration, tetracene is much more favorable due to its higher triplet energies, which are comparable with the crystalline silicon energy gap. MacQueen *et al*. [87] created the first direct SF-sensitized silicon solar cell in 2018 by directly depositing the tetracene film on the *n*-type crystalline silicon layer to form an organic-inorganic heterojunction. Although the PCE of tetracene-based silicon solar cells remained almost the same as the control devices, the optical modeling of the EQE spectrum indicated an 8% photocurrent contribution from the tetracene layer. The triplet exciton transfer does occur in this configuration but is insufficient to improve the device performance. A breakthrough in tetracene-based silicon solar cells was achieved by Baldo's group in 2019. [88] The device with an 8 Å of hafnium oxynitride (HfO_xN_y) layer deposited between silicon and tetracene film produced the best performance. The HfO_xN_y interlayer allowed the transfer of triplet excitons and prevented the triplet-triplet annihilation at the silicon surface due to its passivation effect. The magnetic-dependence detection indicated a decrease in the photocurrent as the magnetic field was increased, which proved the contribution of triplet excitons to the photocurrent. By analyzing the photoluminescence data under a

changing magnetic field, an overall peak exciton transfer efficiency was calculated to be 133% composing by 56% singlet transfer and 76% triplet transfer.

2.4.3 Singlet Fission/Perovskite Heterojunctions

The efficiency of thin-film perovskite solar cells has steadily grown to a record high of 25.7% [84] since 2012, which makes them to be regarded as a viable rival to silicon solar cells. Besides the high efficiency, perovskites exhibit many superior properties over other PV materials, such as tunable energy bandgaps, high absorption coefficient, long charge diffusion length, low manufacturing cost and flexible substrate compatibility. As a promising PV material that will potentially revolutionize the next generation solar cell field, effectively utilizing the SF process in perovskite solar cells gives a valuable alternative for future study.

Pentacene, as a p-type organic semiconductor, has been applied in planar perovskite solar cells solely as an HTL material without the consideration of the possible contribution from its SF characteristic. [89,90] By measuring the energy alignment at the pentacene/$MAPbI_3$ interface, a downward band bending of 0.2 eV was observed on the HOMO level of perovskite, which can promote hole transfer at the interface. Due to the superior film quality, the perovskite film grown on the pentacene layer also demonstrated an effective charge extraction and transfer process. As a result, the pentacene-based $MAPbI_3$ cell produced a higher PCE and J_{sc} than the classical PEDOT:PSS-based cell.

Although various groups have demonstrated that triplet transfer could occur at the interface of SF materials-perovskite nanocrystals/films heterojunctions, there has been no report to date on successful SF-enhanced perovskite solar cells. Because of the low absorption coefficient of polyacenes, using perovskite nanocrystals with a high energy gap, such as $CsPbBr_3$, to sensitize the SF process seems to be a good choice. Lu *et al.* in 2019 [91] and Luo *et al.* in 2020 [92] have separately demonstrated the singlet energy transfer from $CsPbBr_3$ nanocrystals to TIPS-pentacene carboxylic acid and tetracene carboxylic acid, respectively, which was initiated by an energetically favorable hole transfer and followed by triplet generation via SF at the interface.

Lee *et al.* in 2017 [93] and Guo *et al.* in 2020 [94], on the other hand, have investigated the charge transfer dynamics in the TIPS-pentacene/perovskite film heterojunctions. By analyzing the TA spectra and decay profiles of TIPS-pentacene/$MAPbI_3$ bilayer film, Lee *et al.* claimed for the first time that the electron transfer occurred from the triplet states of TIPS-pentacene generated via the SF process to the CB of $MAPbI_3$ in 1.1 ps (Figure 2.13a), while Guo argued that this electron transfer was energetically unfavorable since the energy level of T_1 in TIPS-pentacene was 0.26 eV lower than that of CB in $MAPbI_3$ (Figure 2.13b). According to Guo's investigation, the two-electron transfer should occur from the ^{1}(TT) states of TIPS-pentacene to the CB of $MAPbI_3$ in 1.5 ps along with a much slower hole transfer from $MAPbI_3$ to TIPS-pentacene in 13.8 ns. The increase of electron density in $MAPbI_3$ was estimated to be 38% based on the amplitude percentage of the rise component in the TA kinetics of $MAPbI_3$.

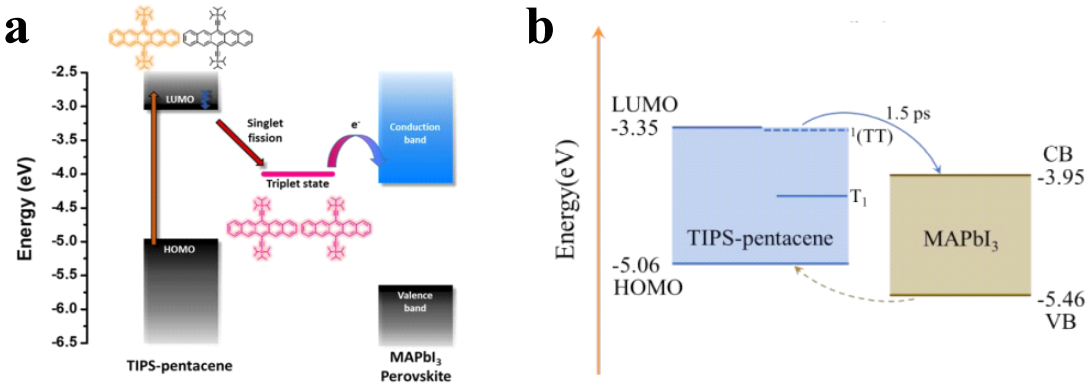

Figure 2.13 (a) Schematic diagram of the electron transfer dynamics from triplet states of TIPS-pentacene to conduction band of $MAPbI_3$ perovskite. Reprint with permission from Ref. 93. Copyright © 2017 American Chemical Society. (b) Schematic diagram of the two-electron transfer dynamics from correlated triplet states of TIPS-pentacene to conduction band of $MAPbI_3$ perovskite, along with a hole transfer process from valence band of $MAPbI_3$ perovskite to the highest occupied molecular orbital of TIPS-pentacene. Reprint with permission from Ref. 94. Copyright © 2020 Royal Society of Chemistry.

Even though the SF-based perovskite solar cell has not even been realized in the laboratory by now, the research on SF-perovskite heterojunctions suggests that effective charge transfer from triplet states to perovskite at the interface is possible. The tunability of energy bandgap makes the energy alignment between perovskite and SF chromophores much more convenient. [95] Considering the bright future of perovskites applied in the next generation of solar cells, the implementation of SF materials into

perovskite solar cells holds a promising pathway towards utilizing the SF process in commercial solar cells.

2.5 PhD in Context of Literature

Perovskite solar cells have undergone rapid development in the last decade in terms of efficiency and stability. Due to the superior properties of perovskites compared to the other types of PV materials, as discussed in the above sections, perovskite solar cells are regarded as the technology that holds the most potential to dominate future PV market. In the field of SF-based PV devices, however, the SF-perovskite devices have not been realized because of the ambiguous illustration of triplet transfer dynamics at the SF-perovskite heterojunctions. In Chapter 4, this process was elucidated by analyzing the transient absorption profiles of the heterojunction consisting of a triple-cation perovskite and TIPS-pentacene films. Since the energy structure of this perovskite is much more aligned with TIPS-pentacene, the exciton transfer process from other energy states can be excluded.

The singlet fission property of polyacene monomers, such as anthracene and pentacene, has been much investigated in the literature, but the study of heteroatom-substituted polyacenes and their corresponding dimers is by far insufficient. Novel SF materials based on polyacenes should be synthesized to expand the choice of SF alternatives for PV devices. In Chapter 5, a series of new nitrogen-incorporated and thiadiazole ring-fused polyacenes have been successfully synthesized to investigate the influence of substituted atoms on the electronic and photophysical properties of polyacenes. More importantly, the relationship between SF properties and molecular structures has been elucidated.

SF monomers have been demonstrated to improve the EQE in various types of solar cells, as mentioned in Section 2.4.2. However, there are still limited studies on the SF dynamics of SF dimers that are capable of undergoing intramolecular SF process. Compared with the intermolecular SF process in monomer, the intramolecular SF process in dimer is independent on the thin film morphology, which is much more promising to be applied in PV devices. In Chapter 6, the surface morphologies, photophysical properties and electronic dynamics of SF dimers in thin film states were

investigated and revealed. A preliminary study on the hole extraction ability of SF dimer/perovskite heterojunction was conducted. These results will contribute to the design of SF-enhanced perovskite solar cells in the future.

References

[1] M. A. Green, *Prog. Photovoltaics*, **2001**, 9, 123.

[2] A. Kojima, K. Teshima, Y. Shirai and T. Miyasaka, *J. Am. Chem. Soc.*, **2009**, 131, 6050-6051.

[3] W. Shockley and H. J. Queisser, *J. App. Phys.*, **1961**, 32, 510-519.

[4] R. Wang, T. Huang, J Xue, J. Tong, K. Zhu and Y Yang, *Nat. Photonics*, **2021**, 15, 411-425.

[5] Y. J. Jiang, and J.-H. Kim, *Chem. Asian J.*, **2022,** 17, e202200265.

[6] A. J. Badlacchino, M. I. Collins, M. P. Nielsen, T. W. Schmidt, D. R. McCamey and M. J. Y. Tayebjee, *Chem. Phys. Rev.*, **2022**, 3, 021304

[7] H. S. Kim, S H. Im and N. G. Park, *J. Phys. Chem. C*, **2014**, 118, 11, 5615-5625.

[8] W-J. Yin, J-H. Yang, J. Kang, Y. Yan and S-H. Wei, *J. Mater. Chem. A*, **2015**, 3, 8926-8942.

[9] Y. Zhang, C-K. Lim, Z. Dai, G. Yu, J. W. Haus, H. Zhang and P. N. Prasad, *Physics Reports*, **2019**, 795, 1-51.

[10] C. Fu, Z. Gu, Y. Tang, Q. Xiao, S. Zhang, Y. Zhang and Y. Song, *Angew. Chem. Int. Ed.*, **2022**, 134, e202117067.

[11] V. M. Goldschmidt, *Naturwisesenschaften*, **1926**, 14, 477-485.

[12] C. Li, X. Lu, W. Ding, L. Feng, Y. Gao and Z. Guo, *Acta Cryst.*, **2008**, B64, 702-707.

[13] J.-P. Correa-Baena, A. Abate, M. Saliba, W. Tress, T. J. Jacobsson, M. Grätzel and A. Hagfeldt, *Energy Environ. Sci.*, **2017**, 10, 710-727.

[14] H. Tsai, W. Nie, J.-C. Blancon, C. C. Stoumpos, R. Asadpour, B. Harutyunyan, A. J. Neukirch, R. Verduzco, J. J. Crochet, S. Tretiak, L. Pedesseau, J. Even, M. A. Alam, G. Gupta, J. Lou, P. M. Ajayan, M. J. Bedzyk, M. G. Kanatzidis and A. D. Mohite, *Nature*, **2016**, 536, 312-316.

[15] B. Saparov and D. B. Mitzi, *Chem. Rev.*, **2016**, 116, 45588-4596.

[16] T. Baikie, Y. Fang, J. M. Kadro, M. Scheryer, F. Wei, S. G. Mhaisalkar, M. Grätzel and T. J. White, *J. Mater. Chem. A*, **2013**, 1, 5628-5641.

[17] A. Sadhanala, S. Ahmad, B. Zhao, N. Giesbrecht, P. M. Pearce, F. Deschler, R. L. Z. Hoya, K. C. Gödel, T. Bein, P. Docampo, S. E. Dutton, M. F. L. De Volder and R. H. Friend, *Nano Lett.*, **2015**, 15, 9, 6095-6101.

[18] Q. Dong, Y. Fang, Y. Shao, P. Mulligan, J. Qiu, L. Cao and J. Huang, *Science*, **2015**, 347, pp 967-970.

[19] T. J. Jacobsson, J.-P. Correa-Baena, M. Pazoki, M. Saliba, K. Schenk, M. Grätzel and A. Hagfeldt, *Energy Environ. Sci.*, **2016**, 9, 1706-1724.

[20] D. P. Mcmeein, G. Sadoughi, W. Rehman, G. E. Eperon, M. Saliba, M. T. Hörantner, A. Haghighirad, N. Sakai, L. Korte, B. Rech, M. B. Johnston, L. M. Herz and H. J. Snaith, *Science*, **2016**, 351, pp 151-155.

[21] F. Briyio, C. Caetano and A. Walsh, J. Phys. Chem. Lett., **2016**, 7, 6, 1083-1087.

[22] H.-S. im, C. R. Lee, J.-H. Im, K.-B. Lee, T. Moehl, A. Marchioro, S.-J. Moon, R. Humphry-Baker, J.-H. Yum, J. E. Moser, M. Grätzel and N.-G. Park, *Sci. Rep.*, **2012**, 2, 591.

[23] P. Lopez-Varo, J. A. Jiménez-Tejada, M. García-Rosell, S. Ravishankar, G. Garcia-Belmonte, J. Bisquert and O. Almora, *Adv. Energy Mater.*, **2018**, 8, 1702772.

[24] N. E. Courtier, J. M. Cave, J. M. Foster, A. B. Walker and G. Richardson, *Energy Environ. Sci.*, **2019**, 12, 396-409.

[25] J. Burschka, N. Pellet, S.-J. Moon, R. Humphry-Baker, P. Gao, M. K. Nazeeruddin and M. Grätzel, *Nature*, **2013**, 499, 316-319.

[26] S. De Wolf, J. Holovsky, S.-J. Moon, P. Löper, B. Niesen, M. Ledinsky, F-J. Haug, J.-H. Yum and C. Ballif, *J. Phys. Chem. Lett.*, **2014**, 5, 6, 1035-1039.

[27] W. Tress, N. Marinova, O. Inganäs, M. K. Nazeeruddin, S. M. Zakeeruddin and M. Grätzel, *Adv. Energy Mater.*, **2015**, 5, 1400812.

[28] J. M. Ball, S. D. Stranks, M. T. Hörantner, S. Hüttner, W. Zhang, E. J. W. Crossland, I. Ramirez, M. Riede, M. B. Johnston, R. H. Friend and H. J. Snaith, *Energy Environ. Sci.*, **2015**, 8, 602-609.

[29] J.-P. Correa-Baena, M. Anaya, G. Lozano, W. Tress, K. Domanski, M. Saliba, T. Matsui, T. J. Jacobsson, M. E. Calvo, A. Abate, M. Grätzel, H. Míguez and A. Hagfeldt, *Adv. Mater.* **2016**, 28, 5031-5037.

[30] N. Marinova, W. Tress, R. Humphry-Baker, M. I. Dar, V. Bojinov, S. M. Zakeeruddin, M. K. Nazeeruddin and M Grätzel, *ACS Nano*, **2015**, 9, 4, 4200-4209.

[31] W. Tress, N. Marinova, T. Moehl, S. M. Zakeeruddin, M. K. Nazeeruddin and M. Grätzel, *Energy Environ. Sci.*, **2015**, 8, 995-1004.

[32] S. Singh, W. J. Jones, W. Siebrand, B. P. Stoicheff and W. G. Schneider, *Chem. Phys.* **1965**, 42, 330-342.

[33] C. E. Swenberg and W. T. Stacy. *Chem. Phys. Lett.*, **1968**, 2, 237-238.

[34] M. C. Hanna and A. J. Nozik, *J. Appl. Phys.*, **2006**, 100, 074510.

[35] A. Suna, *Phys. Rev. B*, **1970**, 1, 1716.

[36] R. D. Pensack, E. E. Ostroumov, A. J. Tilley, S. Mazza, C. Grieco. K. J. Thorley, J. B. Asbury, D. S. Seferos, J. E. Anthony and G. D. Scholes, *J. Phys. Chem. Lett.*, **2016**, 7, 13, 2370-2375.

[37] N. V. Korovina, C. H. Chang and J. C. Johnson, *Nat. Chem.*, **2020**, 12, 391.

[38] D. Casanova, *Chem. Rev.*, **2018**, 118, 7164-7207.

[39] M. B. Smith and J. Michl, *Annu. Rev. Phys. Chem.*, **2013**, 64, 361-386.

[40] M. B. Smith and J. Michl, *Chem. Rev.*, **2010**, 6891-6936.

[41] A. Rao and R. H. Friend, *Nat. Rev. Mater.*, **2017**, 2, 17063.

[42] B. J. Walker, A. J. Musser, D. Beljonne and R. H. Friend, *Nat. Chem.*, **2013**, 5, 1019-1024.

[43] I. Breen, R. Tempelaar, L. A. Bizimana, B. Kloss, D. R. Reichman and D. B. Turner, *J. Am. Chem. Soc.*, **2017**, 139, 44, 11745-11751.

[44] J. C. Johnson, A. J. Nozik and J. Michl, *J. Am. Chem. Soc.*, **2010**, 11, 8757-8770.

[45] B. Carlotti, I. K. Madu, H. Kim. Z. Cai, H. Jiang, A. K. Muthike, L. Yu, P. M. Zimmerman and T. Goodson, *Chem. Sci.*, **2020**, 11, 8757-8770.

[46] A. M. Müller, Y. S. Avlasevich, K. Müllen and C. J. Bardeen, *Chem. Phys. Lett.*, **2006**, 421, 518-522.

[47] J. Zirzlmeier, D. Lehnherr, P. B. Coto, E. T. Chernick, R. Casillas, B. S. Basel, M. Thoss, R. R. Tykwinski and D. M. Guldi, *Proc. Natl. Acad. Sci.*, **2015**, 112, 5325-5330.

[48] J. Xia, S. N. Sanders, W. Cheng, J. Z. Low, J. Liu, L. M. Campos and T. Sun, *Adv. Mater.*, **2017**, 29, 1601652.

[49] J. B. Aladekomo, S. Arnold and M. Pope, *Phys. Status Solidi B,* 1977, 80, 333-340.

[50] P. Martin, J. Klein and R. Voltz, *Phys. Scr.*, **1987**, 35, 575

[51] C. Zenz, G. Cerullo, G. Lanzani, W. Graupner, F. Meghdadi, G. Leising and S. De Silverstri, *Phys. Rev. B*, **1999**, 59, 14336.

[52] H. Rademaker, A. J. Hoff, R. Van Grondell, and L. N. M. Duysens, *Biochem. Biophys. Acta Bioenerg.*, **1980**, 592, 240.

[53] R. H. Austin, G. L. Baker, S. Etemad and R. Thompson, *J. Chem. Phys.*, **1989**, 90, 6642.

[54] J. Hu, K. Xu, L. Shen, Q. Wu, G. He, J.-Y. Wang, J. Pei, J. Xia and M. Y. Sfeir, *Nat. Commun.* **2018**, 9, 2999.

[55] M. K. Gish, N. A. Pace, G. Rumbles and J. C. Johnson, *J. Phys. Chem. C,* **2019**, 123, 7, 3923-3934.

[56] H. Huang, G. He, K Xu, Q. Wu, D. Wu, M. Y. Sfei and J. Xia, *Chem*, **2019**, 5, 2405-2417.

[57] Q. Tang, Z. Liang, J. Liu, J. Xu and Q. Miao, *Chem. Commun.,* **2010**, 46, 2977.

[58] Y. Chen, L. Shen and X. Li, *J. Phys. Chem. A*, **2014**, 118, 5700-5708.

[59] I. Kaur, W. Jia, R. P. Kopreski, S. Selvarasah, M. R. Dokmeci, C. Pramanik, N. E. McGruer and G. P. Miller, *J. Am. Chem. Soc.,* **2008**, 130, 16274-16286.

[60] J. Herz, T. Buckup, F. Paulus, J. Engelhart, U. H. F. Bunz and M. Motzkus, *J. Phys. Chem. Lett.,* **2014**, 5, 2425-2430.

[61] D Polak, R. Jayaprakash, T. P. Lyons, L.Á. Martínez- Martínez, A. Leventis, K. J. Fallon, H. Coulthard, D. G. Bossanyi, K. Georgiou, A. J. Petty II, J. Anthony, H. Bronstein, J. Yuen-Zhou, A. I. Tartakovskii, J. Clark and A. J. Musser, *Chem. Sci.*, **2020**, 11, 343-354.

[62] B. Gu and S. Mukamel, *J. Phys. Chem. Lett.*, **2021**, 12, 2052-2056.

[63] K. Sun, M. F. Gelin and Y. Zhao, *J. Phys. Chem. Lett.,* **2022**, 13, 4280-4288.

[64] S. Takahashi, K. Watanabe and Y. Matsumoto, *J. Chem. Phys.,* **2019**, 151, 074703.

[65] M. Gudem and M. Kowalewski, *Chem. Eur. J.* **2022**, 28, e202200781.

[66] A. Tsargorodska, M. L. Cartron, C. Vasilev, G. Kodali, O. A. Mass, J. J. Baumberg, P. L. Dutton, C. N. Hunter, P. Törmä and G. J. Leggett, *Nano Lett.,* **2016**, 16, 6850-6856.

[67] M. Hertzog, M. Wang, J. Mony and K. Borjesson, *Chem. Soc. Rev.*, **2019**, 48, 937-961.

[68] M. J. Y. Tayebjee, A. A. Gray-Weale and T. W. Schmidt, *J. Phys. Chem. Lett.*, **2012**, 3, 2749-2754.

[69] J. Lee, P. Jadhav, P. D. Reusswig, S. R. Yost, N. J. Thompson, D. N. Congreve, E. Hontz, T. Van Voorhis and M. A. Baldo, *Acc. Chem. Res.*, **2013**, 46, 6, 1300-1311.

[70] R. Casillas, I. Papadopoulos, T. Ullrich, D. Thiel, A. Kunzmann and D. M. Guldi, *Energy Environ. Sci.,* **2020**, 13, 2741-2804.

[71] S. Yoo, B. Domercg and B. Kippelen, *App. Phys. Lett.*, **2004**, 85, 5427.

[71] J. Lee, P. Jadhav and M. A. Baldo, *App. Phys. Lett.,* **2009**, 95, 033301.

[73] P. J. Jadhav, A. Mohanty, J. Sussman. J. Lee and M. A. Baldo, *Nano Lett.,* **2011**, 11, 1405-1498.

[74] D. N Congreve, J. Lee, N. J. Thompson, E. Hontz, S. R. Yost, P. D. Reusswig, M. E. Bahlke, S. Reineke, T. Van Voorhis and M. A. Baldo, *Science*, **2013**, 340, 334-337.

[75] A. K. Pandey, *Sci. Rep.*, **2015**, 5, 7787.

[76] S. Kawata, J. Frudate, T. Kimura, H. Minaki, A. Saito, H. Katagiri and Y.-J. Pu, *J. Mater. Chem. C*, **2017**, 5, 4909-4914.

[77] J. Tang and E. H. Sargent, *Adv. Mater.*, **2011**, 23, 12-29.

[78] B. Ehrler, M. W. B. Wilson, A. Rao, R. H. Friend and N. C. Greenham, *Nano Lett.*, **2012**, 12, 1053-1057.

[79] B. Ehrler, B. J. Walker, M. L. Böhm, M. W. B. Wilson, Y. Vaynzof, R. H. Friend and N. C. Greenham, *Nat. Commun.*, **2012**, 3, 1019.

[80] L. Yang, M. Tabachnyk, S. L. Bayliss, M. L. Böhm, K. Broch, N. C. Greenham, R. H. Friend and B. Ehrler, *Nano Lett.*, **2015**, 15, 354-358.

[81] B. O'Regan and M. Grätzel, *Nature*, **1991**, 353, 737-740.

[82] J. N. Schrauben, Y. Zhao, C. Mercado, P. I. Dron, J. L. Ryerson, J. Michl, K. Zhu and J. C. Johnson, *ACS Appl. Mater. Interfaces*, **2015**, 7, 2286-2293.

[83] A. Kunzmann, M. Gruber, R. Casillas, J. Zirzlmeier, M. Stanzel, W. Peukert, R. R. Tykwinski and D. M. Guldi, *Angew. Chem. Int. Ed.*, **2018**, 57, 10742-10747.

[84] The National Renewable Energy Laboratory (NREL), Best Research-Cell Efficiencies, https://www.nrel.gov/pv/assets/pdfs/best-research-cell-efficiencies.pdf.

[85] B. Ehrler, K. P. Musselman, M. L. Böhm, R. H. Friend and N. G. Greenham, *Appl. Phys. Lett.*, **2012**, 101, 153507.

[86] L. M. Pazos-Outón, J. M. Lee, M. H. Futscher, A. Kirch, M. Tabachnyk, R. H. Friend and B. Ehrler, *ACS Energy Lett.*, **2017**, 2, 476-48.

[87] R. W. MacQueen, M. Liebhaber, J. Niederhausen, M. Mews, C. Gersmann, S. Jäckle, K. Jäger, M. J. Y. Tayebjee, T. W. Schmidt, B. Rech and K. Lips, *Mater. Horiz.*, **2018**, 5, 1065.

[88] M. Einzinger, T. Wu, J. F. Kompalla, H. L. Smith, C. F. Perkinson, Lea Nienhaus, S. Wieghold, D. N. Congreve, A. Kahn, M. G. Bawendi and M. A. Baldo, *Nature*, **2019**, 571, 90-94.

[89] G. Ji, B. Zhao, F. Song, G. Zheng, X. Zhang, K. Shen, Y. Yang, S. Chen and X. Gao, *Applied Surface Science*, **2017**, 393, 419-421.

[90] X. Yang, G. Wang, D. Liu, Y. Yao, G. Zhou, P. Li, B. Wu, X. Rao and Q. Song, *Current Applied Physics*, **2018**, 18, 1095-1100.

[91] H. Lu, X. Chen, J. E. Anthony, J. C. Johnson and M. C. Beard, *J. Am. Chem. Soc.*, **2019**, 141, 4919-4927.

[92] X. Luo, Y. Han, Z. Chen, Y. Li, G. Liang, X. Liu, T. Ding, C. Nie, M. Wang, F. N. Castellano and K. Wu, *Nat. Commun.*, **2020**, 11,28.

[93] S. Lee, D. Hwang, S. Il Jung and D. Kim, *J. Phys. Chem. Lett.*, **2017**, 8, 884-888

[94] D. Guo, L. Ma, Z. Zhou, D. Lin, C. Wang. X. Zhao, F. Zhang, J. Zhang and Z. Nie, *J. Mater. Chem. A*, **2020**, 8, 5572-5579.

[95] M. L. Petrus, J. Schlipf, C. Li, T. P. Gujar, N. Giesbrecht, P. Müller-Buschbaum, M. Thelakkat, T. Bein, S. Hüttner and P. Docampo, *Adv. Energy. Mater.,* **2017**, 7, 1700264.

Chapter 3

Experimental Methodology

This chapter describes the overall experimental design used in the project. First, the rationale for material selection, including the triple-cation perovskite, TIPS-pentacene and heteroatom-substituted polyacenes, is elaborated. Second, the fabrication methods of perovskite and singlet fission material films are presented. Third, the characterization techniques for as-prepared samples are clarified in terms of their underlying physical properties and specific handling procedures, including the structure and morphology characterization methods, and electrochemical and photophysical characterization methods.

3.1 Rationale for Selection

Perovskite is chosen as the triplet exciton acceptor in this project due to its superior properties over the other PV materials, such as high absorption coefficient, tunable energy bandgaps and simple fabrication process, endowing it with a bright future as the next generation PV technology. Specifically, the perovskite applied in this project is a triple-cation type, $Cs_{0.05}(FA_{0.85}MA_{0.15})_{0.95}PbI_{2.25}Br_{0.45}$ (CsMFPbIBr), which can utilize the strengths and avoid the drawbacks of each component at the same time. FA^+ can permit higher efficiency, while MA^+ can prevent the perovskite structure from changing from photoactive cubic phase to photoinactive hexagonal phase. Cs^- can also enhance the crystal quality of the perovskite film. Br^- can modify the energy bandgap and give the devices with high performance, while I^- can eliminate the poor stability and phase segregation brought about by Br^-.

In the first part, TIPS-pentacene/triple-cation perovskite heterojunction was fabricated as a model to investigate the charge transfer dynamics at the interface. TIPS-pentacene is a well-established SF material with intensive investigation due to its high SF rate and efficiency. Compared with pentacene, the incorporation of TIPS groups improves the stability under moisture and oxygen atmospheres and the solubility in most common solvents. Besides, the energy structure of CsMFPbIBr is more aligned with TIPS-pentacene, which excludes the charge transfer process from the other energy states. Perovskite film was formed by spin-coating method, which is a well-developed technology reported in many publications because of its low-cost and facile procedure at low temperatures. On the other hand, TIPS-pentacene film was deposited by thermal evaporation method, which is a clean and solvent-free process that is well established in industry for making films of high quality.

Heteroatom substitution of polyacenes is used as a strategy to design new SF materials with controllable chemistry and electronic properties by altering the number and positions of the substituent atoms. The nitrogen (N) atom substitution of pentacene has been demonstrated to significantly improve the stability towards light and oxygen and accelerate the SF process in spin-coated films because the electron-withdrawing effect brought by N atoms can lower and well delocalize the energy level and reduce the energy gap of singlet and triplet states. [1-3] Thiophene-ring fusion in the pentacene

parent can result in a high absorption coefficient and good charge transport property. Thiadiazole ring has been theoretically proven to increase the diradical character, which will be damaged by the introduction of N atoms. [4,5] In the second part, therefore, a series of N-substituted and thiadiazole ring-fused polyacenes have been proposed and synthesized, which could potentially exhibit higher SF efficiency and improved stability. SF dimers are currently understudied as triplet donors in the SF-based PV devices, but when compared to SF monomers, their SF performance is less dependent on the film morphology, making them more suitable for use in PV devices. In this project, SF dimers with different linkers and distances between two chromophores have also been synthesized to study the structure-electronic property relation accounting for better heterojunctions with perovskites. In the last part, thin films of as-synthesized SF materials with promising electronic and photochemical properties were studied in terms of their photophysical properties. Heterojunctions with perovskite were also fabricated for preliminary studies of the charge transfer dynamics. The results would contribute to the final SF-enhanced perovskite solar cells in the future.

3.2 Film Preparation Method

3.2.1 Spin-coating Method

Spin-coating is a deposition method using centrifugal force commonly used in laboratories to fabricate uniform thin films on flat substrates with small areas. There are usually four steps in a typical spin-coating process: deposition, spin-up, spin-off, and evaporation, as shown in Figure 3.1. The solution is first dispensed on a substrate fixed on a rotary chuck by an aspirator, which is then spun-up to 1000-6000 rpm for around 30 s. After the excess solution spins off the substrate, a flat film with the desired thickness will be deposited due to the viscous force and surface tension. [6] The solvent used usually has high volatility and evaporates during the whole process.

The thickness of deposited film depends on many parameters, such as density and viscosity of volatile solvent, rate of evaporation, spinning time and angular speed of rotation. A simple equation as shown below can be used to estimate the film thickness experimentally:

$$h = A\omega^{-B} \qquad \textbf{Equation 3.1}$$

where h is estimated thickness, A is a constant related to solution system, B is an experimentally calculated constant, ω is the angular speed of rotation. [6] According to this equation, increasing the rotation speed of substrate will decrease the thickness of deposited film.

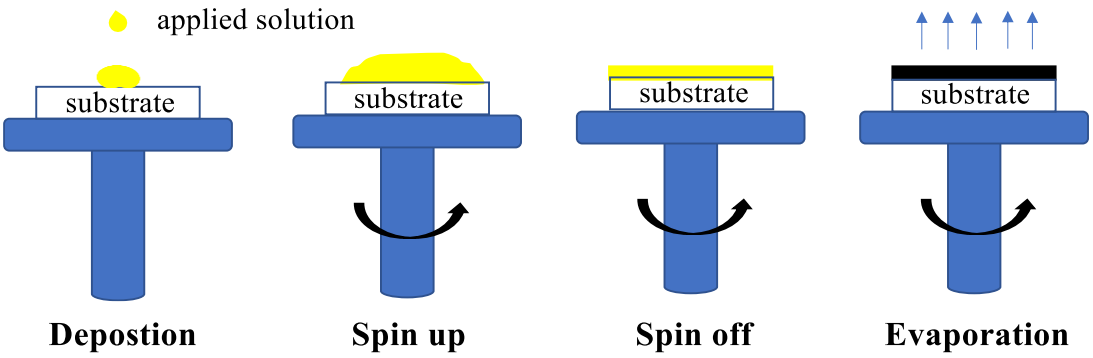

Figure 3.1 Four steps of spin-coating process.

The spin-coating method has many benefits, including straightforward process, relatively low cost, low equipment and maintenance cost as well as good film quality. However, it is suitable for large-sized film deposition and lacks the material efficiency (more than 95% of raw solution will be wasted during the spinning process). Besides, it usually requires an extra antisolvent and thermal annealing process, which can accelerate the growth of perovskite crystals by creating local supersaturation to form a film with improved morphology and photoactive phase. [26]

3.2.2 Thermal Evaporation Method

Thermal evaporation process is one of the traditional physical vapor deposition methods with a low deposition rate of around 10 nm/min. A typical thermal evaporation system is shown in Figure 3.2. The target material is placed inside a crucible boat or a twisted filament, which is generally made of refractory metals such as tungsten, molybdenum or tantalum. The crucible boat/twisted filament is then exposed to a large direct current, which will generate appreciable Joule heat to melt and evaporate or sublime the target material. The vapor flux diffuses from the heat source and reach the substrate to form a thin film on the cold surface. The evaporation rate is determined by the vapor pressure of target material at the heating temperature which can be controlled

by the applied current. The thickness of deposited film can be controlled *in situ* by a computerized process control unit.

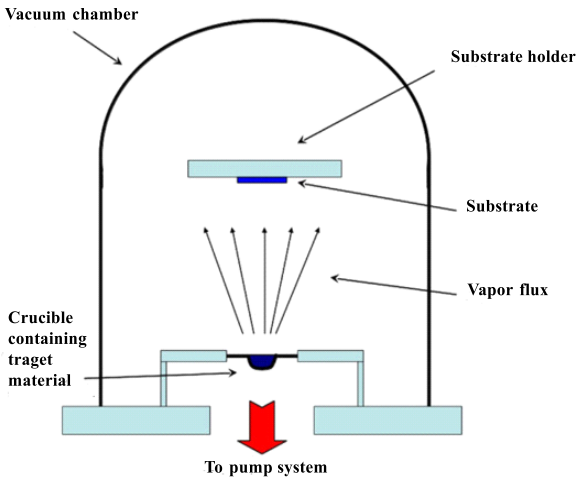

Figure 3.2 Schematic illustration of thermal evaporation system. Reprinted from *Materials Science in Photocatalysis*, E. I. García-López, G. Marcì, Chpater3 – Preparation of photocatalysts by physical methodologies, Page 37-62, Copyright © 2021, with permission from Elsevier.

An important feature of the thermal evaporation method is the ultimate applied pressure, which is usually lower than 10^{-4} Pa. The high vacuum helps to decrease the evaporation temperature of the target material and prevents the evaporated target material from colliding with residual gases in its path to the substrate. Compared with the spin-coating method, the thermal evaporation method is much more feasible for the deposition of multilayers, of which the thickness of each layer can be easily controlled *in situ* by a computerized process control unit.

3.3 Structure and Morphology Characterization

3.3.1 Nuclear Magnetic Resonance Spectroscopy

The chemical structures of as-synthesized SF molecules were determined by the nuclear magnetic resonance (NMR) technique using the AVANCE II NEO 400 MHz Spectrometer (BRUKER). NMR is based on the phenomenon that atomic nuclei will emit electromagnetic signals when they are excited by radio waves with a particular frequency in a strong, constant magnetic field. [7] The NMR phenomenon was first

described and measured by Isidor Rabi in 1938, while the NMR imaging technique was first used by Lauterbur in 1973 to determine and identify the molecular structures of organic compounds. [8]

In an atomic nucleus, the angular momentum or spin of proton or neutron pairs will cancel each other out. Hence, the atoms consisting of even protons or neutrons will possess a net spin of zero; only the atoms with an odd nucleon can possess a net spin that generates a magnetic field and can interact with the externally applied field. Therefore, the most common types of NMR spectroscopy are those detecting hydrogen (^{1}H) and carbon (^{13}C) isotopes, which are naturally abundant elements with odd nucleons. When an atom with a magnetic moment is placed in a uniform, constant magnetic field $\boldsymbol{B_0}$, as shown in the Figure 3.3, the atom will reorient its spin direction to align with the magnetic induction of the applied field. Then, a short radiofrequency (RF) pulse with the direction in the xy plane is applied to induce the nuclear resonance phenomenon. With appropriate RF, the aligned atom will rotate away from the direction of $\boldsymbol{B_0}$ (z axis) with an angle θ, which depends on the power and duration of the RF. When the angle θ increases to 90^0 and is then turned off, the atomic magnetic vector will continue rotating in the xy plane and generate a signal called "free induced decay" (FID) with the maximum amplitude. [9]

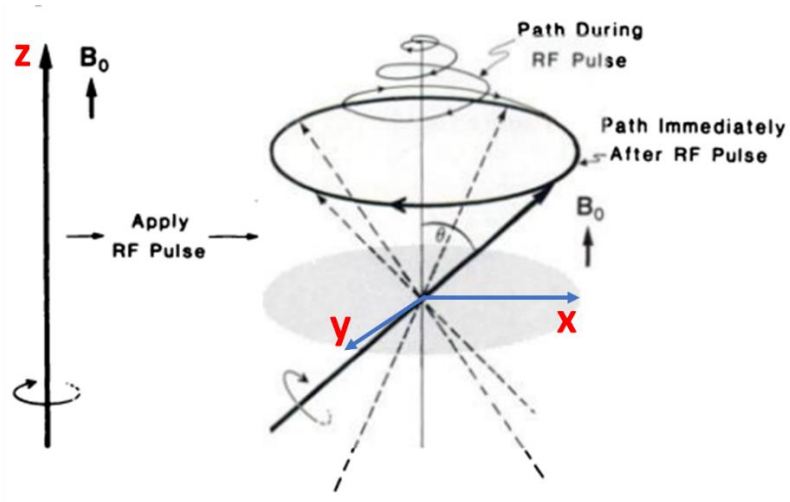

Figure 3.3 Magnetic moment rotation in a uniform constant field $\mathbf{B_0}$ with an applied radiofrequency pulse. Reprint with permission from Ref. 8. Copyright © 1973 Springer Nature.

The resonance frequency f_0 of the applied RF pulse that can stimulate certain atomic nuclei in the constant magnetic field $\boldsymbol{B_0}$ can be described as

$$f_0 = B_0(\frac{\gamma}{2\pi}) \qquad \textbf{Equation 3.2}$$

where γ is the gyromagnetic ratio of the atom. Normally, the waveform of the NMR signals obtained directly is a straight line that represents the relationship between the signal strength and detecting time. To determine the signal strength at each frequency, a mathematical manipulation technique is used, known as Fourier transformation. [10]

According to Equation 3.2, all detecting atoms should have the same resonance frequency in a constant magnetic field. However, for a complex molecule, the resonant signals of atoms of interest will be affected by the contribution of electrons around adjacent atoms. These atoms will generate local magnetic fields that oppose the externally applied field, which can shield the targeted atoms and thus increase their resonance frequency. Such alterations are called chemical shifts and provide valuable information about the chemical structures of the detected molecules. [8]

3.3.2 Infrared Spectroscopy

Infrared (IR) spectroscopy is a popular tool to investigate the interactions and vibrational transitions of a molecule with IR radiation, which can be used to identify certain molecular bonds and functional groups present in the molecule. The IR spectra of as-synthesized SF molecules are characterized by Fourier Transform Infrared (FTIR) spectroscopy (Frontier, PerkinElmer), which uses a single pulse of radiation and stores the spectra in digital form. Several scans can be obtained and added together to increase the signal-to-noise ratio, and the resulting spectra are Fourier−transformed to look more conventional.

There are numerous vibrational modes in complex organic molecules after IR absorption, but only the one that can trigger a change in the molecular dipole moment is IR active; among them, the modes attributed to individual functional groups are the most useful ones to decipher the molecular structures. These characteristic group vibrations can be described as a simplified harmonic oscillator system, whose vibration frequency υ can be given by Hooke's law:

$$v = \frac{1}{2\pi}\sqrt{\frac{k}{\mu}} \text{ or } \bar{v} = \frac{1}{2\pi c}\sqrt{\frac{k}{\mu}} \quad \textbf{Equation 3.3}$$

where k is the force constant of the bond – the stronger the bond the greater the value of k, $\bar{\upsilon}$ is the wavenumber, c is the speed of light (3.0×10^8 m/s), μ is the reduced mass defined by the following equation:

$$\mu = \frac{m_1 \times m_2}{m_1 + m_2} \quad \textbf{Equation 3.4}$$

where m_1 and m_2 are the mass of atoms connected by the bond. According to both equations, a strong bond formed by atoms with light mass will produce an IR active transition with a high frequency (or wavenumber).

3.3.3 X-ray Diffraction

The structure of as-deposited perovskite, SF and bilayer films were characterized by the Bruker D8 Advance X-ray diffraction (XRD) spectroscopy with Cu-Kα radiation operated at 40 KV and 40 mA. XRD is an effective nondestructive method that is commonly used for characterizing crystalline materials to provide information on structures, phases, preferred crystal orientations, crystallinity, and crystal defects. When a monochromatic beam of X-ray is elastically scattered at specific angles from each set of lattice planes in the target sample, a peak will emerge on the XRD pattern. The atomic positions and arrangement within the lattice planes determine the diffraction peak intensities and the angle at which the peak appears. As a result, the periodic atomic arrangement in a certain sample can be uniquely identified by its XRD pattern. [11]

When Bragg's law is satisfied, the diffracted beams will reinforce each other, and incident X-rays have constructive interference with the sample. In a real characterization process, the angle between incident beams and the crystal lattice can be adjusted to ensure the scattered X-rays are in phase. As illustrated in Figure 3.4, two X-ray beams fall upon a series of parallel planes (crystal lattices). In order to obtain reinforcement of the reflective beams, the difference in path length should be a whole number of wavelengths, as described by the Bragg's equation:

$$n\lambda = 2dsin\theta \quad \textbf{Equation 3.5}$$

where n is the order of reflection, λ is the wavelength of X-rays, d is the characteristic spacing between the crystal planes, and θ is the angle between the incident beam and

the lattice. [12] If this condition is met, all these scattered beams will reinforce each other and produce a characteristic peak on the XRD pattern.

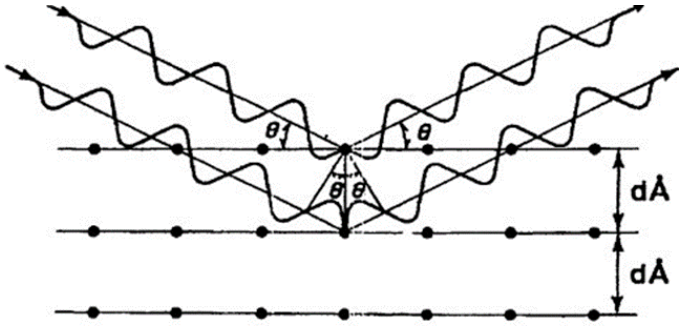

Figure 3.4 Schematic illustration of Bragg's Law.

In a typical XRD instrument with Bragg-Brentano geometry, three basic elements can be found, including the X-ray tube, sample holder, and the detector, as well as a series of slits. Copper is the most common target material to produce X-rays; after passing through the soller slit and divergence slit, these beams are collimated and directed onto the sample. As the detector rotates, the intensity of scattered X-rays is recorded, and when the angle satisfies Bragg's law, a peak with a certain intensity will be observed.

3.3.4 Atomic Force Microscopy

The morphology and surface roughness of as-deposited perovskite, singlet fission and bilayer films were measured by atomic force microscopy (AFM; Asylum Research, Cypher S). AFM was developed by Bining, Quate, and Gerber in 1986 based on the scanning probe microscopy (SPM) technique to obtain the three-dimensional features at the atomic scale of solid surfaces. [13]

The basic components of an AFM are illustrated in Figure 3.5, including the probe tip, sample holder, cantilever, laser, photodetector, scanner, and data processor. A cantilever is a type of spring that can respond to the force between the probe tip and sample. This force can be described by Hooke's Law:

$$F = -kx \qquad \textbf{Equation 3.6}$$

Where F is the force, k is the spring constant, x is the cantilever deflection.

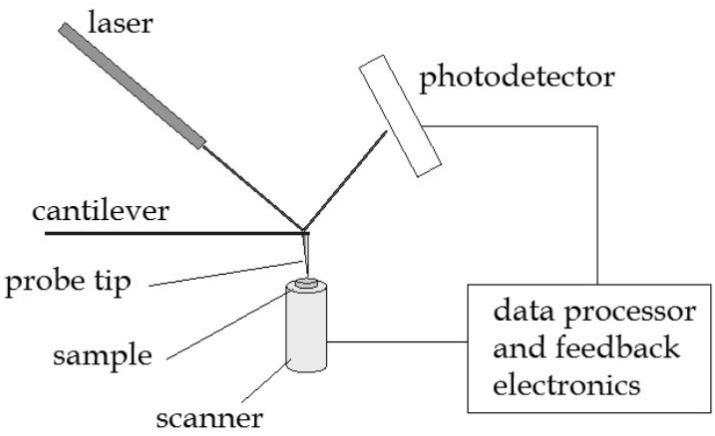

Figure 3.5 Schematic diagram of AFM. Reprint with permission from Ref. 14. Copyright © 2012 INTECH.

Typical forces between the probe tip and the sample surface range from 10^{-11} to 10^{-6} N, which are close to the interaction between two atoms connected by a covalent bond. The tunneling current is generated, detected, and collected by the data processor, which is related to the distance between the tip and sample surface. During the surface reconstruction, the tip can move parallel along the surface plane, and the feedback electronics will control the cantilever to adjust the tip height perpendicular to the sample surface to keep the tip-sample distance and tunneling current constant. Therefore, the pathway based on the probe tip movement can be used to visualize the surface topology of the target sample. [13-15]

One of the most important issues of the surface morphology is the roughness, which is usually determined by the difference in the vertical height with the ideal form of a sample. Roughness average (R_a) is the most widely used parameter to evaluate the roughness of a surface due to its easy accessibility. It can be described as

$$R_a = \frac{1}{L}\int_0^L |Z(x)|\, dx \qquad \textbf{Equation 3.7}$$

where $Z(x)$ is the function related to the vertical height Z and the measured position x of the sample, L is the evaluation length of the sample. However, R_a makes no difference between peaks and valleys from the mean line, which can result in a similar value with a totally different surface profile since the contributions of peaks and valleys will compensate each other. Hence, the root mean square of R_a is used as a more accurate value due to its sensitivity to the difference between peaks and valleys. [14]

3.3.5 Scanning Electronic Spectroscopy

The microstructures on the surface of the as-deposited perovskite, singlet fission and bilayer films were detected by scanning electronic microscopy (SEM) using a field-emission SEM machine (FESEM 7600F, JOEL). When an electron beam bombards onto a sample, the interactions between the electron and the specimen will occur inside the specimen at different depths, and then a variety of secondary emissions are produced. The volume where these interactions occur is called the interaction volume, as illustrated in Figure 3.6. This interaction volume depends on several factors, such as the atomic number of the components in the specimen, the accelerating voltage used, and the angle of the incident electron beam.

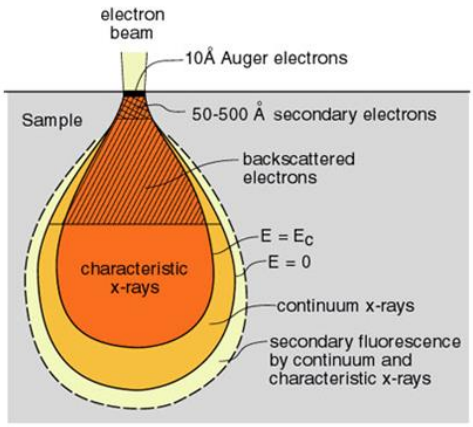

Figure 3.6 Specimen interaction volume.

The secondary electrons are produced by the inelastic interaction between the incident electrons and the outer shell electrons of the atoms on the top surface of the sample, as shown in Figure 3.6. These electrons come from the region that is a few nanometers from the sample surface. The number of secondary electrons emitted from different areas of the specimen and collected by the detector determines the topographic contrast, which means that more emitted secondary electrons being detected will result in a brighter region on the image. Since the number of sputtered electrons will increase as the escape distance decreases, the sharp regions on the surface are supposed to be brighter than the smooth surface on the image. Therefore, topographic contrast can help to obtain the information about the shape and texture of a sample from a well-defined three-dimensional image.

The backscattered electrons, on the other hand, are produced by the elastic scattering process, in which the trajectory of primary electrons is influenced by constant kinetic energy and velocity because of the large mass difference between the electrons and nucleus. These electrons come from a deeper region in the interaction volume than secondary electrons, as shown in Figure 3.6. The number of backscattered electrons will increase with increasing atomic number. Consequently, the brighter region of the image is attributed to the element with a higher atomic number, and the composition can be illustrated with this imaging technique.

When a high-energy electron strikes an atom, it can knock out an electron from this atom and leave a vacancy. X-rays will be generated when an outer-shell electron drops into the vacancy left by the emission of an inner-shell electron. This interaction occurs in a much deeper region of the sample, as shown in Figure 3.6. Each element has a unique atomic structure, which allows a set of characteristic peaks on its X-ray emission spectrum, so the element composition of the sample can be attained on an energy-disperse X-ray spectrum. [16] The utilization of the characteristics X-rays enables the technique called energy-disperse X-ray spectroscopy (EDX).

3.4 Electrochemical and Photophysical Properties Characterization

3.4.1 Cyclic Voltammetry Measurement

Cyclic voltammetry (CV) is an effective and widely used potentiodynamic technique that is applied to study the reactions involving electron transfer process in solution with a three-electrode system as shown in Figure 3.7. The electrolyte solution consists of the solvent and supporting electrolyte. A good solvent should dissolve the analyte and has good chemical stability in the measurement potential range. For a good supporting electrolyte, a large concentration in solvent is required to increase the solution conductivity and restrict the analyte migration. The three electrodes include a reference electrode, a counter electrode, and a working electrode. During the experiment, the potential is measured between the reference and working electrodes, while the current is measured between the counter and working electrodes. The electrochemical reaction of analyte is carried out on the surface of the working electrode, which is made up of material that is inactive in the measurement potential window. The reference electrode

defines the applied potential against other electrodes, which requires a precise and steady equilibrium potential against the vacuum. The function of the counter electrode is to complete the electric circuit and support the current flow. Inert metals like platinum are usually chosen as the counter electrode to avoid the generation of byproducts. [17]

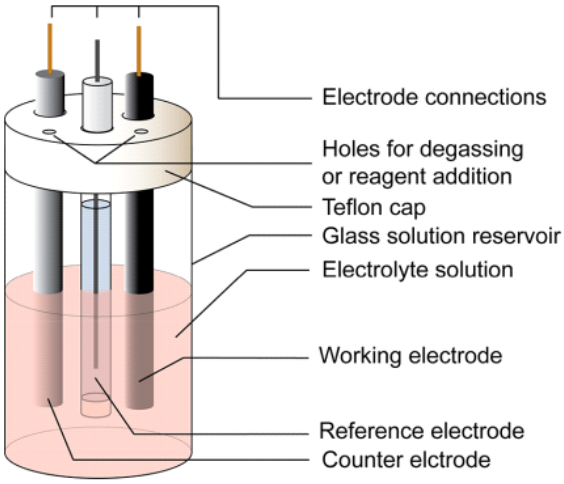

Figure 3.7 Schematic illustration of a three-electrode system for CV measurements. Reprint with permission from Ref. 17. Copyright © 2018 American Chemical Society, Open Access.

The peaks emerging on the CV plot are determined by the redox equilibrium of the analyte, which can be described by the Nernst equation:

$$E = E^0 + \frac{RT}{nF} ln \frac{(Ox)}{(Red)} = E^0 + 2.3026 \frac{RT}{nF} log_{10} \frac{(Ox)}{(Red)} \qquad \textbf{Equation 3.8}$$

where E is the electrochemical cell's potential, E^0 is the analyte's standard potential, (Ox) and (Red) are the relative activities of the analyte in oxidation and reduction form, respectively, R is the universal gas constant, T is the temperature, n is the number of electrons involved, F is the Faraday constant. Considering a redox couple of ferrocenium (Fc^+) and ferrocene (Fc) as an example, its Nernst Equation can be illustrated as Equation 3.9 by replacing relative activities to experimental concentrations [Fc^+] and [Fc], replacing standard potential E^0 to formal potential $E^{0'}$, and setting the electron number n equal to 1:

$$E = E^{0\prime} + \frac{RT}{F} ln \frac{[Fc^+]}{[Fc]} = E^{0\prime} + 2.3026 \frac{RT}{F} log_{10} \frac{[Fc^+]}{[Fc]} \qquad \textbf{Equation 3.9}$$

When a Fc^+ solution is applied with an external potential in an electrochemical cell, the concentration profiles of Fc^+ and Fc as the function of distance from the electrode are shown in Figure 3.8. At starting point A, only Fc^+ exists and is distributed

homogeneously throughout the bulk solution. During the cathodic scan from A to D, the concentration of Fc^+ continues to decrease nearby the electrode surface because Fc^+ is reduced to Fc. Before the potential reaches critical point C, the current steadily increases due to the Faradic current generated by the reduction of Fc^+; while as the potential continues to increase (from C to D), the current begins to decrease as the diffusion layer consisting of the reductant Fc slows down the mass diffusion of Fc^+ from the bulk solution to the electrode surface. Hence, a peak cathodic current is observed at point C. From point D to G, the potential direction is reversed to anodic resulting the oxidation of Fc to Fc^+. This process is similar to the cathodic scan with a peak anodic current at point F. According to Equation 3.9, when the concentration of Fc^+ equals Fc, the applied potential $E_{1/2}$ equals the formal potential $E^{0'}$, as indicated in Figure 3.8b and 3.8e. The value of $E^{0'}$ for a reversible redox reaction can then be directly estimated from the average value of the two peak potentials (C and F), which are not equal due to the different diffusion direction of the analyte. [17]

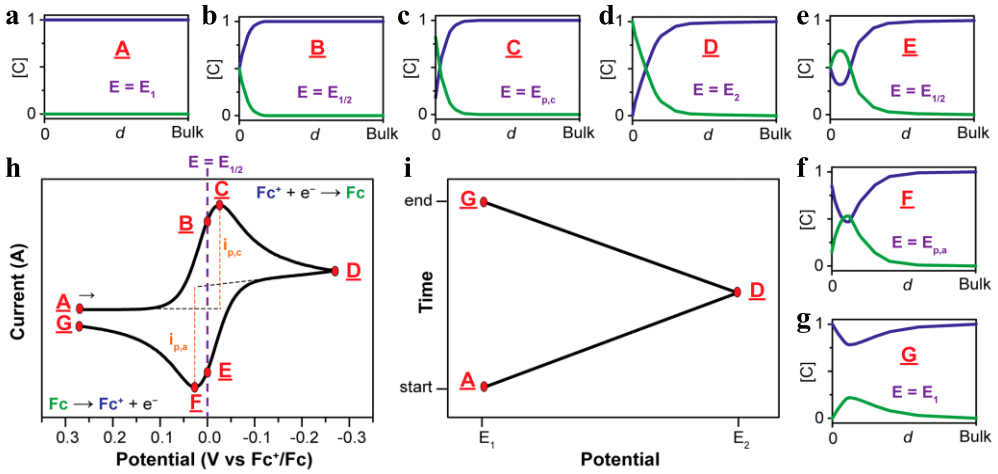

Figure 3.8 (a-g) Concentration profiles of Fc (green) and Fc^+ (blue) vs the distance from the working electrode at different points shown in h. (h) Cyclic voltammogram of Fc^+ and Fc. (i) Potential profile of a whole cycle. Reprint with permission from Ref. 17. Copyright © 2018 American Chemical Society, Open Access.

The CV profiles of a molecule can provide information about its oxidation and reduction potentials, which are commonly used to estimate the energy of the highest occupied molecular orbital (HOMO) and the lowest unoccupied molecular orbital (LUMO) levels by many researchers. [18,19] The oxidation potential is related to the minimum energy required to remove an electron from a molecule, which approximates

the energy of the HOMO level. Similarly, the reduction potential is related to the energy required to add an electron to a molecule, which approximates the energy of the LUMO level. The Fc^+/Fc redox couple is recommended to be used as an internal standard in the CV measurement to obtain the exact value of the HOMO and LUMO levels of the analyte since the iron centre is well shielded from the environmental effects by the two surrounding cyclopentadienyl rings to produce a relatively stable formal potential. Thus, the HOMO and LUMO levels can be calculated by the following equations:

$$E_{HOMO} = -(E_{ox}\ vs.\ Fc^+/Fc + 4.8)\ eV \qquad \textbf{Equation 3.10}$$

$$E_{LUMO} = -(E_{red}\ vs.\ Fc^+/Fc + 4.8)\ eV \qquad \textbf{Equation 3.11}$$

3.4.2 Ultraviolet-Visible Absorption Spectroscopy

The ultraviolet-visible (UV-vis) absorption spectra of as-deposited films and as-synthesized SF molecules in solution were characterized by the Cary 5000 UV-vis Spectrophotometer (Agilent Technologies). As illustrated in Figure 3.9, photons with short wavelength possess enough energy to induce electronic transitions of bonding and nonbonding electrons in organic molecules. At room temperature, most molecules would remain at the lowest energy level, namely the ground state. The absorption of UV-vis light can promote the transition of the electrons from the ground state to a higher excited one, i.e., $\sigma \rightarrow \sigma^*$, $n \rightarrow \sigma^*$, $\pi \rightarrow \pi^*$, $n \rightarrow \pi^*$. Because the energy gap between electronic levels is much greater than that of vibrational and rotational levels, the energetically induced electronics transitions always results in vibrational and rotational transitions. As a result, the UV-vis absorption spectra characteristically appear as broad bands. [10,20]

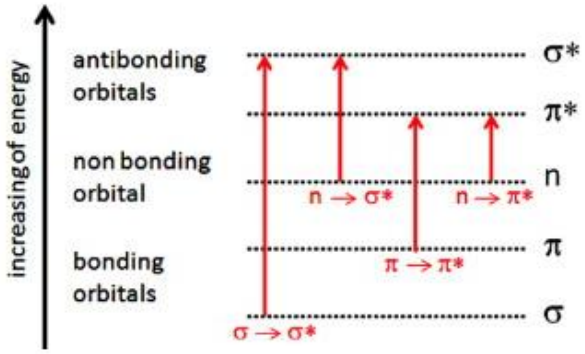

Figure 3.9 Schematic presentation of electronic transitions.

In general, the absorbance A can be determined using the Beer-Lambert Law:

$$A = \varepsilon cl = log_{10}\frac{I_0}{I} \qquad \textbf{Equation 3.12}$$

where ε is the molar absorptivity of the absorbing molecule, c is the concentration of sample, l is the path length of sample cell holder. The light is split into two equal beams at first and then passes through the holder with sample and the holder with the blank solvent, respectively. The detector will compare the intensity of the light through the solvent I_0 with the intensity of the light through the sample I. UV-vis spectroscopy is not suitable for determining molecular structures, but it is an effective way to characterize the optical properties of compounds. [21]

3.4.3 Photoluminescence Spectroscopy

The photoluminescence (PL) spectra of as-deposited films and as-synthesized SF molecules were measured by the Cary Eclipse Fluorescence Spectrophotometer (Agilent Technologies). When the photon is directed onto the sample, it can be absorbed by the molecule to stimulate the electron to transfer from a lower energy level to a higher energy level. Afterwards, the subsequent processes can be complex with a mixture of various behaviors to release the absorbed energy, as illustrated in Figure 3.10. Among these behaviors, the fluorescence and phosphorescence processes will emit photons, which will then be detected by the photodetector in spectroscopy. The generation of photons ceases immediately as soon as the absorption stops in fluorescence, while the generation of photons will continue for a while after the cessation of absorption in phosphorescence. The bandgap between ground state and excited state directly determines the energy or wavelength of the emitted photons. [22]

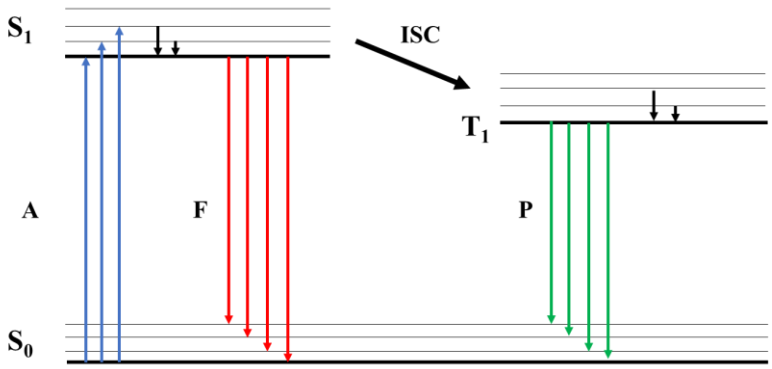

Figure 3.10 Photophysical process in a molecule after absorbing photon. S_0 = ground state, S_1 = first excited singlet state, T_1 = first excited triplet state, A = absorption, F = fluorescence, P = phosphorescence, ISC = inter system crossing.

Generally, the PL peaks of a sample appear at a longer wavelength compared with the peaks of its absorption spectrum. After absorption, some of the energy will be released as non-radiative transitions, including the vibrational and rotational transitions. Hence, the absorption and emission spectra are usually of mirror images of one another. PL is a nondestructive way to determine the electronic band gap of the molecule, and an effective way to evaluate the impurities and defects of a surface.

3.4.4 Ultraviolet Photoelectron Spectroscopy

The valence band (VB) of perovskite and the HOMO level of SF films are measured by ultraviolet photoelectron spectroscopy (UPS) using Kratos AXIS Supra X-ray photoelectron spectroscopy (XPS) with an ultraviolet lamp He I that discharges photons with an energy of 21.22 eV. When photons arrive at the surface of the sample, the molecule can absorb the photons if the energy of the photon is higher than the work function of the molecule and eject photoelectrons, of which the kinetic energy will be detected and analyzed. Due to the lower exciting energy, the emitting electrons come from not the core levels but the shallow valence band levels. [23] According to Albert Einstein's photoelectric law, the kinetic energy E_k of the emitting photoelectrons can be calculated as:

$$E_k = hv - E_B - \Phi_{sam} \qquad \textbf{Equation 3.13}$$

in which h is the Plank's constant, υ is the frequency of the incident photon, E_B is the binding energy of emitting electrons, Φ_{sam} is the work function of sample. When the contact between the sample and the spectrometer is electrically good, the Fermi level E_f of the sample is supposed to be the same as that of the spectrometer. Thus, the work function of the sample Φ_{sam} in Equation 3.13 can be replaced by the work function of the spectrometer Φ_{spe}, which can be obtained through calibration with Au or Ag.

UPS, unlike XPS, is not a quantitively analytical technique for determining the elemental concentration on sample's surface, but it is a powerful tool for providing information about the sample's energy diagram. An example UPS spectrum of bulk

MoS_2 is shown in Figure 3.11. The work function Φ can be calculated from the difference between $h\nu$ and E_B cutoff on the spectra (Φ = 21.22 – 15.98 eV = 5.24 eV), and the energy gap (1.0 eV) between the Fermi level (which is assumed to be zero) and the VB (or HOMO level) can be read directly from the spectra. Hence, the value of the VB (or HOMO level) can be derived from the sum of two values obtained above (5.24 + 1.0 eV = 6.24 eV). Associating with the value of the energy gap from the UV-vis absorption or PL spectra, the whole energy diagram of the sample can be determined.

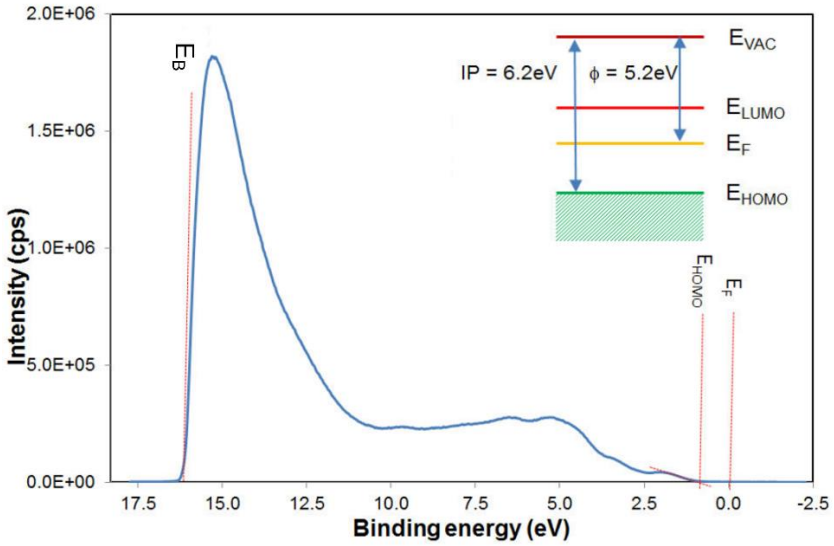

Figure 3.11 UPS spectrum of bulk MoS_2 with energy level diagram (inset).

3.4.5 Transient Absorption Spectroscopy

The photophysical processes of samples in solution and thin film after photoabsorption are investigated by transient absorption spectroscopy. As illustrated in Figure 3.12, the sample is excited by a pump pulse in advance so that a fraction of the molecules will be promoted to the excited state. The pump pulse will be blocked by the aperture to reach the detector. After a delay time τ, a beam of white light with a relatively lower intensity than the pump pulse will pass through the sample cell. The beam, after being absorbed by the sample, will arrive at the diffraction grating, which will separate the beam by wavelength λ and will be collected by the diode array. A difference in absorption ΔA between the sample in the ground state (without pump pulse) and in the excited states (with pump pulse) will be calculated to obtain the TA spectrum. The delay time τ can range from picoseconds to several nanoseconds, and the ΔA at each

delay time τ will be recorded and collected to provide a global spectrum as a function of delay time τ and wavelength λ. By analyzing the $\Delta A(\lambda, \tau)$ profile, information on the photophysical dynamics will be obtained, including the charge transfer, exciton lifetime, intersystem crossing, energy migration, and exciton separation at the interface. [24]

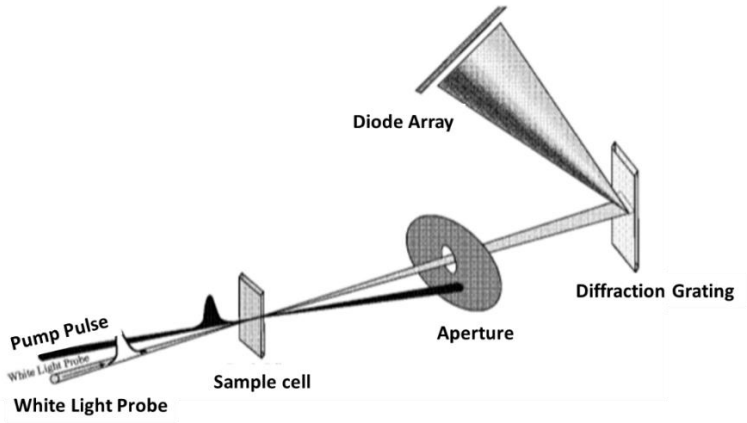

Figure 3.12 Scheme of TA spectroscopy. Reprint with permission from Ref. 24. Copyright © 2009, Springer Nature, Open Access.

In general, three main processes contribute to the TA spectrum, as illustrated in Figure 3.13. The number of molecules at ground state will decrease after being excited by the pump pulse, making the absorption intensity of the sample weaker than it would be without being excited by pump pulse. As a result, a negative peak will be observed on the TA spectrum around the wavelength of the sample's ground state absorption, which is denoted as ground state bleaching (GSB). When the probe light passes through the sample, some of the molecules at the excited state can relax to the ground state by emitting photons, which is called stimulated emission (SE). The emitting photons will be collected and detected together with the probe light, resulting in an increase in the intensity of the probe light. Consequently, a negative signal of absorption will be shown on the TA spectrum, as seen in the blue region in Figure 3.13. The SE band, like the PL peak, always follows closely by the GSB band, and sometimes even overlaps with GSB and merges into a single band. The last contribution on the TA spectrum is excited state absorption (ESA) with a positive signal. The excited molecules can absorb the probe light of a specific wavelength and transfer to a higher excited state. In addition, some other factors can affect the TA spectrum, such as absorption from the photochemical

products, long-lived excitons at triplet excited states, and charge transfer process at the interface.

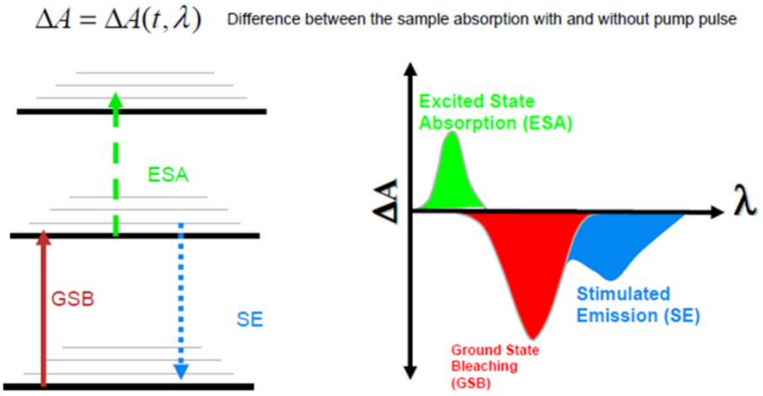

Figure 3.13 Illustration of different contributions to TA spectrum. [25]

3.4.6 Optical-pump Terahertz-probe Spectroscopy

Despite the morphologies and physical properties of materials, charge carriers all response distinctly to the radiation with low-frequency. [27] Therefore, the carrier dynamics at the bilayer interface are investigated by optical-pump terahertz-probe (OPTP) spectroscopy, which probes the frequency-dependent photoconductivity with subpicosecond pulses in the terahertz (THz) range (4.2 meV at 1 THz). A schematic diagram of an OPTP setup is shown in Figure 3.14. The optical pump beam (excitation beam) is generated from an 800 nm mode-locked femtosecond laser. The THz pulse beam is generated by the laser in a ZnTe crystal through optical rectification and split into two beams for the generation and detection. The efficient coupling between the THz emitter and detector is guaranteed by the attachment of lenses of silicon and parabolic mirrors. The delay time between optical pump and THz pulse is controlled by two motorized optical delay lines.

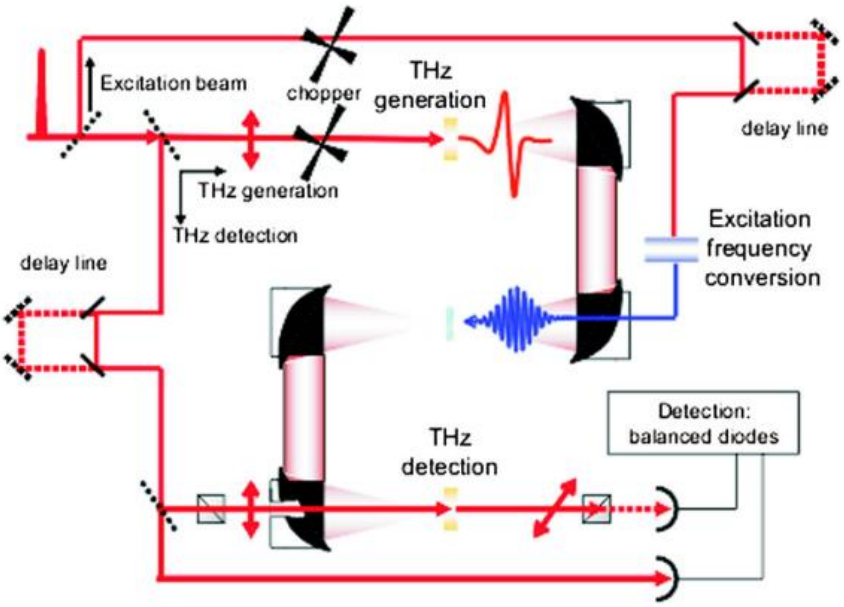

Figure 3.14 Scheme of an OPTP experimental setup. Reprint with permission from Ref. 27. Copyright © 2011 American Physical Society.

In a measurement, the THz electric-field waveform $E\ (t)$ passing through an unexcited sample and the photoinduced change of the electric-field waveform $\Delta E\ (t)$ are recorded. An OPTP measurement of single-walled carbon nanotube dispersion is taken as an example as shown in Figure 3.15. [28] The fractional change of electric-field ($\Delta E/E$) is proportional to the time-dependent photoconductivity ($\Delta\sigma$), which can be used to estimate the photoinduced free carrier density if the carrier mobility is assumed to be constant during the measurement. As shown in Figure 3.15b, the SWCNT dispersion with high defect density exhibits a reduction of 30% in $\Delta E/E$ compared to the pristine dispersion, which suggests a reduction of photoconductivity resulted from the charge scattering at the defects.

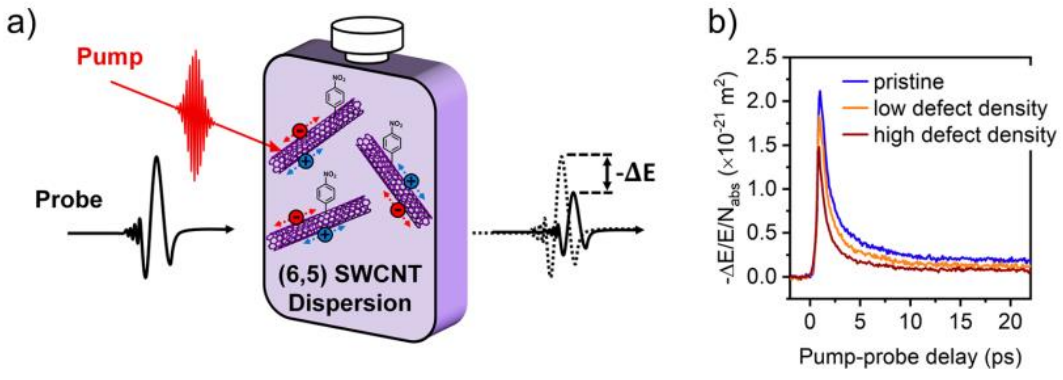

Figure 3.15 (**a**) Schematic illustration of OPTP measurement on single-walled carbon nanotube (SWCNT) dispersion. (**b**) Photoconductivity dynamics of functionalized SWCNT with different defect densities. Reprint with permission from Ref. 28. Copyright © 2022 The Authors. Published by American Chemical Society, Open Access.

3.5 Overview of Methodologies

This project aims to investigate the singlet fission within SF molecules and charge dynamics at SF/perovskite heterojunctions. The synthesis routes of novel SF materials are guided by the literature results and computational simulations. The molecular structures were determined by NMR and IR spectra. The crystal structures and morphologies of the fabricated films were characterized by XRD, SEM and AFM techniques. Favorable energy alignment between SF and perovskite films is essential to the charge transfer process. Therefore, the energy band structures of SF materials and perovskite were determined by the combined results of CV plots, UV-vis absorption and UPS spectra. Meanwhile, the photophysical properties of SF materials were characterized. The charge transfer dynamics were then investigated by transient absorption and PL spectroscopies. All these results illustrate the charge transfer process at the SF/perovskite interface and provide a pathway to SF-enhanced solar cells.

References

[1] M. Winkler and K. N. Houk, *J. Am. Chem. Soc.,* **2007**, 129, 6, 1805-1815.

[2] Y. Chen, L. Shen and X. Li, *J. Phys. Chem. A,* **2014**, 118, 5700-5708.

[3] J. Herz, T. Buckup, F. Paulus, J. U. Engelhart, U. H. F. Bunz and M. Motzkus, *J. Phys. Chem. A.,* **2015**, 119, 25, 6602-6601.

[4] Y. Liu, H. Phan, T. S. Herng, T. Y. Gopalakrishna, J. Ding and J. Wu, *Chem. Asian J.,* **2017**, 12, 2177-2182.

[5] T. Zhang, C. An, P. Bi, Q. Lv, J. Qin, L. Hong, Y. Cui, S. Zhang and J. Hou, *Adv. Energy Mater.,* **2021**, 11, 2101705.

[6] A. Mishra, N. Bhatt and A. K. Bajpai, *Nanomaterials-Based Coatings*, Elsevier **2019**, 397-424.

[7] I. L. Pykett, J. H. Newhouse, F. S. Buonanno, T. J. Brady, M. R. Goldman, J. P. Kistler and G. M. Pohost, *Radiology*, **1982**, 143, 157-168.

[8] P. C. Lauterbur, *Nature*, **1973**, 242, 190-191.

[9] A. Abragam, *The Principles of Nuclear Magnetism*, London: Oxford University Press, **1961**.

[10] R. Tomoyska, A. Agirre, A. Veloso and J. R. Leiza, *Reference Module in Chemistry, Molecular Science and Chemical Engineering*, Elsevier, **2014**.

[11] R. Kohli and K. L. Mittal, *Developments in Surface Contamination and Cleaning*, William Andrew, **2011**, Vol 4.

[12] W. H. Bragg and W. L. Bragg, *Proceeding of the Royal Society A,* **1913**, 88, 428-438.

[13] G. M. McClelland, R. Erlandsson and S. Chiang, "Atomic Force Microscopy: General Principles and a New Implementation", in: D. O. Thompson, D. E. Chimenti, (eds) *Review of Progress in Quantitative Nondestructive Evaluation,* Springer, Boston, **1987**, Vol 6, 1307-1314.

[14] R. R. L. De Oliveira, D. A. C. Albuquerque, T. G. S. Cruz, F. M. Yamaji and F. L. Leite, *Atomic Force Microscopy - Imaging, Measuring, and Manipulating Surface at the Atomic Scale*, INTECH, **2012**, Chapter 7.

[15] E. Meyer, *Progress in Surface Science*, **1992**, Vol 41, 3-49.

[16] J. I. Goldstein, D. E. Newbury, J. R. Michael, N. W. M. Ritchie, J. H. J. Scott and D. C. Joy, *Electron Beam-Specimen Interactions: Interaction Volume,* Springer, New York, **2018**.

[17] N. Elgrishi, K. J. Rountree, B. D. McCarghy, E. S. Rountree, T. T. Eisenhart and J. L. Dempsey, *J. Chem. Educ.,* **2018**, 95, 197-206

[18] C. M. Cardona, W. Li, A. E. Kaifer, D. Stockdale and G. C. Bazan, *Adv. Mater.,* **2011**, 23, 2367-2371.

[19] J. Sworakowski, *Synthetic Metals*, **2018**, 235, 125-130.

[20] R. J. Anderson, D. J. Bendell and P. W. Groundwater, *Organic Spectroscopic Analysis,* Royal Society of Chemistry, **2004**.

[21] K. Dyamenahalli, A. Famili and R. Shandas, *Shape Memory Polymers for Biomedical Applications*, Elsevier Ltd., **2015**.

[22] N. T. Kalyani and S. J. Dhoble, *Rnew. Sust. Energ. Rev.*, **2012**, 16, 2696-2723.

[23] H. Bubert and H. Jenett, *Surface and Thin Film Analysis: Principles, Instrumentation, Applications.* Wiley-VCH Verlag GmbH, **2002**.

[24] R. Berera, R. Van Grondelle and J. T. M. Kennis, *Photosynthesis Research*, **2009**, 101, 105-118.

[25] M. Vengris, *Biological photoreactions explored by multi-pulse ultrafast spectroscopy,* PhD dissertation, **2005**, Vrije Universiteit, Amsterdam.

[26] M. Xiao, F. Huang, W. Huang, Y. Dkhiss, Y. Zhu, J. Etheridge, A. Gray-Weale, U. Bach, Y.-B Cheng and L. Spiccia, *Angew. Chem. Int. Ed.,* **2014**, 53, 9899-9903.

[27] R. Ulbricht, E. Hendry, J. Shan, T. F. Heinz and M. Boon, *Rev. Mod. Phys.,* **2011**, 83(2), 543-586.

[28] W. Zheng, N. F. Zorn, M. Bonn, J. Zaumseil and H. I. Wang, *ACS Nano*, **2022**, 16, 9401-9409.

Chapter 4*

Unveiling Charge-Transfer Dynamics at Singlet Fission Layer/Hybrid Perovskite Interface

Singlet fission (SF) materials have been applied in various types of solar cells to pursue higher power conversion efficiency (PCE) beyond the Shockley−Queisser (SQ) limit. SF implementation in perovskite solar cells has not been successfully realized yet due to the insufficient understanding of the SF/perovskite heterojunctions. In this chapter, an SF/perovskite system has been established to elucidate the electronic dynamics at the interface by incorporating a well-known SF molecule, TIPS-pentacene, and a triple-cation perovskite $Cs_{0.05}(FA_{0.85}MA_{0.15})_{0.95}PbI_{2.55}Br_{0.45}$, owing to their well-matched energy structures. The transient absorption spectra and kinetic fitting plots suggest an electron-transfer process from the triplet state of TIPS-pentacene to perovskite in picosecond regime, which increases the carrier density by 20% in the perovskite layer. This work confirms the existence of an electron-transfer process between the SF material and perovskite, providing a pathway to SF-enhanced perovskite solar cells.

*This section published substantially as X. Xiao, L. Cheng, D. Bao, Q. Y. Tan, T. Salim, C. Soci, E. E. M. Chia and Y. M. Lam, Unveiling Charge-Transfer Dynamics at Singlet Fission Layer/Hybrid Perovskite Interface. *ACS Appl. Mater. Interfaces* 2023, **15**, 31, 38049-38055. DOI: 10.1021/acsami.3c06933. Reprint with permission.

4.1 Introduction

Organometal halide perovskite was first applied in a dye-sensitized solar cell (DSSC) as visible-light sensitizer in 2009, which achieved an efficiency of 3.8%. [1] Three years later, the first solid-state perovskite solar cell was introduced by applying 2,2ʾ7,7ʾ-tetrakis[*N*,*N*-di(4-methoxyphenyl)amino]-9,9ʾ-spirobifluorene (Spiro-OMeTAD) as a solid hole transport layer (HTL), which attracted more attention over DSSCs since the solid-state solar cells could circumvent the intrinsic instability of liquid electrolyte used in DSSCs. [2] Although the power conversion efficiency (PCE) of hybrid perovskite-based solar cells has reached a remarkable value of 25.7% [3] within a relatively short time, nevertheless the PCE of the single-junction solar cell is still restricted by the theoretical Shockley−Queisser (SQ) efficiency limit of 34% as the excess energy of absorbed photons with energy above the band gap cannot be utilized, resulting in thermalization losses. [4]

Singlet fission (SF) is a process found in organic chromophores involving the conversion of a singlet exciton to multiple triplet excitons. [5] Since more than one electron−hole pair can be generated per absorbed photon, the SF process is believed to provide a higher chance to boost the PCE of solar cells beyond the SQ limit. The implementation of SF materials in solar cells has been recently investigated, such as the application of a tetracene layer in a single-junction silicon solar cell, as well as the silicon−pentacene tandem solar cell with high spectral stability, both of which have realized a high external quantum efficiency (EQE) over 100%. [6,7]

Compared to other solar cell materials, like silicon, quantum dots, and organic semiconductors, hybrid perovskite shows great advantages as a light absorber due to its tunable energy band gap ranging from 1.2 to 2.3 eV and high light extinction coefficient. [8] P-type SF materials, such as pentacene and its derivative, 6,13-bis(triisopropylsilylethynyl)pentacene (TIPS-pentacene), have been studied as HTL materials in planar perovskite solar cells to increase the short circuit current and overall PCE because of the favorable energy-level alignment with the perovskite layer that enables highly efficient charge extraction.[9,10] However, most of the studies on perovskite solar cells so far have focused on the hole transport properties and none have successfully exploited the triplet excitons generated by the SF process to overcome the

SQ limit and to boost the PCE via an efficient SF material−perovskite heterojunction.[11]

Understanding how SF/perovskite heterojunction works is essential to enable future breakthrough improvements. To elucidate the charge dynamic between SF materials and perovskite, D. Kim et al. [12] measured the transient absorption (TA) spectra of a TIPS-pentacene/$MAPbI_3$ bilayer film and claimed for the first time that the electron-transfer process occurred from the triplet state (T_1) of TIPS-pentacene to the conduction band (CB) of $MAPbI_3$ perovskite due to the good matching of the optical energy states of both materials. While D. Guo's work [13] suggests that the electron-transfer process should occur from the correlated triplet pair $^1(TT)$ of TIPS-pentacene to $MAPbI_3$ along with a hole transport process from $MAPbI_3$ to TIPS-pentacene, which occurred in the tens of nanoseconds (ns) regime, since the as-measured CB energy level of $MAPbI_3$ (−3.95 eV) was slightly higher than the T_1 energy level of TIPS-pentacene (−4.21 eV). This ambiguous illustration of the energy-level structures for TIPS-pentacene and $MAPbI_3$ films significantly undermines the interpretation of the charge-transfer dynamics within the bilayer.

Herein, a triple-cation perovskite $Cs_{0.05}(FA_{0.85}MA_{0.15})_{0.95}PbI_{2.55}Br_{0.45}$ with a much lower CB energy level (-4.31 eV) than that of $MAPbI_3$ was chosen to ensure that the electron transfer from the triplet state of TIPS-pentacene is energetically favorable. The distinct TA signatures of perovskite, TIPS-pentacene, and TIPS-pentacene/perovskite bilayer films, as well as their corresponding temporal evolutions, clearly showed a fast electron-transfer process (1.2 ps) from the triplet state of TIPS-pentacene to the CB of triple-cation perovskite. Furthermore, optical-pump terahertz-probe (OPTP) measurements demonstrated a significant increase (~20%) in carrier density within the perovskite layer attributed to the electron injection from TIPS-pentacene in the bilayer film.

4.2 Experimental Methods

4.2.1 Materials

Lead iodide (PbI_2), lead bromide ($PbBr_2$), cesium iodide (CsI), formamidinium iodide (FAI), methylammonium bromide (MABr), dimethylformamide (DMF), dimethyl sulfoxide (DMSO), 6,13-bis(triisopropylsilylethynyl)pentacene (TIPS-pentacene), and chlorobenzene were purchased from Sigma-Aldrich. All chemicals were used as received without further purification. Quartz substrates were purchased from Sigma-Aldrich.

4.2.2 Preparation of precursor solutions

The perovskite precursor solution was prepared by mixing three solutions A, B, and C. Solution A was prepared by dissolving FAI (208.30 mg, 1.211 mmol) and PbI_2 (587.79 mg, 1.275 mmol) in 2 mL of DMF/DMSO (v/v = 4/1) mixed solvent. Solution B was prepared by dissolving MABr (159.6 mg, 1.425 mmol) and $PbBr_2$ (550.5 mg, 1.5 mmol) in 2 mL of DMF/DMSO (v/v = 4/1) mixed solvent. Solution C was prepared by dissolving CsI (77.9 mg, 0.3 mmol) in 800 μL of DMSO. Solutions A, B, and C were mixed with a volume ratio of 10:1.5:1 to provide $Cs_{0.05}(FA_{0.85}MA_{0.15})_{0.95}PbI_{2.55}Br_{0.45}$ precursor solution with a concentration of 0.6 M.

4.2.3 Treatment of film substrates

The quartz substrates were sequentially cleaned with a water-based optical lens detergent (1%, Mailang, MIGHTY ZS-120), deionized (DI) water, acetone, isopropanol (IPA), and ethanol in a ultrasonication bath for 30 min each, followed by drying with a compressed nitrogen gun and an ultraviolet−ozone treatment for 15 min to improve the wettability before applying for film fabrication.

4.2.4 Preparation of perovskite, TIPS-pentacene, and bilayer films

The perovskite films were deposited onto the quartz substrate by spin-coating, and the TIPS-pentacene films were fabricated by thermal evaporation methods in a glovebox. The perovskite precursor solution was spin-coated at 5000 rpm for 30 s by using ethyl acetate as an antisolvent. The film was then annealed at 100 ^oC for 10 min. The TIPS-pentacene film was thermally evaporated onto a quartz substrate under the pressure below 2×10^{-6} Pa with a deposition rate of 0.1−0.2 nm/s. The bilayer film was fabricated

by thermally evaporating the TIPS-pentacene film onto the as-prepared perovskite film. All films were tested immediately without any encapsulation.

4.2.5 General characterizations

The morphologies of as-prepared films and cross-sectional structure of the bilayer film were examined by field-emission scanning electron microscopy (FESEM 7600F, JOEL) and an atomic force microscopy (AFM, Asylum Research, Cypher S). The crystal structure of as-prepared films was measured by X-ray diffraction spectroscopy (D8 Advance, Bruker) with Cu Kα radiation at 40 kV and 40 mA. The valence band (VB) energy level of perovskite and the highest occupied molecular orbital (HOMO) level of TIPS-pentacene film were determined by ultraviolet photoelectron spectra (UPS) obtained from a Kratos AXIS Supra X-ray photoelectron spectroscopy (XPS). The ultraviolet−visible (UV−vis) absorption characteristics of as-prepared films were characterized by a Cary 5000 UV−vis spectrophotometer (Agilent Technologies).

4.2.6 Transient absorption measurement

The Helio Fire system from Ultrafast Systems was used to measure the transient absorption (TA) spectra of the as-prepared films. An 800 nm femtosecond laser with a 35 fs pulse width, a 1 kHz repetition rate, and a 4 mJ pulse energy was used to generate the 650 nm pump beam by passing through a β-$Ba(BO_2)_2$ crystal and the white-light probe by focusing an 800 nm beam on a sapphire crystal.

4.2.7 Time-resolved photoluminescence measurement

Time-resolved photoluminescence (TRPL) measurements were performed on an upright microscope setup. A fiber-coupled picosecond pulsed laser (Pico Quant P-C-405B) with an output wavelength λ = 405 nm and a repetition rate f = 2.5 MHz was used as the excitation source. The laser was focused on the samples using a 10x microscope objective. The emissions were filtered using a long-pass filter with a cutoff wavelength λ = 420 nm and directed into a spectrometer (Acton Spectra Pro 2300i), within which the emissions were then impinged onto a monochromator. Emissions that are around the wavelength of 760 nm are subsequently transmitted and collected into a

single photon avalanche detector (Micron Photon Devices). A single photon counting module (Pico Harp 300) was used to extract the data. All measurements were conducted at room temperature.

4.2.8 Optical-pump terahertz-probe measurement

Optical-pump terahertz-probe (OPTP) measurements were performed on a homebuilt setup. The sample films were excited by a 400 nm pump pulse that was generated by an 800 nm femtosecond laser, followed by a terahertz (THz) probe beam with a frequency range of 0.5−2.5 THz that was generated in a ZnTe crystal through optical rectification. The pump-probe delay was adjusted by moving two motorized delay stages. Both the transmitted THz electric field (E) and the photoinduced change (ΔE) were measured simultaneously using two lock-in amplifiers by modulating the pump and probe beams.

4.3 Results and Discussion

4.3.1 Morphology and crystal structure characterization of films

To investigate the dynamics of charge generation and transfer processes between TIPS-pentacene and perovskite, the TIPS-pentacene/perovskite bilayer film and its corresponding monolayer films were fabricated by spin-coating and thermal evaporation methods as described in the Experimental section. The films were first characterized to assess the film quality before they were subjected to further time-resolved photophysical studies. Figure 4.1 shows the morphologies of as-fabricated films characterized by FESEM in low and high resolution. Both perovskite and TIPS-pentacene films are compact without pinholes and formed by grains with a uniform size distribution. As observed in the enlarged FESEM images (Figure 4.1d and e), the average size of perovskite grains is around 100 nm, while the average size of TIPS-pentacene grains is much smaller (around 10 nm). In the bilayer film, thermally evaporated TIPS-pentacene film uniformly covers the underneath spin-coated perovskite film without any visible pinholes and large TIPS-pentacene grains are formed by the fusion of small grains (Figure 4.1 c and f).

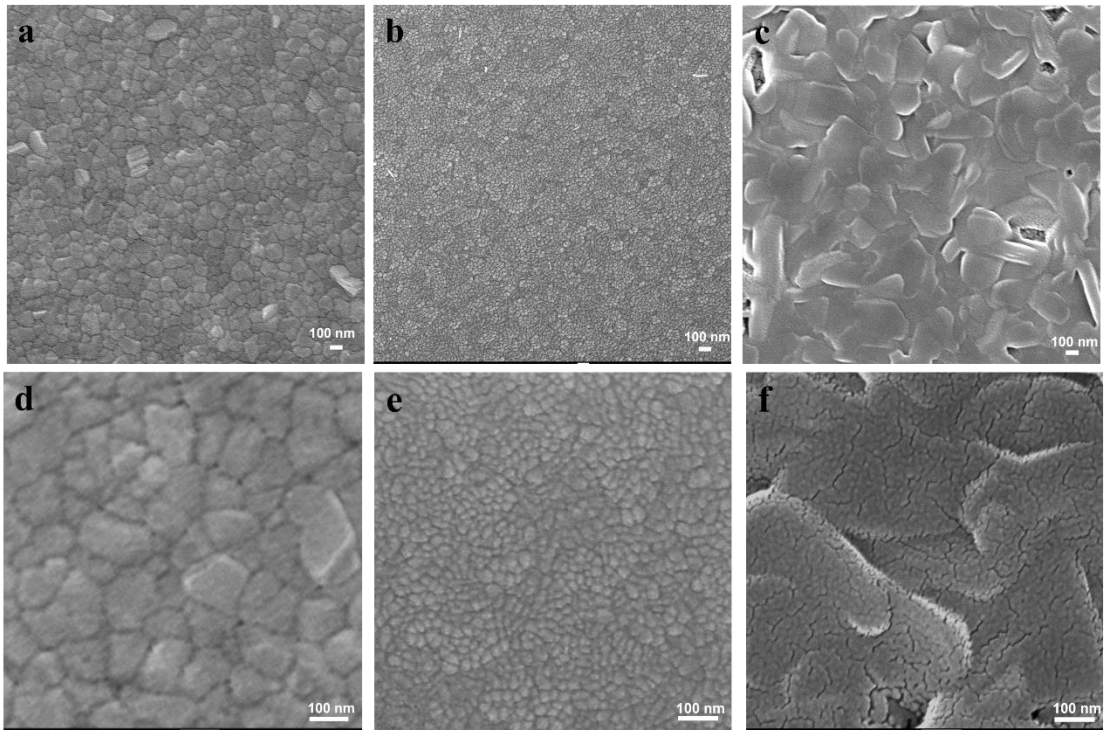

Figure 4.1 FESEM images of as-fabricated films: (**a, d**) perovskite, (**b, e**) TIPS-pentacene and (**c, f**) bilayer films in low (up) and high (down) magnification, respectively.

The thickness and roughness of perovskite and TIPS-pentacene films are characterized by cross-sectional FESEM and AFM techniques, as shown in Figure 4.2. From the vertical distance profiles obtained by AFM, the thicknesses of perovskite and TIPS-pentacene are determined to be 138.3 and 103 nm, respectively, which is consistent with the cross-sectional FESEM image of bilayer film (Figure 4.2a). The film roughness (RMS) of monolayers is derived from the topological AFM images. As shown in Figure 4.2b and c, the roughness is 6.16 nm for spin-coated perovskite film, and 3.45 nm for thermal-evaporated TIPS-pentacene film. A smaller roughness of TIPS-pentacene film indicates a much flatter surface morphology compared with perovskite film, which corresponds well with the FESEM images shown in Figure 4.1.

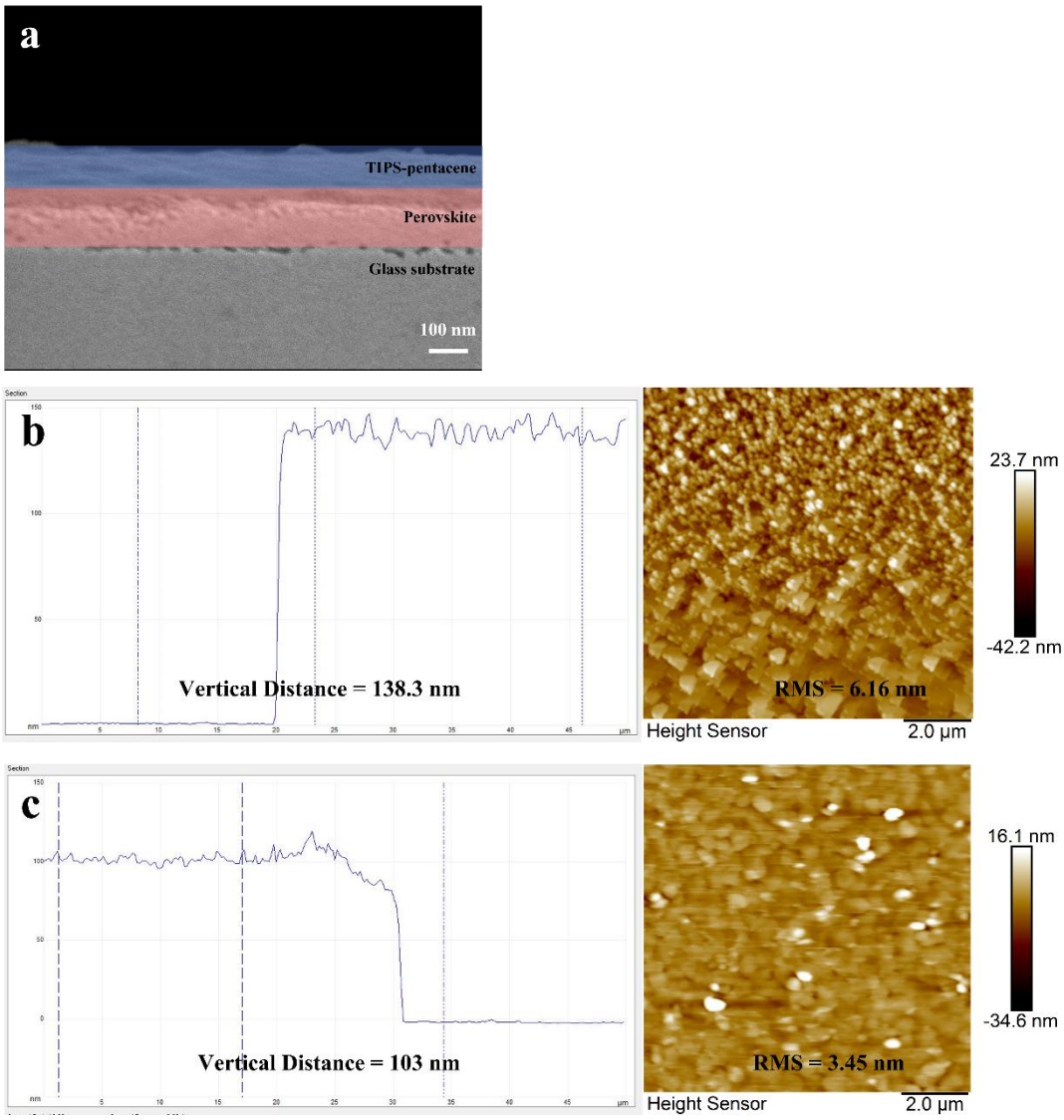

Figure 4.2 (**a**) Cross-sectional FESEM image of bilayer film. Vertical distance profiles and AFM images of (**b**) perovskite and (**c**) TIPS-pentacene films.

The XRD pattern of the thermally annealed perovskite film shown in Figure 4.3 indicates the presence of a highly crystalline photoactive cubic α-phase. The diffraction peaks at 2θ = 14.08, 19.92, 24.50, 28.32, 31.82, 40.58, and 43.13° can be attributed to the (101), (012), (021), (202), (211), (024), and (131) planes, respectively, which are in good agreement with the reported patterns. [14-16] Two small peaks at 2θ = 30.25 and 35.04° are assigned to the ITO substrate. On the other hand, an intense diffraction peak at 2θ = 5.37° is observed in the XRD pattern of the TIPS-pentacene film, which can be assigned to the (001) crystal plane with a layer distance of 16.5 Å, identical to the *c*-axis unit cell length, followed by two peaks at 2θ = 10.74 and 16.09°, corresponding to the (002) and (003) crystal planes, respectively. The XRD results show that the

thermally evaporated TIPS-pentacene film possesses a well-organized π-stacking molecular structure with a high degree of crystallinity. [17,18] The XRD pattern of the bilayer film is the superposition of the individual diffractograms, indicating that crystal structures of TIPS-pentacene and perovskite films were not affected during the fabrication of bilayer film and that both films remained highly crystalline.

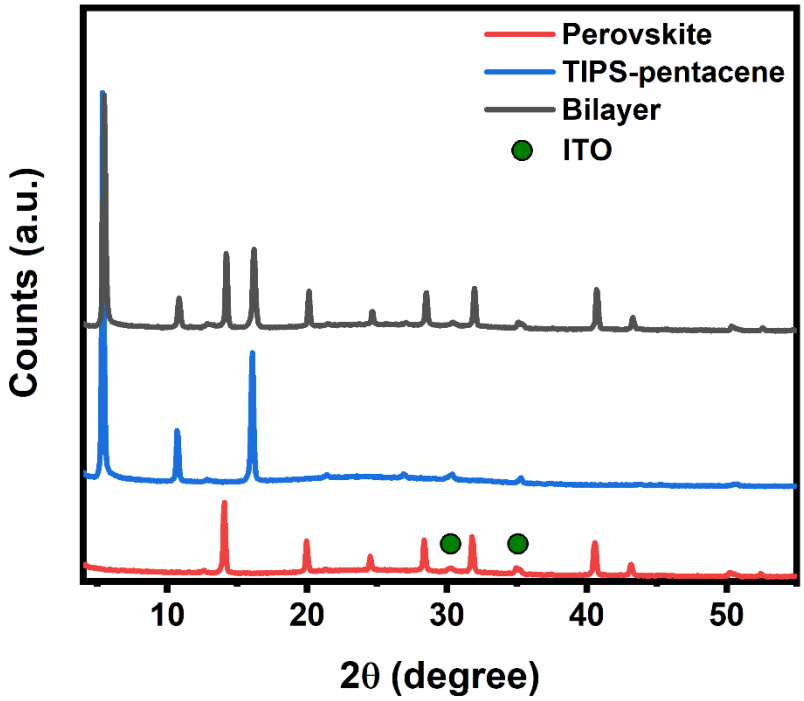

Figure 4.3 Thin film XRD patterns of as-fabricated films: perovskite (red), TIPS-pentacene (blue) and bilayer (black). The green circles denote the XRD peaks of ITO substrate.

4.3.2 Energy alignment determination

The energy-level alignment between perovskite and TIPS-pentacene plays a significant role in facilitating an efficient charge-transfer process at the bilayer interface. Hence, the exact energy band structure of both triple-cation perovskite and TIPS-pentacene films employed in this work must be properly determined. A combination of UV−vis absorption spectroscopy and UPS techniques was used for this purpose. The UV−vis absorption spectra of the as-fabricated films are presented in Figure 4.4a. The perovskite film demonstrates extensive absorption with a band edge cutoff at around 750 nm owing to the cubic phase as determined from the XRD. Compared with

perovskite, the absorption of TIPS-pentacene is much smaller due to the small thickness and low extinction coefficient. The absorption spectrum of the bilayer film is dominated by the more absorbing perovskite, where the feature looks almost identical to that of the perovskite film. Figure 4.4b shows the zoomed-in UV−vis absorption profile of TIPS-pentacene, which provides both intramolecular and intermolecular exciton transition information. The absorption peak at 642 nm corresponds to the fundamental intramolecular $S_0 \rightarrow S_1$ transition. The absorption peak at 450 nm is attributed to the pentacene core transition along the dipole orientation (short axis of pentacene skeleton), while the intermediate peak at 586 nm is ascribed to the transition oriented parallel to the dipole orientation. The absorption peak at 695 nm arises from the intermolecular exciton transition orienting close to the $\pi - \pi$ stacking direction, which indicates the high crystallinity of the TIPS-pentacene film. [19-21]

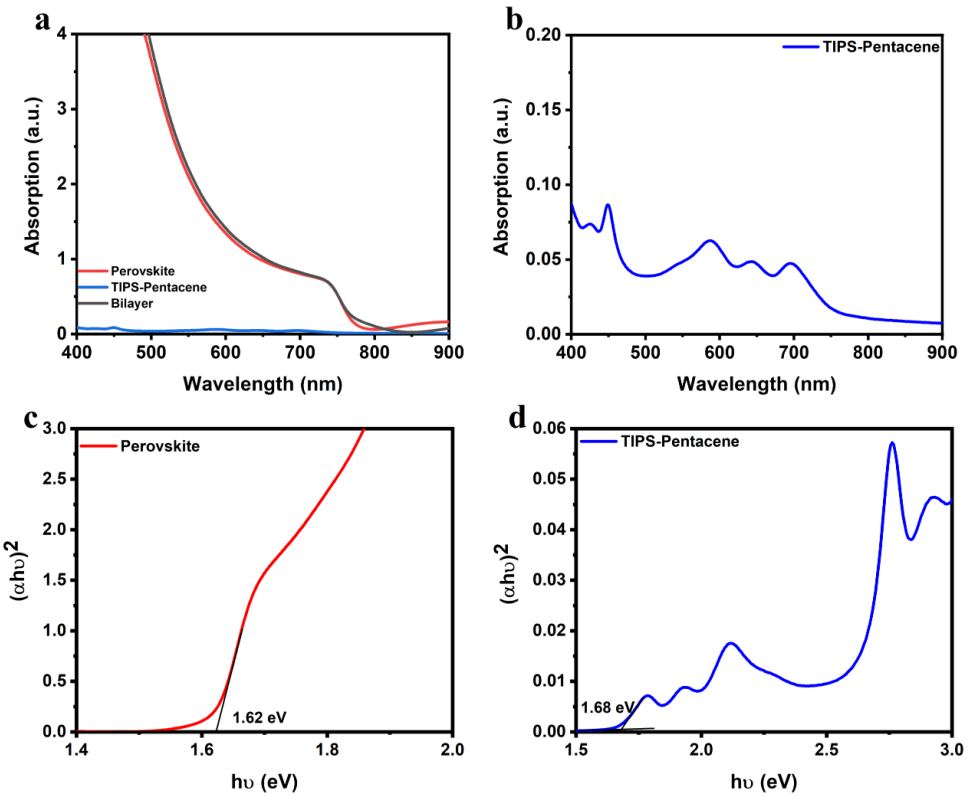

Figure 4.4 (**a**) UV−vis absorption spectra of perovskite (red), TIPS-pentacene (blue) and bilayer (black) films. (**b**) Zoomed-in UV−Vis absorption spectrum of TIPS-pentacene. Tauc plots of (**c**) perovskite and (**d**) TIPS-pentacene films.

The optical band gaps of perovskite and TIPS-pentacene films are determined to be 1.62 and 1.68 eV based on the Tauc plots (Figure 4.4c and d), which are reproduced

from the UV−vis absorption spectra, respectively. The valence band maximum (VBM) of the perovskite film and the highest occupied molecular orbital (HOMO) energy level of the TIPS-pentacene film are determined by the UPS technique. As shown in Figure 4.5, the cut-off energy of the perovskite and TIPS-pentacene film are extrapolated to be 16.52 and 16.78 eV, and the edge energy of perovskite and TIPS-pentacene film are 1.23 and 0.59 eV, respectively. According to Equation 3.13, the VBM and HOMO energy level can be calculated to be −5.93 and −5.03 eV. Combining both the UV−vis and UPS results, the conduction band minimum (CBM) of the perovskite film and the lowest unoccupied molecular orbital (LUMO) energy level of the TIPS-pentacene film are calculated to be −4.31 and −3.35 eV, respectively. The energy level of the triplet states (T_1) of TIPS-pentacene is estimated to be −4.19 eV by adding half the energy of the first excited singlet state (0.84 eV) to the HOMO level of TIPS-pentacene [13], assumed to be the ground state (S_0). Herein, the energy level of T_1 in TIPS-pentacene is slightly higher than that of CB in the triple-cation perovskite, as shown in Figure 4.8, which satisfies the requirement for energetically favourable electron transfer from T_1 of TIPS-pentacene to the CB of perovskite.

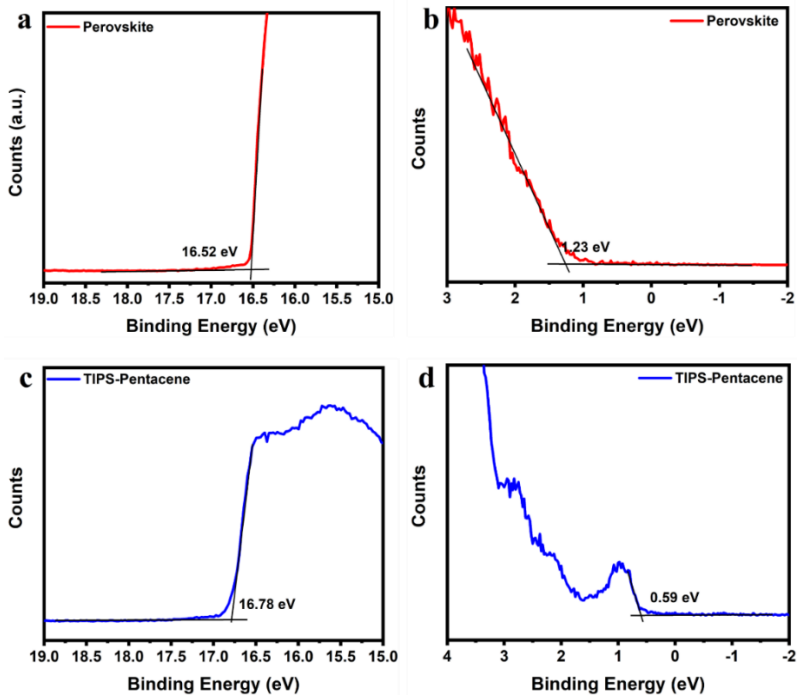

Figure 4.5 UPS spectra of perovskite and TIPS-pentacene film. (**a**) Cut-off and (**b**) edge of perovskite film; (**c**) cut-off and (**d**) edge of TIPS-pentacene film.

4.3.3 Charge-transfer dynamics

Transient absorption (TA) spectroscopy is a very useful technique to reveal the ultrafast optical dynamics of the excited states in materials. Two main features can be observed in the TA spectrum of the perovskite film (Figure 4.6a). An excited-state absorption (ESA) band is centred at around 525 nm. A broad negative band, which is a combination of ground-state bleaching (GSB) signal and stimulated emission (SE) signal, appears in the range of 675−775 nm, consistent with the UV−vis absorption (Figure 4.4a) and photoluminescence (PL) (Figure 4.9b) spectra of the perovskite film.

On the other hand, as shown in Figure 4.6b, the TA spectrum of the TIPS-pentacene film displays three GSB bands at 450, 590, and 700 nm, which are consistent with the peaks observed in the steady-state UV−vis absorption spectrum (Figure 4.4b), except the fundamental intramolecular $S_0 \rightarrow S_1$ transition peak at 642 nm due to the overlap of the pump pulse signal. A broad ESA band centred at 525 nm is assigned to the absorption of the $T_1 \rightarrow T_3$ transition, where the T_1 is generated by the efficient SF process. Two weak positive absorption peaks at 617 and 677 nm are attributed to the absorption of the $S_1 \rightarrow S_n$ transition due to their short decay time. The broad ESA band in the near-infrared region above 740 nm is assigned to the absorption of the correlated triplet pair $^1(TT)$ along with a much weaker absorption of $T_1 \rightarrow T_2$ transition. [22-25]

The TA profile of the TIPS-pentacene/perovskite bilayer film is shown in Figure 4.6c. Compared with the TA spectral features of the pristine TIPS-pentacene film, a new peak at 490 nm arises from the broad ESA band of $T_1 \rightarrow T_3$ transition, which has been demonstrated to be caused by the absorption of TIPS-pentacene cations. [12,26] The peak intensity ratio of a probe wavelength at 490 and 525 nm increases significantly in the bilayer film, which indicates an increasing population of TIPS-pentacene cations in the bilayer film, further suggesting an electron-transfer process from TIPS-pentacene to perovskite in the bilayer film. Furthermore, the fast decay rate of S_1 ESA peaks at 617 and 677 nm indicates a short lifetime of singlet state in TIPS-pentacene after photon excitation. In addition, a previous study reported by M. R. Wasielewski's group [27] proved that the electron transfer from the S_1 state of TIPS-pentacene to PDI molecules was restricted by the ultrafast singlet fission process in TIPS-pentacene. Herein, the

electron-transfer process within the TIPS-pentacene/perovskite bilayer film is proposed to be from T_1 other than S_1 of TIPS-pentacene to the CB of perovskite.

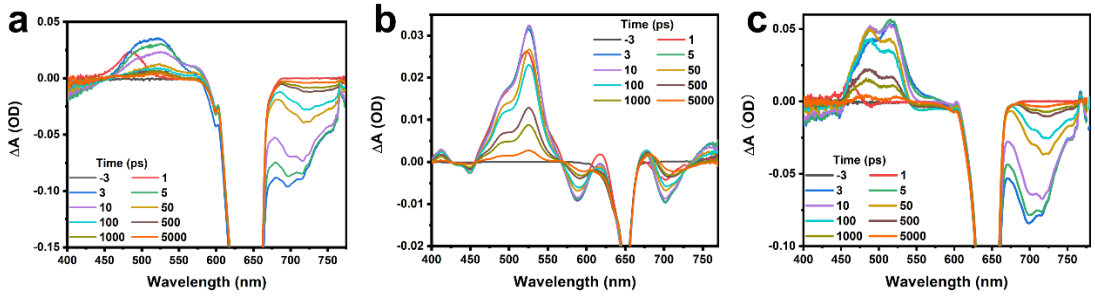

Figure 4.6 TA spectra under pump pulse at 650 nm of (**a**) perovskite, (**b**) TIPS-pentacene and (**c**) bilayer films.

More information about the dynamics of excitons in these films obtained from the fitting of the normalized kinetic plots, as shown in Figure 4.7, supports the electron-transfer process from T_1 of TIPS-pentacene to the CB of perovskite via singlet fission after the photoexcitation. All of the fitting parameters of the kinetic plots at probe wavelengths of 490 and 525 nm are summarized in Table 1, where t_0 represents the time zero, the point of max amplitude at the signal sign inversion. As shown in the kinetic profiles of TIPS-pentacene and bilayer film at 490 nm (Figure 4.7a), an obvious long-rising component with a time constant of 1.2 ps appears in the profile of the bilayer film, which is more than twice as long as the rise time in pure TIPS-pentacene film (0.54 ps). As discussed above, the emergence of the ESA peak at 490 nm is attributed to the absorption of TIPS-pentacene cations. The higher rise time constant at 490 nm implies that there is an electron-transfer process generating cations in 1.2 ps within the bilayer film. As for the kinetic profile of TIPS-pentacene and bilayer films at 525 nm (Figure 4.7b), although both profiles show a similar rise component with a time constant of around 0.8 ps, which is consistent with the previous report, [12] the lifetime of the excitons in TIPS-pentacene film (160 ps) is much longer than the lifetime of excitons in the bilayer film (0.47 ps), which indicates an additional decay pathway of the T_1 excitons generated by the SF process in the bilayer after photoexcitation.

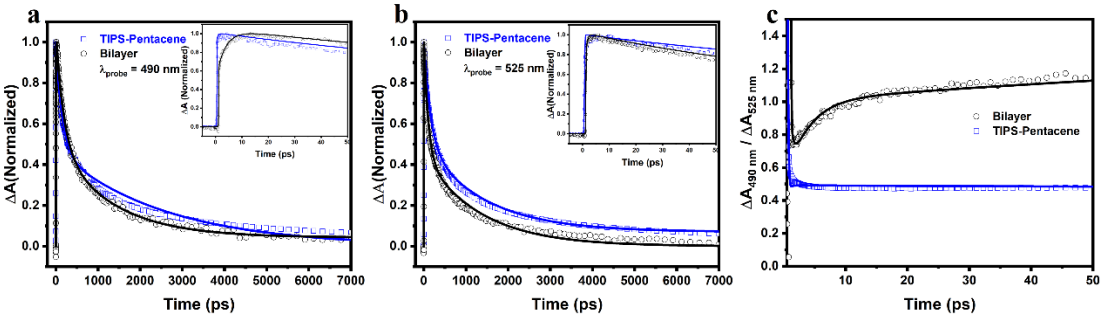

Figure 4.7 Normalized kinetic profiles (scattering dots) and fitting plots (solid line) under excitation wavelength of 650 nm of TIPS-pentacene (blue) and bilayer (black) films at probe wavelength of (**a**) 490 and (**b**) 525 nm. The inset images are kinetic plots over a short time interval. (**c**) Kinetic profiles of absorption difference ratio between the probe wavelengths at 490 and 525 nm for TIPS-pentacene (blue) and bilayer films (black).

The intensity ratio profiles between 490 and 525 nm of TIPS-pentacene and bilayer films are shown in Figure 4.7c. In the pristine TIPS-pentacene film, the intensity ratio decays in a very short time and finally arrives at a constant ratio of around 0.5. The intensity ratio of the bilayer film, on the other hand, shows a constantly rising profile and surpasses 1.0 after around 10 ps. Since the ESA band of perovskite peaks at around 525 nm (Figure 4.6a), the intensity of peak at 525 nm in the bilayer film should be higher than that in the pure TIPS-pentacene film due to the additional contribution from the perovskite layer. However, the intensity ratio of the bilayer film is much higher than that of the pristine TIPS-pentacene film, even showing an increasing trend over a long time interval, which indicates the emergence of an additional long-lived ESA component at 490 nm. Such a long-lived component cannot be the cations generated from the short-lived S_1 excitons of TIPS-pentacene because of their fast decay via the SF process. Based on the observation from the TA spectra and their kinetic profiles, the electron-transfer process from T_1 of TIPS-pentacene to the CB of perovskite – the offset between both levels is energetically favourable – can be confirmed. Therefore, the charge carrier dynamics in the TIPS-pentacene/perovskite bilayer film after photoexcitation is illustrated in Figure 4.8, involving processes such as the ultrafast singlet fission in TIPS-pentacene and the electron transfer from T_1 of TIPS-pentacene to the CB of perovskite within 1.2 ps.

Table 4.1 Fitting parameters of normalized kinetic plots for TIPS-pentacene and bilayer films.

	λ_{probe} (nm)	t_0 (ps)	t_1 (ps)	t_2 (ps)	t_3 (ns)
TIPS-pentacene	490	0.537±0.0086	0.43±0.46	148.1±9.9	2.58±0.17
	525	0.75±0.012	159.9±42	1406±950	3.156±2.4
Bilayer	490	1.2±0.0079	3.4±0.28	186±18	1.32±0.17
	525	1.244±0.01	0.472±0.13	102.7±6.1	1.34±0.086

Time-resolved photoluminescence (TRPL) spectroscopy is a powerful technique to investigate the electronic processes at a longer time scale. As shown in Figure 4.9a, the steady-state photoluminescence (PL) of the bilayer only exhibits a single emission peak of perovskite at around 760 nm but with a much weaker intensity than that of the pristine perovskite layer because TIPS-pentacene does not show any emission due to the ultrafast and efficient SF process. [28] The decrease of the PL intensity in the bilayer can be attributed to the hole transfer process from perovskite to TIPS-pentacene, which is much energetically favourable compared to electron transfer from TIPS-pentacene to perovskite as shown in Figure 4.8. [13] The average PL lifetimes of perovskite and bilayer films are fitted to be 6.39 and 4.90 ns, respectively, from the TRPL spectra (Figure 4.9b). The shorter PL lifetime of the bilayer indicates faster recombination of charge carriers, which can be attributed to an efficient charge transfer at the TIPS-pentacene/perovskite interface, in turn facilitating the injection of SF-generated electrons from TIPS-pentacene and increasing the electron density in the perovskite layer.

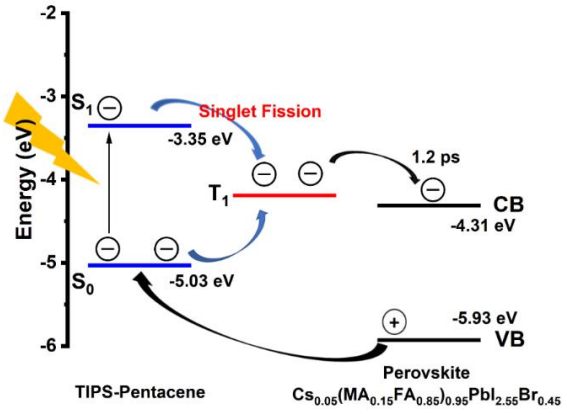

Figure 4.8 Schematic illustration of charge dynamics in TIPS-pentacene/ $Cs_{0.05}(FA_{0.85}MA_{0.15})_{0.95}PbI_{2.25}Br_{0.45}$ bilayer film after photoexcitation, including singlet fission, electron and hole transfer processes.

Table 4.2 Fitting parameters of normalized time-resolved photoluminescence spectra for perovskite and bilayer films.

	τ_1 (ns)	τ_2 (ns)	Average lifetime (ns)
perovskite	0.29	2.27	**6.39**
bilayer	0.84	0.45	**4.90**

Optical-pump THz-probe (OPTP) spectroscopy is an all-optical generation and detection technique that involves using a pulse at the short optical wavelength to excite samples and using a probe in the THz radiation (4.1 meV at 1 THz) range to track dynamics of the generated free carriers. This technique allows the monitoring of the photoinduced change of the transmitted THz electric field (ΔE), whose fractional change ($\Delta E/E$) is proportional to the time-dependent photoconductivity ($\Delta\sigma$), which gives a way to estimate the photoinduced free carrier density if the carrier mobility is assumed to be time-independent. [29-31]

Figure 4.9c displays a comparison of $\Delta E/E$ in response to a 400 nm pump beam at different pump−probe delays for TIPS-pentacene, perovskite, and bilayer films. In the TIPS-pentacene film, the photoinduced change remains negligible and constant throughout the measurement, suggesting that no free carriers were generated by the pump excitation. However, when TIPS-pentacene was deposited onto the perovskite film, a significant (~20%) increase in $\Delta E/E$ is observed compared to the pristine perovskite film. This increase implies that the carrier density in the bilayer film is enhanced by 20% due to the charge transfer from TIPS-pentacene to perovskite, as the TIPS-pentacene film alone does not contribute to the carrier density. The plots are fitted with a double exponential decay function, which are represented by solid lines in Figure 4.9c. The bilayer film is found to exhibit a faster short decay (τ_1 = 12.9 ps) compared to the perovskite film (τ_1 = 18.6 ps), indicating that the defects form at the TIPS-pentacene/perovskite interface, which traps the charge carriers and facilitates the formation of excitons. [30,32] Surface defects in TIPS-pentacene associated with

vacancies or lattice distortion, and structural defects in perovskite, such as undercoordinated Pb or halide vacancies, could act as recombination centres. [33-36] It is worth noting that the long decay component of the bilayer (τ_2 = 721 ps) is almost twice as long as the pristine perovskite film (τ_2 = 366 ps), which indicates a significantly longer lifetime of photogenerated free carriers in the bilayer film.

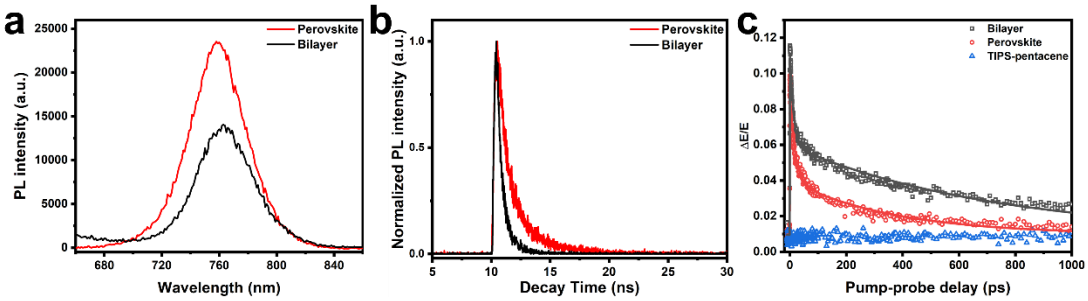

Figure 4.9 (**a**) Steady-state photoluminescence (PL) spectra and (**b**) Time-resolved PL decay curves of perovskite (red) and bilayer (black) films. (**c**) Photoinduced terahertz transmission change of TIPS-pentacene (blue), perovskite (red) and bilayer (black) films.

4.4 Conclusions

In summary, the charge-transfer dynamics of a bilayer film comprising TIPS-pentacene and energetically well-matching perovskite, $Cs_{0.05}(FA_{0.85}MA_{0.15})_{0.95}PbI_{2.55}Br_{0.45}$, has been thoroughly investigated in this work. Transient absorption profiles clearly demonstrated that the ultrafast singlet fission and the electron-transfer processes occurred in 1.2 ps from the triplet state of TIPS-pentacene to the conduction band of perovskite in the bilayer film. In addition, the time-resolved photoluminescence spectra showed that an efficient hole transfer occurred in nanoseconds from the valence band of perovskite to TIPS-pentacene. The electron injection from TIPS-pentacene resulted in an increase in the free carrier density in the perovskite layer, which was demonstrated to be around 20% by the OPTP measurements. This work confirms the feasibility of increasing the carrier density in perovskite by SF sensitization and thus enhancing the PCE of SF-sensitized perovskite solar cells.

Reference

[1] A. Kojima, K. Teshima, Y. Shirai and T. Miyasaka, *J. Am. Chem. Soc.*, **2009**, 131, 6050-6051.

[2] H.-S. Kim, C.-R. Lee, J.-H. Im, K.-B. Lee, T. Moehl, A. Marchioro, S.-J. Moon, R. Humphry-Baker, J.-H. Yum, J. E. Moser, M. Grätzel and N.-G. Park, *Sci. Rep.*, **2012**, 2, 591.

[3] The National Renewable Energy Laboratory (NREL), Best Research-Cell Efficiencies, https://www.nrel.gov/pv/assets/pdfs/best-research-cell-efficiencies.pdf

[4] W. Shockley and H. J. Queisser, *J. App. Phys.*, **1961**, 32(3), pp. 510-519.

[5] M. B. Smith and J. Michl, *Chem. Rev.*,**2010**, 110(11), 6891-6936.

[6] M. Einziger, T. Wu, J. F. Kompalla, H. L. Smith, C. F. Perkinson, L. Nienhaus, S. Wieghold, D. N. Congreve, A. Kahn, M. G. Bawendi and M. A. Baldo, *Nature*, **2019**, 571(7763), 90-94.

[7] L. M. Pazos-Outón, J. M. Lee, M. H. Futscher, A. Kirch, M. Tabachnyk, R. H. Friend and B. Ehrler, *ACS Energy Lett.*, **2017**, 2(2), 476-480.

[8] J. S. Manser, J. A. Christians and P. V. Kamat, *Chem. Rev.*, **2016**, 116(21), 12956-13008.

[9] X. Yang, G. Wang, D. Liu, Y. Yao, G. Zhou, P. Li, B. Wu, X. Rao and Q. Song, *Curr. Appl. Phys.*, **2018**, 18(10), 1095-1100.

[10] G. Ji, B. Zhao, F. Song, G. Zheng, X. Zhang, K. Shen, Y. Yang, S. Chen and X. Gao, *Appl. Surf. Sci.*, **2017**, 393, 417-421.

[11] R. Casillas, I. Papadopoulos, T. Ullrich, D. Thiel and D. M. Guldi, *Energy Environ. Sci.*, **2020**, 13(9), 2741-2804.

[12] S. Lee, D. Hwang, S. I. Jung and D. Kim, *J. Phys. Chem. Lett.*, **2017**, 8, 884-888.

[13] D. Guo, L, Ma, Z. Zhou, D. Lin, C. Wang, X. Zhao, F. Zhang, J. Zhang and Z. Nie, *J. Mater. Chem. A*, **2020**, 8(11), 5572-5579.

[14] M. Saliba, T. Matsui, J. Y. Seo, K. Domanski, J. P. Correa-Baena, M. K. Nazeeruddin, S. M. Zakeeruddin, W. Tress, A. Abate, A. Hagfeldt and M. Grätzel, *Energy Environ. Sci.*, **2016**, 9(6), 1989-1997.

[15] Y. Hu, M. F. Aygüler, M. L. Petrus, T. Bein and P. Docampo, *ACS Energy Lett.*, **2017**, 2(10), 2212-2218.

[16] T. Bu, X. Liu, Y. Zhou, J. Yi, X. Huang, L. Luo, J. Xiao, Z. Ku, Y. Peng, F. Huang and Y.B. Cheng, *Energy Environ. Sci.*, **2017**, 10(12), 2509-2515.

[17] J. E. Anthony, J. S. Brooks, D. L. Eaton and S. R. Parkin, *J. Am. Chem. Soc.*, **2001**, 123, 9482-9483.

[18] S.-I. Shin, J.-H. Kwon, H. Kang and B.-K. Ju, *Semicond. Sci. Technol.*, **2008**, 23(8), 085009.

[19] D. T. James, J. M. Frost, J. Wade, J. Nelson and J.-S. Kim, *ACS Nano*, **2013**, 7(9), 7983-7991.

[20] M. Niu, F. Zheng, X. Yang, P. Bi, L. Feng and X. Hao, *Org. Electron.*, **2017**, 49, 340-346.

[21] M. J. Y. Tayebjee, K. N. Schwarz, R. W. MacQueen, M. Dvorak, A. W. C. Lam, K. P. Ghiggino, D. E. McCamey, T. W. Schmidt and G. J. Conibeer, *J. Phys Chem. C*, **2016**, 120(1), 157-165.

[22] Z. Zhou, L. Ma, D. Guo, X. Zhao, C. Wang, D. Lin, F. Zhang, J. Zhang and Z. Nie, *J. Phys Chem. C*, **2020**, 124(27), 14503-14509.

[23] B. J. Walker, A. J. Musser, D. Beljonne and R. H. Friend, *Nature Chem.*, **2013**, 5, 1019-1024.

[24] A. J. Musser, M. Liebel, C. Schnedermann, T. Wende, T. B. Kehoe, A. Rao and P. Kukura, *Nature Phys.*, **2015**, 11(4), 352-357.

[25] C. K. Yong, A. J. Musser, S. L. Bayliss, S. Lukman, H. Tamura, O. Bubnova, R. K. Hallani, A. Meneau, R. Resel, M. Maruyama, S. Hotta, L. M. Herz, D. Beljonne, J. E. Anthony, J. Clark and H. Sirringhaus, *Nature Commun.*, **2017**, 8, 15953.

[26] T. Sakanoue and H. Sirringhaus, *Nature Mater.*, **2010**, 9(9), 736-740.

[27] R. Charusheela, A. L. Smeigh, J. E. Anthony, T. J. Marks and M. R. Wasielewski, *J. Am. Chem. Soc.*, **2012**, 134(1), 386-397.

[28] A. D. Platt, J. Day, S. Subramanian, J. E. Anthony and O. Ostroverkhova, *J. Phys. Chem. C*, **2009**, 113, 14006-14014.

[29] R. Ulbricht, E. Hendry, J. Shan, T. F. Heinz, and M. Bonn, *Rev. Mod. Phys.*, **2011**, 83(2), 543-586.

[30] D. Zhao, H. Hu, R. Haselsberger, R. A. Marcus, M.-E. Michel-Beyerle, Y. M. Lam, J.-X. Zhu, C. La-o-vorakiat, M. C. Beard and E. E. M. Chia, *ACS Nano*, **2019**, 13, 8826-8835.

[31] W. Zheng, N. F. Zorn, M. Bonn, J. Zaumseil and H. I. Wang, *ACS Nano*, **2022**, 16, 9401-9409.

[32] F. W. de S. Lucas, A. W. Welch, L. L. Baranowsi, P. C. Dippo, H. Hempel, T. Unold, R. Eichberger, B. Blank, U. Rau, L. H. Mascaro and A. Zakutayev, *J. Phys. Chem. C,* **2016**, 120, 18377-18385.

[33] B. Nickel, R. Barabash, R. Ruiz, N. Koch, A. Kahn, L. C. Feldman, R. F. Haglund and G. Scoles, *Phys. Rev. B*, **2004**, 70, 125401.

[34] G. J. Deve, J. R. Vicente, J. Chen and J. W. Ciszek, *J. Phys. Chem. C,* **2018**, 122(27), 15582-15587.

[35] J. M. Ball, A. Petrozza, *Nat. Energy*, **2016**, 1(11), 1-13.

[36] S. Zhang, F. Ye, X. Wang, R. Chen, H. Zhang, L. Zhan, X. Li, X. Ji, S. Liu, *Science*, **2023**, 380(6643), 404-409.

Chapter 5

Systematic Investigation on Electronic Dynamics in Novel Singlet Fission Materials − Nitrogen-Substituted and Thiadiazole-Fused Polyacenes

Singlet fission (SF) is regarded as a promising strategy to boost the power conversion efficiency of single-junction solar cells beyond Shockley-Queisser limit. The traditional SF material, polyacene, has limited application in the field of solar cells due to the poor stability, solubility and the dependence of intermolecular SF performance on film morphologies. In this chapter, a family of dimers composed of nitrogen-substituted and thiadiazole-fused polyacenes has been successfully synthesized to allow the investigation on the effect of molecular geometries on intramolecular SF process. The generation rate of triplets is found to be fastest of 1.09 ps via SF in directly-linked dimer due to its smallest chromophore proximity and found to be slowest of 270.2 ps via intersystem crossing pathway in phenylene-bridged dimer with meta-linked pattern due to the smallest electronic coupling. This work elucidates the relationship between SF property and molecular structure and provides a new perspective for the design of novel SF materials.

5.1 Introduction

The desire for economic and population expansion, along with increasing concerns about environmental issues, has stimulated extensive research on shifting the utilization of energy from fossil fuels towards renewable energy sources with a specific focus on harnessing solar energy. [1-3] Photovoltaic cells based on solar energy have gained a remarkable progress in power conversion efficiency (PCE), which, however, is theoretically restricted by the Shockley-Queisser (SQ) limit of 33.7% for single junction devices. [4,5] Singlet fission (SF) is a phenomenon where an excited chromophore in singlet state can share its energy with a neighboring chromophore and both reach their triplet states. Once these triplets diffuse separately to the electrode ends, a two-fold increase in photocurrent can be achieved. As a result, SF is believed to hold the potential to facilitate photovoltaic technology to exceed the SQ limit. [6,7] Despite high internal quantum efficiency (IQE) over 100% realized in many SF-based solar cells, the current PCE of these devices are not yet optimal, which leaves room for modification in terms of the SF material design. [8]

SF was first discovered in anthracene single crystals [9] and has been tremendously investigated in linearly fused polyacenes (i.e., tetracene and pentacene). A major hurdle to the application of polyacenes in solar cells is their poor solubility in common solvent and high sensitivity to oxygen and moisture. Attaching side group, such as 6,13-bis(triisopropylsilylethynyl) (TIPS) can improve the solubility of polyacenes by preventing self-aggregation. [10] The other structural modification such as incorporation of nitrogen atoms into benzene rings has also been demonstrated to lower and well delocalize the energy level of the frontier molecular orbitals, which leads to the solubility and chemical stability improvement. Besides, the energy structures of acenes can be finely adjusted by changing the number and position of incorporated nitrogen atoms. [11,12] The substitution of nitrogen atoms, on the other hand, will result in a decreasing diradical character, which can be optimized by replacing the benzene ring with a thiophene ring. [13,14] Moreover, the thiophene ring can impart high absorption coefficient and good charge transport property to the parent polyacene. [15]

In most of the polyacenes investigated thus far, SF process occurs through an intermolecular mechanism involving two separate molecules. This mechanism is

inherently dependent on the film morphology, which can pose another challenge to rationally modify their photophysical behavior when they are employed in practical devices. Intramolecular singlet fission (iSF), which is confined within a single molecule with covalently linked chromophores, is regarded as a more suitable solution since iSF can be rationally controlled by adjusting the chromophore geometries. [16,17] Efficient iSF has been demonstrated in many dimers which exhibit effective electronic coupling through π-conjugation and orbital overlap. [18-20] Nevertheless, dimers of nitrogen and sulfur-incorporated polyacenes have been rarely explored in terms of their iSF properties.

Herein, a series of dimers comprising nitrogen-substituted and thiadiazole-fused polyacenes has been successfully synthesized and the relationship between their iSF properties and chromophore geometries has been investigated for the first time. The substitution of nitrogen atoms results in a significant change in the electronic structures of the polyacenes and dimers. The energy levels of frontier molecular orbitals are stabilized and lowered by 0.4 eV for diazapentacene (DAP), 0.03 eV for anthrathiadiazole (ATDA) and 0.7 eV for phenazinothiadiazole (PhTDA). Transient absorption spectroscopy has demonstrated SF process in all dimers, which shows a structure−function relationship, specifically in ATDA dimers with different geometries. The triplet generation rate observed in ATDA dimers varies over three orders of magnitude with the fastest rate of 1.09 ps for directly-linked ATDA-dimer and the lowest rate of 270.2 ps for meta-ATDA-dimer linked by phenylene bridge. The ortho-ATAD-dimer has demonstrated the highest triplet yield of 170%. These results provide a new perspective for the design rule of novel materials with enhanced SF properties to be applied in solar cells.

5.2 Diazapentacene and its dimers

5.2.1 Synthesis and molecular structure characterization

All reagents and solvents were purchased from Sigma Aldrich, and Tokyo Chemical Industry (TCI) corporations and were used in this project as received without any further purification. Thin layer chromatography (TLC) was conducted on aluminum foil pasted with silica gel from Sigma Aldrich under ultraviolet (UV) light of 254 and

365 nm to monitor the reaction. The silica gel used for column chromatography was purchased from Sigma Aldrich, with particle sizes ranging from 0.040 to 0.063 mm and a mean pore size of 60 Å. All the products were dried in a vacuum oven (GONGXIN DZF) at 40 ^{o}C overnight. The molecular structures were characterized by nuclear magnetic resonance (NMR) spectroscopy, Fourier transform infrared (FTIR) spectroscopy and thermogravimetric analysis (TGA) techniques.

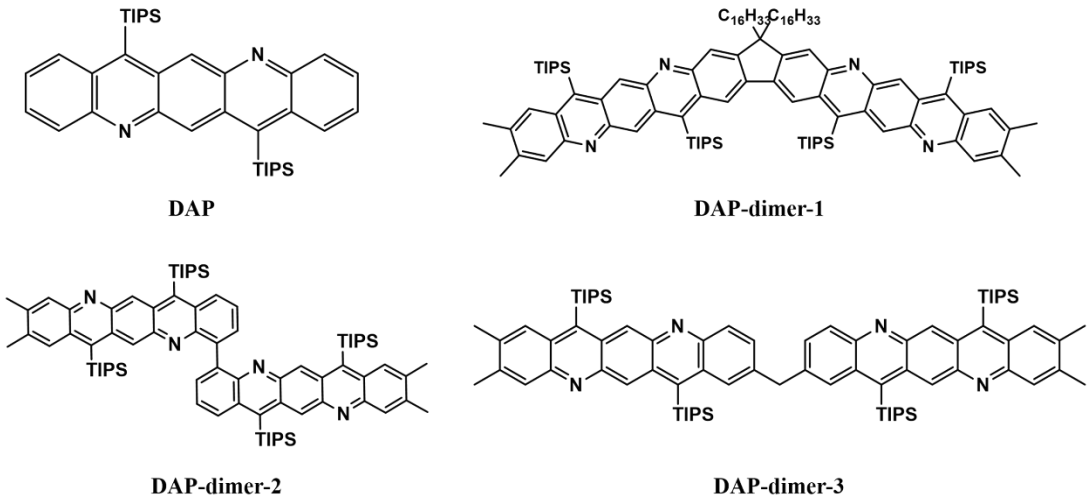

Figure 5.1 Molecular structure illustration of diazapentacene and its dimers.

The molecular structures of the proposed nitrogen-substituted diazapentacene (DAP) and its dimers are illustrated in Figure 5.1, and the overall synthesis route is shown in Scheme 5.1, of which the design strategy is mostly based on the work published by Fang's group [21]. Three dimers are proposed to investigate the effect of structural conjugation and flexibility on electronic properties. DAP-dimer-1 possesses a rigid structure while the other two dimers possess flexible structure; the chromophores in DAP-dimer-3 are unconjugated while the chromophores in other two dimers are conjugated. DAP was synthesized from a quinacridone (QA) unit, which is a pentacene derivative with the incorporation of two N atoms, while the dimers were synthesized based on the "condensation-followed-by-cyclization" method. [22] In this method, the intermediate molecule L-DHDF-2 was synthesized by a two-step imine condensation using amino-functionalized fluorene, dimethyl-2,5-dibromoterephthalate [23], and 3,4-dimethylaniline as the starting materials. L-DHDF-3 was then formed by the Friedel-Crafts cyclization reaction with a rigid aromatic structure, which results in an extremely poor solubility in various common organic solvents.

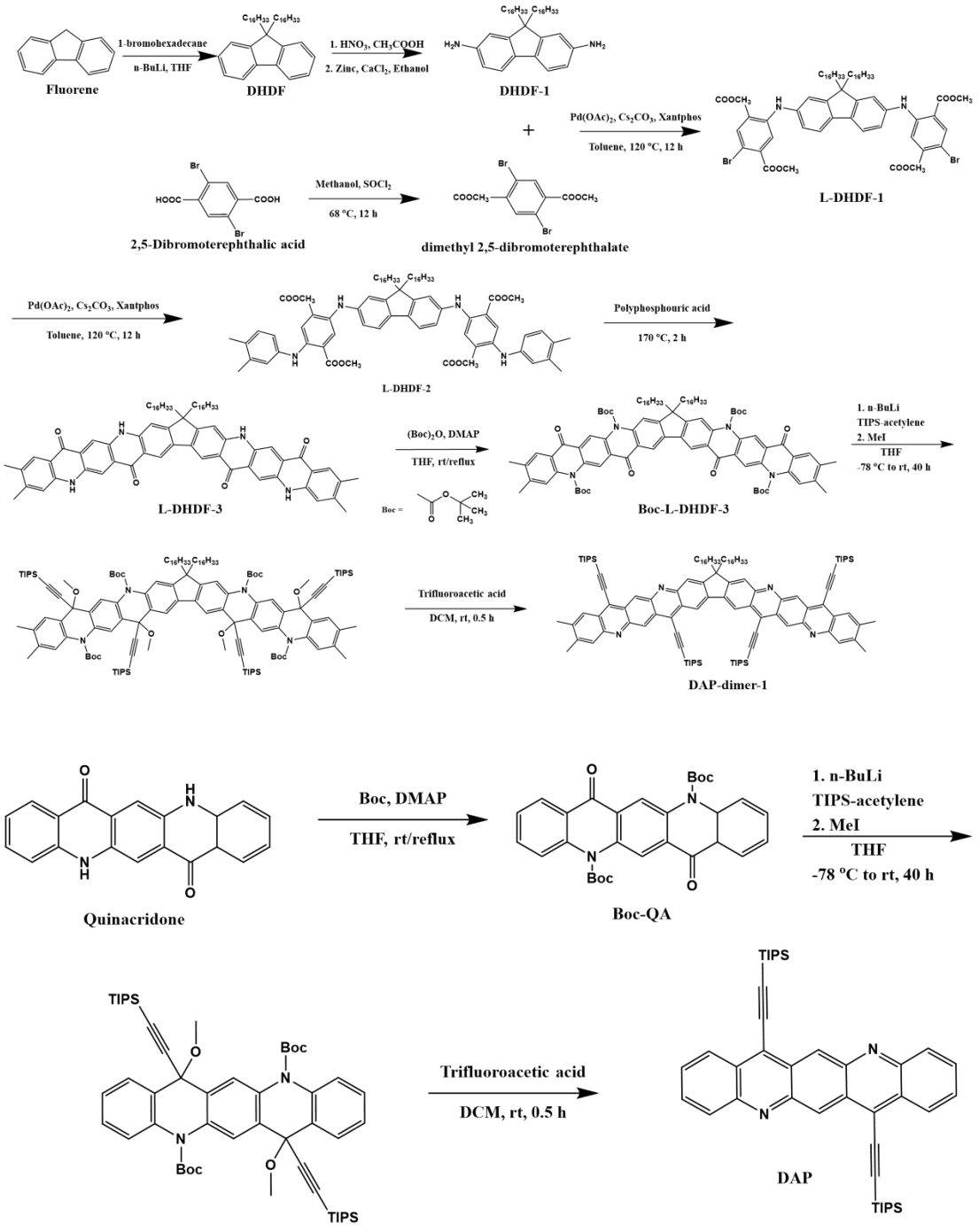

Scheme 5.1 Synthesis routes of DAP-dimer-1 and DAP.

A reversible protection method by attaching tert-butyloxycarbonyl (Boc) groups can be applied to both improve the solubility and protect the N-H groups in L-DHDF-3 in the following reactions. [24] However, the insoluble nature of the intermediates for DAP-dimer-2 and DAP-dimer-3 (synthesis scheme seen in Appendix 1 &2) makes the Boc-protection procedure itself impossible to carry out, which results in the failure of the synthesis of these two dimers. It is noted that the long alkyl side group (-$C_{16}H_{33}$) in L-

DHDF-3 improves the solubility of the rigid backbone, which satisfies the requirement of Boc protection reaction.

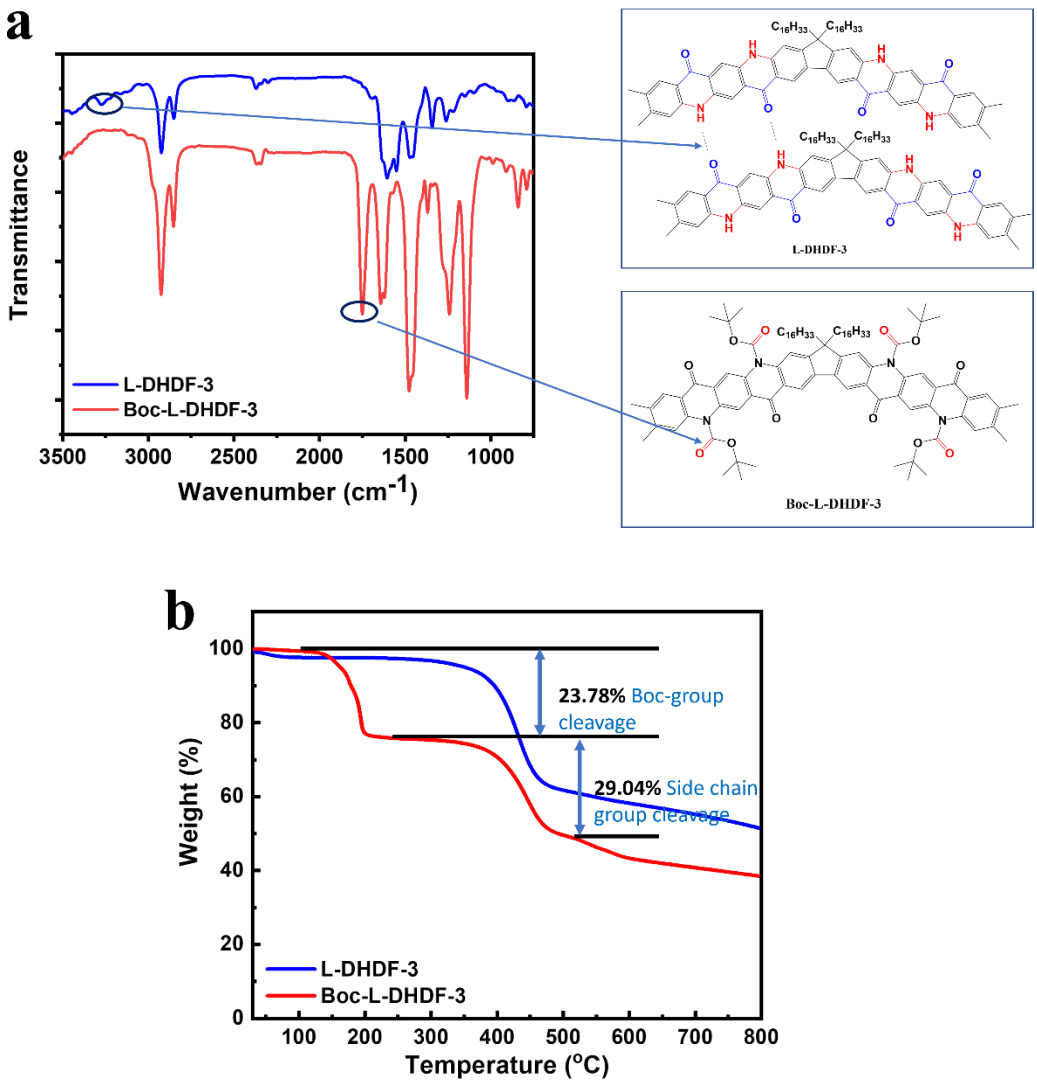

Figure 5.2 (a) FTIR spectra and (b) TGA curves of L-DHDF-3 (blue) and Boc-L-DHDF-3 (red). Two significant bond stretching modes are denoted in (a).

The presence of Boc groups was further verified by using combined FTIR and TGA techniques, as shown in Figure 5.2. In the FTIR spectrum of Boc-L-DHDF-3, a new peak appeared at 1751 cm^{-1}, which can be assigned to the C=O stretching in the Boc group; meanwhile, the peak at 3275 cm^{-1} disappeared, which is assigned to the N-H stretching and indicates the breaking of hydrogen bonding between the QA units after the attachment of Boc groups. [25] The weight loss shown in the TGA profile (Figure 5.1b) further proved the existence of Boc groups in Boc-L-DHDF-3. The weight loss

of 23.78% in the temperature range of 150−200 ºC corresponds to the cleavage of Boc groups [24], which agrees well with the calculated weight percentage of Boc groups in the Boc-L-DHDF-3 (26%). The weight loss of 29.04% in the temperature range of 250−500 ºC is attributed to the cleavage of alky side chain $-C_{16}H_{33}$ (29.2%).

As discussed in Chapter 2, the functionalization of polyacenes with TIPS groups can improve their solubility and stability, which in this project was achieved by adding lithiated silylacetylenes after the Boc protection. [26] The addition of methyl iodide (MeI) produced an intermediate, which was then treated with trifluoroacetic acid (TFA) to remove the Boc and methoxy groups, yielding DAP and its dimers. The detailed discussion about the synthesis procedure is provided in the following section.

Synthesis of DHDF-1. The overall synthesis route of DHDF-1 from fluorene is shown in Scheme 5.2 with three steps, involving alkylation of hexadecane, nitration and reduction to diamine, respectively. [27-29]

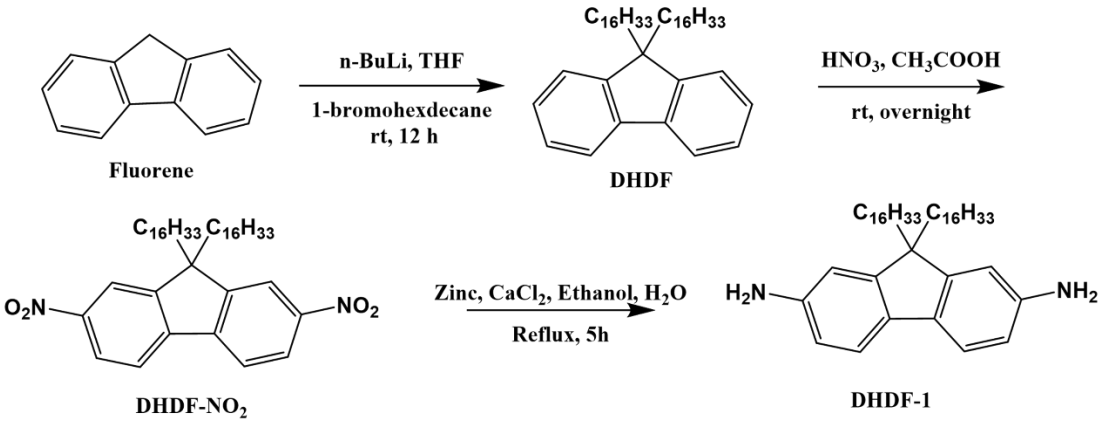

Scheme 5.2 Synthesis route of DHDF-1 from fluorene by three steps.

Step 1: Alkylation of fluorene. One portion of n-butyllithium (n-BuLi) solution (2 M in hexane, 8.8 mL, 17.6 mmol) was first added dropwise into fluorene solution (2.5 g in 50 mL of tetrahydrofuran, THF, 15.04 mmol) over half hour, and the mixture was kept on stirring for another half hour at room temperature. Afterwards, 1-bromohexadecane (11.47 g, 37.5mmol) was added dropwise over 10 min, and the mixture was stirred for 4 h. The second portion of n-BuLi solution and 1-bromohexadecane were added similarly. After being left overnight, the reaction mixture was quenched by saturated NH_4Cl solution (100 mL) and extracted by dichloromethane

(DCM, 2 × 100 mL). The extracted solution was then dried by Na_2SO_4, and rotary evaporated under vacuum to remove the solvent. The pale-yellow solid product of 9,9-dihexadecylfluorene (DHDF) was then obtained by column chromatography using hexane as eluent with a yield of 44%.

^{1}H NMR (400 MHz, $CDCl_3$): δ = 7.70 (2H, d, J = 6.88 Hz, Ar-H), 7.28-7.37 (6H, m, Ar-H), 1.92-1.99 (4H, m, CH_2), 1.01-1.36 (52H, br, CH_2), 0.84-0.93 (6H, t, J = 6.6 Hz, CH_3), 0.56-0.67 (4H, m, CH_2).

Step 2: Nitration of DHDF. To 10 mL of acetic acid (AcOH) was added DHDF (2.0 g, 3.25 mmol) in an ice water bath at 15 ^{o}C followed by the addition of fuming HNO_3 (6 mL) dropwise. The resulting mixture was then warmed to 35^{o}C and continuously stirred overnight. The reaction was monitored by TLC using hexane/ethyl acetate (EtOAc) (95/5) as the eluent to confirm the completion of DHDF consumption. The reaction mixture was quenched by ice water and extracted by EtOAc. The obtained organic layer was washed by deionized (DI) water, saturated $NaHCO_3$, and NaCl, dried over Na_2SO_4, and concentrated by vacuum evaporation to remove the solvent to result in a red oil, which was then purified by column chromatography using hexane/EtOAc (97/3) as the eluent and recrystallized in methanol (MeOH). The aimed product DHDF-NO_2 was obtained as yellow flakes with a yield of 82%.

^{1}H NMR (400 MHz, $CDCl_3$): δ = 8.33 (2H, dd, J_1 = 8.36 Hz, J_2 = 2.06, Ar-H), 8.27 (2H, d, J = 1.96 Hz, Ar-H), 7.93 (2H, d, J = 6.95 Hz, Ar-H), 1.99-2.06 (4H, m, CH_2), 0.96-1.35 (52 H, br, CH_2), 0.88 (6H, t, J = 6.84 Hz, CH_3), 0.51-0.61 (4H, m, CH_2).

Step 3: Reduction of DHDF-NO_2. DHDF-NO_2 (1.88 g, 2.66 mmol), Zn powder (4.44 g) and anhydrous $CaCl_2$ (0.665 g) were mixed in a mixture solvent of ethanol (EtOH, 45 mL) and DI water (10 mL) under reflux for 5 h. After the reflux, the hot reaction mixture was filtered to remove Zn powder and quenched by DI water and DCM (100 mL). The aqueous layer was then extracted by DCM (2 × 100 mL) and combined with the organic layer, which was dried by Na_2SO_4 and concentrated by rotary evaporation to remove the solvent. The residue was purified by column chromatography using hexane/EtOAc (3/1) as eluent to afford the aimed product DHDF-1 with a yield of 94%.

^{1}H NMR (400 MHz, $CDCl_3$): δ = 7.34 (2H, d, J = 6.90 Hz, Ar-H), 6.65 (4H, d, J = 7.9 Hz, Ar-H), 3.70 (4H, br, NH_2) 1.78-1.86 (4H, m, CH_2), 1.18-1.28 (52H, br, CH_2), 0.89 (6H, t, J = 6.88 Hz, CH_3), 0.62-0.68 (4H, m, CH_2).

Synthesis of L-DHDF-1 and L-DHDF-2. L-DHDF-1 and L-DHDF-2 were synthesized by Buchwald-Hartwig coupling reaction under optimized condition[30], as illustrated in Scheme 5.3.

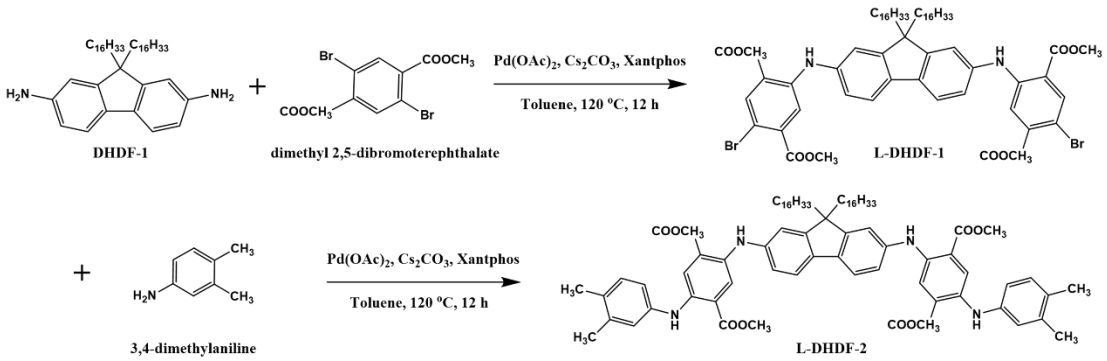

Scheme 5.3 Synthesis route of L-DHDF-1 and L-DHDF-2 by optimized Buchwald-Hartwig coupling reaction.

L-DHDF-1. A mixture of DHDF-1 (540 mg, 0.837 mmol), dimethyl 2,5-dibromoterephthalate (1.18 g, 3.35 mmol), Palladium (II) acetate ($Pd(OAc)_2$, 18.8 mg, 0.0837 mmol), Xantphos (72.56 mg, 0.125 mmol) and Cs_2CO_3 (1.636 g, 5.02 mmol) in 15 mL of dry toluene was degassed by N_2 for 30 min and then heated at 120 ^{o}C overnight. The reaction mixture was cooled and diluted by DCM, followed by filtering through a Celite pack. The residue was concentrated under reduced pressure and purified by column chromatography using hexane/EtOAc (5/1) as the eluent to afford the aimed product L-DHDF-1 as a yellow powder with a yield of 87%.

^{1}H NMR (400 MHz, $CDCl_3$): δ = 9.56 (2H, s, NH), 8.24 (2H, s, Ar-H), 7.66 (2H, d, J = 7.98 Hz, Ar-H), 7.61 (2H, s, Ar-H), 7.22 (2H, dd, J_1 = 8 Hz, J_2 = 1.81 Hz, Ar-H), 7.17 (2H, d, J = 1.92 Hz, Ar-H), 3.98 (6H, s, OCH_3), 3.88 (6H, s, OCH_3), 1.89-1.96 (4H, m, CH_2), 1.09-1.27 (52H, br, CH_2), 0.89 (6H, t, J = 7.06, CH_3), 0.66-0.74 (4H, m, CH_2).

L-DHDF-2. L-DHDF-2 was synthesized using the same synthesis procedure as that for L-DHDF-1 using L-DHDF-1 and 3,4-dimethylaniline as the starting materials. The

pure L-DHDF-2 was obtained by column chromatography using Hexane/EtOAc (8/1) as wine-red powder with a yield of 87%.

^{1}H NMR (400 MHz, $CDCl_3$): δ = 8.87 (2H, s, NH), 8.68 (2H, s, NH), 8.03 (2H, s, Ar-H), 7.98 (2H, s, Ar-H), 7.56 (2H, d, J = 8 Hz, Ar-H), 7.06-7.16 (6H, m, Ar-H), 6.97-7.00 (4H, m, Ar-H), 3.87 (6H, s, OCH_3), 3.84 (6H, s, OCH_3), 2.26 (12H, s, Ar-CH_3), 1.85-1.93 (4H, m, CH_2), 1.07-1.26 (52H, br, CH_2), 0.86 (6H, t, J = 7.14, CH_3), 0.7-0.81 (4H, m, CH_2).

Synthesis of L-DHDF-3. In the presence of polyphosphoric acid (PPA), L-DHDF-2 can be cyclized to provide L-DHDF-3 at high temperature, as shown in Scheme 5.4.

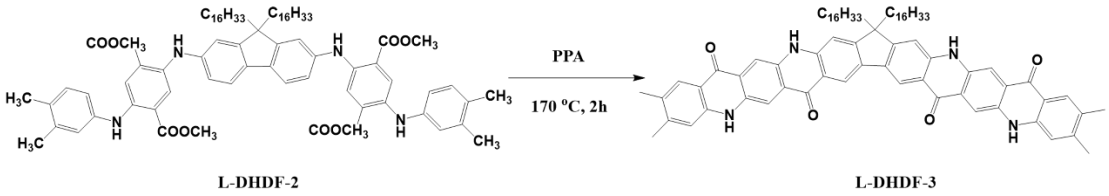

Scheme 5.4 Synthesis route of L-DHDF-3 by cyclization

To the vigorously stirred polyphosphoric acid (PPA, 10 mL) heated at 170 °C was slowly added the starting material L-DHDF-2 (507 mg, 0.4 mmol). After 2 h, the reaction mixture was cooled to room temperature, quenched with ice water and stirred overnight. The reaction mixture was then filtered, and the black solid was washed with plenty of water to remove the unreacted PPA. MeOH and DCM were used to wash away the organic byproducts. The aimed product L-DHDF-3 was obtained as an insoluble dark solid with a yield of 80%.

No NMR data was obtained due to the insolubility of L-DHDF-3 in the common deuterated solvents.

FTIR (KBr): ν = 3447, 3275, 2924, 2852, 1606, 1551, 1464, 1343, 1262, 1209, 875, 796 cm^{-1}.

Synthesis of Boc-L-DHDF-3. The Boc protection pathway of L-DHDF-3 to afford Boc-L-DHDF-3 is illustrated in Scheme 5.5.

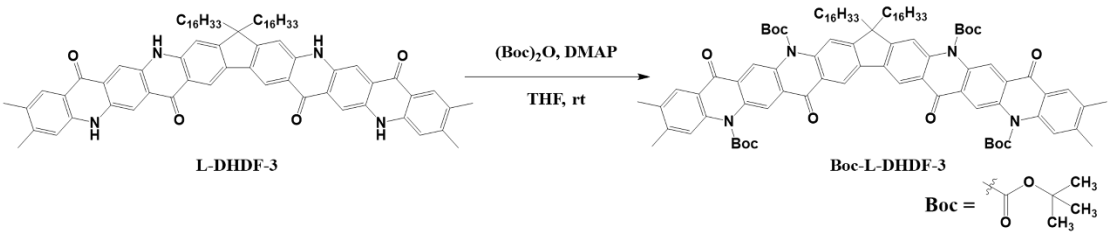

Scheme 5.5 Synthesis route of Boc-L-DHDF-3.

L-DHDF-3 (171 mg, 0.15 mmol), di-tert-butyldicarbonate ($(Boc)_2O$, 0.95 g), and N,N-dimethyl-4-aminopyridine (DMAP, 100 mg) were stirred in 20 mL of dry THF at ambient temperature for 7 days. The reaction mixture was then filtered, and rotary evaporated under vacuum to remove the solvent. The residue solid was washed with excess acetone to afford the aimed product as brown solid with a yield of 35%.

^{1}H NMR (400 MHz, $CDCl_3$): δ = 8.80 (4H, d, J = 8.47, Ar-H), 8.73 (2H, d, J = 10.72, Ar-H), 8.14 (2H, s, Ar-H), 7.78 (2H, s, Ar-H), 7.66 (2H, d, J = 12, Ar-H), 2.43 (6H, d, J = 4.8, Ar-CH_3), 2.38 (6H, d, J = 4.8, Ar-CH_3), 2.03-2.13 (4H, m, CH_2), 1.67-1.81 (36H, m, CH_3 in Boc groups), 0.97-1.26 (52H, br, CH_2), 0.84 (6H, t, J = 7.13, CH_3), 0.64-0.76 (4H, m, CH_2)

^{13}C NMR (400 MHz, $CDCl_3$): δ = 178.61, 178.49, 157.03, 151.75, 144.51, 140.16, 138.65, 136.09, 135.10, 134.72, 133.05, 132.95, 127.01, 126.76, 126.45, 126.32, 123.07, 121.43, 121.27, 119.58, 117.72, 113.42, 86.29, 86.26, 86.20, 56.41, 41.22, 31.90, 29.97, 29.66, 29.63, 29.61, 29.57, 29.52, 29.33, 29.24, 28.04,27.95, 27.90, 24.01, 22.66, 21.02, 19.21, 19.19, 14.10.

FTIR (KBr): 2924, 2852, 1751, 1642, 1622, 1477, 1369, 1242, 1140, 842, 791 cm^{-1}.

Synthesis of DAP-dimer-1. The addition of TIPS groups onto Boc-L-DHDF-3 is based on the reported procedure in T. Wiesner's paper [6], as shown in Scheme 5.6.

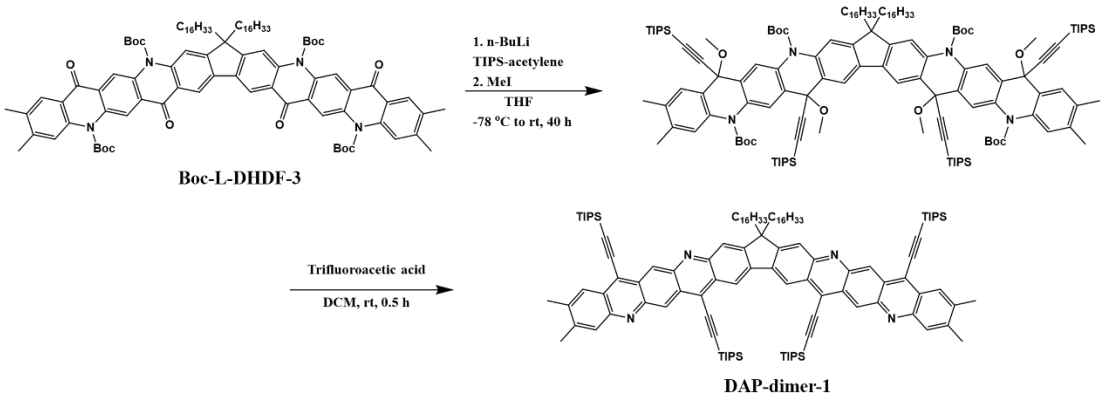

Scheme 5.6 Synthesis route of DAP-dimer-1.

The crude product was purified by column chromatography using hexane/EtOAc (97/3) as the eluent and recrystallized from the saturated DCM solution by adding EtOH to afford the aimed product as black crystalline needles with a yield of 47%.

^{1}H NMR (400 MHz, $CDCl_3$): δ = 9.70 (2H, s, Ar-H), 9.56 (2H, d, J = 14.79, Ar-H), 8.97 (2H, s, Ar-H), 8.29 (2H, d, J = 8.17, Ar-H), 8.16 (2H, s, Ar-H), 7.97 (2H, d, J = 7.39, Ar-H), 2.54 (12H, t, J = 5.36, Ar-CH_3), 2.25-2.34 (4H, m, CH_2), 1.64 (12H, s, CH in TIPS groups), 1.32-1.45 (72H, m, CH_3 in TIPS groups), 1.02-1.20 (52H, br, CH_2), 0.78-0.87 (10H, m, CH_2CH_3).

^{13}C NMR (400 MHz, $CDCl_3$): δ = 155.45, 151.78, 151.06, 150.80, 144.66, 144.22, 142.44, 128.84, 127.25, 125.63, 123.67, 117.52, 112.25, 110.18, 102.37, 101.74, 32.01, 29.75, 29.66, 29.44, 22.79, 20.82, 19.26, 19.13, 19.10, 19.05, 14.22, 11.96, 11.72, 11.70.

Synthesis of DAP. Similar to DAP-dimer-1, the DAP monomer was synthesized from QA via Boc protection and TIPS addition reactions as described above.

The NMR data of Boc-QA and DAP agrees well with the reported results. [6]

5.2.2 Electrochemical and photophysical properties

Cyclic voltammetry (CV) technique was used to analyse the electrochemical behaviours of DAP and DAP-dimer-1. The measurements were performed using a three-electrode system connected to an electrochemical workstation (SP-150, Bio-

Logic SAS), where the glassy carbon was chosen as the working electrode, platinum wire as the counter electrode and saturated Ag/AgCl as the reference electrode. The measurements were conducted at room temperature in an anhydrous DCM solution, which was degassed with nitrogen for 10 min before each experiment, with 0.1 M of tetrabutylammonium hexafluorophosphate (nBu$_4$NPF$_4$) as the supporting electrolyte. The redox couple ferrocene/ferrocenium (Fc/Fc$^+$) was chosen as the internal standard.

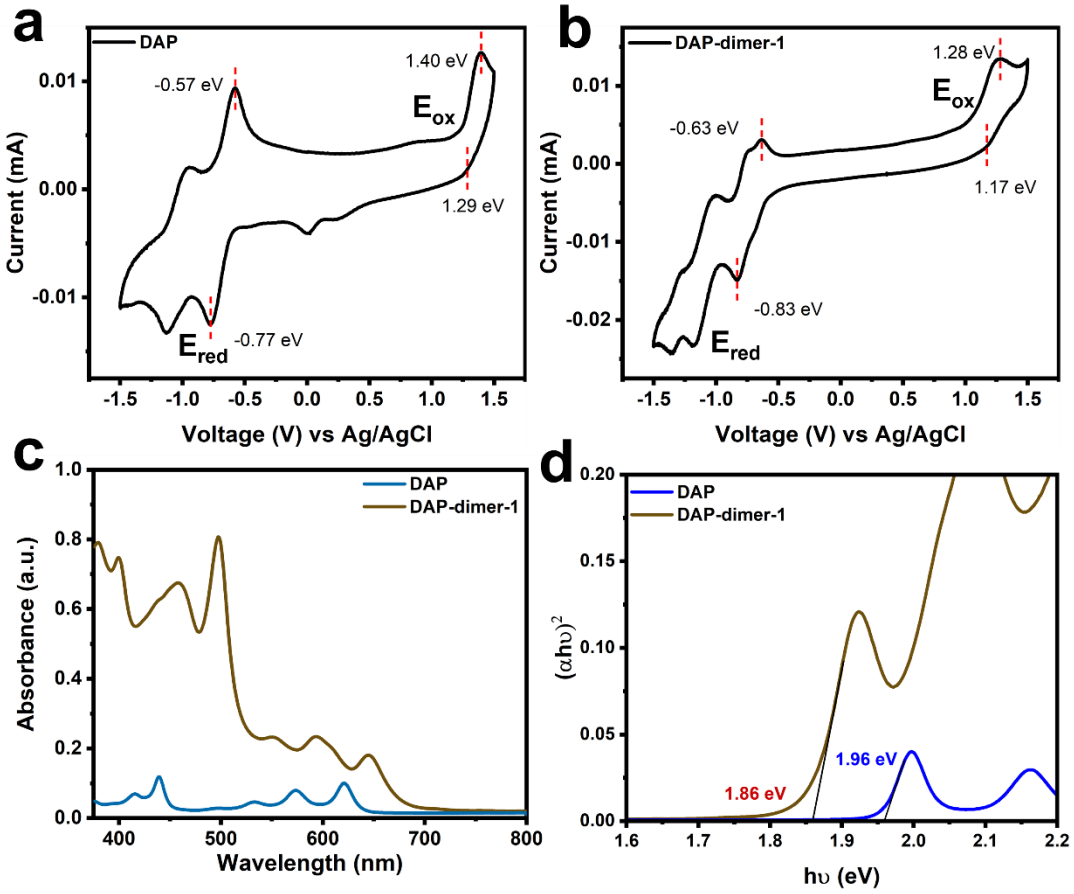

Figure 5.3 Cyclic voltammetry plots of (**a**) DAP and (**b**) DAP-dimer-1 at the scan rate of 50 mV/s. (**c**) UV-Vis absorption spectra and (**d**) Tauc plots of DAP and DAP-dimer-1.

As shown in the CV plots (Figure 5.3a and b), both DAP and DAP-dimer-1 presents an irreversible oxidation peak, while DAP presents two reversible reduction peaks and DAP-dimer-1 presents three reversible reduction peaks. Their highest occupied molecular orbital (HOMO) and lowest unoccupied molecular orbital (LUMO) energy levels can be calculated using the Equations 3.10 and 3.11. The redox potential of Fc/Fc$^+$ vs. Ag/AgCl was measured to be 0.585 V, accordingly the oxidation potentials of DAP and DAP-dimer-1 vs. Fc/Fc$^+$ were determined to be 0.76 and 0.64 V,

corresponding to the HOMO energy levels of −5.56 and −5.44 eV, respectively. The first reduction potentials vs. Fc/Fc^+ of DAP and DAP-dimer-1 were determined to be −1.26 and −1.32 V, corresponding to the LUMO energy levels of −3.54 and −3.48 eV, respectively. Therefore, the energy gaps from CV measurements ($E_{gap, CV}$) of DAP and DAP-dimer-1 were calculated to be 2.02 and 1.96 eV, as summarized in Table 5.1. The reported HOMO and LUMO energy levels of TIPS-pentacene are −5.16 and −3.35 eV, [31] which are higher than those values of DAP, proving the incorporation of nitrogen atoms into polyacenes can significantly lower the energy levels of molecular frontier orbitals. Dimerization of DAP, on the other hand, slightly upshifts both the HOMO and LUMO energy levels and narrows the energy gap by 0.06 eV.

Table 5.1 Electrochemical and photophysical properties of DAP and DAP-dimer-1.

Compound	E(HOMO) (eV)	E(LUMO) (eV)	$E_{gap, CV}$ (eV)	$\lambda_{max, abs}$ (nm)	$E_{gap, opt}$ (eV)
DAP	-5.56	-3.54	2.02	621, 573, 533, 439, 415	1.96
DAP-dimer-1	-5.44	-3.48	1.96	644, 594, 551, 497, 458	1.86

The photophysical properties of DAP and DAP-dimer-1 were characterized by steady-state UV-Vis absorption spectra in dilute DCM solution, as shown in Figure 5.3c. In the long wavelength region above 500 nm, DAP shows three absorption peaks at 621 and 573, 533 nm, which are attributed to the first electronic transition (HOMO → LUMO) of the vibronic fine structure brought by the rigid pentacene backbone. Two peaks emerged at the shorter wavelengths of 415 and 439 nm, which corresponds to the electronic transitions between two nonadjacent molecular orbitals (HOMO−1 → LUMO and HOMO → LUMO+1). DAP-dimer-1 showed a similar absorption pattern as the monomer but with a redshift of around 20 nm for peaks in the long wavelength region and a redshift of around 50 nm for peaks in the short wavelength region due to the extension of π-conjugated system in dimer [32]. Unlike the weak absorption in DAP, the peaks at short wavelength were significantly intensified in DAP-dimer-1 because of the higher oscillator strength of the corresponding electronic transition. The optical energy gaps ($E_{gap, opt}$) for both compounds are obtained from the Tauc plots (Figure 5.3d), which are relatively smaller than the electrochemical energy gaps and this is expected since an interface barrier is formed during the CV measurements.

5.2.3 Singlet fission analysis

Transient absorption (TA) spectroscopy was used to investigate the singlet fission process of DAP and DAP-dimer-1 in DCM dilute solution from picosecond to nanosecond. The pump beam used was centred at 610 nm with a beam energy of 10 μW, and the probe wavelength was from 400 to 800 nm.

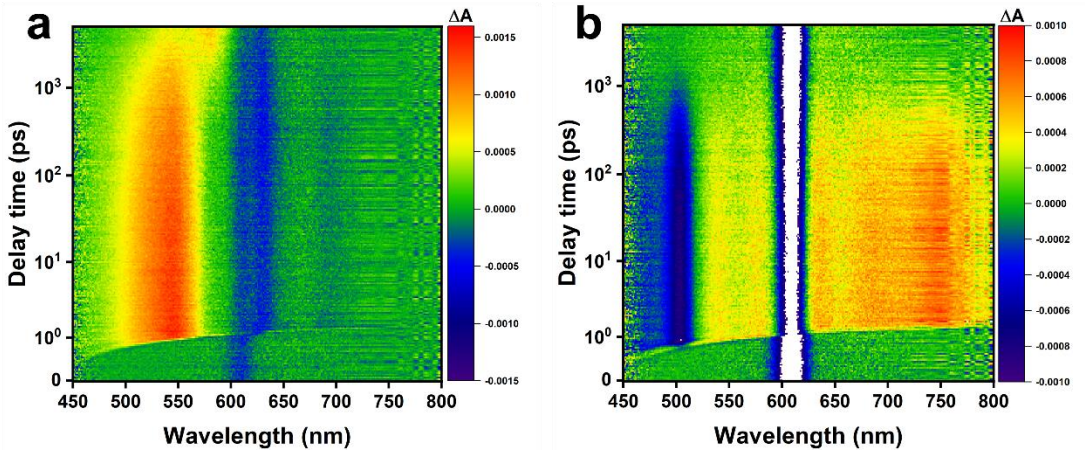

Figure 5.4 Transient absorption spectra of (**a**) DAP and (**b**) DAP-dimer-1.

The obtained TA results are presented as pseudocolor maps (Figure 5.4). As shown in the TA spectra of DAP (Figure 5.4a), the main absorption peak appears at 540 nm, which is attributed to the excited state absorption (ESA) band of the singlet state ($S_1 \rightarrow S_n$). The signal decays with the delay time, and a new peak emerging at 574 nm in the nanosecond region, which is supposed to be the ESA signal of the triplets. [33] For DPA-dimer-1,the TA spectrum (Figure 5.4b) exhibits a negative peak at 500 nm and a series of positive bands ranging from 500 to 800 nm. The negative peak at 500 nm can be attributed to the ground state bleaching (GSB) of the $S_0 \rightarrow S_1$ transition, which is consistent with the strongest peak shown in the UV-Vis absorption spectrum (Figure 5.3c). However, it was observed that DAP solution became unstable under light exposure. It would be gradually oxidized to form colourless peroxide products, which has been reported by T. Wiesner and also observed in its phenylene substituted derivatives. [34,35] The photostability of the compound could have caused the signal intensity to decrease during TA measurement, which complicates the data collection and makes it impossible to obtain meaningful understanding of the electronic dynamics of the SF process.

To conclude, the nitrogen-substituted pentacene DAP and the dihexadecylcyclopentane-linked dimer (DAP-dimer-1) were successfully synthesized, while the synthesis of directly-linked dimer (DAP-dimer-2) and methylene-linked dimer (DAP-dimer-3) failed due to the extremely low solubility of the intermediate molecules. The substitution of nitrogen significantly lowers the energy level of the molecular frontier orbitals. However, due to the instability of DAP and the dimer in solution under light exposure, the conclusive electronic dynamics from TA measurements cannot be obtained despite that the triplet signal has been observed in the TA spectra of DAP.

5.3 Anthrathiadiazole and its dimers

5.3.1 Synthesis and molecular structure characterization

Anthrathiadiazole (ATDA) is a three-ring polyacene with an additional thiadiazole ring. The molecular structures of ATDA and its dimers formed by connecting two chromophores with a phenylene bridge at different positions, along with a directly-linked homodimer, are illustrated in Figure 5.5. The idea of constructing ATDA dimers is based on N. Alagna's work [36] in which the monomer ATDA was demonstrated to perform an ultrafast SF process with a quantum yield of 200% in thin film but not in dilute solution. Dimers, as discussed above, can undergo the intramolecular SF process that is independent on the molecular interactions but sole an intrinsic property of the molecule. Therefore, four different dimers of ATDA have been proposed, synthesized and analyzed to systematically study the effect of molecular geometries on their SF properties.

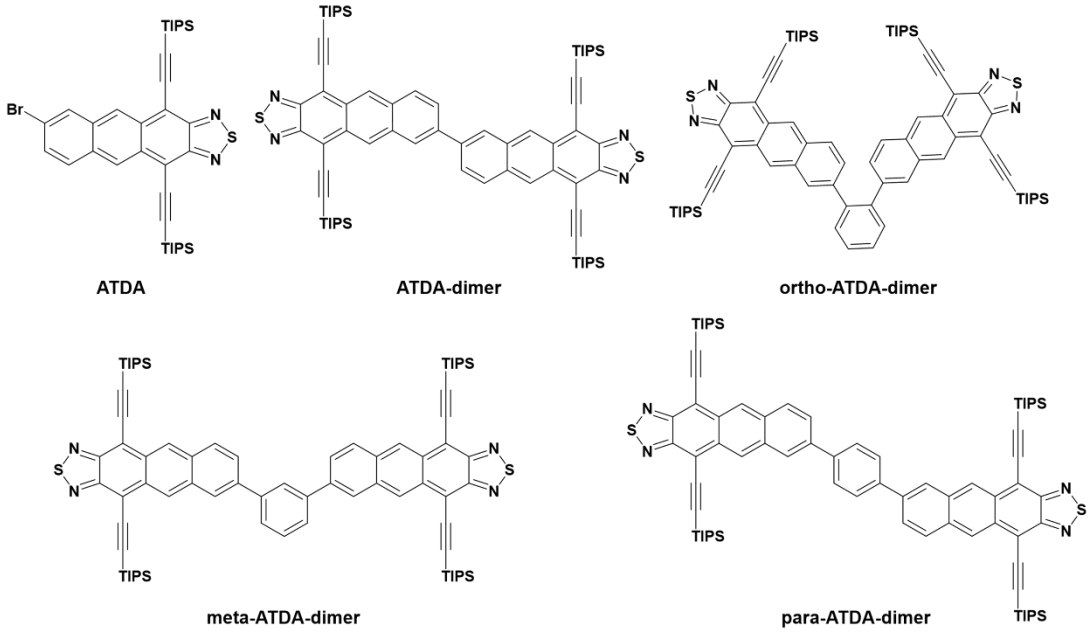

Figure 5.5 Molecular structure illustration of anthrathiadiazole and its dimers.

The overall synthesis route of ATDA monomer is illustrated in Scheme 5.7. The synthesis of ATDA-2 from the starting materials hydroquinone and 5-bromoisobenzofuran-1,3-dione follows the procedure described in T. Honda's paper [37]. ATDA-3 was then prepared by bromination of ATDA-2 in a hydrobromic acid solution. The synthesis route of the final product ATDA from ATDA-3 follows a similar method reported by A. L. Appleton [38] but a relatively higher yield was obtained for each step, which can be attributed to the electron-withdrawing effect of Br atom attached at the end of anthracene backbone.

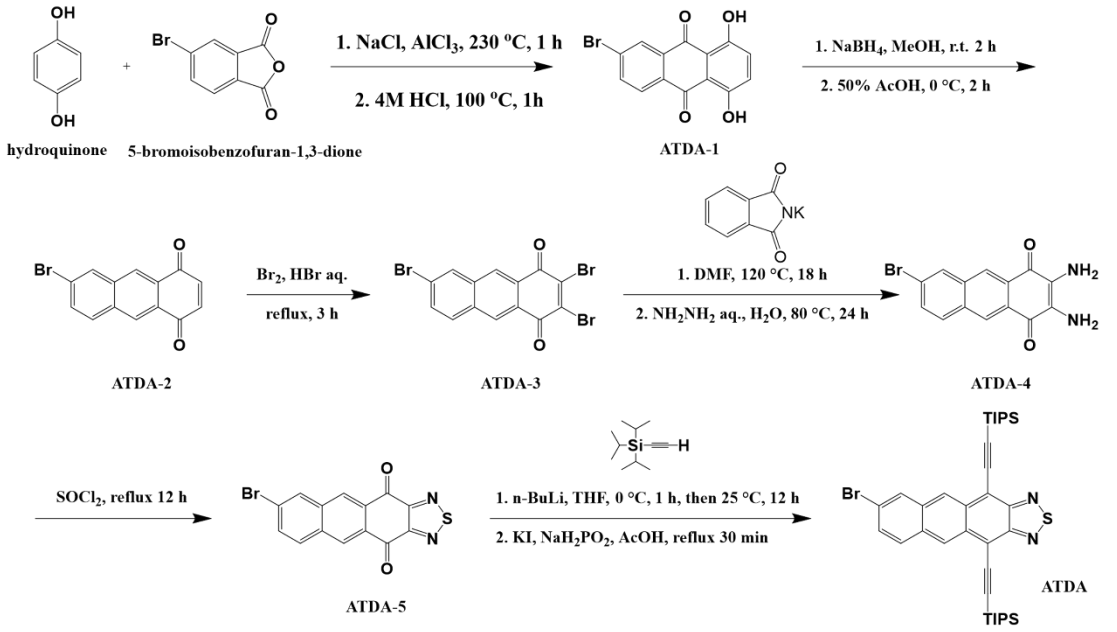

Scheme 5.7 Synthesis route of ATDA.

The ATDA dimers were synthesized by Suzuki cross-coupling reactions, as illustrated in Scheme 5.8. The ortho-, meta- and para-ATDA-dimer were obtained by coupling ATDA with 1,2-, 1,3- and 1,4-benzendiboronic acid bis(pinacol) ester, respectively. On the other hand, the directly-linked ATDA-dimer was synthesized by forming an intermediate molecule, ATDA-BPin, which was obtained by coupling ATDA with bis(pinacolato)diboron, followed by further coupling with another portion of ATDA to afford ATDA-dimer.

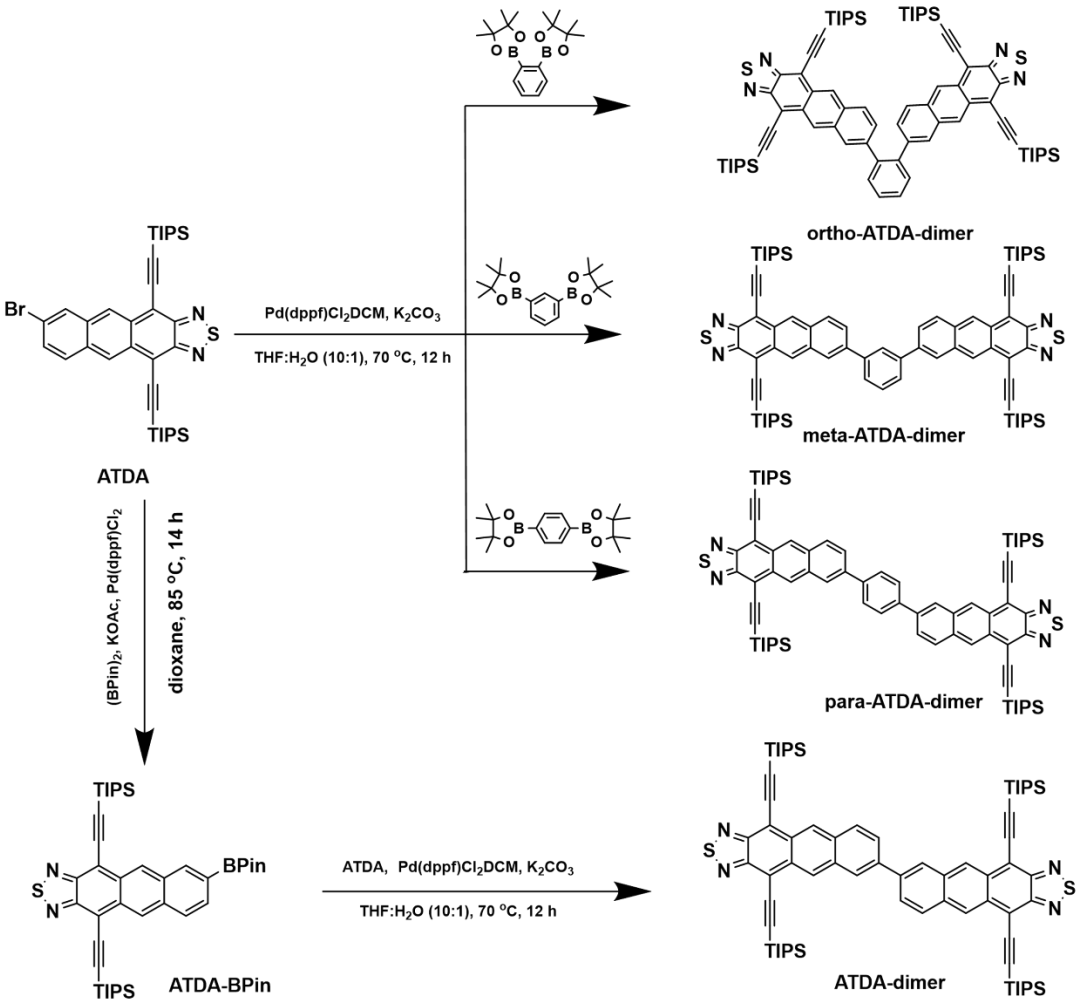

Scheme 5.8 Synthesis route of ATDA dimers.

Synthesis of ATDA-1 and ATDA-2. The synthesis procedures of ATDA-1 and ATDA-2 follow the method reported in T. Honda's paper. The NMR patterns of ATDA-1 and ATDA-2 agree well with the reported results. [37]

ATDA-1 ^{1}H NMR (400 MHz, $CDCl_3$): δ = 8.46 (1H, s), 8.20 (1H, d, J = 8 Hz), 7.94 (1H, d, J = 4 Hz), 7.33 (2H, s)

ATDA-2 ^{1}H NMR (400 MHz, $CDCl_3$): δ = 8.60 (1H, s), 8.53 (1H, s), 8.24 (1H, s), 7.94 (1H, d, J = 8 Hz), 7.77 (1H, d, J = 8 Hz), 7.09 (2H, s)

Synthesis of ATDA-3. A mixture of ATDA-2 (3.42 g, 11.91 mmol) and 48% hydrobromic acid (HBr, 5 mL) was heated to 100 °C under nitrogen atmosphere. Bromine (Br_2, 1.84 mL, 35.74 mmol) was then added into the mixture drop by drop

over one hour. The product precipitated and another portion of HBr (10 mL) was poured. The mixture was kept on stirring under reflux for 2 hours, and then filtered when it was still hot. The precipitate was washed with a large amount of deionized water, and then recrystallized from ethanol and a mixture of chloroform/hexane (2:1) to afford pure ATDA-3 with a yield of 99%.

^{1}H NMR (400 MHz, DMSO-d_6): δ = 8.78 (1H, s), 8.74 (1H, s), 8.65 (1H, s), 8.29 (1H, d, J = 8 Hz), 7.95 (1H, dd, J_1 = 8 Hz, J_2 = 4 Hz).

Synthesis of ATDA-4, ATDA-5 and ATDA. The synthesis procedures of ATDA-4, ATDA-5 and ATDA are similar to the ones described in A. L. Appleton's paper. [38]

ATDA-4 ^{1}H NMR (400 MHz, DMSO-d_6): 8.39 (1H, s), 8.31 (2H, d, J = 12 Hz), 8.06 (1H, d, J = 8 Hz), 7.74 (1H, d, J = 8 Hz), 5.72 (4H, d, J = 12 Hz, -NH_2).

ATDA-5 ^{1}H NMR (400 MHz, $CDCl_3$): 8.97 (1H, s), 8.90 (1H, s), 8.33 (1H, s), 8.03 (1H, d, J = 8 Hz), 7.88 (1H, s), 7.85 (1H, d, J = 4 Hz).

ATDA: ^{1}H NMR (400 MHz, $CDCl_3$): 9.19 (1H, s), 9.11 (1H, s), 8.08 (1H, d, J = 4 Hz), 7.79 (1H, d, J = 8 Hz), 7.45 (1H, d, J = 8 Hz), 1.28-1.38 (42H, m, -CH and -CH_3 in TIPS groups)

Synthesis of ATDA-dimer. ATDA dimer was synthesized by a two-step Suzuki coupling reaction.

ATDA (200 mg, 0.3 mmol) and bis(pinacolato)dibron (113.5 mg, 0.45 mmol) were added into a sealed round bottom flask, followed by the addition of the catalyst Pd(dppf)Cl_2·DCM (13.1 mg, 0.015 mmol) and potassium acetate (KOAc, 103 mg, 1.05 mmol). The mixture was treated by sequential vacuum and nitrogen degassing three times to remove the air, and then added with dry and degassed dioxane (5 mL). The mixture was heated to 85 ^{o}C and kept on stirring for 14 h in the dark. The reaction was quenched with DI water (10 mL) and extracted by DCM (10 mL × 3). The organic phase was combined, dried over sodium sulfate, filtered and rotary evaporated under

reduced pressure to remove the solvent. The crude product was purified by column chromatography (DCM/hexane, 1/4) to yield the intermediate molecule ATDA-BPin.

ATDA (100 mg, 0.15 mmol) and ATDA-BPin (130.1 mg, 0.18 mmol) were added into a sealed round bottom flask, followed by the addition of the catalyst Pd(dppf)Cl_2·DCM (13.1 mg, 0.015 mmol) and potassium carbonate (K_2CO_3, 352.5 mg, 2.55 mmol). The mixture was treated by sequential vacuum and nitrogen degassing three times to remove the air, and then added with dry and degassed DI water/THF (1/10) mixed solvent. The reaction was warmed up to 70 ^oC and kept on stirring overnight in the dark. The reaction mixture was then extracted with DCM (10 mL × 3), dried over sodium sulfate, filtered and rotary evaporated under reduced pressure to remove the solvent. The crude product was purified by column chromatography (DCM/hexane, 1/4) to afford the product ATDA-dimer.

^{1}H NMR (400 MHz, $CDCl_3$): 9.33 (2H, s), 9.28 (2H, s), 8.28 (2H, s), 8.10 (2H, d, J = 8 Hz), 7.91 (2H, dd, J_1 = 6 Hz, J_2 = 4 Hz). 1.24-1.42 (84H, m, -CH and -CH_3 in TIPS groups).

Synthesis of ortho-, meta-, and para-ATDA-dimer. The synthesis procedures of the three phenylene-linked dimers are similar to the second step of the synthesis procedure of ATDA-dimer but by using the corresponding benzendiboronic acid bis(pinacol) ester, respectively, instead.

Ortho-ATDA-dimer. ^{1}H NMR (400 MHz, $CDCl_3$): 9.15 (4H, d, J = 3.96 Hz), 7.97 (2H, s), 7.72-7.78 (4H, m), 7.62-7.67 (2H, m) 7.3 (2H, d, J = 9.2 Hz), 1.18-1.32 (84H, m, -CH and -CH_2 in TIPS groups).

Meta-ATDA-dimer. ^{1}H NMR (400 MHz, $CDCl_3$): 9.31 (4H, d, J = 6.96 Hz), 8.20 (2H, s), 8.15 (1H, t, J = 1.6 Hz), 8.10 (2H, d, J = 9.16 Hz), 7.86 (4H, tdd, J_1 = 10.8 Hz, J_2 = 8.92, J_3 = 1.52 Hz), 7.74 (1H, t, J = 7.72), 1.27-1.43 (84H, m, -CH and -CH_2 in TIPS groups).

Para-ATDA-dimer. ^{1}H NMR (400 MHz, $CDCl_3$): 9.29 (4H, s), 8.16 (2H, s), 8.08 (2H, d, J = 8.96 Hz), 7.92 (4H, s), 7.81 (2H, dd, J_1 = 8.96 Hz, J_2 = 1.6 Hz), 1.22-1.44 (84H, m, -CH and -CH_2 in TIPS groups).

5.3.2 Electrochemical and photophysical properties

The cyclic voltammetry measurement setup for ATDA and its dimers was the same as the one described in Section 5.2.2, and the obtained CV results are plotted in Figure 5.6. In a dimer, the oxidation of both chromophores should occur step by step, and the conjugation between the chromophores will significantly affect the oxidation process. In a highly conjugated dimer, the difference between the two oxidation potentials can be easily observed; while in a less conjugated dimer, there is almost no difference as both units are acting independently and oxidized at the same potential. [39] Therefore, the extent of conjugation of the dimers can be estimated from CV results.

As shown in Figure 5.6, ATDA monomer shows two reversible reduction peaks, one weak and one strong reversible oxidation peaks. All phenylene-linked dimers show similar pattern to that of the monomer in the cathodic region with two reversible reduction peaks, while the directly-linked ATDA-dimer only shows a reversible peak. On the anodic scan, meta- and para-ATDA-dimer both show two reversible oxidation peaks similar to the monomer with splitting oxidation potentials of 0.28 and 0.33 eV, respectively. Moreover, the weak oxidation peak of meta-ATDA-dimer has the same potential as that of ATDA, which means the two chromophores act more independently from each other. On the other hand, ATDA-dimer and ortho-ATDA-dimer both show one strong reversible and one weak irreversible oxidation peaks, and their splitting oxidation potentials are 0.56 and 0.65 eV, respectively. Based on the splitting oxidation potentials, the phenylene-linked chromophores are the most conjugated in ortho dimer, while the least conjugated in meta dimer.

The oxidation potentials of ATDA, ATDA-dimer, ortho-ATDA-dimer, meta-ATDA-dimer and para-ATDA-dimer vs. Fc/Fc^+ thus are calculated to be 0.73, 0.57, 0.67, 0.63, 0.63 V, which indicates that the four dimers can be oxidized more easily than the monomer because of their extended conjugation length and higher electron density. Accordingly, their corresponding HOMO energy levels are calculated to be −5.53,

−5.37, −5.47, −5.43 and −5.43 eV by using the Equation 3.10. For comparison, the HOMO energy level of TIPS-tetracene is −5.5 eV. The reduction potentials of ATDA, ATDA-dimer, ortho-ATDA-dimer, meta-ATDA-dimer and para-ATDA-dimer vs. Fc/Fc^+ are calculated to be −1.23, −1.31, −1.31, −1.27 and −1.27 V, respectively, and their LUMO energy levels are calculated to be −3.57, −3.49, −3.49, −3.53 and −3.53 eV by using the Equation 3.11. The energy gaps from CV measurements of ATDA, ATDA-dimer, ortho-ATDA-dimer, meta-ATDA-dimer and para-ATDA-dimer, therefore, are calculated to be 1.96, 1.88, 1.98, 1.90 and 1.90 eV, respectively. The energy gaps obtained from CV measurements provide a pathway to evaluate the intramolecular charge resonance (CR) states of the dimers, which are important in the SF mechanism. [41] The values of HOMO and LUMO energy levels, and energy gaps of all molecules including TIPS-tetracene are summarized in Table 5.2.

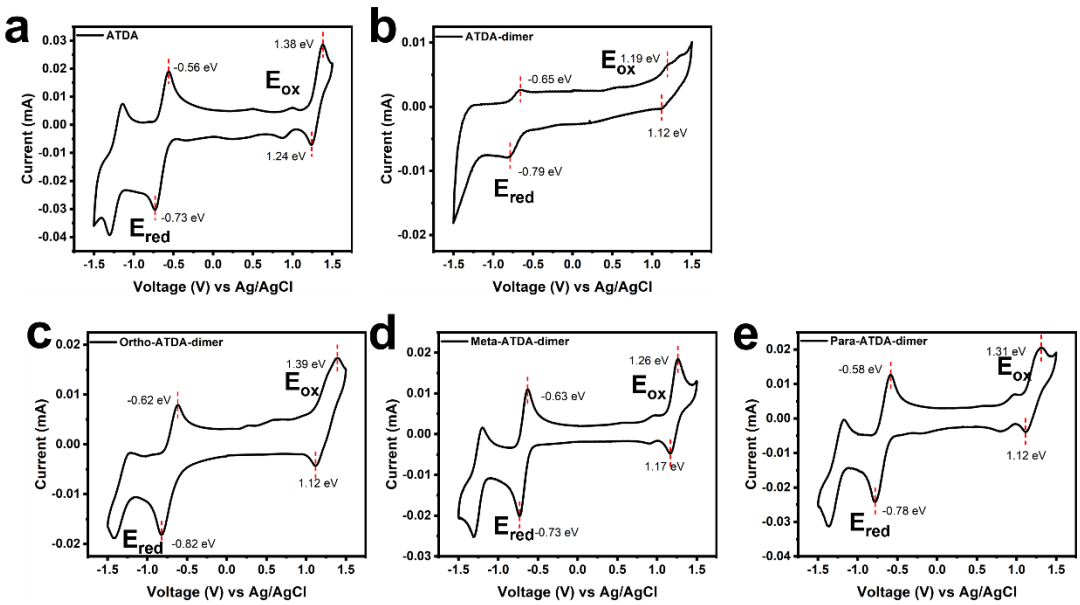

Figure 5.6 Cyclic voltammetry plots of (**a**) ATDA, (**b**) ATDA-dimer, (**c**) ortho-ATDA-dimer, (**d**) meta-ATDA-dimer and (**e**) para-ATDA-dimer at the scan rate of 50 mV/s.

The photophysical properties of ATDA and the four dimers were characterized by steady-state UV-vis absorption spectroscopy in dilute DCM solution, as shown in Figure 5.7a. Similarly, all compounds show two sets of absorption peaks in the short wavelength region below 450 nm and in the long wavelength region above 500 nm. ATDA shows a maximum absorption at 651 nm, which corresponds to the first electronic transition, accompanied with a shoulder peak at 604 nm, which can be

attributed to the intramolecular charge transfer. [42] Four dimers display similar absorption features to that of ATDA in the long wavelength but with a red shift of 15 nm because of the extended conjugated systems in the dimers. In the short wavelength region, ATDA and all phenylene-linked dimers present almost identical absorption patterns with a maximum absorption at around 417 nm, and the para-ATDA-dimer also shows a shoulder peak at 443 nm. But for the directly-linked dimer, a new peak is observed in the middle wavelength region at 485 nm. This distinctive feature peak has been also observed by Sanders but only in the directly linked 2,2'-bipentacene and not in the other oligopentacene derivatives with phenylene linkers. [43] The optical energy gaps of all compounds are obtained from the Tauc plots (Figure 5.7b). Compared with ATDA monomer, all the four dimers exhibit relatively smaller energy gaps, which are consistent with the CV results and summarized in Table 5.2.

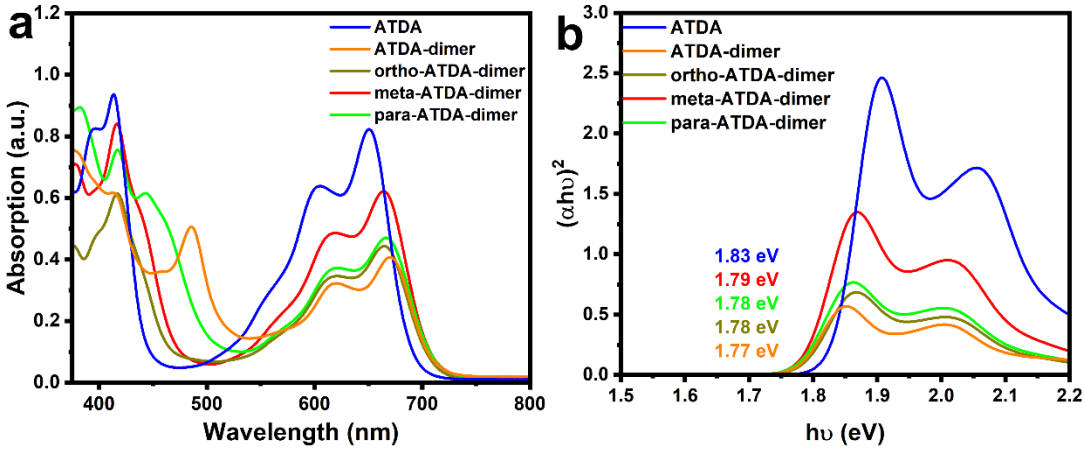

Figure 5.7 (**a**) Ultraviolet-visible absorption spectra and (**b**) corresponding Tauc plots of ATDA, ATDA-dimer, ortho-ATDA-dimer, meta-ATDA-dimer and para-ATDA-dimer.

The energy of the singlet state (S_1), first triplet state (T_1), second triplet state (T_2) and diradical characters (y_0) have also been calculated and are summarized in Table 5.2. The substitution of thiadiazole ring significantly reduces the energy of S_1 from 2.432 eV in the reference TIPS-tetracene (TIPS-Tc) to 1.915 eV in ATDA. The dimerization of ATDA further reduces the energy of S_1 slightly, which is consistent with the experimental results. The energy of T_1 also decreases to 0.883 eV in ATDA from 1.398 eV in TIPS-Tc and are almost constant in the ATDA dimers. This trend also agrees well with the calculation results of y_0, which increases remarkably from 0.342 in TIPS-Tc to 0.503 in ATDA as an increase in y_0 will decrease the energy of T_1. [44] The energy

difference $\Delta E(S_1 - 2T_1)$ of TIPS-Tc is −0.364 eV, indicating an endoergic SF process, while this energy difference reverses to a positive value (i.e., 0.150 eV) in ATDA, indicating an exothermic SF process. For all ATDA dimers, the values of $\Delta E(S_1 - 2T_1)$ are all positive to ensure an efficient SF process. However, a slightly less positive value might be more favourable in photovoltaic systems due to the less energy loss during the SF process. In addition, as the energy difference $\Delta E(T_2 - 2T_1)$ in TIPS-Tc is −0.162 eV, triplet-triplet annihilation to produce higher-energy triplet states will play an important role to restrict the SF process in TIPS-Tc. While in ATDA and its dimers, the energy of T_2 is more than twice as high as that of T_1, which further implies more efficient SF processes and longer triplet lifetimes.

Table 5.2 Electrochemical and photophysical properties of ATDA and its dimers.

	TIPS-Tetracene[a]	ATDA	ATDA-dimer	Ortho-ATDA-dimer	Meta-ATDA-dimer	Para-ATDA-dimer
E(HOMO) (eV)	-5.50	-5.53	-5.37	-5.47	-5.43	-5.43
E(LUMO) (eV)		-3.57	-3.49	-3.49	-3.53	-3.53
$E_{gap,CV}$ **(eV)**		1.96	1.88	1.98	1.90	1.90
λ_{abs} **(nm)**		413, 604, 651	413, 485, 619, 671	417, 619, 665	417, 617, 665	417, 443, 619, 666
$E_{gap,opt}$ **(eV)**		1.83	1.77	1.78	1.79	1.78
E(S_1) (eV)[b]	2.432	1.9100	1.9028	1.8965	1.8967	1.8915
E(T_1) (eV)[b]	1.398	0.8808	0.8849	0.8847	0.8813	0.8788
E(T_2) (eV)[b]	2.634	2.341	2.2920	2.2795	2.2791	2.2350
$\Delta E(S_1 - 2T_1)$ **(eV)**	-0.364	0.1484	0.1330	0.1271	0.1341	0.1339
$\Delta E(T_2 - 2T_1)$ **(eV)**	-0.162	0.5794	0.5222	0.5101	0.5165	0.4774
y_0[c]	0.342	0.503	0.559	0.555	0.556	0.555

[a]The computational and calculation results are referred from [36]. [b]Calculated using TD-DFT for E(S_1) and E(T_2), TDA-DFT for E(T_1) with M06-2X/6-31G*. [c]Evaluated from occupation numbers of unrestricted natural orbitals at PUHF/6-31+G*.

5.3.3 Singlet fission analysis

The TA spectra of ATDA and the four dimers were measured in dilute DCM solution under the similar condition as the one described in Section 5.2.3 with a beam energy of 100 μW to investigate their singlet fission performance, and the TA spectra are presented as pseudocolor maps in Figure 5.8.

As shown in the TA spectrum of the monomer ATDA (Figure 5.8a), a strong ESA band of $S_1 \rightarrow S_n$ transition appears at 490 nm with a relatively slow decay rate during the

measurement. The negative band attributed to GSB and stimulated emission (SE) signals appears centred at 663 nm, which is consistent with the steady-state absorption result shown in Figure 5.7a. No triplet signals were observed in the dilute solution of ATDA, which agrees well with N. Alagna's paper [36].

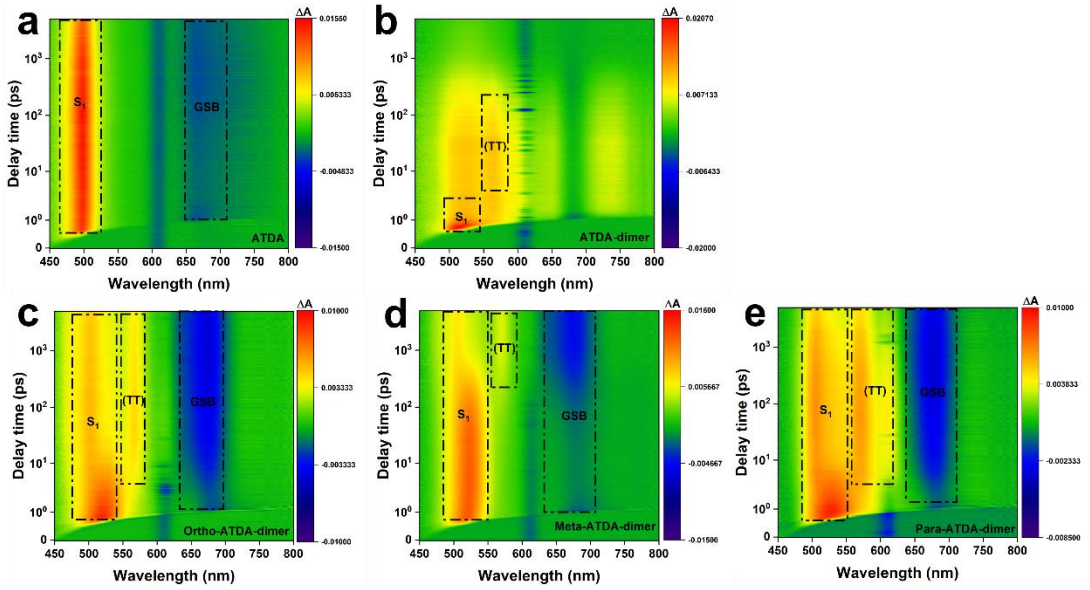

Figure 5.8 Transient absorption spectra of (**a**) ATDA, (**b**) ATDA-dimer, (**c**) ortho-ATDA-dimer, (**d**) meta-ATDA-dimer and (**e**) para-ATDA-dimer in dilute DCM solutions.

The TA spectra of ATDA dimers show a distinct evolution profile compared to that of the monomer. Similarly, the significant ESA bands of $S_1 \rightarrow S_n$ transition for ATDA-dimer, ortho-ATDA-dimer, meta-ATDA-dimer and para-ATDA-dimer are observed at 520 nm, 517 nm, 517 nm and 514 nm, respectively, but with a different decay rate (vide infra). The signatures of GSB and SE bands of four dimers all appear centred at around 670 nm, which is consistent with the steady-state absorption spectra. The GSB signal of ATDA-dimer is overlapping with the triplet ESA feature (Figure 5.8b). Unlike the monomer, a new species emerges at around 565 nm along with the decay of S_1 in all dimers, which has been proved to be the triplet state based on the comparison between the experimental signals and the calculated oscillator strength of the triplet state. [36] Specifically, the triplet signal in the meta-ATDA-dimer only appeared at long time delay (>10^2 ps) and decayed with a very slow rate compared to other dimers, which indicates that the triplet generation pathway was different for the meta dimer (vide infra).

To elucidate the effect of the different chemical bridging of the chromophores on the intramolecular singlet fission mechanism, the exciton dynamics are further investigated by fitting the kinetic profiles with a convolution of a Gaussian instrument response function (IRF) and multiple-exponential function (Figure 5.9), and the parameters are summarized in Table 5.3.

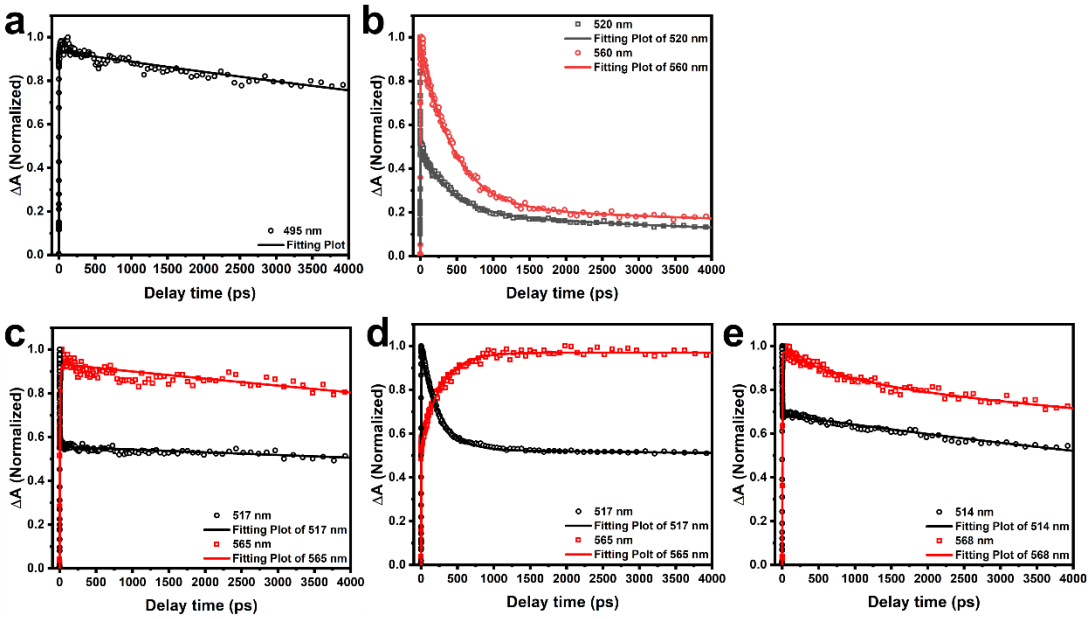

Figure 5.9 Normalized transient absorption kinetic profiles (scattering dots) and fitting plots (solid lines) of (**a**) ATDA, (**b**) ATDA-dimer, (**c**) ortho-ATDA-dimer, (**d**) meta-ATDA-dimer and (**e**) para-ATDA-dimer at probe wavelengths of singlet and triplet signals.

For the monomer ATDA, the ESA signal of S_1 shows a single exponential decay profile with a time constant of 18.7 ± 0.8 ns. In the directly-linked ATDA-dimer, the singlet decays in a rapid rate due to the SF at the early stage with a time constant of 0.23 ± 0.02 ps, which is accompanied by the generation of triplet in a subpicosecond time range (1.09 ± 0.26 ps) due to the efficient SF process. The characteristic singlet signal at 520 nm and triplet signal at 560 nm then both deliver a relatively slow decay rate with a time constant of a few hundred picoseconds back to the ground state. Since the triplets generated by intramolecular SF process in the ATDA-dimer are confined to a single molecule, they will deliver a fast triplet-triplet recombination dynamics with a decay time constant of 439.6 ps. [43] The fast SF rate results from the direct conjugation and

close proximity of both chromophore units, however, the resulting fast triplet-triplet recombination inadvertently restricts its potential application in photovoltaic devices.

As for ortho-, meta- and para-ATDA-dimer, the insertion of a phenylene bridge increases the physical distance between the two chromophores compared to the directly linked ATDA-dimer and is thus expected to affect the exciton dynamics. But this structural change has an insignificant effect on the singlet state, judging from the high resemblance of the optical spectra features between the dimers and the monomer particularly in the low energy range (Figure 5.7). Apart from the meta-dimer, the ortho- and para-dimer deliver similar decay profiles for both singlet and triplet states at 515 nm and 565 nm, respectively. All the three phenylene-linked dimers show a much faster singlet decay rate compared to the monomer, which indicates an additional decay pathway other than the relaxation to the ground state, i.e., the SF process. Despite the similarity in singlet state absorption profile, the singlet state decay profile of the phenylene-linked dimers is distinct from that of the 2,2'-linked ATDA-dimer. The short time constants of the singlet decay for ortho- and para-ATDA-dimer are 3.68 ± 0.14 and 2.44 ± 0.11 ps, respectively, which are an order of magnitude higher than that of ATDA-dimer. Notably, the short time constant for meta-ATDA-dimer is 246.28 ± 7.18 ps, which is three orders of magnitude higher compared to ATDA-dimer. The slower singlet decay rate indicates a smaller SF rate, which results from the increased spacer length in phenylene-linked dimers.

Accompanied with the slow decay of singlet, the triplets were also generated at a much slower rate in phenylene-linked ATDA-dimers. The rising time constants of triplet for ortho- and para-ATDA-dimer are 8.63 ± 1.69 ps and 5.29 ± 0.50 ps, respectively. In meta-ATDA-dimer, the time constant of triplet rising component increases to be 270.2 ± 12.4 ps, which is consistent with the slow decay rate of singlet signal at 565 nm. This huge difference in the decay of singlet and generation of triplet (i.e., SF rate) between ortho-, para- and meta-ATDA-dimer comes from the different coupling strength of conjugation. In ortho- and para-ATDA-dimer, the two chromophore units are π-conjugated via through-bond coupling, while in meta-ATDA-dimer, the two chromophores are weakly conjugated via small through-space coupling. [39] In addition, the two chromophores in ortho-ATDA-dimer are strongly electronically coupled with a π-overlap configuration due to the small proximity. Calculations of

many polyacene dimers (e.g. anthracene, tetracene and pentacene dimers) have shown a huge difference in electronic coupling among the ortho-, para- and meta-geometries, i.e., the direct through-space coupling is always two or three orders of magnitude higher in ortho-dimer than those in para- and meta-dimers; and the link-mediated through-bond coupling is always two or three orders of magnitude smaller in meta-dimer than those in ortho- and para-dimers. [45-48] The triplet lifetimes for ortho- and para-ATDA-dimers are fitted to yield a time constant of 28.28 ± 4.36 and 24.35 ± 6.5 ns, respectively, which increases dramatically to 42 μs (almost an infinite value) in meta-ATDA-dimer. The extremely long rise time (270.2 ps) and lifetime (42 μs) suggest that the triplets are generated by intersystem crossing in the meta-dimer rather than SF process, which can be attributed to the weak nonadiabatic coupling found in many tetracene meta-dimers. [39,45]

Table 5.3 Fitting parameters of normalized kinetic profiles and triplet yield (Φ_T) for ATDA and dimers.

	λ_{probe} (nm)	t_0*	t_1	t_2	Φ_T
ATDA	495		18.68 ± 0.77 ns		
ATDA-dimer	520		0.23 ± 0.02 ps	394.7 ± 35.63 ps	
	560	1.09 ± 0.26 ps	439.6 ± 11.37 ps	16.63 ± 5.17 ns	
Ortho-ATDA-dimer	517		3.68 ± 0.14 ps	41.65 ± 5.46 ns	148%
	565	8.63 ± 1.69 ps	28.28 ± 4.36 ns		
Meta-ATDA-dimer	517		246.28 ± 7.18 ps	135.6 ± 89.2 ns	
	565	270.2 ± 12.4 ps	42 μs		
Para-ATDA-dimer	514		2.44 ± 0.11 ps	13.97 ± 0.49 ns	170%
	568	5.29 ± 0.50 ps	24.35 ± 6.5 ns		

*t_0 represents the time constant of rising component.

The triplet yields resulting from SF process of ortho- and para-ATDA-dimer then are evaluated through the assessment of the absorption increment in the corresponding GSB bands, which are indicative of the changes in the population of molecules at their ground states. The comprehensive calculation procedure is described in the Appendix 5. The calculated SF-induced triplet yields are found to be 148% and 170% for the ortho- and para-ATDA-dimer in dilute DCM solution, respectively. It is reasonable that the para-ATDA-dimer presents a higher triplet yield, giving that the driving force of the SF process (i.e. $\Delta E(S_1 - 2T_1)$) is greater for the para-dimer compared to the ortho-dimer.

To conclude, ATDA and its dimers have been successfully synthesized. The dimerization of ATDA with linkers at different positions has a significant effect on the SF properties. The ATDA monomer did not exhibit any SF signal in dilute solution during the testing period, but triplet signals were observed in all four dimers. Due to the small proximity of the two chromophores, the directly-linked ATDA-dimer shows the highest SF rate in subpicosecond compared to the other phenylene-linked dimers. Ortho- and para-ATDA-dimer both exhibit triplet generation rate in picoseconds via SF process with high triplet yield over 100% because of their relatively stronger through-bond electronic conjugation, while the triplets are generated via intersystem crossing process with a much slower rate (hundreds of picoseconds) in meta-ATDA-dimer because of both weak through-space and through-bond electronic conjugation.

5.4 Phenazinothiadiazole and its dimers

5.4.1 Synthesis and molecular structure characterization

Phenazinothiadiazole (PhTDA) is derived from ATDA with the introduction of two additional nitrogen atoms, which modifies the HOMO-LUMO energy gap, reduces the energy difference $\Delta E(S_1 - 2T_1)$ and decelerates the SF process. [36] Here, two dimers of PhTDA are proposed with the expected characteristics: one is a propane-2,2'-linked type with weak electronic conjugation and large proximity between the chromophores, and the other one is a directly-linked type with strong electronic conjugation and small proximity. The molecular structures of PhTDA and its two dimers are illustrated in Figure 5.10.

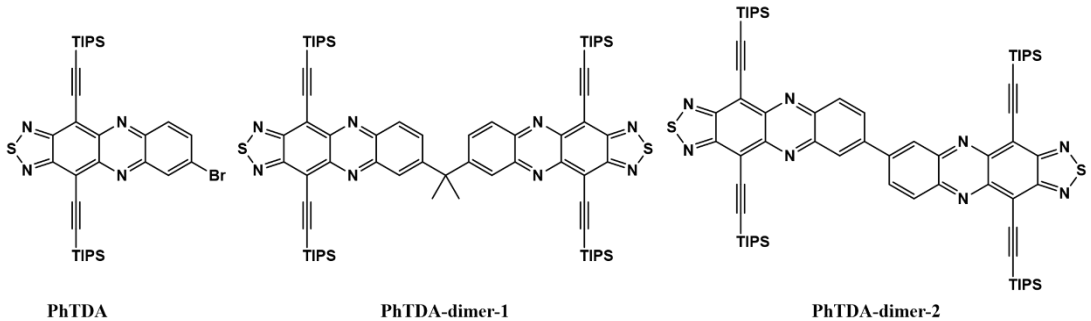

Figure 5.10 Molecular structure illustration of phenazinothiadiazole and its dimers.

The proposed overall synthesis route of PhTDA and its dimers is illustrated in Scheme 5.9. The BTA-2 was synthesized from commercial benzothiadiazole (BTA) via bromination and nitration, which was then reacted with triisopropyl((trimethylstannyl)ethynyl)silane (TIPS-$SnMe_3$) via Stille coupling to attach two TIPS groups. After the reduction by iron powder in acetic acid, the intermediate TIPS-BTA-3 was obtained, which was directly applied to condense with corresponding diones to produce the monomer PhTDA and PhTDA-dimer-1, respectively. The other dimer, PhTDA-dimer-2, was obtained from monomer by Suzuki coupling. However, the oxidation of 4-bromocatechol (detail procedure seen Appendix 3) always yields an unidentified mixture. In addition, the aimed product, 4-bromobenzoquinone, was extremely sensitive to light and air at room temperature and would be immediately oxidized to muconic acid [49]. Consequently, the synthesis of PhTDA monomer and PhTDA-dimer-2 was unsuccessful as the identified 4-bromobenzoquione could not be obtained.

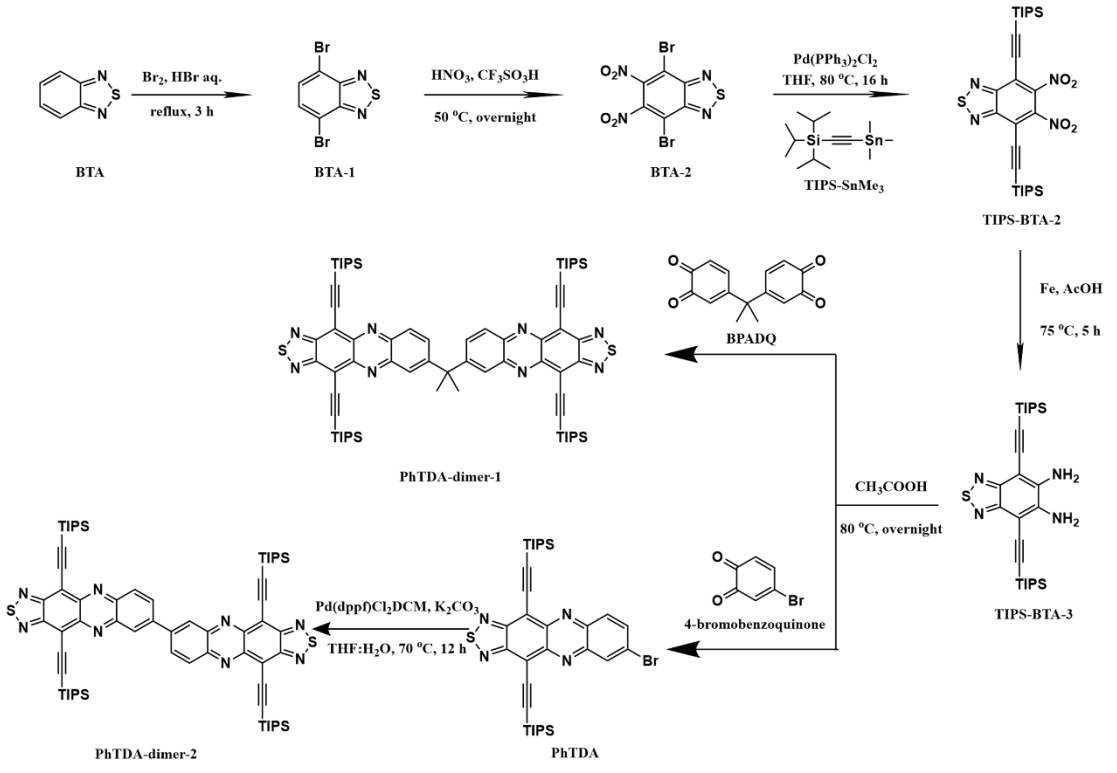

Scheme 5.9 Synthesis route of PhTDA and dimers.

Synthesis of BTA-1. The bromination of BTA followed the synthesis procedure of ATDA-3, as described in the Section 5.3.1.

^{1}H NMR (400 MHz, $CDCl_3$): δ = 7.75 (2H, s).
^{13}C NMR (400 MHz, $CDCl_3$): δ = 153.02, 132.44, 113.95.

Synthesis of BTA-2. First, an insoluble CF_3SO_3H/HNO_3 mixture was formed by dropwise adding fuming HNO_3 (1.5 g, 23.8 mmol) into fuming CF_3SO_3H (15 g, 100 mmol) in an ice bath. Then, BTA-1 (2.5 g, 8.5 mmol) was added portion by portion into the acid mixture over 20 min. The reaction mixture was heated to 50 °C and kept on stirring overnight until TLC showed that the starting material was almost completely consumed. The reaction mixture was poured into the ice water slowly and neutralized by NaOH (5%) solution. The resultant precipitate was filtered, washed with plenty of water, dried and finally purified by recrystallization from ethanol to yield aimed product BTA-2 as a light-yellow powder with a yield of 74%.

^{13}C NMR (400 MHz, DMSO-d_6): δ = 151.99, 144.14, 111.85.

Synthesis of TIPS-BTA-3. The reactant triisopropyl((trimethylstannyl)ethynyl)silane was synthesized via the procedure as described in Scheme 5.10, which can be referred to DeCicco's paper. [50] The obtained crude product as a yellow oil was directly applied to react with BTA-2 to produce TIPS-BTA-2. By reducing with iron powder, crude TIPS-BTA-3 was obtained as a red oil and directly applied into the next step, which is based on the procedure reported in An's paper [51].

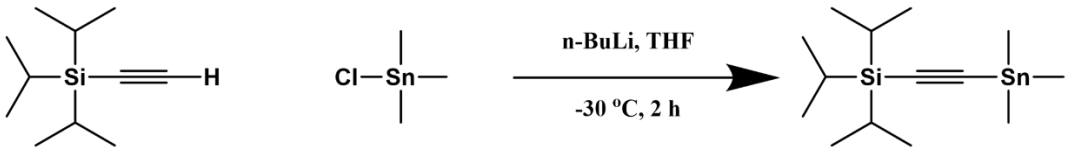

triisopropylsilyl acetylene **TIPS-SnMe$_3$**

Scheme 5.10 Synthesis route of TIPS-$SnMe_3$.

TIPS-BTA-2, ^{1}H NMR (400 MHz, CD_2Cl_2): δ = 1.22 (42H, m, br),
^{13}C NMR (400 MHz, CD_2Cl_2): δ = 153.11, 115.05, 112.65, 94.90, 18.28, 11.18.

Synthesis of BPADQ. The synthesis route of di-*o*-quinone of bisphenol A (BPA), BPADQ, was illustrated in Scheme 5.11 following Stack's work. [52] The oxidation

agent, 2-iodoxybenzoic acid (IBX), was synthesized from 2-iodobenzoic acid according to the reported procedure. [53]

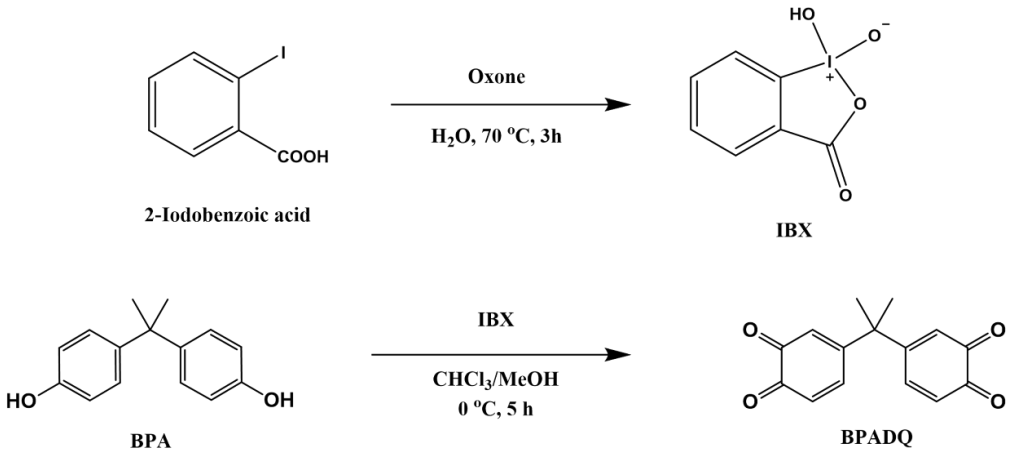

Scheme 5.11 Synthesis route of IBX and BPADQ.

IBX, ^{1}H NMR (400 MHz, DMSO-d_6): δ = 8.15 (1H, d, J = 7.92 Hz), 8.02 (2H, m), 7.85 (1H, t, J = 7.4 Hz)

BPADQ, ^{1}H NMR (400 MHz, DMSO-d_6): δ = 7.08 (1H, dd, J_1 = 5.32 Hz, J_2 = 2.44 Hz), 6.35-6.40 (2H, m), 1.44 (3H, s).

Synthesis of PhTDA-dimer-1. To 25 mL of AcOH was added BPADQ (56.4 mg, 0,22 mmol) and crude TIPS-BTA-3 oil (230 mg, 0.425 mmol). The reaction mixture was then heated to 80 °C under argon atmosphere and kept on stirring overnight. The reaction was quenched by 250 mL of NaOH (5%) solution, and the mixture was extracted with DCM (3 × 75 mL). The combined organic phases were dried over $MgSO_4$, filtered and rotary evaporated under reduced pressure to remove the solvent. The crude product was then purified by column chromatography using hexane/DCM (from 4:1 to 2:1) as eluent to afford PhTDA-dimer-1 with a yield of 51.3%.

^{1}H NMR (400 MHz, $CDCl_3$): δ = 8.24 (2H, d, J = 1.84 Hz), 7.99 (2H, d, J = 9.36 Hz), 7.54 (2H, dd, J_1 = 9.31 Hz, J_2 = 2.08 Hz), 2.04 (6H, s, −C(CH_3)$_2$−), 1.25-1.40 (84 H, m, br, TIPS groups)

^{13}C NMR (400 MHz, $CDCl_3$): δ = 154.56, 154.48, 152.38, 145.56, 144.82, 142.93, 142.86, 133.34, 130.41, 125.69, 114.62, 114.29, 111.79, 111.68, 102.09, 101.99, 44.50, 29.71, 28.39, 18.90, 18.85, 11.62, 11.56.

5.4.2 Electrochemical and photophysical properties

The electrochemical and photophysical properties of PhTDA-dimer-1 were characterized by CV and UV-Vis absorption measurements, of which the set-ups are the same as described in the previous sections. The obtained results are depicted in Figure 5.11 and summarized in Table 5.4.

As shown in the CV plot (Figure 5.11a), PhTDA-dimer-1 shows two reversible reduction peaks and one irreversible oxidation peak. The oxidation potential vs. Fc/Fc^+ is calculated to be 0.93 V, and the HOMO energy level is calculated to be −5.73 eV according to the Equation 3.10. Similarly, the reduction potential vs. Fc/Fc^+ is calculated to be −0.97 V, and the LUMO energy level is calculated to be −3.83 eV according to the Equation 3.11, which is 0.34 eV lower than the LUMO energy level of the ATDA-dimer due to the electron withdrawing effect brought by substituted N atoms. For comparison, the LUMO energy level of PhTDA without Br in THF reported by B. D. Lindner et. al. [54] was −4.27 eV, which is calculated using a value of −5.1 eV for Fc/Fc^+ and needs to be added an additional 0.3 eV to be compared with the value of −3.83 eV. Herein, the dimerization of PhTDA shifted up the LUMO energy level by around 0.12 eV, which agrees well with the trend of the other dimers described above. The energy gap obtained from CV is then calculated to be 1.9 eV.

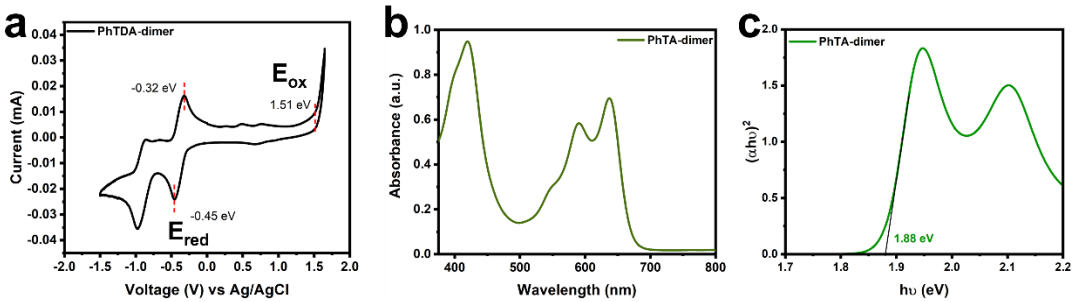

Figure 5.11 (**a**) Cyclic voltammetry plot, (**b**) UV-Vis absorption spectrum and (**c**) Tauc plot of PhTDA-dimer-1.

The steady-state UV-Vis absorption spectrum (Figure 5.11b) of PhTDA-dimer-1 shows two sets of absorption band regions, which resembles the absorption patterns of the previous DAP and ATDA molecules. The absorption peak in the short wavelength

region appears at 420 nm, which is attributed to the n−π* transitions of the conjugated aromatic systems. The main absorption peak in the long wavelength region appears at 637 nm, which can be ascribed to the first electronic transition. The accompanied shoulder peak at 591 nm is attributed to the intramolecular charge transfer transitions. [55] In comparison, the absorption peak of nonbrominated PhTDA monomer in hexane was reported at 643 nm. [54] The optical energy gap obtained from the Tauc plot (Figure 5.11c) is determined to be 1.88 eV, which is consistent with the CV results.

Table 5.4 Electrochemical and photophysical properties of PhTDA and PhTDA-dimer-1.

Compound	E(HOMO) (eV)	E(LUMO) (eV)	$E_{gap, CV}$ (eV)	$\lambda_{max, abs}$ (nm)	$E_{gap, opt}$ (eV)
PhTDA-dimer-1	-5.73	-3.83	1.90	420, 591, 637	1.88
PhTDA*	-	-4.27	-	592, 643	1.86

*Data obtained from Ref [54].

5.4.3 Singlet fission analysis

The TA spectrum of PhTDA-dimer-1 was measured in dilute DCM solution under the same condition as the one described in Section 5.3.3. The obtained TA profiles at different delay time and kinetic traces at the wavelengths of singlet and triplet signals are presented in Figure 5.12.

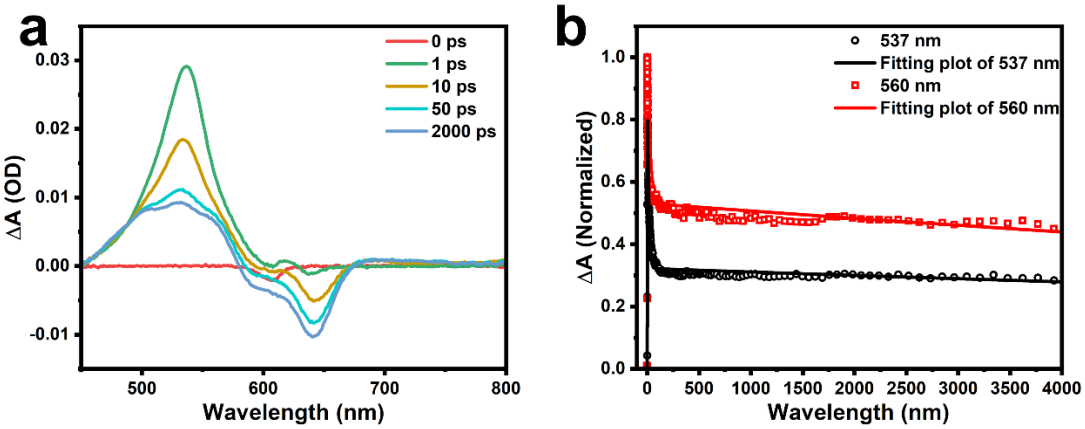

Figure 5.12 (**a**) Transient absorption spectra of PhTDA-dimer-1 at selected probe delay time; (**b**) Normalized kinetic profiles (scattering dots) and corresponding fitting plots (solid lines) of PhTDA-dimer-1 at 537 nm (black) and 560 nm (red).

As shown in the TA spectra (Figure 5.12a), a strong ESA band at the early time stage (≤ 10 ps) is observed at 537 nm, which is attributed to the $S_1 \rightarrow S_n$ transition. Negative GSB band can be observed at 640 nm, which is consistent with the UV-Vis absorption peak. As time delay increases, the shape of ESA band changes with the emergence of a shoulder peak at 560 nm, which is assigned to ESA signal of the triplets. [36] At the same time, the intensity of GSB band further increases, which indicates that the population of S_0 has not recovered along with the decay of S_1. This suggests the existence of an additional decay pathway for S_1 other than relaxation to ground state. At longer delay time (≥ 2 ns), the TA profile is almost unchanged with negligible evolution.

The kinetic dynamics of singlet at 537 nm and triplet at 560 nm are fitted with a convolution of a Gaussian IRF and multiple-exponential function, as shown in Figure 5.12b, and the fitting parameters are summarized in Table 5.5. For the decay of S_1 at 537 nm, a biexponential decay function is fitted to yield a short time constant of 13.99 ± 0.26 ps showing a rapid decay rate, and a long time constant of 27.85 ± 3.76 ns which agrees well with the lifetime of S_1 in PhTDA monomer in thin film state. [36] For the dynamics of triplet, an exponential rise and a biexponential decay function is fitted, which yields a rise time constant of 0.21 ± 0.014 ps indicating a fast SF process. Compared to ATDA dimers, however, PhTDA-dimer-1 shows a rapid decay of triplet with a time constant of 9.82 ± 0.89 ps due to triplet-triplet annihilation.

Table 5.5 Fitting parameters of normalized kinetic profiles for PhTDA-dimer-1

	λ_{probe} (nm)	t_0	t_1	t_2
PhTDA-dimer-1	537		13.99 ± 0.26 ps	27.85 ± 3.76 ns
	560	0.21 ± 0.014 ps	9.82 ± 0.89 ps	20.74 ± 3.81 ns

To conclude, the propane-2,2'-linked phenazinothiadiazole (PhTDA-dimer-1) was successfully synthesized, while the synthesis of PhTDA monomer and directly-linked failed since the synthesis reaction of the intermediate, 4-bromobenzoquinone, always produced unidentified mixture. Similarly, the substitution of nitrogen further decreases the LUMO energy level. From the TA spectra in dilute DCM solution, the triplet signal appears at 560 nm with a rising time constant of 0.21 ps and a short decay time constant of 9.82 ps.

5.5 Conclusions

In summary, a series of nitrogen-substituted and thiadiazole-ring fused polyacenes and dimers with distinct chemical geometries has been successfully synthesized. Their electronic and photophysical properties were investigated and the SF dynamics was characterized by TA spectroscopy. Substitution of nitrogen atoms into polyacene skeleton can significantly lower the energy level of frontier molecular orbitals, and thus improve the chemical stability. Dimerization has resulted in the triplet formation in dilute solution, which has not been observed in the corresponding monomers. The SF rate and triplet lifetime have a strong dependence on the geometries of dimers, i.e., the linker bridge and connection patterns. For ATDA dimers, the directly-linked dimer shows the fastest SF rate in subpicoseconds and the shortest triplet lifetime due to the smallest chromophore proximity and highest electronic coupling strength. Among the phenylene-linked ATDA dimers, ortho- and para-dimers show moderate SF rate in few picoseconds and longer triplet lifetime compared to directly-linked dimer. As for the meta-dimer, however, the triplet was generated by intersystem crossing channel rather than SF process, which resulted in the lowest triplet generation rate in hundreds of picoseconds and a very long triplet lifetime in microseconds. This is because the both weak through-space and through-bond conjugation in the meta-dimer are not compatible for SF process. This work indicates that the electronic properties and electronic coupling can be finely tuned by chemical modification and confirms that dimerization can result efficient SF process in dilute solution. It also provides new perspectives and design guide for the potential SF materials that can be applied in photovoltaic devices.

Reference

[1] M. Grätzel, *Nature*, **2001**, 414, 338-344.

[2] M. Riede, D. Spoltore, and K. Leo, *Adv. Energy. Mater.*, **2020**, 11, 2002653.

[3] A. Mahmood and J.-L. Wang, *Energy Environ. Sci.*, **2021**, 14, 90-105.

[4] W. Shockley and H. J. Queisser, *J. App. Phys.*, **1961**, 32(3), pp. 510-519.

[5] J. Y. Kim, J.-W. Lee, H. S. Jung, H. Shin and N.-G. Park, *Chem. Rev.*, **2020**, 120, 7867-7918.

[6] M. B. Smith and J. Michl, *Chem. Rev.*, **2010**, 6891-6936.

[7] M. C. Hanna and A. J. Nozik, *J. Appl. Phys.*, **2006**, 100, 074510.

[8] A. J. Baldacchino, M. I. Collins, M. P. Nielsen, T. W. Schmidt, D. R. McCamey and M. J. Y. Tayebjee, *Chem. Phys. Rev.*, **2022**, 3, 021304.

[9] S. Singh, W. J. Jones, W. Siebrand, B. P. Stoicheff and W. G. Schneider, *Chem. Phys.*, **1965**, 42, 330-342.

[10] B. J. Walker, A. J. Musser, D. Beljonne and R. H. Friend, *Nat. Chem.*, **2013**, 5, 1019-1024.

[11] I. Kaur, W. Jia, R. P. Kopreski, S. Selvarasah, M. R. Dokmeci, C. Pramanik, N. E. McGruer and G. P. Miller, *J. Am. Chem. Soc.*, **2008**, 130, 16274-16286.

[12] Q. Tang, Z. Liang, J. Liu, J. Xu and Q. Miao, *Chem. Commun.*, **2010**, 46, 2977.

[13] T. Minami, S. Ito and M. Nakano, *J. Phys. Chem. Lett.*, **2013**, 3 (2), 145-150.

[14] S. Ohta, M. Nakano, T. Kubo, K. Kamada, K. Ohta, R. Kishi, N. Nakagawa, B. Champagne, E. Botek, S. Y. Umezaki, A. Takebe, H. Takahashi, S. I. Furukawa, Y. Morita, K. Nakasuji, K. Yamaguchi, *Chem. Phys. Lett.*, **2006**, 420, 432-437.

[15] Y. Liang, Z. Xu, J. Xia, S.-T. Tsai, Y. Wu, G. Li, C. Ray and L. Yu, *Adv. Mater.*, **2010**, 22, E135-E138.

[16] E. A. Margulies, C. E. Miller, Y. Wu, L. Ma, G. C. Schatz, R. M. Young and M. R. Wasielewski, *Nat. Chem.*, **2016**, 8, 1120-1125

[17] D. M. E. Freeman, A. J. Musser, J. M. Frost, H. L. Stern, A. K. forster, K. J. Fallon, A. G. Rapidis, F. Cacialli, I. McCulloch, T. M. Clarke, R. H. Friend and H. Bronstein, *J. Am. Chem. Soc.*, **2017**, 139, 11073-11080.

[18] N. V. Korovina, N. F. Pompetti and J. C. Johnson, *J. Chem. Phys.*, **2020**, 152, No. 040904

[19] J. Zirzlmeier, D. Lehnherr, P. B. Coto, E. T. Chernick, R. Casillas, B. S. Basel, M. Thoss, R. R. Tykwinski and D. M. Guldi, *PNAS*, **2015**, 112(07), 5325-5330.

[20] O. Millington, S. Maontanaro, A. Leventis, A. Sharma, S. A. Dowland, N. Sawhney, K. J. Fallon, W. Zeng, D. G. Congrave, A. J .Musser, A. Rao and H. Bronstein, *J. Am. Chem. Soc.,* **2023**, 145, 2499-2510.

[21] Y. Zou, X. Ji, J. Cai, T. Yuan, D. J. Stanton, Y.-H. Lin, M. Naraghi and L. Fang, *Chem*, **2017**, 2, 139-152.

[22] Y. Zou, T. Yuan, D. J. Frazier, D. J. Stanton, H.-J. Sue and L. Fang, *Org. Lett.,* **2015**, 17, 3146-3149.

[23] M. Hempe and M. Reggelin, *RSC Adv.*, **2017**, 7, 47183-47189.

[24] E. D. Glowacki, G. Romanazzi, C. Yumusak, H. Coskun, U. Monkowius, G. Voss, M. Burian, R. T. Lechner, N. Demitri, G. J. Redhammer, N. Sünger, G. P. Suranna and S. Sariciftci, *Adv. Funct. Mater.,* **2015**, 25, 776-787.

[25] Z.-H. Guo, N. Ai, C. R. McBroom, T. Yuan, Y.-H. Lin, M. Roders, C. Zhu, A. L. Ayzner, J. Pei and L. Fang, *Polym. Chem.,* **2016**, 7, 648.

[26] T. Wiesner, L. Ahrens, F. Rominger, J. Freudenberg and U. H. F. Bunz, *Chem. Eur. J.*, **2021**, 27, 4553-4556.

[27] D. B. Shinde, G. Sheng, X. Li, M. Ostwal, A.-H. Emwas, K.-W. Huang and Z. Lai, *J. Am. Chem. Soc.,* **2018**, 140. 43, 14342-14349.

[28] S. P. Dudek, M. Pouderoijen, R. Abbel, A. P. H. J. Schenning and E. W. Meijer, *J. Am. Chem. Soc.,* **2005**, 127, 33, 11763-11768.

[29] D. Li, X. Wang, Y. Jia, A. Wang and Y. Wu, *Chin. J. Chem.,* **2012**, 30. 861-868.

[30] X. Ji, H. Xie, C. Zhu, Y. Zou, A. U. Mu, M. Al-Hashimi, K. R. Dunbar and L. Fang, *J. Am. Chem. Soc.,* **2020**, 142, 641-648.

[31] Y.-F. Lim, Y. Shu, S. R. Parkin, J. E. Anthony and G. G. Malliaras, *J. Mater. Chem.,* **2019**, 19, 3049-3056.

[32] G. Audran, S. Péralta, M. A. Tehfe, B. Graff, F. Goubard, J. Lalevée, D. Gigmes and F. Dumur, *Curr. Smart Mater.*, **2017**, 2, 102-111.

[33] J. Herz, T. Buckup, F. Paulus, J. Engelhart, U. H. F. Bunz and M. Motzkus, *J. Phys. Chem. Lett.,* **2014**, 5, 2425-2430.

[34] T. Wiesner, L. Ahrens, F. Rominger, J. Freudenberg and U. H. F. Bunz, *Chem. Eur. J.* **2021**, 27, 4553-4556.

[35] A. V. Lunchev, S. A. Morris, R. Ganguly and A. C. Grimsdale, *Chem. Eur. J.* **2019**, 25, 1819-1823.

[36] N. Alagna, J. Han, N. Wollscheid, J. L. P. Lustres, J. Herz, S. Hahn, S. Koser, F. Paulus, U. H. F. Bunz, A. Dreuw, T. Buckup and M. Motzkus, *J. Am. Chem. Soc.*, **2019**, 141, 8834-8845.

[37] T. Honda, M. Nagahara, N. Taka, J. Nishida, T. Kawase, K. Ono, T. Kobayashi, H. Naito and C. Kitamura, *Eur. J. Org. Chem.*, **2019**, 2107-2114.

[38] A. L. Appleton, S. Miao, S. M. Brombosz, N. J. Berger, S. Barlow, S. R. Marder, B. M. Lawrence, K. I. Hardcastle and U. H. F. Bunz, *Org. Lett.*, **2009**, 11(22), 5222-5225.

[39] N. V. Korovina, J. Joy, X. Feng, C. Feltenberger, A. I. Krylov, S. E. Bradforth and M. E. Thompson, *J. Am. Chem. Soc.*, **2018**, 140, 10179-10190.

[40] V. Gray, Z. Zhang, S. Dowland, J. R. Allardice, A. M. Alvertis, J. Xiao, N. C. Greenham, J. E. Anthony and A. Rao, *J. Phys. Chem. Lett.*, **2020**, 11, 7239-7244.

[41] S. R. Yost, J. Lee, M. W. B. Wilson, T. Wu, D. P. McMahon, R. R. Parkhurst, N. J. Thompson, D. N. Congreve, A. Rao, K. Johnson, M. Y. Sfeir, M. G. Bawendi, T. M. Swager, R. H. Friend, M. A. Baldo and T. V. Voorhis, *Nat. Chem.*, **2014**, 6, 492-497.

[42] M. Fan, G. Chen, Y. Xiang, J. Li, X. Yu, W. Zhang, X. Long, L. Xu, J. Wu, Z. Xu and Q. Zhang, *Chem. Eur. J.*, **2021**, 27, 10898-10902.

[43] S. N. Sanders, E. Kumarasamy, A. B. Pun, M. T. Trinh, B. Choi, J. Xia, E. J. Taffet, J. Z. Low, J. R. Miller, X. Roy, X.-Y. Zhu, M. L. Steigerwald, M. Y. Sfeir and L. M. Campos, *J. Am. Chem. Soc.*, **2015**, 137, 8965-8972.

[44] T. Minami and M. Nakano, *J. Phys. Chem. Lett.*, **2012**, 3, 2, 145-150.

[45] A. M. Müller, Y. S. Avlasevich, W. W. Schoeller, K. Müllen and C. J. Bardeen, *J. Am. Chem. Soc.*, **2007**, 129, 46.

[46] N. V. Korovina, S. Das, Z. Nett, X. Feng, J. Joy, R. Haiges, A. I. Krylov, S. R. Bradforth and M. E. Thompson, *J. Am. Chem. Soc.*, **2016**, 138, 617-627.

[47] X. Feng, D. Casanova and A. I. Krylov, *J. Phys. Chem. C,* **2016**, 120, 34, 19070-19077.

[48] S. Ito, T. Nagami and M. Nakano, *J. Phys. Chem. A,* **2016**, 120, 6236-6241.

[49] W. A. Pieken and J. W. Kozarich, *J. Org. Chem.*, **1989**, 54, 510-512.

[50] R. C. DeCicco, A. Black, L. Li and N. S. Goroff, *Eur. J. Org. Chem.*, **2012**, 4699-4704.

[51] C. An, S. Zhou and M. Baumgarten, *Cryst. Growth Des.*, **2015**, 15, 1934-1938.

[52] D. E. Stack and B. Mahmud, *Syn. Commun.*, **2017**, 48, 161-167.

[53] M. Frigerio, M. Santagostino and S. Sputore, *J. Org. Chem.*, **1999**, 64, 4537-4538.

[54] B. D. Lindner, F. Paulus, A. L. Appleton, M. Schaffroth, J. U. Engelhart, K. M. Schelkle, O. Tverskoy, F. Rominger, M. Hamburger and U. H. F. Bunz, *J. Mater. Chem. C*, **2014**, 2, 9609-9612.

[55] G. Qian, Z. Zhong, M. Luo, D. Yu, Z. Zhang, D. Ma and Z. Y. Wang, *J. Phys. Chem. C*, **2009**, 113, 1589-1595.

[56] Y.-D. Zhang, Y. Wu, Y. Xu, Q. Wang, K. Liu, J.-W. Chen, J.-J. Cao, C. Zhang, H. Fu and H.-L, Zhang, *J. Am. Chem. Soc.*, **2016**, 138, 6739-6754

Chapter 6

Electronic Dynamics in Anthrathiadiazole Thin Film and Bilayer Heterojunction with Hybrid Perovskite

Intramolecular singlet fission (SF) material whereby the SF performance is independent of the film morphology should be more suitable to be applied in photovoltaic devices to boost the quantum efficiency and power conversion efficiency. However, the demonstration of intramolecular SF in thin film has been far from sufficient due to the complexity of SF process in condensed solid phase. In this chapter, the SF dynamics of as-prepared anthrathiadiazole (ATDA) molecules was investigated in their thin-film state. Surprisingly, all ATDA derivatives, both monomer and dimers, showed fast SF rate in picoseconds and high triplet yield over 100%. The distinction with the SF dynamics in solution reveals the different effects of inter- and intramolecular coupling on SF process in thin films. This work verifies that efficient intramolecular SF can be retained in thin film and highlights the conditions to be fulfilled for intramolecular SF to prevail. Finally, this study sheds a light on the applications of ATDA molecules in practical photovoltaic devices.

6.1 Introduction

As one of the multiple-exciton generation process, singlet fission (SF) was first discovered in anthracene and tetracene crystals, where two coupled triplet excitons were formed from one singlet excited molecule. [1-3] In 2006, Hanna and Nozik theoretically demonstrated the potential of SF materials for boosting the power conversion efficiency of photovoltaic (PV) devices to exceed the Shockley-Queisser (SQ) limit. [4,5] Since then, significant efforts have been dedicated to the exploration of the underlying SF mechanisms, the development of more efficient novel SF materials and their application in various PV architectures. [6-8]

Intermolecular SF process occurring between two neighboring chromophores has been demonstrated to deliver ultrafast SF rate with near quantitative triplet yield in concentrated solutions and highly ordered solid states, showing a highly dependence on the molecular packing pattern. [9-11] In contrast, intramolecular SF process, which is confined within a single molecule of two or more connected chromophores, can be finely tuned by molecular engineering approaches to establish the structure-function relationship. [12] Therefore, the inherent independence of intramolecular SF on the film morphologies makes it more suitable to be incorporated into solid-state PV devices. Until now, a variety of SF materials composed of different chromophores to exploit the intramolecular coupling has been successfully prepared using versatile organic synthesis strategies, and their SF properties were mostly investigated in solution. [13-16] However, the demonstration of efficient intramolecular SF in condensed solid phase has been scarce, likely due to the complexity of SF dynamics in solid state, i.e., both intramolecular and intermolecular coupling will exist and the interplay between both interactions may affect the SF dynamics. [17-19] More importantly, the main drawback of intramolecular SF is that the triplet excitons are highly localized and difficult to separate, which can be overcome in thin film, where intermolecular coupling offers additional pathways for the separation of triplet excitons. [20] It is no wonder that the ideal SF materials for PV applications should possess both intramolecular coupling to ensure fast and efficient SF rate, and intermolecular coupling to permit the triplet separation. A key issue that needs to be addressed is to evaluate the synergistic effect of both types of electronic coupling in thin films.

Herein, the SF dynamics of as-synthesized ATDA molecules has been investigated in their thin-film state. Compared to the intramolecular SF dynamics in solution. as discussed in last chapter, it is observed that the effect of intermolecular coupling in ATDA monomer and meta-ATDA-dimer thin films becomes so significant that it will stimulate the intermolecular SF process originally absent in solution. On the other hand, for the ortho- and para-ATDA-dimers already with strong intramolecular coupling, efficient SF process was still detected even when the intermolecular interactions were weak. When employed in the bilayer structure with the perovskite film, the ATDA monomer and ortho-ATDA-dimer demonstrated an effective hole extraction capability. These results successfully demonstrated efficient SF rate and excellent charge transfer capability of intramolecular SF materials, which strengthens the confidence in incorporating intramolecular SF molecules into PV devices.

6.2 Experimental Methods

6.2.1 Materials

Lead iodide (PbI_2), methylammonium iodide (MAI), N,N-dimethylformamide (DMF), dimethyl sulfoxide (DMSO), chlorobenzene, dichloromethane (DCM) and quartz substrates were purchased from Sigma-Aldrich and used as received without further purification.

6.2.2 Preparation of precursor solution

The perovskite precursor solution was prepared by mixing three solutions A, B and C. Solution A was prepared by dissolving FAI (208.30 mg, 1.211 mmol) and PbI_2 (587.79 mg, 1.275 mmol) in 2 mL of DMF/DMSO (v/v = 4/1) mixed solvent. Solution B was prepared by dissolving MABr (159.6 mg, 1.425 mmol) and $PbBr_2$ (550.5 mg, 1.5 mmol) in 2 mL of DMF/DMSO (v/v = 4/1) mixed solvent. Solution C was prepared by dissolving CsI (77.9 mg, 0.3 mmol) in 800 μL of DMSO. Solution A, B and C were mixed with a volume ratio of 10:1.5:1 to provide $Cs_{0.05}(FA_{0.85}MA_{0.15})_{0.95}PbI_{2.55}Br_{0.45}$ precursor solution with a concentration of 0.6 M.

The SF precursor solutions were prepared by dissolving 40 mg of ATDA, ortho-ATDA-

dimer, meta-ATDA-dimer and para-ATDA-dimer in 1 mL of chlorobenzene, respectively.

6.2.3 Treatment of film substrates

The quartz substrates were sequentially cleaned with water-based optical lens detergent (1%, Mailang, MIGHTY ZS-120), deionized (DI) water, acetone, isopropanol (IPA) and ethanol in a ultrasonication bath for 30 min each, followed by drying with a compressed nitrogen gun and an ultraviolet-ozone treatment for 15 min to improve the wettability before applying for film fabrication.

6.2.4 Preparation of perovskite, ATDA-based SF and bilayer films

The perovskite, SF and bilayer films were deposited onto the quartz substrates by spin-coating method in a glove box. The perovskite precursor solution was spin-coated at 5000 rpm for 30 s by using ethyl acetate as an antisolvent, and the film was then annealed at 100 ^{o}C for 10 min. The SF precursor solutions were spin-coated at 2000 rpm for 30 s, and the films were then annealed at 80 ^{o}C for 20 min. The bilayer films were prepared by spin-coating SF films onto the as-prepared perovskite films. All film were applied to test without any encapsulation.

6.2.5 General characterizations

The morphologies of as-prepared films and cross-sectional structure of bilayer film were examined by field-emission scanning electron microscopy (FESEM 7600F, JOEL) and an atomic force microscopy (AFM, Asylum Research, Cypher S). The crystal structure of as-prepared films was measured by X-ray diffraction spectroscopy (D8 Advance, Bruker) with Cu-Kα radiation at 40 kV and 40 mA. The valence band (VB) energy level of perovskite and high occupied molecular orbital (HOMO) level of SF films were determined by ultraviolet photoelectron spectra (UPS) obtained from Kratos AXIS Supra X-ray photoelectron spectroscopy (XPS). The ultraviolet-visible (UV-vis) absorption characteristics of as-prepared films were characterized by Cary 5000 UV-Vis Spectrophotometer (Agilent Technologies).

6.2.6 Transient absorption measurement

The modified HELIOS Fire system from Ultrafast Systems (LLC) was used to conduct the transient absorption measurements of as-prepared films. The 610 nm pump pulse was generated by passing the 800 nm fundamental output with 1 kHz repetition rate, 35 fs pulse width (Coherent Libra) through a β-$Ba(BO_2)_2$ crystal. The white light probe pulse was generated by focusing the 800 nm fundamental output onto a sapphire crystal.

6.2.7 Time-resolved photoluminescence measurement

Time-resolved photoluminescence (TRPL) measurements were performed on an upright microscope setup. A fiber-coupled picosecond pulsed laser (Pico Quant P-C-405B) with an output wavelength λ = 405 nm and a repetition rate f = 2.5 MHz was used as the excitation source. The laser was focused on the samples using a 10x microscope objective. The emissions were filtered using a long-pass filter with a cutoff wavelength λ = 420 nm and directed into a spectrometer (Acton Spectra Pro 2300i), within which the emissions were then impinged onto a monochromator. Emissions that are around the wavelength of 760 nm are subsequently transmitted and collected into a single photon avalanche detector (Micron Photon Devices). A single photon counting module (Pico Harp 300) was used to extract the data. All measurements were conducted at room temperature.

6.3 Results and Discussion

6.3.1 Morphology and crystal structure characterization of SF films

Smooth and fully-formed films of ATDA, ortho-ATDA-dimer and meta-ATDA-dimer were successfully achieved using the spin-coating method, as described in Experimental section 6.2.4. However, obtaining a similarly smooth and complete para-ATDA-dimer film was more challenging due to the relatively poor solubility in the common organic solvents used. The surface morphologies of the as-prepared SF films were characterized using FESEM and AFM techniques, as depicted in Figure 6.1. All films are smooth and condensed devoid of any observable pinholes. The surface roughness of the as-prepared SF films was quantified by the AFM Z-height images. The

mean root square (RMS) values of the average surface roughness were determined to be 2.66, 1.28, 2.18 nm for ATDA, ortho-ATDA-dimer and meta-ATDA-dimer film, respectively, which is comparable to the thermal-evaporated TIPS-pentacene film. Although these films featured some aggregates formed during the spin-coating process, they still maintained relatively low surface roughness, which is in coherence with the observations from FESEM images.

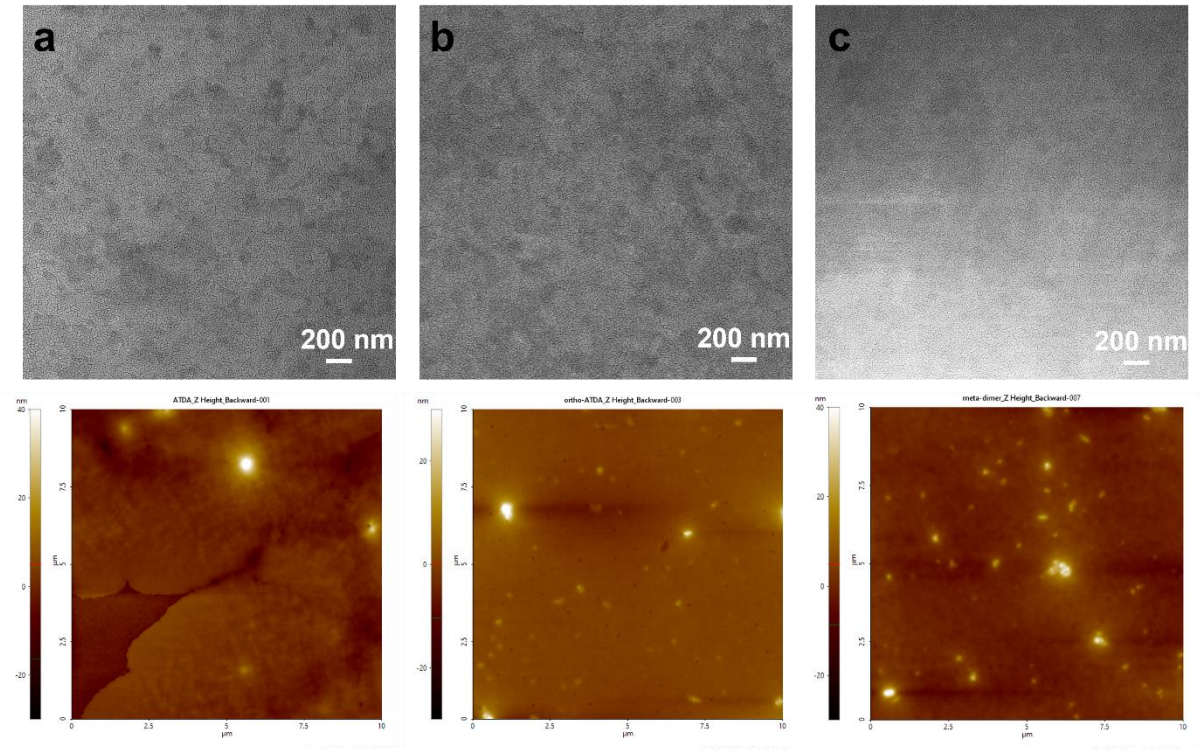

Figure 6.1 FESEM (top row) and AFM (bottom row) images of (**a**) ATDA, (**b**) ortho-ATDA-dimer and (**c**) meta-ATDA-dimer films.

The crystallinity of the as-prepared SF films was characterized by XRD spectroscopy and the obtained patterns are presented in Figure 6.2. For the ATDA film, the XRD pattern displayed an extremely intense diffraction peak at 2θ = 5.19°, which can be attributed to the domain (001) crystal plane with a layer spacing of 17.1 Å. Minor peaks corresponding to the (002) and (003) crystal planes appeared at 2θ = 10.38° and 15.57°, respectively. Interestingly, none of the ATDA dimer films exhibited any peaks apart from those attributed to the ITO substrate [21], which suggests that the spin-coated dimer films were amorphous, indicating the suppression of the intermolecular packing and long-range order π-conjugation in these dimer films. [22] However, it is possible

that even in an amorphous film, to a certain extent, there is some short range intermolecular π overlap of the azaacene moieties.

The XRD result highlights the highly crystalline nature of the spin-coated ATDA monomer film, with a predominant orientation along the (001) phase, suggesting the strong intermolecular interactions along the out-of-plane direction. Conversely, the spin-coated ATDA dimer films are poorly crystallized exhibiting a random orientation due to the suppression of intermolecular interactions.

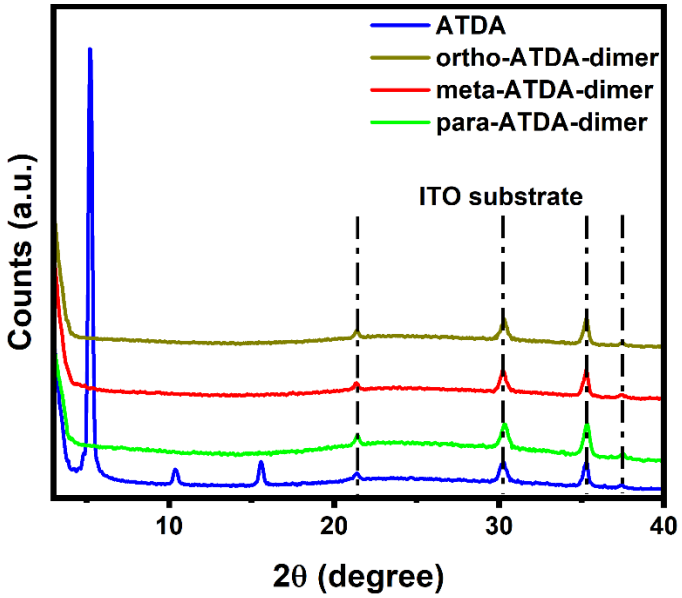

Figure 6.2 Thin film XRD patterns of ATDA-based SF films. The signals denoted by dash-dot lines are ascribed to the ITO substrate.

6.3.2 Energy structure characterization of SF films

Accurate determination of the energy structures of the as-prepared SF films is essential for advancing the study of charge dynamics between SF materials and perovskite. To this end, the energy levels of the highest occupied molecular orbitals (HOMO) and the lowest unoccupied molecular orbitals (LUMO) of the SF films were characterized by the combination of UV-vis absorption and UPS techniques. The obtained UV-vis and UPS spectra are presented in Figure 6.4 and 6.5, respectively.

Analogous to the UV-vis absorption spectra in solution (Figure 5.7a), the UV-vis absorption spectra of the SF films (Figure 6.3a) can also be divided into two sets of

peaks. Despite these similarities, differences in the primary absorption onsets and the relative ratios of 0-0/0-1 vibronic absorption were noticeable between the UV-vis absorption spectra of the SF molecules in spin-coated thin film and solution. These differences provide insights into the intermolecular interactions in thin films, which are significantly influenced by the variations in molecular geometries. [23,24]

The UV-vis absorption spectra of ortho- and meta-ATDA-dimer showed minimal changes from thin film to solution. The absorption onset of the ortho-ATDA-dimer remained unchanged, while the meta dimer exhibited a slight redshift of 0.05 eV. In addition, the relative intensity ratio of the 0-0 and 0-1 vibronic bands increased by 0.09 for ortho-ATDA-dimer and by 0.02 for meta-ATDA-dimer from solution to thin film. Conversely, the absorption spectra of ATDA and para-ATDA-dimer showed significant differences between thin films to solution. The absorption onsets of ATDA and para-ATDA-dimer in thin films redshifted by 0.11 and 0.10 eV, respectively. Moreover, the 0-0/0-1 ratio in thin films decreased by 0.31 and 0.26, respectively. These huge changes imply a much-delocalized singlet excited state and stronger intermolecular interactions in ATDA and para-ATDA-dimer compared to the ortho- and meta-ATDA-dimer, which agrees well with the XRD results.

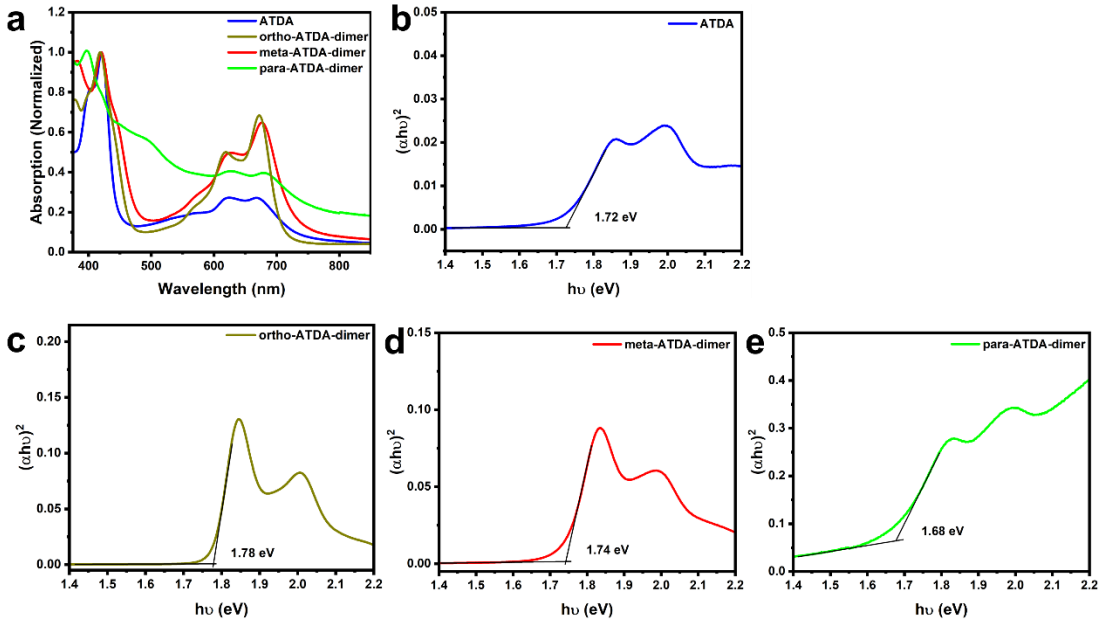

Figure 6.3 (**a**) UV-Vis absorption spectra of ATDA-based SF films. Tauc plots of (**b**) ATDA, (**c**) ortho-ATDA-dimer, (**d**) meta-ATDA-dimer and (**e**) para-ATDA-dimer. (Replotted from the corresponding UV-Vis absorption spectra).

The optical band gaps of ATDA, ortho-, meta- and para-ATDA-dimer films are extrapolated to be 1.72, 1.78, 1.74 and 1.68 eV, respectively, from the Tauc plots (Figure 6.3b–e). By analyzing the cut-off and edge values of the UPS spectra (Figure 6.4) with Equation 3.3, the calculated HOMO energy levels are found to be −5.40, −5.80, −5.55 and −5.44 eV for ATDA, ortho-, meta- and para-ATDA-dimer films, respectively. Combining the UV-vis and UPS results, the LUMO energy levels of ATDA, ortho-, meta- and para-ATDA-dimer films are determined to be −3.68, −4.02, −3.81 and −3.76 eV, respectively. Referring to the calculation results shown in Table 5.2, the energy levels of the triplet state (T_1) in ATDA, ortho-, meta- and para-ATDA-dimer films are estimated to be −4.61, −4.97, −4.74 and −4.66 eV, respectively. The maximum absorption peaks, optical energy gaps, HOMO, LUMO and triplet state energy levels of as-prepared SF films are summarized in Table 6.1.

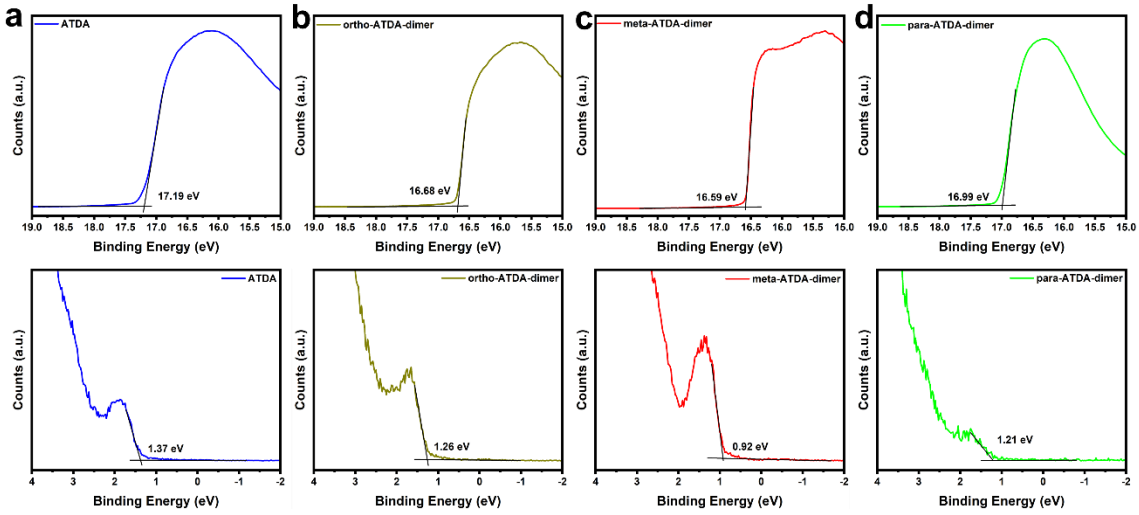

Figure 6.4 UPS spectra of (**a**) ATDA, (**b**) ortho-ATDA-dimer, (**c**) meta-ATDA-dimer and (**d**) para-ATDA-dimer films at cut-off (up) and edge (down) region.

Table 6.1 Photophysical properties of ATDA and its dimers in thin films.

	$\lambda_{abs,\ max}$ (nm)	$E_{opt,\ gap}$ (eV)	E(HOMO) (eV)	E(LUMO) (eV)	E(T_1) (eV)
ATDA	420, 624, 668	1.72	−5.40	−3.68	−4.61
Ortho-ATDA-dimer	418, 618, 672	1.78	−5.80	−4.02	−4.97
meta-ATDA-dimer	421, 626, 677	1.74	−5.55	−3.81	−4.74
para-ATDA-dimer	397, 627, 681	1.68	−5.44	−3.76	−4.66

6.3.3 Singlet fission dynamics in SF films

Transient absorption spectroscopy is a powerful technique used to unveil the SF dynamics in the as-prepared films from picosecond to nanosecond. The pump beam was centered at 610 nm with a beam energy of 200 μW. The obtained TA results are visualized as pseudocolor maps as shown in Figure 6.5.

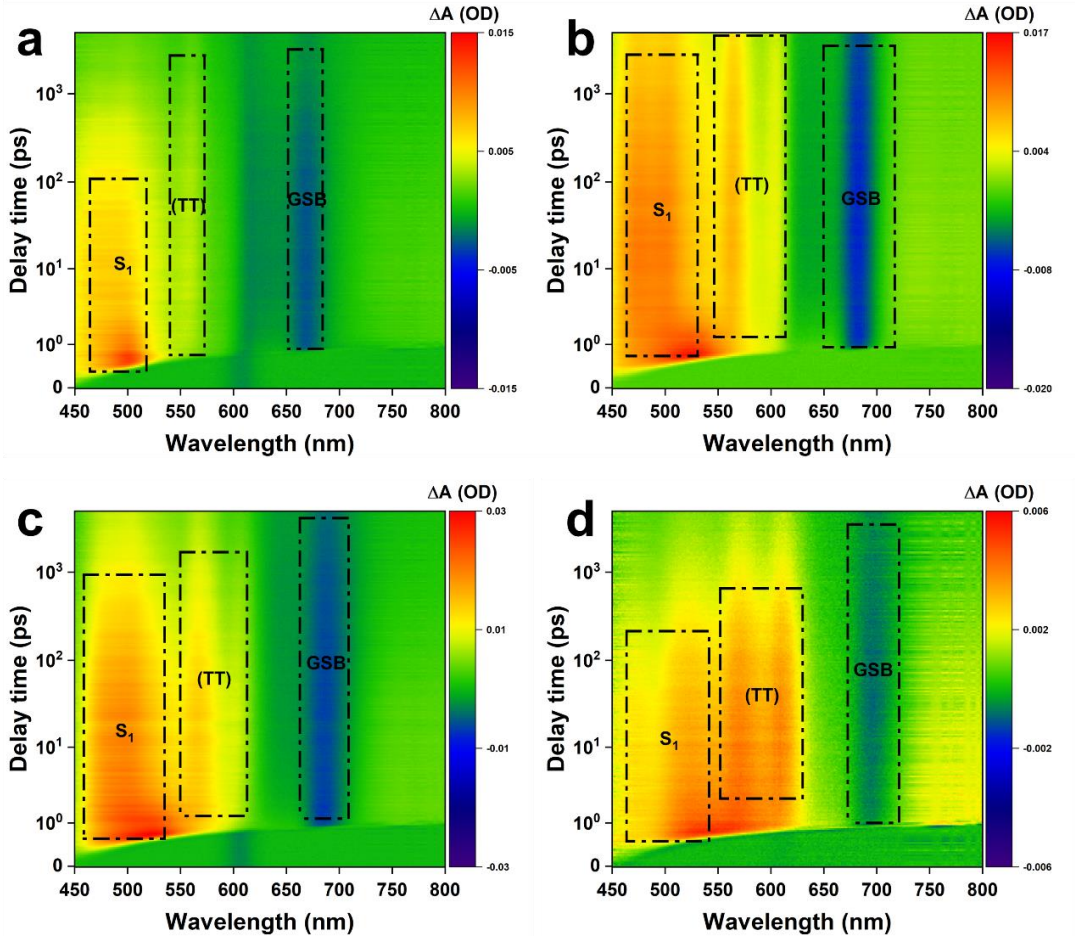

Figure 6.5 Transient absorption spectra under pump pulse at 610 nm of (**a**) ATDA, (**b**) ortho-ATDA-dimer, (**c**) meta-ATDA-dimer and (**d**) para-ATDA-dimer films.

In Figure 6.5a, an excited state absorption (ESA) band corresponding to the $S_1 \rightarrow S_n$ transition appears at around 500 nm, and the negative ground state bleaching (GSB) appears centred at 664 nm, which aligns with the steady-state absorption spectra shown in Figure 6.3a. Notably, unlike the TA spectra of ATDA in dilute DCM solution (Figure 5.8a), the ESA signal of S_1 decays much faster, accompanying by the emergence of a new band at 556 nm, which is attributed to the ESA signal of triplet state. The rapid decay of S_1 and the formation of the triplet state suggest that the SF process occurs in the ATDA film, which is absent in the ATDA dilute solution.

The TA spectra of the three dimer films exhibit a similar evolution pattern as monomer film but with different kinetics. Specifically, for ortho-, meta- and para-ATDA-dimer films, the ESA bands of $S_1 \rightarrow S_n$ transition appear at 523, 517 and 523 nm, respectively, and the GSB bands of S_1 are detected at 678, 684 and 691 nm, respectively, which is consistent with the steady-state absorption results displayed in Figure 6.3a. In addition, compared to the dilute solution (Figure 5.8d), the triplet state signal of the meta-ATDA-dimer in thin film appears at a much earlier delay time and decays with a much faster rate that assembles the behaviour observed in ortho- and para-ATDA-dimer films. This huge difference indicates that, for meta-ATDA-dimer, the generation of the triplet state in thin film occurs via the SF process, rather than the intersystem crossing process that was observed in the dilute solution.

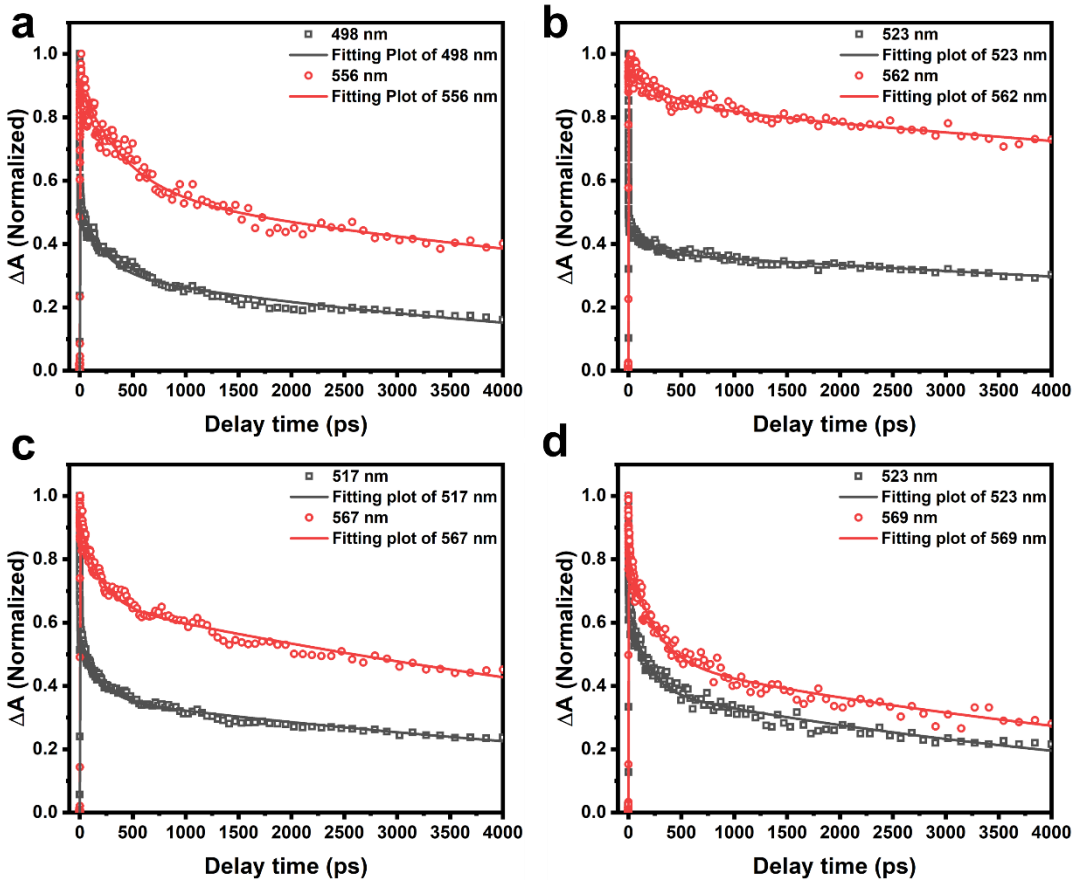

Figure 6.6 Normalized transient absorption kinetic profiles (scattering dots) and fitting plots (solid lines) under excitation wavelength of 610 nm of (**a**) ATDA, (**b**) ortho-ATDA-dimer, (**c**) meta-ATDA-dimer and (**d**) para-ATDA-dimer films at probe wavelength of singlet and triplet signals.

The singlet and triplet dynamics are investigated by fitting the kinetic profiles with a convolution of a Gaussian instrument response function (IRF) and multiple-exponential function as shown in Figure 6.6, and the fitting parameters are summarized in Table 6.2.

For the monomer ATDA, the singlet shows a much faster decay in film (222.9 ps) than in solution (18.7 ns). Interestingly, the intermolecular SF dynamics of ATDA in film are highly identical to the intramolecular SF dynamics of directly-linked ATDA-dimer in dilute solution (the triplet generation constants are 1.17 and 1.09 ps, and the short decay constants are 429.8 and 439.6 ps for ATDA film and ATDA-dimer solution, respectively). This similarity suggests that the intermolecular coupling strength in monomer ATDA film can be regarded to be comparable with the intramolecular coupling strength in directly-linked ATDA dimer solution. In all dimers, the SF rate is

much faster in films compared to that in dilute solution. Especially for meta-ATDA-dimer, the triplet formation time constant changes from 270.2 ps in dilute solution to 0.04 ps in thin film. As discussed in Chapter 5, the triplet in meta-ATDA-dimer solution was generated in a slow rate via intersystem crossing pathway due to its weak through-space intramolecular coupling. While the fast triplet generation rate in meta-ATAD-dimer film is attributed to the intermolecular SF process because of a small proximity between two molecules in a condense solid phases. [25] For ortho- and para-ATDA-dimer, the triplet formation rate has also increased from solution (8.63 and 5.29 ps) to thin film (0.07 and 2.11 ps), which is a combination result of intermolecular and intramolecular SF processes despite the weak intermolecular coupling. The similarity in triplet generation and decay rates of different dimer thin films suggest that the SF process is a localized and constrained phenomenon. [22]

Table 6.2 Fitting parameters of normalized kinetic plots and triplet yield (Φ_T) for SF films.

	λ_{probe} (nm)	t_0*	t_1	t_2	Φ_T
ATDA	498		1.17 ± 0.05 ps	222.9 ± 16.5 ps	133%
	556	1.17 ± 0.20 ps	429.8 ± 42.47 ps	10.42 ± 1.47 ns	
Ortho-ATDA-dimer	523		1.30 ± 0.03 ps	166.7 ± 15.3 ps	142%
	562	0.07 ± 0.004 ps	409.8 ± 96.6 ps	27.45 ± 4.63 ns	
Meta-ATDA-dimer	517		1.33 ± 0.04 ps	171.3 ± 9.60 ps	123%
	567	0.04 ± 0.017 ps	179.76 ± 12.24 ps	8.99 ± 0.46 ns	
Para-ATDA-dimer	523		1.73 ± 0.12 ps	168.47 ± 11.7 ps	168%
	569	2.11 ± 0.35 ps	239.7 ± 16.8 ps	7.21 ± 0.55 ns	

*t_0 represents the time constant of rising component.

Although the triplets are generated with a faster rate in film for ortho-ATDA-dimer due to the concerted inter- and intramolecular SF process, the relative population of triplets after long time delay decreases slightly from solution (0.81, Figure 5.9c) to film (0.73, Figure 6.6b). This suggests a much slow diffusion of triplet pair in ortho-dimer film because of the confined intramolecular SF and week intermolecular coupling strength. In contrast, the relative population of triplets after long time delay decreased significantly for meta-ATDA-dimer in thin film (0.45, Figure 6.6c), which is comparable to the ATDA monomer film (0.40, Figure 6.6a) as triplets are generated by intermolecular SF in both films. This large depopulation of triplets is the result of the prompt triplet-triplet annihilation of separated triplets. [26-28] For para-ATDA-dimer, the depopulation of triplets (0.72, Figure 5.9e) resembles the ortho-ATDA-dimer in

solution due to similar intramolecular SF process. While in film state, the relative population of triplets reduces dramatically to 0.27 due to the strong intermolecular coupling. [29]

The triplet yields (Φ_T) of these films are evaluated using the same procedure described in Appendix 5, and the calculated Φ_T values derived from ATDA, ortho-, meta- and para-ATDA-dimer films are 133%, 142%, 123% and 168%, respectively. Because of the synergetic effect of intramolecular and intermolecular SF, the ortho- and para-ATDA-dimer films produces a higher Φ_T compared to the ATDA and meta-ATDA-dimer films, which depends solely on the intermolecular SF. Furthermore, the Φ_T value only exhibits slight changes from solution to film for the ortho- and para-ATDA-dimer, implying that the molecular arrangement has a marginal impact on the intramolecular SF process.

To conclude, SF films have been successfully fabricated by spin-coating method and thoroughly characterized in terms of the surface morphology, crystallinity and energy structure. The SF dynamics are investigated by employing TA spectroscopy, which reveals that the SF process in the solid film states is influenced by both intermolecular and intramolecular coupling strength depending on the molecular structures. For the ATDA monomer lacking intramolecular coupling and the meta-ATDA-dimer with weak intramolecular coupling, the intermolecular coupling will be *de facto* component to stimulate the SF process in the solid state. However, in the case of the ortho- and para-ATDA-dimer with inherent strong intramolecular coupling, the intermolecular coupling, as deduced from the triplet yield in solution, only has a minimal effect on the overall SF process in their solid states. Thus, this study verifies that molecules capable of promoting intramolecular SF are less likely to be affected by the morphology and intermolecular interactions. And interestingly, the most efficient SF in solid state is still obtained from the molecules that exhibit efficient intramolecular SF previously assessed in solution, highlighting the importance of molecular design. The efficient SF process and high triplet yield observed in these ATDA-based SF films pave the way for the further investigation on the SF/perovskite bilayer structure.

6.3.4 Characterization on SF/hybrid perovskite bilayer films

Since all SF films have been demonstrated to deliver excellent SF properties, the investigation proceeds to explore the potential of SF/hybrid perovskite bilayer structures for PV devices, similar to the TIPS-pentacene/hybrid perovskite discussed in Chapter 4. The para-ATDA-dimer was not employed to construct the bilayer structure due to its poor film quality, hence not included in the subsequent characterizations. However, unlike TIPS-pentacene, it is noteworthy that the energy levels of the triplet states in these ATDA-based SF films are remarkably low (Figure 6.7), to the extent that no perovskite (PVK) found in the literature possesses a suitable conduction band (CB) capable of facilitating the electron transfer process between them. Here, the triple cation perovskite $Cs_{0.05}(FA_{0.85}MA_{0.15})_{0.95}PbI_{2.55}Br_{0.45}$, characterized by a deep CBM, was employed to create bilayer structures to conduct a preliminary study about the effects of ATDA-based SF films on the morphologies and photophysical properties of perovskite films.

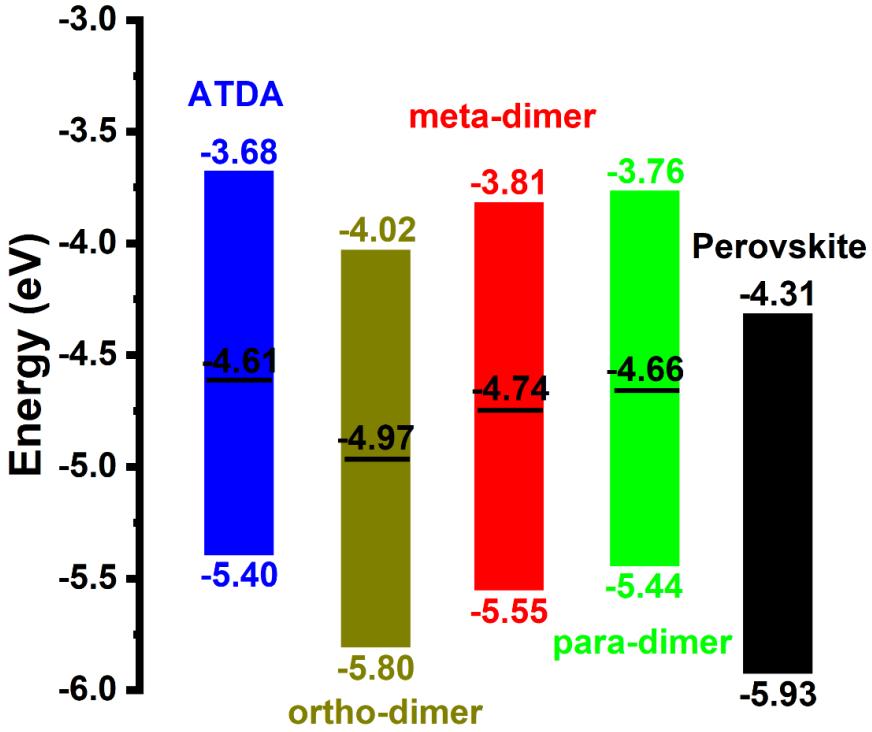

Figure 6.7 Energy structure diagram of ATDA-based films and perovskite film.

Perovskite film was fabricated by spin-coating method, and the SF/PVK bilayer films were prepared by directly spin-coating the SF film onto the perovskite film. FESEM images (Figure 6.8a) show that perovskite film was compact and composed of uniformly distributed grains with an average size of 100 nm. Figures 6.8b–d show that

the perovskite films were fully covered by the SF films without any pinholes in the bilayer films. At higher magnification of the FESEM images, the small grains of SF layers and the boundaries from perovskite grains can be observed. Cross-sectional FESEM images (Figure 6.9) of the bilayer films further demonstrated complete coverage of the underlying perovskite layer by the SF layers, delivering the thickness of each layer. The average thickness of the perovskite layer was found to be 158 nm, and the ATDA-film was 153 nm, the ortho-ATDA-film was 144 nm and the meta-ATDA-film was 150 nm.

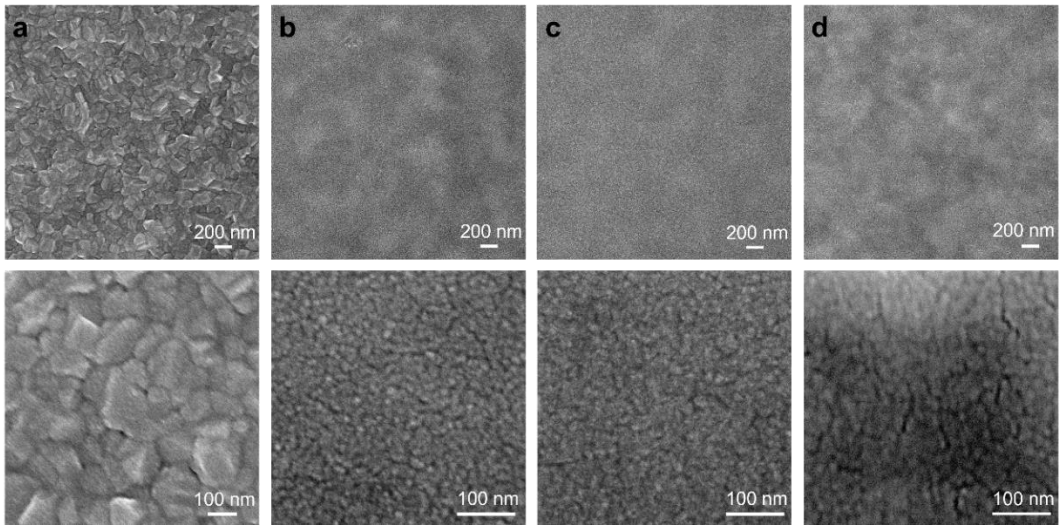

Figure 6.8 FESEM images of (**a**) perovskite, (**b**) ATDA/PVK, (**c**) ortho-ATDA-dimer/PVK and (**d**) meta-ATDA-dimer/PVK films in (up) low and (down) high magnification.

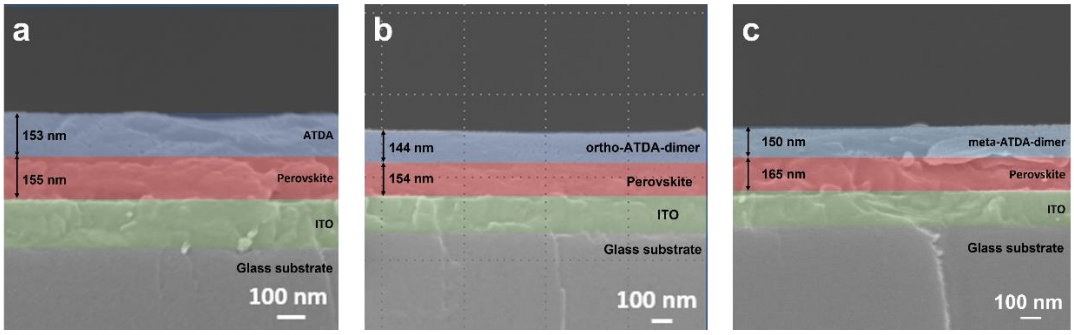

Figure 6.9 Cross-sectional FESEM images of (**a**) ATDA/PVK, (**b**) ortho-ATDA-dimer/PVK and (**c**) meta-ATDA-dimer/PVK films on the ITO glass substrate.

The film roughness (RMS) values of the perovskite and bilayer films were obtained from the Z-height AFM images (Figure 6.10), which were calculated to be 13.34 nm for perovskite film, 2.34 nm for ATDA/PVK bilayer film, 3.27 nm for ortho-ATDA-

dimer/PVK bilayer film and 4.02 for meta-ATDA-dimer/PVK bilayer film, respectively. The higher RMS value of perovskite film compared to the pure SF film suggests a much more uneven surface, which agrees well with the observations of the FESEM images (Figure 6.8). The RMS of bilayer films increased slightly compared to the corresponding SF films likely due to the influence of the underlying perovskite film.

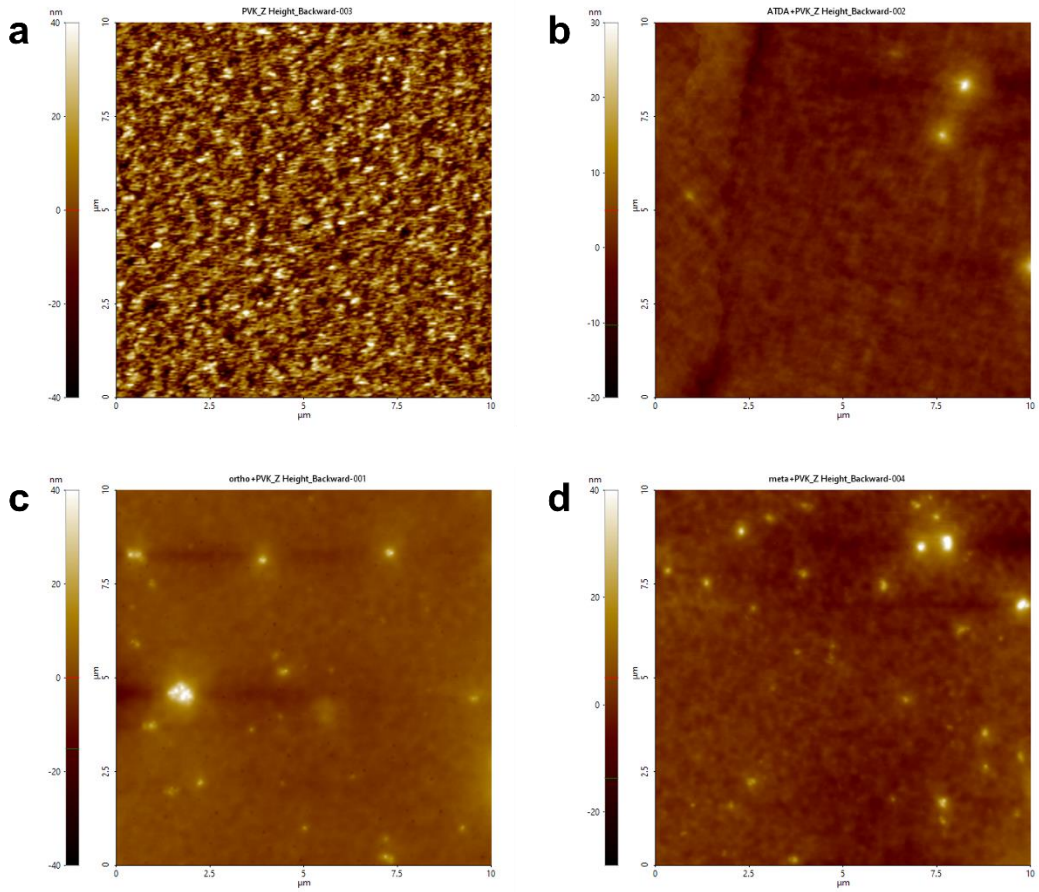

Figure 6.10 AFM images of (**a**) perovskite, (**b**) ATDA/PVK, (**c**) ortho-ATDA-dimer/PVK and (**d**) meta-ATDA-dimer/PVK films.

The effects of SF films on the crystallinity and photophysical performance in SF/PVK bilayer films were evaluated by XRD, UV-vis absorption and photoluminescence techniques. The XRD pattern of spin-coated perovskite film shown in Figure 6.11a presented a series of diffraction peaks with a typical peak at $2\theta = 14.1^{o}$ that can be attributed to the photoactive black phase with high crystallinity. [30] The diffraction peaks brought by the ITO substrate were denoted as green stars. All the bilayer films exhibited almost identical diffraction patterns as that of the perovskite film, suggesting that the high crystallinity of perovskite was not affected by the coating of SF films.

Additionally, the sharp peak at 2θ = 5.19° attributed to the ATDA (001) crystal plane can be clearly observed in the ATDA/perovskite bilayer film, which indicates that the underlying perovskite film has little impact on the growth of ATDA crystal phase. The UV-vis absorption spectra (Figure 6.11b) of SF/perovskite bilayer films almost resembled the more absorbing pristine perovskite layer, featuring the characteristic absorption peaks of ATDA molecules at around 420, 620 and 670 nm.

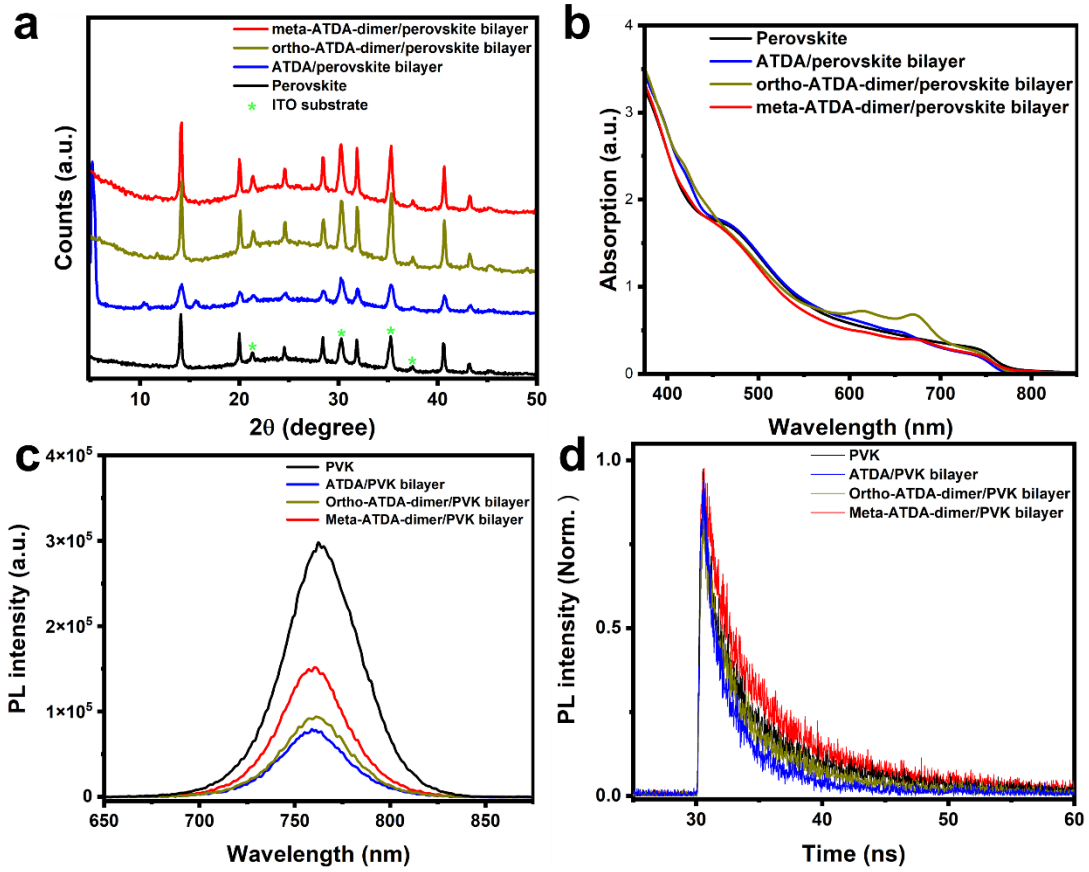

Figure 6.11 Effects of SF films on crystallinity and photophysical properties of in SF/PVK bilayer films. (**a**) Thin film XRD patterns (the green stars denote the diffraction peaks of ITO substrate), (**b**) UV-vis spectra, (**c**) Steady-state photoluminescence (PL) spectra and (**d**) time-resolved PL spectra of perovskite and SF/PVK bilayer films.

Transient absorption photoluminescence (TRPL) technique was applied to investigate the charge transfer process at the bilayer interface, specifically the hole transfer process from the valence band (VB) of perovskite to the HOMO of SF films in the nanosecond scale. An extensive emission peak at around 760 nm was observed in the steady-state PL spectra of the pure perovskite film (Figure 6.11c), while no emission peak was found

in the steady-state PL spectra of all the ATDA-based SF films (Figure A.5) because of their ultrafast and efficient SF process demonstrated above. Consequently, all SF/perovskite bilayer films only exhibited the emission peak of perovskite layer but with much lower intensity, which was reduced by 73% for ATDA/PVK bilayer, 69% for ortho-ATDA-dimer/PVK bilayer and 50% for meta-ATDA-dimer/PVK bilayer, indicating great PL quenching efficiency of ATDA-based SF films. The TRPL dynamics was fitted using the biexponential equation [31]:

$$y = A_1 e^{\frac{-t}{\tau_1}} + A_1 e^{\frac{-t}{\tau_2}} \qquad \textbf{Equation 6.1}$$

where the short decay time τ_1 corresponds to the non-radiative recombination induced by the defects, and the long decay time τ_2 corresponds to the radiative recombination. The pristine perovskite film displayed an average PL lifetime of 3.70 ns, while both the ATDA/PVK and ortho-ATDA-dimer/PVK bilayer films displayed shorter PL lifetime of 2.15 and 3.31 ns, respectively. This reduced PL lifetime suggests an effective hole extraction ability of ATDA and ortho-ATDA-dimer films. [32] Interestingly, the meta-ATDA-dimer/PVK bilayer film exhibited a longer average PL lifetime of 4.77 ns, which may be attributed to the relatively poor hole extraction ability and the surface passivation effect of meta-ATDA-dimer, resulting in an interface with less defects. [33]

Table 6.3 Fitting parameters of normalized time-resolved photoluminescence spectra of perovskite and SF/PVK bilayer films.

	τ_1	τ_2	Average lifetime (ns)
Perovskite	1.29	7.39	3.70
ATDA /PVK Bilayer	0.86	3.77	2.15
Ortho-ATDA-dimer/PVK Bilayer	1.50	6.23	3.31
Meta-ATDA – dimer/PVK Bilayer	1.84	8.34	4.77

6.4 Conclusions

In summary, the electronic dynamics of as-synthesized ATDA and dimers have been

investigated in thin-film state. All ATDA-based films were able to realize ultrafast SF process in picoseconds with high triplet yield over 100%. Unlike in the solution, intermolecular coupling plays a significant role to facilitate the SF process in the ATDA and meta-ATDA-dimer thin films, which inherently lack the intramolecular coupling. While for the ortho- and para-ATDA-dimer, the strong intramolecular coupling still dominates the SF process in the thin-film state, thus reducing the degree of dependence on intermolecular interactions. Here, it is also verified that the ATDA dimers capable of undergoing efficient intramolecular SF have less dependence on film morphology and molecular packing. Furthermore, comparing the SF dynamics of all the ATSA-based films, the most efficient SF is still demonstrated by the dimers with the most efficient intramolecular SF, highlighting the importance of molecular design over control of intermolecular interactions. In terms of the ATDA-based SF/perovskite bilayer structures, although the energy levels of the triplet states for these SF materials might be unfavorable for electron transfer to the CB of perovskite, TRPL results have demonstrated their effective hole extraction capability, which still holds significant potential for their application in the other types of SF-enhanced photovoltaic devices.

Reference

[1] M. B. Smith and J. Michl, *Chem. Rev.*, **2010**, 6891-6936.

[2] S. Singh, W. J. Jones, W. Siebrand, B. P. Stoicheff and W. G. Schneider, *J. Chem. Phys.* **1965**, 42, 330-342.

[3] C. E. Swenberg and W. T. Stacy. *Chem. Phys. Lett.*, **1968**, 2, 237-238.

[4] M. C. Hanna and A. J. Nozik, *J. Appl. Phys.*, **2006**, 100, 074510.

[5] W. Shockley and H. J. Queisser, *J. App. Phys.*, **1961**, 32, 510-519.

[6] T. Ullrich, D. Munz and D. M. Guldi, *Chem. Soc. Rev.*, **2021**, 50, 3485-3581.

[7] T. Wang, H. Liu, X. Wang, L. Tang, J. Zhou, X. Song, L. Lv, W. Chen, Y. Chen and X. Li, *J. Mater. Chem. A,* **2023**, 11, 8515.

[8] A. J. Baldacchino, M. I. Collins, M. P. Nielsen, T. W. Schmidt, D. R. McCamey and M. J. Y. Tayebjee, *Chem. Phys. Rev.,* **2022**, 021304.

[9] B. J. Walker, A. J. Musser, D. Beljonne and R. H. Friend, *Nat. Chem.*, **2013**, 5, 1019-1024.

[10] A. K. Le, J. A. Bender, D. H. Arias, D. E. Cotton, J. C. Johnson and S. T. Roberts, *J. Am. Chem. Soc.,* **2018**, 140, 814-826.

[11] K. Broch, J. Dieterle, F. Branchi, N. J. Hestand, Y. Oliver, H. Tamura, C. Cruz, V. M. Nichols, A. Hinderhofer, D. Beljonne, F. C. Spano, G. Cerullo, C. J. Bardeen and F. Schreiber, *Nat. Commun.*, **2018**, 9(1), 954.

[12] N. V. Korovina, J. Joy, X. Feng, C. Feltenberger, A. I. Krylov, S. E. Bradforth and M. E. Thompson, *J. Am. Chem. Soc.*, **2018**, 140, 10179-10190

[13] S. N. Sanders, E. Kumarasamy, A. B. Pun, M. L. Steigerwald, M. Y. Sfeir and L. M. Campos, *Angewandte. Chemie*, **2016**, 128(10), 3434-3438.

[14] O. Millington, S. Maontanaro, A. Leventis, A. Sharma, S. A. Dowland, N. Sawhney, K. J. Fallon, W. Zeng, D. G. Congrave, A. J .Musser, A. Rao and H. Bronstein, *J. Am. Chem. Soc.,* **2023**, 145, 2499-2510.

[15] Y. Hong, M. Rudolf, M. Kim, J. Kim, T. Schembri, A.-M. Karuse, K. Shoyama, F. Bialas, M. I. S. Röhr, T. Joo, H. Kim, D. Kim and F. Würthner, *Nat. Commun.,* **2022**, 13, 4488.

[16] R. Casillas, I. Papadopoulos, T. Ullrich, D. Thiel, A. Kunzmann and D. M. Guldi, *Energy Environ. Sci.*, **2020**, 13, 2741-2804.

[17] N. A. Pace, W. Zhang, D. H. Arias, I. McCulloch, G. Rumbles and J. C. Johnson, *J. Phys. Chem. Lett.,* **2017**, 8, 6086-6091.

[18] H. Huang, G. He, K. Xu, Q. Wu, D. Wu, M. Y. Sfeir and J. Xia, *Chem*, **2019**, 5, 2405-2417.

[19] T. S. Lee, Y. L. Lin, H. Kim, R. D. Pensack, B. P. Rand and G. D. Scholes, *J. Phys. Chem. Lett.*, **2018**, 9, 14, 4087-4095.

[20] M. T. Trinh, Y. Zhong, Q. Chen, T. Schiros, S. Jockusch, M. Y. Sfeir, M. Steigerwald, C. Nuckolls and X. Zhu, *J. Phys. Chem. C*, **2015**, 119, 1312-1319.

[21] M. Thirumoorthi and J. T. J. Prakash, *J. Asian Ceram. Soc.*, **2016**, 4:1, 124-132.

[22] H. Huang, G. He, K. Xu, Q. Wu, D. Wu, M. Y. Sfeir and J. Xia, *Chem*, **2019**, 5, 2405-2417.

[23] D. Beljonne, H. Yamagata, J. L. Brédas, F. C. Spano and Y. Olivier, *Phys. Rev. Lett.*, **2013**, 110, 226402.

[24] N. J. Hestand and F. C Spano, *Chem. Rev.*, **2018**, 118, 15, 7069-7163.

[25] B. D. Folie, J. B. Haber, S. Refaely-Abramson, J. B. Neaton and N. S. Ginsberg, *J. Am. Chem. Soc.*, **2018**, 140, 6, 2326-2335.

[26] L. Wang, C. Feng, C. Wu, S. Xie, Y. Wu, H. Fu and J. Yao, *J. Phys. Chem. C*, **2021**, 125, 22093-22099.

[27] C. M. Mauck, P. E. Hartnett, E. A. Margulies, L. Ma, C. E. Miller, G. C. Schatz, T. J. Marks and M. R. Wasielewski, *J. Am. Chem. Soc.*, **2016**, 138, 11749-11761.

[28] S. N. Sander, E. Kumarasamy, A. B. Pun, K. Appavoo, M. L. Steigerwald, L. M. Campos and M. Y. Sfeir, *J. Am. Chem. Soc.*, **2016**, 138, 7289-7297.

[29] S. N. Sander, E. Kumarasamy, A. B. Pun, M. T. Trinh, B. Choi, J. Xia, E. J. Taffet, J. Z. Low, J. R. Miller, X. Roy, X.-Y. Zhu, M. L. Steigerwald, M. Y. Sfeir and L. M. Campos, *J. Am. Chem. Soc.*, **2015**, 137, 28, 8965-8972.

[30] M. Saliba, T. Matsui, J. Y. Seo, K. Domanski, J. P. Correa-Baena, M. K. Nazeeruddin, S. M. Zakeeruddin, W. Tress, A. Abate, A. Hagfeldt and M. Grätzel, *Energy Environ. Sci.*, **2016**, 9(6), 1989-1997.

[31] Q. Han, S. H. Bae, P. Sun, Y. T. Hsieh, Y. M. Yang, Y. S. Rim, H. Zhao, Q. Chen, W. Shi, G. Li and Y. Yang, *Adv. Mater.*, **2016**, 28, 2253-2258.

[32] X. Liu, E. Rezaee, H. Shan, J. Xu, Y. Zhang, Y. Feng, J. Dai, Z.-K. Chen, W. Huang and Z.-X. Xu, *J. Mater. Chem. C*, **2018**, 6, 4706-4713.

[33] W. S. Yang, B.-W. Park, E. H. Jung, N. J. Jeon, Y. C. Kim, D. U. Lee, S. S. Shin, J. Seo, E. K. Kim, J. H. Noh and S. I. Seok, *Science*, **2017**, 356(6345), 1376-1379.

Chapter 7

Conclusions and Recommendations

This chapter draws together the threads of the thesis. The general conclusions have been summarized, along with the implications of the research. Then the outstanding questions for the future work are presented. Finally, the extent to which the proposed hypothesis was proven has been discussed.

7.1 General Conclusions

This thesis has explored the charge transfer dynamics at the SF/perovskite heterojunctions, and the impact of molecular structures on SF dynamics in both solution and solid film states. It provides a design guide in the molecular perspective to achieve the SF-enhanced perovskite solar cells.

First, the heterojunctions consisting of a well-studied SF molecule, TIPS-pentacene and a triple-cation perovskite has been constructed due to their well-matched energy structures. The electron transfer process from the triplet state of TIPS-pentacene to the CB of perovskite has been demonstrated to occur in 1.2 ps by TA measurement, and the hole transfer process from the VB of perovskite to the ground state of TIPS-pentacene has been demonstrated to occur in nanoseconds by TRPL spectroscopy. The efficient charge transfer process has resulted in an increase of 20% in the carrier density in perovskite layer. These results support the possibility of a SF-enhanced solar cell.

Next, to elucidate the structure-function relationship of SF materials, a series of novel materials composed by the nitrogen and sulfur substituted polyacenes has been proposed based on the calculation results and finally successfully synthesized. The CV, UV-vis and UPS results have shown that the nitrogen and sulfur atoms can well-delocalize and lower the frontier molecular orbital, which will improve the chemical stability of these SF molecules. By using TA measurement, efficient SF process occurring in picoseconds has been demonstrated in the directly-linked, ortho- and para-ATDA-dimer solution with high triplet yield, which was absent in the ATDA monomer and meta-ATDA-dimer solution. The distinctive SF process of these molecules in dilute solution is resulted from the different molecule structures, which implies the possibility of achieving target SF properties by precisely monitoring the molecular structures.

Lastly, moving towards the goal of practical solar cells, the SF dynamics of the as-synthesized materials in thin film states has been investigated. The ATDA and meta-ATDA-dimer lacking intramolecular coupling showed an efficient SF process, which has not been observed in their solution. This phenomenon suggests the significant effect of intermolecular coupling to facilitate the SF process in a closed molecular packing pattern. In contrast, for ortho- and para-ATDA-dimer with strong intramolecular

coupling strength, their SF process showed almost the same evolution dynamics from solution to thin film states. This resemblance demonstrated the dominative effect of intramolecular coupling over intermolecular coupling on the SF process even in a condense molecular packing pattern. This result indicates that for SF materials with strong intramolecular coupling, the SF process would not rely on the morphologies, which is more suitable for the application in solar cells.

Overall, this thesis proved the feasibility of SF-enhanced perovskite heterojunction and justified the versatility of molecular design to engineer the SF process in solution and solid film states. The findings presented in this thesis will contribute to the achievement of the future SF-enhanced perovskite solar cells.

7.2 Outstanding Questions and Future Work

7.2.1 TIPS-pentacene-enhanced perovskite solar cell

Since the charge transfer process at the TIPS-pentacene/perovskite interface has been demonstrated in Chapter 4 leading to an increase in the charge density in perovskite layer, it is reasonable to construct a whole perovskite solar cell with TIPS-pentacene layer to demonstrate the SF enhancement in external quantum efficiency (EQE) and power conversion efficiency. A preliminary trial has been conducted to investigate the impact of singlet fission layer on the performance of perovskite solar cells, the device structure and the current-voltage ($J-V$) curves are shown in Figure 7.1.

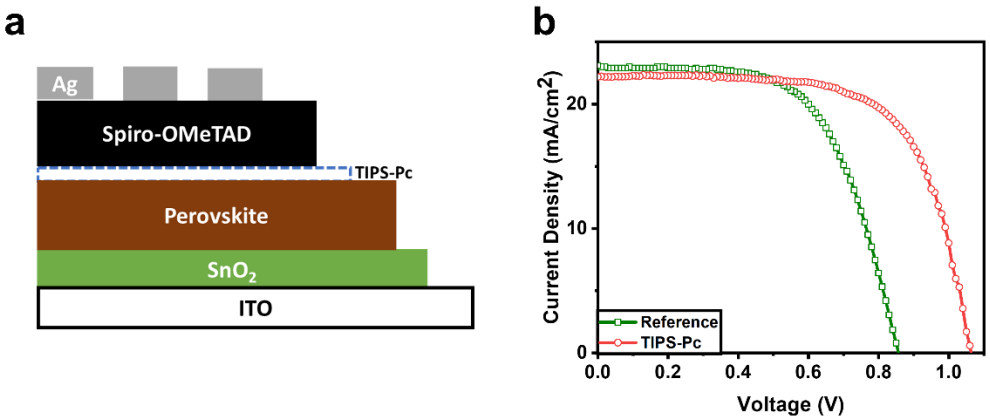

Figure 7.1 (**a**) Configuration of perovskite solar cells with TIPS-pentacene layer. (**b**) $J-V$

curves of the perovskite solar cells with and without TIPS-pentacene layer in their best performance.

Although the performance of the controlled devices is not good enough as the fabrication conditions have not been well-modified, the improvement of the TIPS-pentacene devices in open-circuit voltage, short-circuit current, fill factor and power conversion efficiency implies the positive effect of TIPS-pentacene layer on the perovskite solar cell to some extent. Therefore, the EQE of these devices under different wavelength irradiation will be measured in the future to quantify the contribution of triplet excitons generated by the SF process. In addition, the photocurrent of devices will be further monitored in-situ under varied applied magnetic field since SF process is subjected to the magnetic field. [1]

7.2.2 Sensitizing singlet fission with perovskite

As discussed in Chapter 6, the triplet state energy levels of the as-synthesized ATDA-based SF materials are so low that they are not suitable for constructing the heterojunctions with the perovskites to examine the electron transfer process at the interface. However, from another perspective, the triplet energy transfer process from photoexcited perovskite to these SF materials is energetically favorable. In this case, the SF material is sensitized by the more absorbing perovskite and thereby produces multiple triplets, which can also take the advantage of SF to boost the power conversion efficiency when applied to the photovoltaic devices.

Inorganic perovskite nanocrystals $CsPbBr_3$ has been extensively studied as a sensitizer for singlet and triplet energy transfer coupled with polycyclic aromatic hydrocarbons due to its high extinction coefficient and high PL quantum yield. [2-6] However, the mechanism of energy transfer pathway and the excitons produced by sensitization still remain unsettled. For instance, both H. Lu [4] and X. Luo [5] proposed the Dexter-type energy transfer pathway from $CsPbBr_3$ to SF molecule. Lu suggests that the energy transfer was achieved by the electron transfer to the singlet state of SF molecule, which then produce the triplet exciton via SF process [Figure 7.2a]. On the other hand, Luo suggests that the energy transfer was achieved through an energetically favored hole transfer process, directly leading to the generation of triplet exciton [Figure 7.2b]. By

alloying chloride into the $CsPbBr_3$ nanocrystals, J. T. DuBose [6] monitored the spectral overlap between perovskite nanocrystal and Rhodamine B and suggests that Förster energy transfer dominated in the case of high spectra overlap, which produced singlet excitons rather than the reported triplet excitons [7].

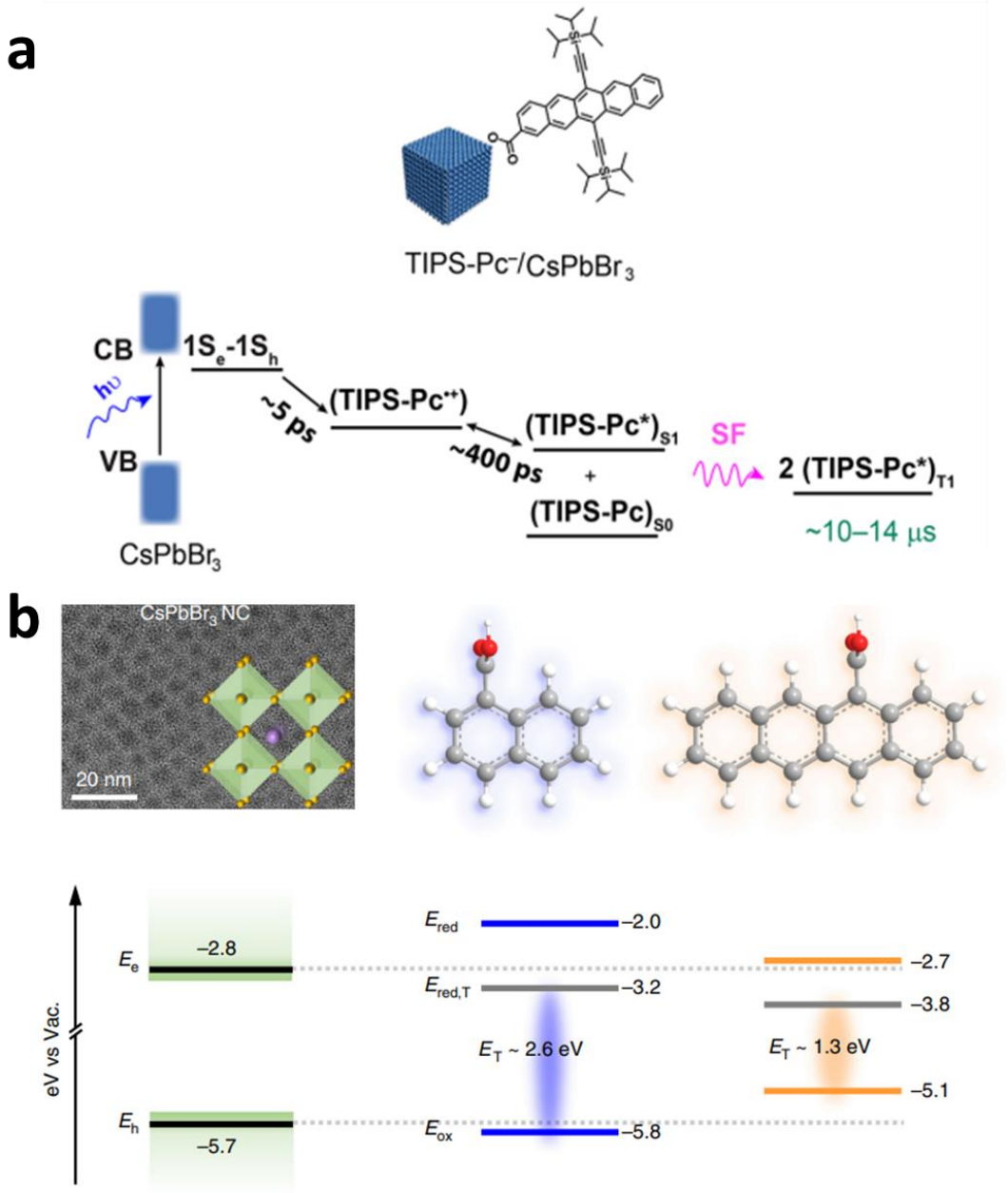

Figure 7.2 (**a**) Illustrative mechanism of triplet sensitization from $CsPbBr_3$ nanocrystals to surface attached TIPS-pentacene molecules. Reprint with permission from Ref. 4. Copyright © 2019 American Chemical Society. (**b**) Schematic energy level alignment between $CsPbBr_3$ nanocrystals and naphthalene carboxylic acid and 5-tetracene carboxylic acid. Reprint with permission from Ref. 5. Copyright © 2020 Springer Nature, Open Access.

Overall, most of the perovskite-sensitized SF study focuses on nanocrystals, the study on thin film almost remains unexplored. As demonstrated in Chapter 4, the charge transfer processes including both electron and hole transfer processes have been confirmed to be feasible between SF molecules and perovskite thin film, which implies the satisfaction of the distance requirements for charge transfer process. Moreover, the preliminary study clearly demonstrated an effective hole transfer process from perovskite film to the as-synthesized SF materials. Therefore, future work will explore the SF-sensitization capability of perovskite film to provide another perspective to achieve the SF-enhanced perovskite solar cell.

7.2.3 Thermal effect on SF process in ATDA thin films

Temperature can significantly affect the SF process regarding to the efficiency, rate and mechanism. Evaluated temperatures can provide additional thermal energy to overcome energy barriers, which can facilitate and enhance the rate of endothermic SF process. On the other hand, higher temperature may also promote competing pathways such as exciton diffusion and energy dissipation, which will reduce the SF rate and efficiency. K. Wantanabe's group has demonstrated the temperature dependance of exciton spectral diffusion in both tetracene [8] and 3,4,9,10-perylenetetracarboxylicdimide (PTCDI) [9] thin films. Moreover, the thermal stability of SF materials should be evaluated as it will affect the performance and lifetime of applied photovoltaic devices.

Therefore, it is crucial to elucidate the thermal effects on SF process in the as-synthesized ATDA and dimers films, which will guide the optimization of ATDA-enhanced photovoltaic devices in the future.

7.3 Outcomes Reflected in the Original Hypothesis

Overall, the hypothesis mentioned in Chapter 1 has partially proved by the outcomes. The charge transfer process from the triplet state of TIPS-pentacene to perovskite has been demonstrated, which led to the increase in the charge density of perovskite layer. The structure-function relationship of SF materials has been proved by systematically investigating a series of novel SF molecules with different structures. By characterizing

the thin film SF properties, the intramolecular SF process was proved to be more suitable for the application in photovoltaic devices as the SF performance was not related to the film morphology.

However, the SF-enhanced perovskite solar cells with improved quantum efficiency and power conversion efficiency have not been practically realized, which remains to be explored in the future work.

Reference

[1] P. J. Jadhav, P. R. Brown, N. Thompson, B. Wunsch, A. Mohanty, S. R. Yost, E. Hontz, T. Van Voorhis, M. G. Bawendi, V. Bulović and M. A. Baldo, *Adv. Mater.,* **2012**, 24(46), pp 6169-6174.

[2] L. Protesescu, S. Yakunin, M. I. Bodnarchuk, F. Krieg, R. Caputo, C. H. Hendon, R. X. Yang, A. Walsh and M. V. Kovalenko, *Nano Lett.,* **2015**, 15 (6), 3692-3696.

[3] J. De Roo, M. Ibanez, P. Geiregat, G. Nedelcu, W. Walravens, J. Maes, J. C. Martins, I. Van Driessche, M. V. Kovalenko and Z. Hens, *ACS Nano*, **2016**, 10(2), 2071-2081.

[4] H. Lu, X. Chen, J. E. Anthony, J. C. Johnson and M. C. Beard, *J. Am. Chem Soc.,* **2019**, 141, 4919-4927.

[5] X. Luo, Y. Han, Z. Chen, Y. Li, G. Liang, X. Liu, T. Ding, C. Nie, M. Wang, F. N. Castellano and K. Wu, *Nat. Commun.,* **2020**, 11(1), 28.

[6] J. T. DuBose and P. V. Kamat, *J. Am. Chem. Soc.,* **2021**, 143, 45, 19214-19223.

[7] X. Luo, G. Liang, Y. Han, Y. Li, T. Ding, S. He, X. Liu and K. Wu, *J. Am. Chem. Soc.,* **2020**, 142, 11270-11278.

[8] T. Yoshida, K. Watanabe, M. Petrović and M. Kralj, *J. Phys. Chem. Lett.,* **2020**, 11, 5248-5254.

[9] T. Yoshida and K. Watanabe, *J. Phys. Chem. B*, **2021**, 125, 9350-9356.

APPENDIX

Chapter 5 Systematic Investigation on Electronic Dynamics in Novel Singlet Fission Materials − Nitrogen-Substituted and Thiadiazole-Fused Polyacenes

1. Synthesis of DAP-dimer-2

The proposed synthesis route of DAP-dimer-2 is shown Scheme A.1, which was not achieved because the Boc-group attachment to the L-BP-3 was not successful due to its extremely low solubility.

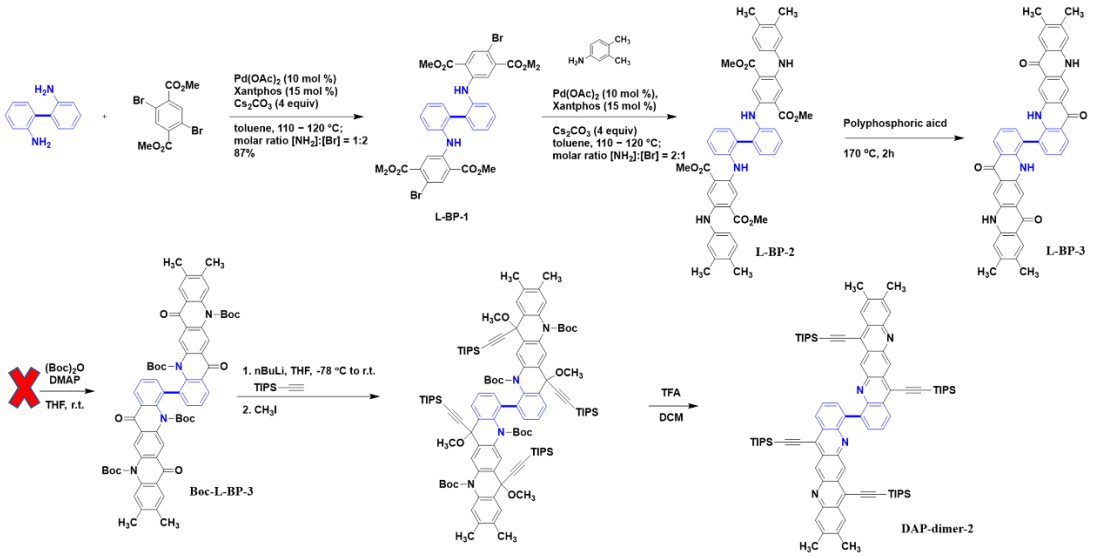

Scheme A.1 Proposed synthesis route of DAP-dimer-2.

Synthesis of L-BP-1 and L-BP-2. L-BP-1 and L-BP-2 were synthesized by Buchwald-Hartwig coupling reaction under optimized condition as illustrated in Scheme A.1. The synthesis procedure assembled as that of L-DHDF-1 as described in Chapter 5.

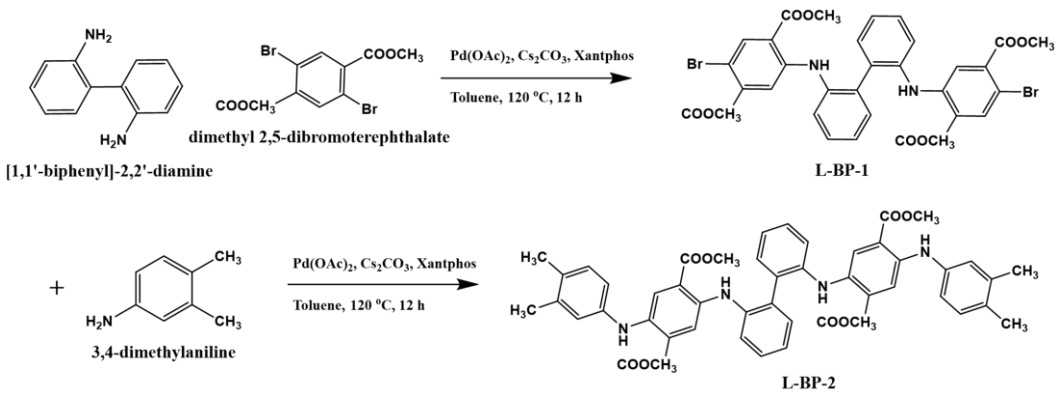

Scheme A.2 Synthesis route of L-BP-1 and L-BP-2 by optimized Buchwald-Hartwig coupling reaction.

L-BP-1. A mixture of [1,1'-biphenyl]-2,2'-diamine (191.6 mg, 1.04 mmol), dimethyl 2,5-dibromoterephthalate (1.464 g, 4.16 mmol), Palladium (II) acetate ($Pd(OAc)_2$, 24 mg, 0.106 mmol), Xantphos (90.26 mg, 0.156 mmol) and Cs_2CO_3 (2.10 g, 6.448 mmol) in 20 mL of dry toluene was degassed by N_2 for 30 min and then heated at 120 ^oC overnight. The reaction mixture was cooled and diluted by DCM, followed by filtering through a Celite pack. The residue was concentrated under reduced pressure and purified by column chromatography using hexane/EtOAc (4/1) as the eluent to afford the aimed product L-BP-1 as a yellow powder with a yield of 82%.

^1H NMR (400 MHz, $CDCl_3$): δ = 8.88 (2H, s, NH), 7.67 (2H, s, Ar-H), 7.29-7.53 (8H, m, Ar-H), 7.18 (2H, s, Ar-H), 3.79 (6H, s, OCH_3). 3.69 (6H, s, OCH_3).

^{13}C NMR (400 MHz, $CDCl_3$): δ = 166.12, 165.30, 145.02, 136.91, 136.04, 135.32, 132.05, 131.75, 129.09, 125.13, 122.19, 114.65, 114.56, 105.15, 52.65, 52.42.

L-BP-2. A mixture of L-BP-1 (726.37 mg, 1.0 mmol), 3,4-dimethylaniline (484.72 mg, 4.0 mmol), $Pd(OAc)_2$, (22.4 mg, 0.10 mmol), Xantphos (86.8 mg, 0.15 mmol) and Cs_2CO_3 (1.95 g, 6.0 mmol) in 20 mL of dry toluene was degassed by N_2 for 30 min and then heated at 120 ^oC overnight. The reaction mixture was cooled and diluted by DCM, followed by filtering through a Celite pack. The residue was concentrated under reduced pressure and purified by column chromatography using hexane/EtOAc (4/1) as the eluent to afford the aimed product L-BP-2 as wine-red powder with a yield of 88%.

^1H NMR (400 MHz, DMSO-d_6): δ = 8.33 (2H, s, NH), 8.20 (2H, s, NH), 7.54 (2H, s, Ar-H), 7.34-7.43 (8H, m, Ar-H), 7.21 (2H, t, J = 7.48, Ar-H), 7.02 (2H, d, J = 8.4, Ar-H), 6.75 (4H, m, Ar-H), 3.69 (6H, s, OCH_3), 3.62 (6H, s, OCH_3), 2.16 (12H, s, Ar-CH_3).

Synthesis of L-BP-3 and Boc-BP-3. L-BP-3 was synthesized from L-BP-2 at the presence of PPA, and the synthesis route is illustrated in Scheme A.3.

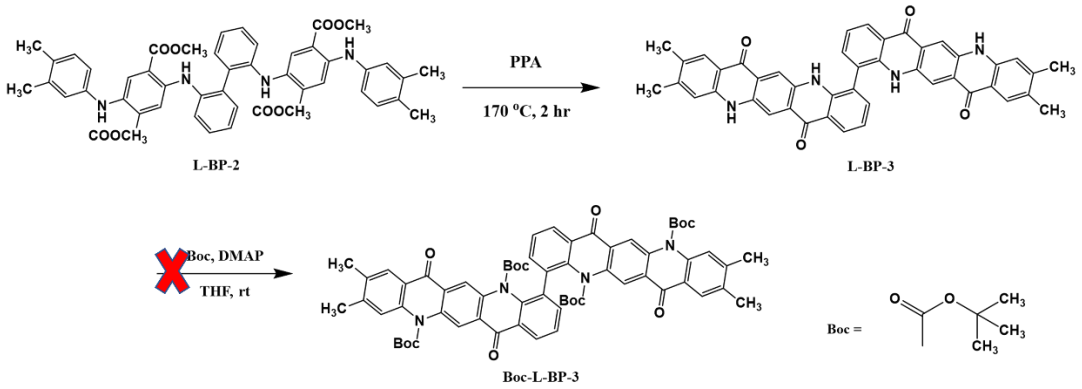

Scheme A.3 Synthesis route of L-BP-3 and Boc-L-BP-3.

L-BP-3. To the vigorously stirred polyphosphoric acid (PPA, 10 mL) heated at 170 °C was slowly added the starting material L-BP-2 (363.1 mg, 0.45 mmol). After 2 h, the reaction mixture was cooled to room temperature, quenched with ice water and stirred overnight. The reaction mixture was then filtered, and the black solid was washed with plenty of water to remove the unreacted PPA. MeOH and DCM were used to wash away the organic byproducts. The aimed product L-BP-3 was obtained as an insoluble dark solid with a yield of 99%.

No NMR data was obtained due to the extremely low solubility of L-BP-3 in deuterated solvents.

FTIR (KBr): ν = 3409, 3274, 2977, 1607, 1547, 1479, 1440, 1339, 1261, 1072, 896, 764 cm^{-1}.

2. Synthesis of DAP-dimer-3

The proposed synthesis route of DAP-dimer-3 is shown Scheme A.4, which was not achieved because the Boc-group attachment to the L-MDA-3 was not successful due to its extremely low solubility.

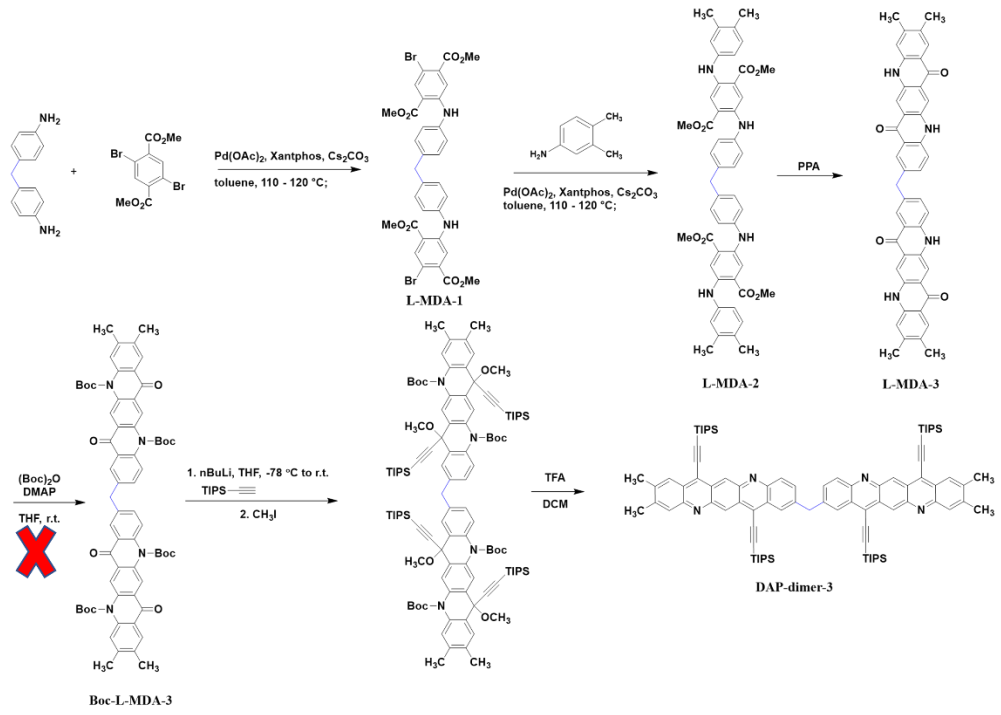

Scheme A.4 Proposed synthesis route of DAP-dimer-3.

Synthesis of L-MDA-1 and L-MDA-2. L-MDA-1 and L-MDA-2 were synthesized by Buchwald-Hartwig coupling reaction under optimized condition as illustrated in Scheme A.5. The synthesis procedure assembled as that of L-DHDF-1 as described in Chapter 5.

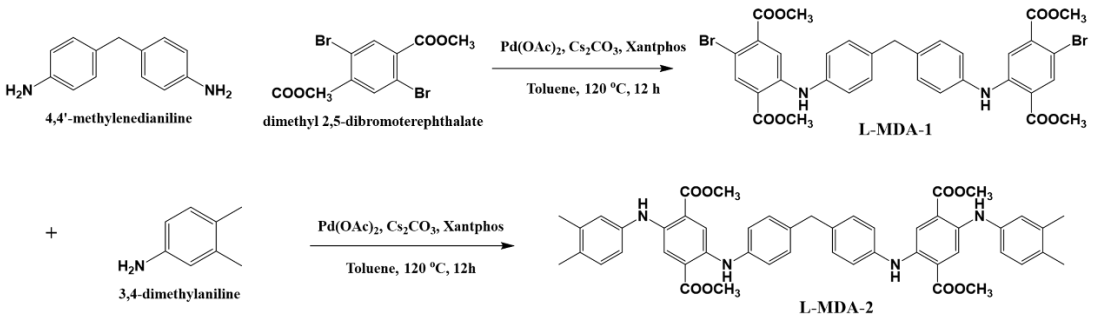

Scheme A.5 Synthesis route of L-MDA-1 and L-MDA-2.

L-MDA-1. A mixture of 4,4'-methylenedianiline (198.2 mg, 1.0 mmol), dimethyl 2,5-dibromoterephthalate (1.408 g, 4.0 mmol), $Pd(OAc)_2$, (22.5 mg, 0.10 mmol), Xantphos (86.79 mg, 0.15 mmol) and Cs_2CO_3 (1.96 g, 6.0 mmol) in 20 mL of dry toluene was degassed by N_2 for 30 min and then heated at 120 ^oC overnight. The reaction mixture was cooled and diluted by DCM, followed by filtering through a Celite pack. The residue was concentrated under reduced pressure and purified by column

chromatography using hexane/EtOAc (4/1) as the eluent to afford the aimed product L-MDA-1 as a yellow powder with a yield of 94.5%.

^{1}H NMR (400 MHz, $CDCl_3$): δ = 9.42 (2H, s, NH), 8.20 (2H, s, Ar-CH_2-Ar), 7.51 (2H, s, Ar-H), 7.25 (2H, d, J = 1.44 Hz, Ar-H), 7.21 (6H, dt, J_1 = 14.96, J_2 = 2.12, Ar-H), 7.18 (2H, d, J = 2 Hz, Ar-H), 3.95 (6H, s, OCH_3), 3.90 (6H, s, OCH_3).

L-MDA-2. A mixture of L-MDA-1 (740.40 mg, 1.0 mmol), 3.4-dimethylaniline (484.72 mg, 4.0 mmol), $Pd(OAc)_2$, (22.5 mg, 0.10 mmol), Xantphos (86.79 mg, 0.15 mmol) and Cs_2CO_3 (1.96 g, 6.0 mmol) in 20 mL of dry toluene was degassed by N_2 for 30 min and then heated at 120 ^{o}C overnight. The reaction mixture was cooled and diluted by DCM, followed by filtering through a Celite pack. The residue was concentrated under reduced pressure and purified by column chromatography using hexane/EtOAc (3/1) as the eluent to afford the aimed product L-MDA-2 as a wine-red powder with a yield of 70%.

^{1}H NMR (400 MHz, $CDCl_3$): δ = 8.69 (4H, d, J = 3.6 Hz, NH), 7.99 (2H, s, Ar-H), 7.96 (2H, s, Ar-H), 7.19 (4H, d, J = 4 Hz, Ar-H), 7.14 (4H, d, J = 4.24 Hz, Ar-H), 7.10 (2H, s, Ar-H), 6.97-7.01 (4H, m, Ar-H), 3.95 (2H, s, Ar-CH_2-Ar), 3.88 (6H, s, OCH_3), 3.86 (6H, s, OCH_3), 2.27 (12H, d, J = 2.68, Ar-CH_3).

Synthesis of L-MDA-3 and L-MDA-4. L-MDA-3 was synthesized by cyclization of L-MDA-2 at the presence of PPA, and the synthesis route is illustrated in Scheme A.6.

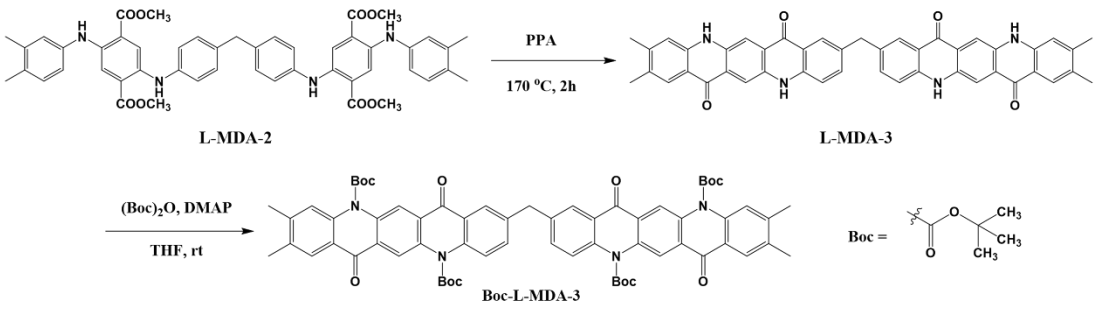

Scheme A.6 Synthesis route of L-MDA-3 and Boc-L-MDA-3.

L-MDA-3. To the vigorously stirred polyphosphoric acid (PPA, 10 mL) heated at 170 ^{o}C was slowly added the starting material L-MDA-2 (410.5 mg, 0.5 mmol). After 2 h,

the reaction mixture was cooled to room temperature, quenched with ice water and stirred overnight. The reaction mixture was then filtered, and the black solid was washed with plenty of water to remove the unreacted PPA. MeOH and DCM were used to wash away the organic byproducts. The aimed product L-BP-3 was obtained as an insoluble dark solid with a yield of 93.3%.

No NMR data was obtained due to the extremely low solubility of L-MDA-3 in common deuterated solvents.

FTIR (KBr): ν = 3403, 3270, 3161, 2969, 1605, 1584, 1550, 1474, 1342, 1263, 1146, 1085, 1047, 890, 791 cm^{-1}.

3. Synthesis of 4-bromobenzoquinone

The intermediate molecule of PhTDA monomer and PhTDA-dimer-2, 4-bromobenzoquinone was synthesized by the oxidation of 4-bromocatechol, as illustrated in Scheme A.7.

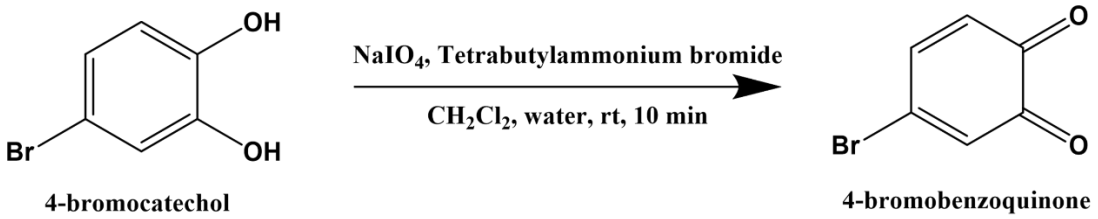

Scheme A.7 Synthesize route of 4-bromobenzoquinone.

4-bromocatechol (189 mg, 1 mmol) was first dissolved in methyl chloride (CH_2Cl_2, 3.75 mL) and kept on stirring. Then, a solution of sodium periodate ($NaIO_4$, 256 mg, 1.2 mmol) and tetrabutylammonium bromide (1.25 mg) in deionized water (3.13 mL) was added and the mixture solution was kept on stirring at ambient temperature for 15 minutes. Afterwards, the mixture was separated and the organic layer was kept, dried with sodium sulfate and concentrated under reduced pressure. The aimed molecule 4-bromobenzoquinone was obtained as a dark red solid.

4. Transient absorption spectra

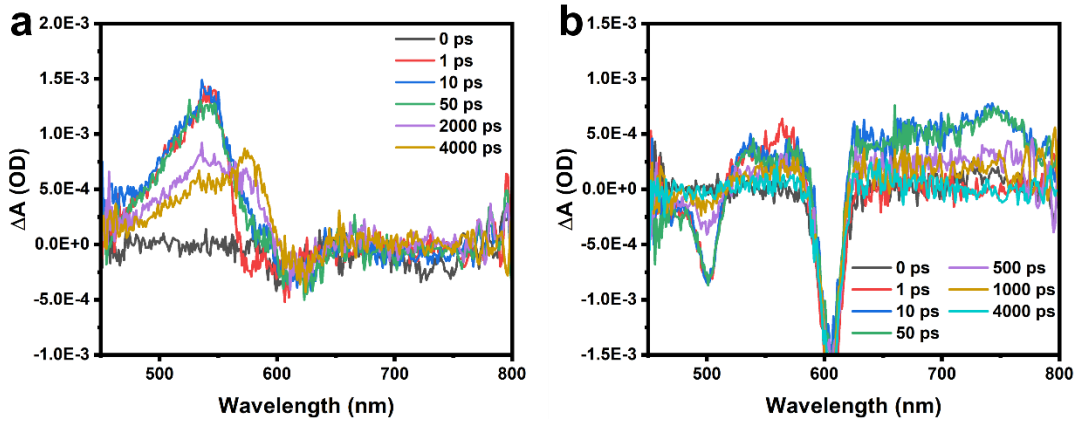

Figure A.1 Transient absorption spectra of (**a**) DAP and (**b**) DAP-dimer-1 at selected probe delay time.

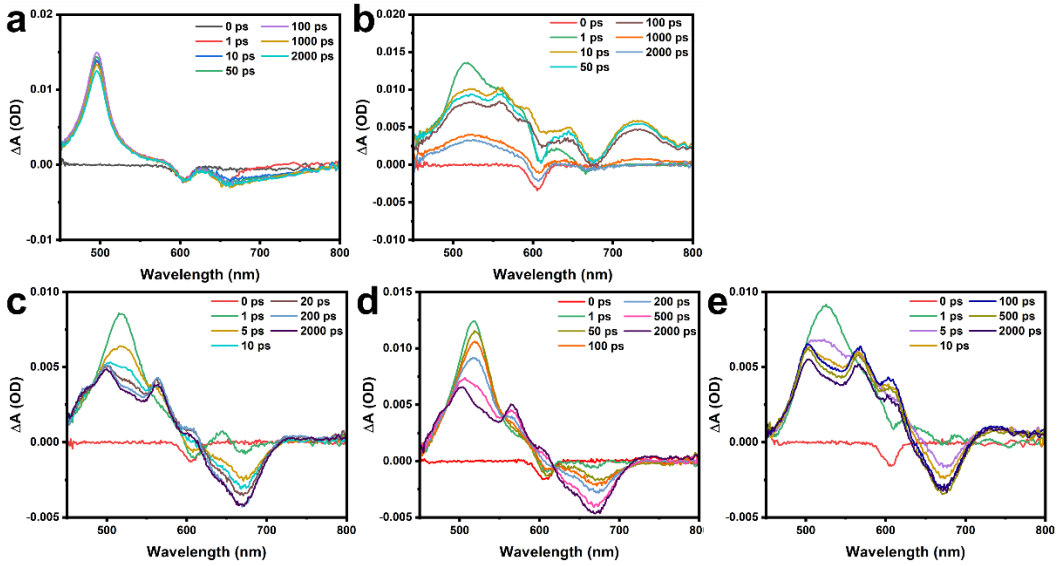

Figure A.2 Transient absorption spectra of (**a**) ATDA, (**b**) ATDA-dimer (**c**) ortho-ATDA-dimer, (**d**) meta-ATDA-dimer and (**e**) para-ATDA-dimer at selected probe delay time.

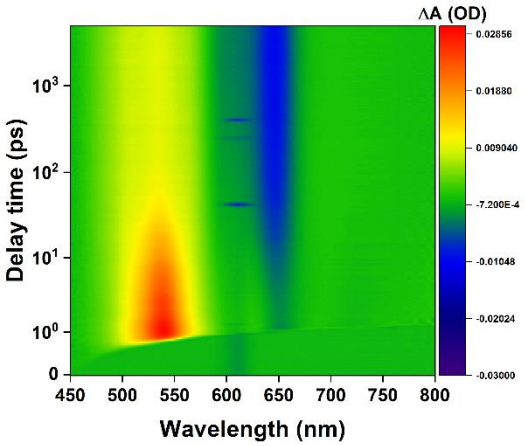

Figure A.3 Transient absorption spectra of PhTDA-dimer in pseudocolor map.

5. Triplet yield determination from GSB band.

First, the concentration of initial molecule at the ground states S_0 is assumed to be unity during the TA measurement. At the sharp of the triplet rising time after photoexcitation, the concentration of singlet S_1 is $C_1(S_1)$ and concentration of T_1 is regarded as nearly zero, thus the concentration of S_0 at this moment can be obtained as:

$$C_1(S_0) = 1 - C_1(S_1) - C_1(T_1) \quad \textbf{Equation A.1}$$

The concentration change of ground-state is obtained as

$$\Delta C_1(S_0) = C_1(S_0) - C_0(S_0) = 1 - C_1(S_1) - 0 - 1 = -C_1(S_1) \quad \textbf{Equation A.2}$$

At the long time delay, the singlet fully depopulated due to the generation of triplets by efficient SF process. Herein, the concentration of S_0 at this moment can be obtained as

$$C_2(S_0) = 1 - C_2(S_1) - C_2(T_1) \quad \textbf{Equation A.3}$$

$$\Delta C_2(S_0) = C_2(S_0) - C_0(S_0) = 1 - 0 - C_2(T_1) - 1 = -C_2(T_1) \quad \textbf{Equation A.4}$$

Therefore, the triplet yield (Φ_T) can be calculated as follows:

$$\Phi_T = \frac{C_2(T_1)}{C_1(S_1)} = \frac{-\Delta C_2(S_0)}{-\Delta C_1(S_0)} \quad \textbf{Equation A.5}$$

Since the intensity of GSB signal is proportional to the concentration of molecules at the ground state, the value of Φ_T can be evaluated from the increment of the TA intensity of GSB signal. For ortho-ATDA-dimer, the triplet rises at around 7-8 ps after excitation, and the intensity of GSB signal remained almost constant after 200 ps. Thus, the Φ_T of ortho-ATDA-dimer is calculated to be 148%. And accordingly, the Φ_T of para-ATDA-dimer is calculated to be 170%.

Chapter 6 Electronic Dynamics in Anthrathiadiazole Thin Film and Bilayer Structure with Hybrid Perovskite

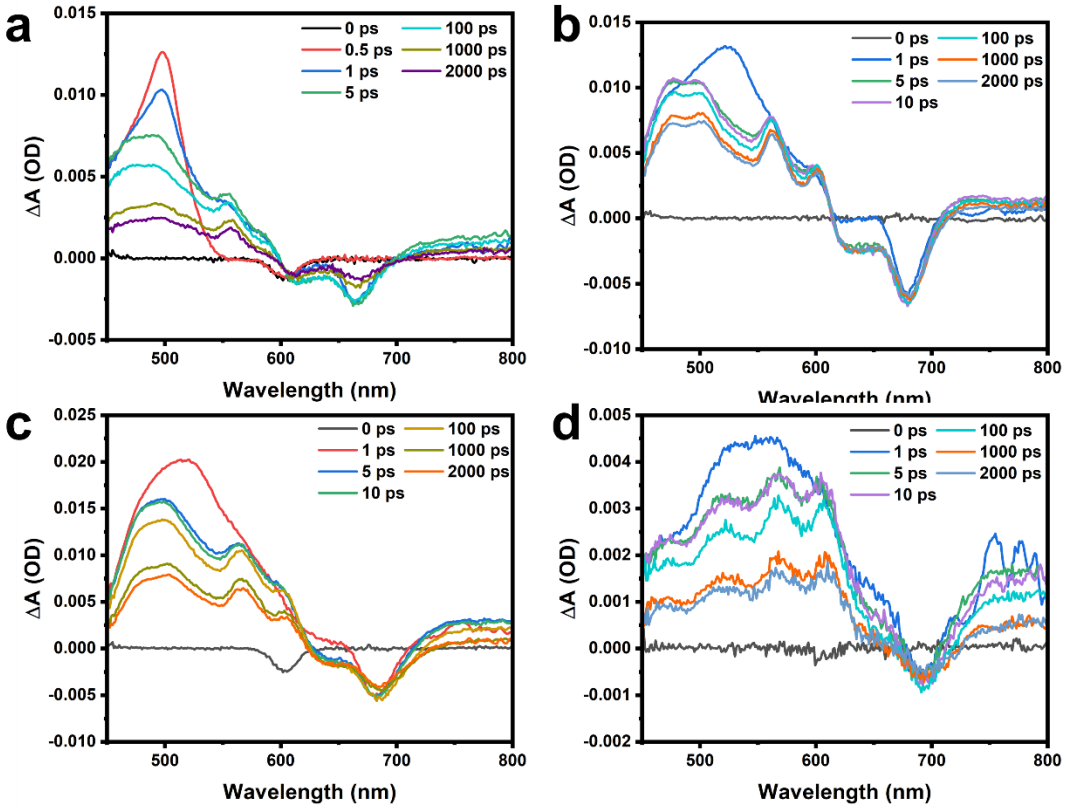

Figure A.4 Transient absorption spectra of (**a**) ATDA, (**b**) ortho-ATDA-dimer, (**c**) meta-ATDA-dimer and (**d**) para-ATDA-dimer films at selected probe delay time.

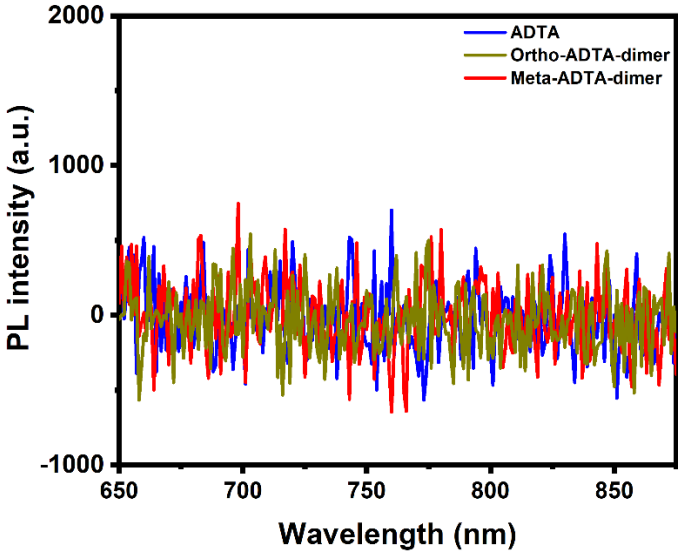

Figure A.5 Steady-state photoluminescence spectra of ATDA, ortho-ATDA-dimer and meta-ATDA-dimer films.